

GDANSK UNIVERSITY OF TECHNOLOGY
FACULTY OF OCEAN ENGINEERING AND SHIP TECHNOLOGY
SECTION OF TRANSPORT TECHNICAL MEANS
OF TRANSPORT COMMITTEE OF POLISH ACADEMY OF SCIENCES
UTILITY FOUNDATIONS SECTION
OF MECHANICAL ENGINEERING COMMITTEE OF POLISH ACADEMY OF SCIENCE

ISSN 1231 – 3998
ISBN 83 – 900666 – 2 – 9

Journal of

POLISH CIMAC

**SELECTED PROBLEMS
OF DESIGNING
AND OPERATING
TECHNICAL SYSTEMS**

Vol. 5

No. 3

Gdansk, 2010

Science publication of Editorial Advisory Board of POLISH CIMAC

Editorial Advisory Board

J. Girtler (President) - *Gdansk University of Technology*
L. Piaseczny (Vice President) - *Naval Academy of Gdynia*
A. Adamkiewicz - *Maritime Academy of Szczecin*
J. Adamczyk - *University of Mining and Metallurgy of Krakow*
J. Blachnio - *Air Force Institute of Technology*
L. Będkowski - *WAT Military University of Technology*
C. Behrendt - *Maritime Academy of Szczecin*
P. Bielawski - *Maritime Academy of Szczecin*
J. Borgoń - *Warsaw University of Technology*
T. Chmielniak - *Silesian Technical University*
R. Cwilewicz - *Maritime Academy of Gdynia*
T. Dąbrowski - *WAT Military University of Technology*
Z. Domachowski - *Gdansk University of Technology*
C. Dymarski - *Gdansk University of Technology*
M. Dzida - *Gdansk University of Technology*
J. Gronowicz - *Maritime University of Szczecin*
V. Hlavna - *University of Žilina, Slovak Republic*
M. Idzior - *Poznan University of Technology*
A. Iskra - *Poznan University of Technology*
A. Jankowski - *President of KONES*
J. Jaźwiński - *Air Force Institute of Technology*
R. Jedliński - *Bydgoszcz University of Technology and Agriculture*
J. Kiciński - *President of SEF MEC PAS, member of MEC*
O. Klyus - *Maritime Academy of Szczecin*
Z. Korczewski - *Naval Academy of Gdynia*
K. Kosowski - *Gdansk University of Technology*
L. Ignatiewicz Kowalczyk - *Baltic State Maritime Academy in Kaliningrad*
J. Lewitowicz - *Air Force Institute of Technology*
K. Lejda - *Rzeszow University of Technology*

J. Macek - *Czech Technical University in Prague*
Z. Matuszak - *Maritime Academy of Szczecin*
J. Merksiz - *Poznan University of Technology*
R. Michalski - *Olsztyn Warmia-Mazurian University*
A. Niewczas - *Lublin University of Technology*
Y. Ohta - *Nagoya Institute of Technology*
M. Orkisz - *Rzeszow University of Technology*
S. Radkowski - *President of the Board of PTDT*
Y. Sato - *National Traffic Safety and Environment Laboratory, Japan*
M. Sobieszczański - *Bielsko-Biala Technology-Humanistic Academy*
A. Soudarev - *Russian Academy of Engineering Sciences*
Z. Stelmasiak - *Bielsko-Biala Technology-Humanistic Academy*
M. Ślęzak - *Ministry of Scientific Research and Information Technology*
W. Tarelko - *Maritime Academy of Gdynia*
W. Wasilewicz Szczagin - *Kaliningrad State Technology Institute*
F. Tomaszewski - *Poznan University of Technology*
J. Wajand - *Lodz University of Technology*
W. Wawrzyński - *Warsaw University of Technology*
E. Wiederuh - *Fachhochschule Giessen Friedberg*
M. Wyszynski - *The University of Birmingham, United Kingdom*
M. Zablocki - *V-ce President of KONES*
S. Żmudzki - *West Pomeranian University of Technology in Szczecin*
B. Żółtowski - *Bydgoszcz University of Technology and Life Sciences*
J. Żurek - *Air Force Institute of Technology*

Editorial Office:

GDANSK UNIVERSITY OF TECHNOLOGY
Faculty of Ocean Engineering and Ship Technology
Department of Ship Power Plants
G. Narutowicza 11/12 80-233 GDANSK POLAND
tel. +48 58 347 29 73, e – mail: sek4oce@pg.gda.pl

www.polishcimac.pl

This journal is devoted to designing of diesel engines, gas turbines and ships' power transmission systems containing these engines and also machines and other appliances necessary to keep these engines in movement with special regard to their energetic and pro-ecological properties and also their durability, reliability, diagnostics and safety of their work and operation of diesel engines, gas turbines and also machines and other appliances necessary to keep these engines in movement with special regard to their energetic and pro-ecological properties, their durability, reliability, diagnostics and safety of their work, and, above all, rational (and optimal) control of the processes of their operation and specially rational service works (including control and diagnosing systems), analysing of properties and treatment of liquid fuels and lubricating oils, etc.

All papers have been reviewed

@Copyright by Faculty of Ocean Engineering and Ship Technology Gdansk University of Technology

All rights reserved

ISSN 1231 – 3998

ISBN 83 – 900666 – 2 – 9

Printed in Poland

CONTENTS

S. Borowski: ANALYSIS OF DISTRIBUTION OF ADDITIVES IN ROUND BALES OF MOIST HAY	9
A. Cichański, T. Tomaszewski: NUMERICAL VERIFICATION OF QUASI-STATIC STRENGTH OF THE HORIZONTAL BICYCLE WELDED FRAME	13
A. Cichański, M. Wirwicki: ERGONOMICS ANALYSIS OF ANTHROPO-TECHNICAL SYSTEMS IN THE ENVIRONMENT OF CATIA PROGRAM	19
T. Giętka, S. Dymski: THE APPLICATION OF THE COMPUTER PROGRAMME TO THE ANALYSIS OF MICROSTRUCTURE OF THE MATRIX OF AUSTEMPERING DUCTILE IRON	27
H. Holka: DOUBLE DYNAMIC VIBRATION ABSORBER	37
A. Kaźmierczak, M. Reksa, P. Moczko, R. Wróbel: COMPARATIVE ANALYSIS OF THE BODY VIBRATIONS OF NEW CARS WITH A SPARK-IGNITION ENGINE WITH AND WITHOUT A SUPERCHARGER	43
A. Kaźmierczak, M. Reksa, P. Moczko, R. Wróbel: COMPARATIVE ANALYSIS OF THE VIBRATIONS OF A SPARK-IGNITION ENGINE WITH AND WITHOUT SUPERCHARGING, MOUNTED IN NEW MOTOR VEHICLES	49
P. Kolber: INFLUENCE OF UNBALANCE OF LOADS ON QUALITY OF ELECTRIC ENERGY IN A LOW VOLTAGE LINE	55
B. Landowski, R. Poliński: PARAMETERIZATION OF A TECHNICAL OBJECT IN SOLID EDGE	63
B. Ligaj: GERALIZATION OF GOODMAN'S DIAGRAM ON THE HIGH-CYCLE FATIGUE RANGE	71
B. Ligaj: IMPACT OF THE METHOD OF ELABORATION OF A LOAD SPECTRUM ON THE RESULTS OF THE CALCULATION OF S355J0 STEEL FATIGUE LIFE ...	79
Z. Ławrynowicz: TEM INVESTIGATIONS OF DAMAGE STRUCTURE OF PURE GOLD AFTER NITROGEN PLASMA IMMERSION ION IMPLANTATION (PIII) USING RF DISCHARGES	87
A. Mazurkiewicz, T. Topoliński: RELATIONSHIP BETWEEN BMD, APPARENT AND ASH DENSITY OF HUMAN TRABECULAR BONE	95
A. Mazurkiewicz, T. Topoliński, A. Cichański, K. Nowicki: RELATIONSHIP BETWEEN FATIGUE LIFE AND STRUCTURAL INDICES OF HUMAN TRABECULAR BONE	101
T. Mikołajczyk: ROBOT APPLICATION TO SURFACE FINISH MACHINING	107
A. Mroziński: MODELLING OF WASTE-PAPER STOCK TREATMENT PROCESS IN DISC REFINERS	113

S. Mroziński, S. Dymski: PROPERTIES AND MICROSTRUCTURE OF BRASS UNDER VARIABLE LOADING	121
T. Paczkowski: NUMERICAL SIMULATION FOR ECM MACHINING OF NONLINEAR SHAPED SURFACES	133
K. Pepliński, A. Mozer: ANSYS-POLYFLOW SOFTWARE USE TO SELECT THE PARISON DIAMETER AND ITS THICKNES DISTRIBUTION IN BLOWING EXTRUSION	143
R. Polasik: DRY CONSTANT-LOAD STEEL ALUMINA GRINDING ENERGY PARTITION	149
J. Rudnicki: THE CONCEPTION OF DECISION-MAKING SUPPORT SYSTEM FOR COMPLEX ENERGETIC SYSTEM ON EXAMPLE OF SHIP PROPULSION SYSTEM	155
J. Sawicki: ECM MACHINING OF CURVILINEAR ROTARY SURFACES	167
J. Sempruch, P. Strzelecki: VERIFICATION OF SELECTED METHODS FOR RAPID DETERMINATION OF WÖHLER CURVE CONSIDERING HIGH-CYCLE FATIGUE	177
D. Skibicki: FATIGUE CRITERION BASED ON THE HUBER-VON MISES-HENCKY CRITERION FOR NON-PROPORTIONAL LOADINGS	187
R. Sołtysiak: LOCAL STRAIN ANALYSIS IN FRICTION STIR WELDED 2024-T3 ALUMINIUM JOINTSUNDER CICLIC LOADING	193
D. Sykutera, M. Bieliński: THE USE OF INJECTION MOULDING PROCESS SIMULATION SOFTWARE CADMOULD FOR INJECTION MOULD DESIGNING	201
D. Sykutera: PROPERTIES OF SOLID POLYURETHANE RECYCLAT OBTAINED IN THE COMPACT MULTISTAGE SYSTEM OF CUTTING MILLS	207
G. Szala: EMPIRICAL EXAMINATION OF THE IMPACT OF THE CYCLE ASYMMETRY COEFFICIENT OF THE LOAD ON THE FATIGUE LIFE OF S355J0 STEEL	215
V. Tesař, K. Peszyński: SYNTHETIC JET APPLIED TO DETECT POTENTIAL TERRORISTS	221
V. Tesař, K. Peszyński: EXPERIMENTS WITH SYNTHETIC JET FOR DETECTING POTENTIAL TERRORISTS	229
M. Trepczyńska-Łent: COMPETITIVE GROWTH AND COUPLET GROWTH ZONE IN EUTECTIC ALLOYS IN DIRECTIONAL SOLIDIFICATION	235
H. Tylicki: RULES IN THE GENESIS OF MACHINES STATE	243
H. Tylicki, R. Bochen: MODERNIZATION OF THE SYSTEM MAINTENANCE THE MACHINES LINE HOR 6000	249
M. Zastempowski, A. Bochat: ANALYSIS OF THE KNIFE-BAR DYNAMICS MOVEMENT IN CUTTING UNIT	257
J. Zimniak: IMPORTANCE OF COMMINUTION IN PLASTICS PROCESSING	265



Introduction

In contemporary science we can observe higher and higher specialization in particular scientific disciplines. The specialization causes that research is conducted with not proper consideration of the knowledge from other scientific disciplines even if they belong to the same field of knowledge. Thus, specialists dealing with a subject from the „machine building and operating” discipline, study reluctantly the achievements of the related disciplines such as: „automation and robotics”, „electronics”, „electrical engineering”, „energetics”, „computer science”, „mechanics” or “ transport”. Much more unconcerned is the knowledge from such disciplines as: „biocybernetics & biomedical engineering” and „biotechnology”, although they are classified to the field of knowledge defined as „technical sciences”. The situation is justifiable. It follows from the anxiety that studying developments in other disciplines may cause falling behind with developments in the discipline practiced by the given scientist. In consequence making a Doctoral Thesis is easier but Habilitation Thesis – much more difficult. Habilitation qualification can be achieved among others when a candidate in his/her research accomplishments can show application to for the first time the knowledge from any other field of knowledge, like for example. „mathematical sciences”.

In each scientific discipline, independently which field of knowledge it belongs to, the science is being developed in result of applying proper scientific methods. However, apart from the specific methods, in each scientific discipline there are also used deductive and inductive methods if the created knowledge is supposed to be of essential for science cognitive properties. Deductive methods are used when it is necessary to prove a theorem. When a hypothesis (hypotheses) is (are) to be verified we apply inductive or deductive methods. As a rule the importance of the method called analogy is not appreciated. The analogy, however, enables searching for the common *rightness (premise, cause)* characterizing different research objects (being characteristic for particular scientific disciplines), while deduction consists in matching *consequence (result, conclusion)* to *rightness*, and *induction* – in matching *rightness* to *consequence*.

From this reason it can be interesting for many scientists and at the same time beneficial for development of technical sciences when the *Journal of POLSH CIMAC*, which is destined for papers concerning the knowledge enclosed in „machine building and operating” discipline, will present also these papers which are classified to the other scientific disciplines from the field of knowledge called „technical sciences”, including “biocybernetics & biomedical engineering” and „biotechnology”. Among such papers placed in this journal are: *Analysis of distribution of additives in round bales of moist hay*, *Numerical verification of quasi-static strength of the horizontal bicycle welded frame*, *Ergonomics analysis of anthropo-technical systems in the environment of CATIA program*, *The application of the computer programme to the analysis of microstructure of the matrix of austempering ductile iron*, *Double dynamic vibration absorber*, *Comparative analysis of the body vibrations of new cars with a spark-ignition engine with and without a supercharger*, *Comparative analysis of the vibrations of a spark-ignition engine with and without supercharging, mounted in new motor vehicles*, *Influence of unbalance of loads on quality of electric energy in a low voltage line*, *Parameterization of a technical object in solid*

edge, Generalization of goodman's diagram on the high-cycle fatigue range, Impact of the method of elaboration of a load spectrum on the results of the calculation of S355J0 steel fatigue life, TEM investigations of damage structure of pure gold after nitrogen plasma immersion ion implantation using RF discharges, Relationship between BMD, apparent and ash density of human trabecular bone, Relationship between fatigue life and structural indices of human trabecular bone, Robot application to surface finish machining, Properties and microstructure of brass under variable loading, Modelling of waste-paper stock treatment process in disc refiners, Numerical simulation for ECM machining of nonlinear shaped surfaces, ANSYS-POLYFLOW software use to select the parison diameter and its thickness distribution in blowing extrusion, Dry constant-load steel alumina grinding energy partition, ECM machining of curvilinear rotary surfaces, Verification of selected methods for rapid determination of Wohler curve considering high-cycle fatigue, Fatigue criterion based on the Huber-Von Mises-Hencky criterion for non-proportional loadings, Local strain analysis in friction stir welded 2024-t3 aluminium joints under cyclic loading, Properties of solid polyurethane recycled obtained, In the compact multistage system of cutting mills, The use of injection moulding process simulation software CadMould for injection mould designing, Empirical examination of the impact of the cycle asymmetry coefficient of the load on the fatigue life of S355J0 steel, Experiments with synthetic jet for detecting potential terrorists, Synthetic jet applied to detect potential terrorists, Competitive growth and couplet growth zone in eutectic alloys in directional solidification, Rules in the genesis of machines state, Modernization of the system maintenance the machines line HOR 6000, Analysis of the knife-bar dynamics movement in cutting unit, Importance of comminution in plastics processing.

In that case we cannot exclude that after reading at least a few of the papers mentioned above, many readers will discover new opportunities for developing their own interests. That can happen, although the journal is addressed mainly to the people dealing with research on combustion engines and the systems ensuring their correct operation.

This is just what I cordially wish to all readers of our journal.

Editor-in-Chief
prof. Jerzy Girtler



ANALYSIS OF DISTRIBUTION OF ADDITIVES IN ROUND BALES OF MOIST HAY

Sylwester Borowski

*University of Technology and Life Sciences
ul. Kaliskiego 7, 85-796 Bydgoszcz, Poland
tel.: +48 52 3408208, fax: +48 52 3408208
e-mail: sylwa@utp.edu.pl*

Abstract

This article shows the results of studies regarding the distribution of microbiological additive Inoculant 1155 in bales of moist hay formed in round baler. Its greatest amount was observed in the central part of a bale. An improvement of the irregularity index was observed during storage. The reproduction of bacteria reduces the negative effects of errors while applying the preparation. The applied technology assures obtainment of the good quality of the fodder from moist hay without energetistic stocks on his drying.

Keywords: alfalfa, microbiological additives, moist hay

1. Introduction

Application of conservation additives in hay harvest technology enables hay harvest from alfalfa with increased moisture content. The enlargement moisture harvested hay it is allowed from 15 to 24 % [5, 9]. This method of moist hay conservation is energy saving which provides gaining more dry matter and feed from one hectare [1, 7].

Effectiveness of the additive depends on its given amount distribution in the harvested hay, especially in the form of a round bale [3], [4]. Existence in the bale of moist spots which have no contact with the additive can lead to formation of harmful bacteria clusters which can cause destruction of the whole bale or even its self ignition. So the harvested fodder can be harmful for animals [6].

The paper aims at analyzing non uniformity of microbiological granulated material distribution in a bale of moist hay.

2. Material and methods

The plant material used for the tests was alfalfa (*Medicago media*) in the phase of its blossom beginning. The hay moisture while harvesting was 22%. The average crop of the green matter was for I swath 440 q ha. Microbiological granulated preparation Inoculant 1155, produced by Pioneer company, was being added to moist hay. The additive was applied in the amount of 1 kg per 1 tones. It contained drought of natural bacteria *Bacillus spp.* and calcium carbonate. This is the bacterium stepping out on plants of lucerne however in small quantities. The additive had the following properties: the average radius of granules 0.87mm; moisture content of 2.5%; density of

1040 kg m⁻³; number of living bacteria in colony forming units (cfu) 108 cfu g⁻¹ (the number guaranteed by the producer). The preparation was being added by means of an applicator Gandy Jumbo (Fig. 1), mounted to a round baler Z-279/1.

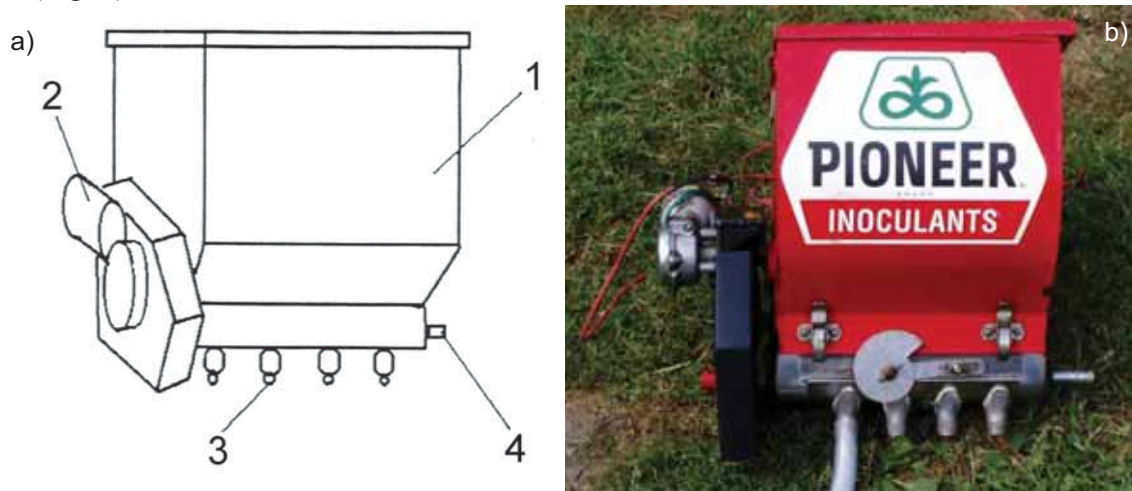


Fig. 1. Applicator "Gandy Jumbo": a - the scheme, b - view, 1 - the bulb of the preparation, 2 - electric engine with chain transmission, 3 - nozzles, 4 - the shaft raking out

The assessment of the preparation distribution non uniformity was performed with the use of two methods:

- **directly** through an analysis of the preparation marker particles, for the samples of hay taken from bales, just right after the harvest; the assessment was made in cooperation with the Department of Chemical Engineering and Environment Protection. A method of marking biologically active preparations with n-hexane, developed specially for this research, was used. Samples were taken from 15 places of the bale.
- **indirectly**, through quantitative assessment of *Bacillus pumilus* bacteria samples of hay taken 15 days after harvesting from 5 different places of bales according the scheme of single envelope [2]. The amount of bacteria was made in the Department of Microbiology at the University of Technology and Life Sciences [8].

Uniformity of the additive distribution in the hay was characterized by a mixing non uniformity index (variability coefficient) K:

$$K = \frac{\varphi}{\bar{x}} \cdot 100 \%, \quad (1)$$

where:

φ - standard deflection,

\bar{x} - mean arithmetic content.

3. Results and discussion

The results are presented in the form of histograms in Figure 2.

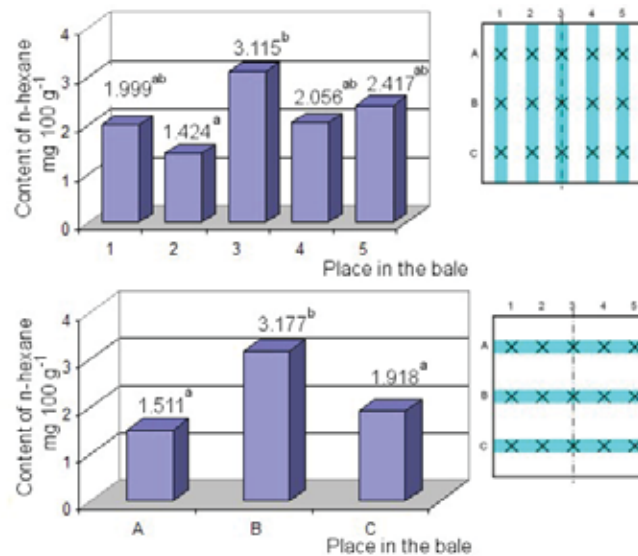


Fig. 2 Histograms of n-Hexane content in hay samples (mean value). a, b - differences are statistically significant with relevance level $p \leq 0.05$

As figure 1 demonstrates, the measurement, vertical planes 1,3,4,5 do not vary significantly from each other in terms of n-Hexane content. No statistically significant differences between vertical planes 1,2,4,5 were found, either Smallest Difference of Significance ($NIR_{0.05} = 1.136$). The differences occurred only between vertical planes 2 and 3. It indicates small differences in the amounts of the applied preparation. Statistical differences between horizontal planes A and C were not found. Horizontal plane B was different ($NIR_{0.05} = 0.749$) from the other ones, and the highest amount of n-Hexane was found in some places, there. The calculated index of distribution non uniformity was $K_1 = 61.1\%$.

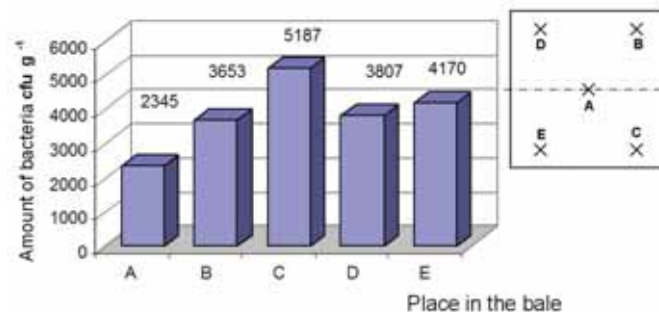


Fig. 3 Amount of bacteria in hay samples obtained in the studies (mean value)

As figure 2 shows, the smallest number of bacteria was found in the middle of the bale (point A) whereas higher values were found in its external layers. Apart from all the significant differences between the number of bacteria in the examined samples, the statistical analysis did not revealed differences. For relevance level $p \leq 0.05$ the Smallest Difference of Significance ($NIR_{0.05}$) was 3166 cfu g⁻¹. The calculated index of bacteria distribution non uniformity (variability coefficient) was $K_2 = 53.9\%$.

4. Conclusion

- Chemical assessment showed that the best quality feed resulted when the hay had a moisture content of 22%.
- The biggest amount of the preparation was found in the middle part of the bale. An influence of the bale local thickness on its content has been observed.

- Multiplying bacteria can penetrate a bale of hay, occurring in bigger amounts in moist places. Their behavior makes it possible to minimize application errors which affect the preparation distribution uniformity in the bale.
- Improvement of the preparation distribution non uniformity index has been observed.

References

- [1] Bernes, G., Persson, Waller, K., Jensen, S.K., *Hay and silage as vitamin sources in organic sheep production*, Proc. of the 22nd General Meeting of the European Grassland Federation, pp. 565-567, June 2008, Uppsala.
- [2] BN-74-9162-011.
- [3] Dulcet, E., *Quality assessment of the mixing of vegetable with additives in a forage harvester* J. agric. Engng Res. 79 (3), pp. 275-282, 2001.
- [4] Dulcet, E., Woropay, M., Kaszkowiak, J., *Effect on silage quality o moisture content in a baled crop with morphological and enzymatic additives during harvesting*, Proc. of the Agricultural Engineering into the Third Millennium. Ag Eng., pp. 87-88, University of Warwick, UK, 2000.
- [5] Dulcet, E., Mikołajczak, J., Olszewski, T., *Technika zastosowania konserwantów przy zbiorze wilgotnego siana*, Wyd. Uczelniane ATR w Bydgoszczy, 2002.
- [6] Meisser, M., *Konservierung von Feuchtheu*, AgrarForschung 8 (2), pp. 87-92, 2001.
- [7] Mir, Z., Jan, E. Z., Robertson, J.A., Mir, P.S., McCartney, D.H., *Effects of microbial inoculant and moisture content on preservation and quality of round-baled alfalfa*, Canadian Journal of Animal Science 75, pp. 15-23, 1995.
- [8] PN-R-647911.
- [9] Tomes, N.J., Shelley, T., Allen, G., Badner, G., Price, J., Soderlund S., *Preservation of alfalfa hay by microbial inoculation at baling*, Landbauforschung Volkenrode, Sonderheft 123, pp. 344-347, 1991.



NUMERICAL VERIFICATION OF QUASI-STATIC STRENGTH OF THE HORIZONTAL BICYCLE WELDED FRAME

Artur Cichański, Tomasz Tomaszewski

University of Technology and Life Sciences in Bydgoszcz
ul. Kaliskiego 7, 85-796 Bydgoszcz, Poland
tel.: +48 52 3408202, fax: +48 52 3408245
e-mail: tomasz.tomaszewski@utp.edu.pl

Abstract

Horizontal bicycles can be classified as means of transport powered by one's own muscles that are in the lead as regards low aerodynamic drag, riding comfort and safety. This kind of construction is influenced by load that in the case of inadequately engineered bicycle frame may lead to the construction damage. To prevent this, strength and stiffness analyses are conducted whose boundary conditions correspond with these during real exploitation. Various extrusion profiles of the bicycle frame are connected with the use of welding technique which additionally makes us conduct analysis strength of welded joints. These kinds of calculations are carried out with the use of the software basing on the finite element method making it possible to gain stress and deformation values for complex cases of frame load and whose results cannot be obtained in an analytical way. The frame of the horizontal bicycle was put to analysis in the three different load variants. We achieved maximum deformation, stress in the critical points and in the welding joints of the frame, which then were compared to the allowable values. The correct verification of the received values contributed to determining joints vulnerable to damaging and modifying the frame construction to minimize the possibility of its destruction.

Keywords: *finite element method, horizontal bicycle, welded joints calculation, strength of welded frame*

1. Introduction

One of the means of transport that doesn't consume any fuel, doesn't emit any pollution or make noise is a bicycle. It is easily accessible and widely used thanks to its simplicity, by all people who want to move only thanks to their muscles power [7, 9]. The strivings of the manufacturers and construction designers to reduce aerodynamic drag, improve comfort and riding safety contributed to the creation of horizontal bicycles. These are not numerous solutions and are used because of their constructions, which are often influenced by unpredictable loads [8]. The main strength problem for that construction is correct designing of a frame. That is the most important part ensure safe riding.

One of the features of a correctly applied mechanical construction is meeting the strength conditions, with boundary conditions corresponding to real exploitation conditions. In order to check them, the construction must be put to strength and stiffness analysis. In the case of the analysis of welded parts, it is necessary to carry out calculations of the welded joints. There are geometric and structural notches leading to the stress concentration and making the welded joints the weakest area of the construction. The analysis of such problems is very complicated as the strength of a given joints depends on many factors: welding stress, chemical composition of welded materials, process of welding, local change in mechanical characteristics within the heat

influence range [1, 2]. Most of them are included in the standardized calculation algorithms by applying correct coefficients depending on the kind of welded joints, border of plasticity of the material of original joints [3, 5].

2. Static strength of welded joints

The calculations of welded joints in the process of designing consist in a correct determining of the size of the connection. That must ensure work safety of the construction. When designing welded joints, one should take into account the minimalisation of the connection size, simple shape and applying optimum production technique as regards its costs [2].

In order to design a welded construction, there are various norms that can be used to check the strength of welded joints. They include procedures used to calculate the strength of a construction such as Polish Norms (PN-90/B-03200 [3], PN-82/S-10052 [4]), Eurocode 3 [5]).

Static strength of welded joints is calculated according to the instructions contained in the above norms. For the purpose of this calculation, the norm [3] which defines the condition of strength for fillet welds in a complex state of stress was used (Fig. 1):

$$\sigma_{red} = \kappa \sqrt{\sigma_{\perp}^2 + 3(\tau_{\parallel}^2 + \tau_{\perp}^2)} \leq \alpha_{\perp} \frac{R_e}{x} \quad (1)$$

where:

σ_{\perp} - the normal stress perpendicular to the throat,

σ_{\parallel} - the normal stress parallel to the axis of the weld,

τ_{\perp} - the shear stress (in the plane of the throat) perpendicular to the axis of the weld,

τ_{\parallel} - the shear stress (in the plane of the throat) parallel to the axis of the weld,

α_{\perp} - factor of strength weld.

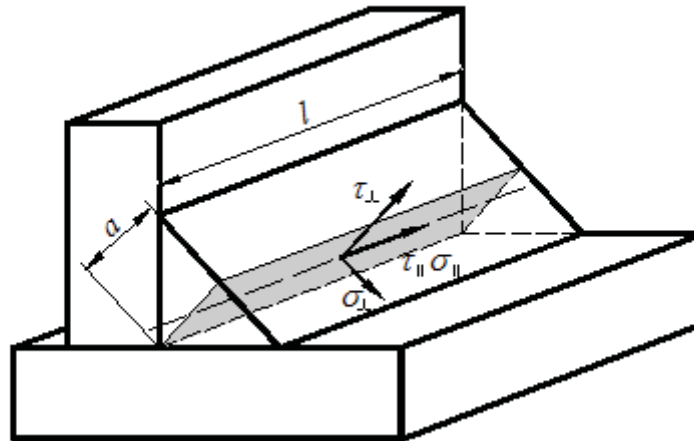


Fig. 1. Level of stress in fillet weld: a – calculation thickness of weld, l – length of weld [3]

3. Strength and stiffness analysis of the bicycle frame

Numerical analyses of stress and deformation were carried out with the use of ANSYS Workbench software that bases on the finite element method. The application of this method is connected with many conditions that influence final results connected with the possibility of a slight mistake. In order to eliminate this problem, numerical calculations for simple variants of this

issue were carried out and these results were verified by analytical calculations. The parameters of the discrete model were defined (type, size of element, kind of stress) for which results with slight relative error were obtained. In the analysis of the complex model, the same parameters of the discrete model were applied.

The calculations of the complex problem were carried out for the construction of the horizontal bicycle frame consisting of closed sections made of aluminum 6061 (PA45) in the T6 state ($R_e = 240$ MPa). The profiles were connected by welded joints. The geometry and boundary conditions of the frame are presented in Fig. 2. The bicycle is powered by solar energy stored in a battery powering an electric engine [6].

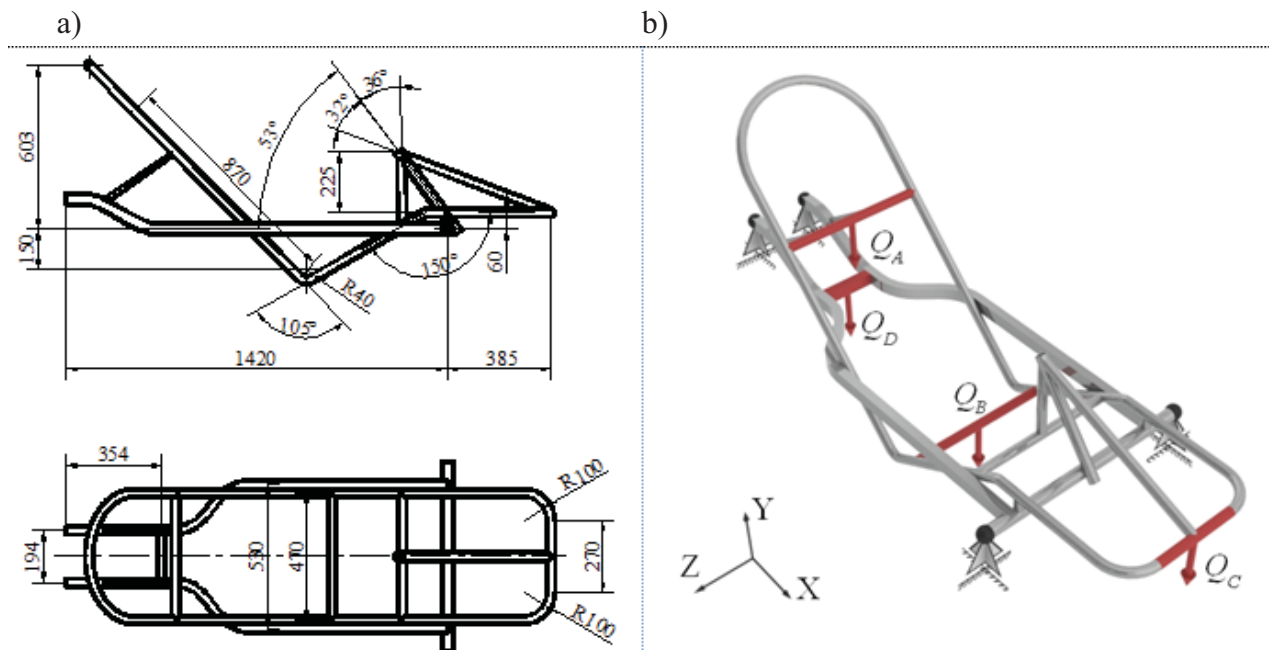


Fig. 2. A diagram of the frame: a) geometric features, b) boundary conditions ($A \div D$ – profiles under load)

In the analysis of the bicycle frame, the supports are in the place of fixing wheels which were deprived of some freedom in the vertical direction and turn around this direction. The frame load results mainly from the cyclist's and battery weight (Q_D).

The stress value is strictly dependent on the cyclist body posture. A slight transfer of the body weight to the front or backwards will considerably change the frame load. During riding, it is also possible to change support points which take place while riding in standing position. Most of the mentioned problems, make it possible to define correctly load of the frame: mountain bikes, road bikes, bmx, etc.

In the case of the quasi-static bicycle analyze, the determination of load values is possible as the frame construction makes cyclist keep one position while normal riding (Fig. 4) additionally limiting body movements by the application of safety belts. In order to determine the distribution of forces exerted by a sitting person, the following measures were made: a person with a weight of mass $m_r = 80$ kg (average weight of an adult) sitting on a saddle-chair (Fig. 3). The leaning angles α_{B1} , α_{B3} correspond to the location of a saddle-chair in the designed bicycle [6].

The analysis was carried out for three different stress variants, when a cyclist:

1. Sits on a saddle-chair in a riding position.
2. Is in the process of getting into the saddle-chair load only the central part of the saddle-chair.
3. Is sitting on a saddle-chair of the bicycle, that is parked on a leaning area of 34° (maximum angle when the bicycle doesn't capsizes).

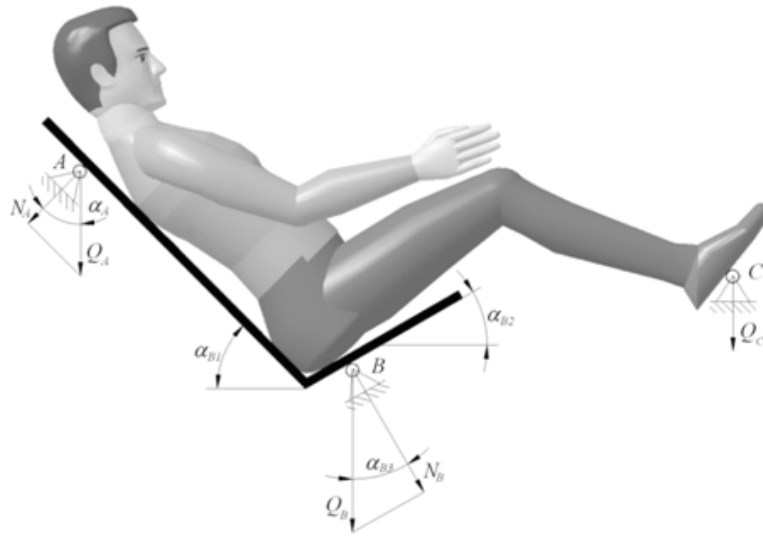


Fig. 3. A diagram of determining forces acting on the frame: $\alpha_A = \alpha_{B1} = 45^\circ$, $\alpha_{B2} = \alpha_{B3} = 30^\circ$

Table 1. Load values of the frame construction

Variant	Force [N]											
	Q _A			Q _B			Q _C			Q _D		
1	360			590			120			100		
2	0			1000			0			100		
3	0X	0Y	0Z	0X	0Y	0Z	0X	0Y	0Z	0X	0Y	0Z
	62	298	201	102	489	330	21	99	67	17	83	56

In the ANSYS Workbench software the strength and stiffness analyses for frame geometry modeled by shell elements (Shell181) were made. Example results in the form a distribution of deformation map are presented on Fig. 4. Reduced stress was determined for components of stress measured at the most strained parts of the frame (Fig. 5) and then compared to the allowable values (Tab. 2).

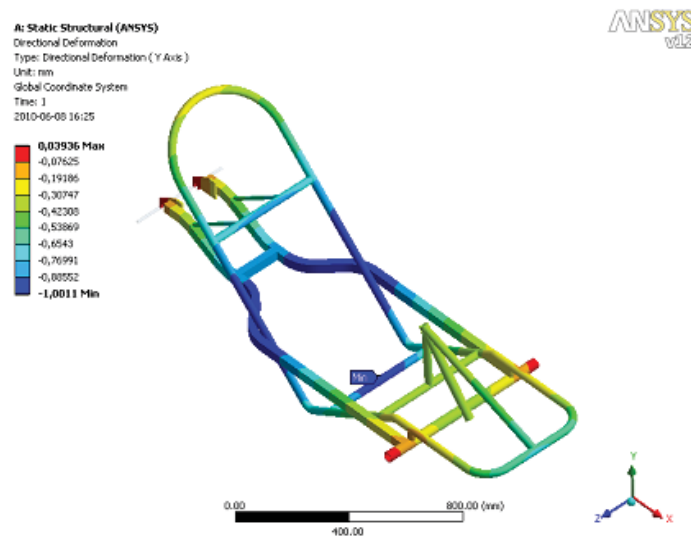


Fig. 4. A deformation map of the frame (variant 1)

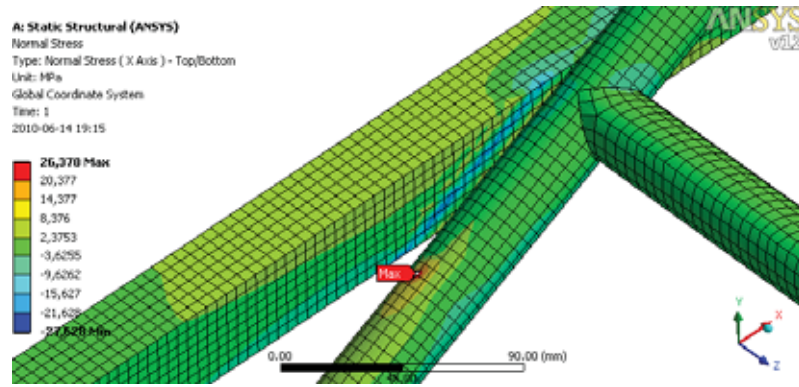


Fig. 5. A map stress in the place of maximum stress

Table 2. A comparison of stress values in the most strained point

Var.	Def. [mm]	Stress [MPa]							σ_{red}	σ_{allow}
		σ_x	σ_y	σ_z	τ_{xy}	τ_{yz}	τ_{xz}			
1	1.001	36.378	9.39	12.951	13.56	3.054	4.295	31.023	60	
2	1.313	35.336	12.271	20.496	17.205	4.318	7.378	31.041	60	
3	1.14	44.611	21.713	19.114	28.095	10.35	12.234	46.473	60	

4. Strength of the welded joints

The next stage is the verification of the strength of welded joints. A new applied method was the method of determining stress in the welded joints, which is not well described in the subject literature. A procedure giving correct values of stress in welded joints of the bicycle frame has been worked out. The numerical calculations were based on the application of contact elements responsible for undividable surface connection in the place of welded joint. Correct application of the contacts led to a fast and simple reading out of the stress in the welded joints (Fig. 6), whose determination in an analytical way is very complicated.

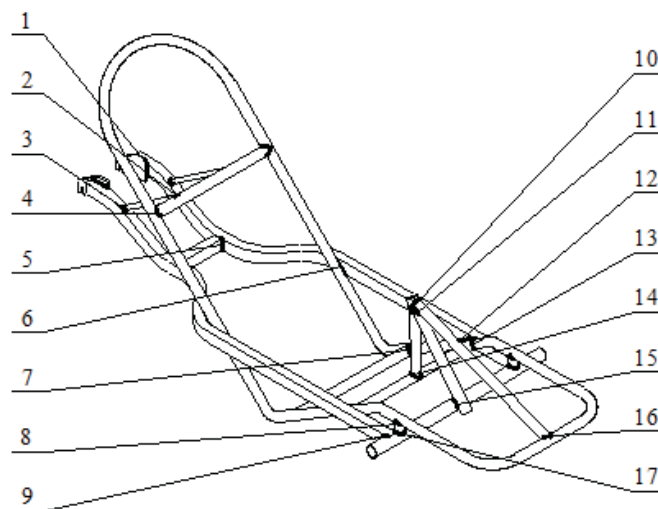


Fig. 6. The placement of welded joints in the frame construction

The values from the obtained distribution of stress in contact elements were averaged with the use of numerical integration. The obtained values for the most stressed joints were presented in Table 3. Reduced stress (σ_{red}) were compared to the allowable stresses.

Table 3. A comparison of stress values for the most strained weld joints

Nr	Stress [MPa]									σ_{allow}
	variant 1			variant 2			variant 3			
	σ_{\perp}	τ_{\parallel}	σ_{red}	σ_{\perp}	τ_{\parallel}	σ_{red}	σ_{\perp}	τ_{\parallel}	σ_{red}	
4	3.074	10.205	12.559	18.231	7.961	16.001	35.91	18.006	33.294	42
6	22.693	5.662	17.305	7.212	7.451	10.349	9.719	7.681	11.533	42
7	22.975	10.33	20.384	35.256	15.983	31.378	48.104	10.116	35.837	42
8	14.723	3.341	11.074	22.414	6.615	17.621	30.478	8.925	23.922	42
13	11.626	11.583	16.231	29.597	13.048	26.067	9.267	18.098	22.881	42
17	8.441	8.789	12.185	7.84	9.633	12.905	16.41	17.739	24.383	42

5. Summary

The frame construction of a horizontal bicycle was analyzed as regards its strength and stiffness For 3 different variants of boundary conditions. The stress and deformation values obtained from numerical analyses for frame geometry are within allowable values. The analyses verifying the strength of weldment have also been carried out. In order to do it, a procedure of determining stress in welded joints by applying suitable contact elements was prepared. Adequate processing of the results allowed us to obtain values with only slight mistakes, which proved the correctness of the applied method. The stress values in various welds are lower than the allowable ones. The analysis results showed a correct size of the applied frame sections in given conditions with static strain. To complete the construction calculations, dynamic analyses for strain occurring in extreme conditions are planned.

References

- [1] Ferenc, K., *Konstrukcje spawane. Połączenia*, WNT, Warszawa, 2000.
- [2] Pilarczyk, J., *Poradnik inżyniera. Spawalnictwo - Tom 1*, WNT, Warszawa, 2003.
- [3] PN-90/B-03200 *Konstrukcje stalowe – Obliczenia statyczne i projektowanie*.
- [4] PN-82/S-10052 *Obiekty mostowe – Konstrukcje stalowe – Projektowanie*.
- [5] Eurocode 3: *Design of Steel Structures*, Part 1-8: Design of Joints.
- [6] Studziński, R., *Rower solarny - projekt konstrukcji mechanicznej*, Uniwersytet Technologiczno – Przyrodniczy, Praca magisterska, Bydgoszcz, 2008.
- [7] Wilson, D.G., *Bicycling science*, MIT PRESS, Massachusetts, 2004.
- [8] <http://www.ihpva.org/> (update: 02.2010).
- [9] <http://www.wrower.pl/> (update: 06.2010).



ERGONOMICS ANALYSIS OF ANTHROPO-TECHNICAL SYSTEMS IN THE ENVIRONMENT OF CATIA PROGRAM

Artur Cichański, Mateusz Wirwicki

University of Technology and Life Sciences in Bydgoszcz
ul. Kaliskiego 7, 85-796 Bydgoszcz, Poland
tel.: +48 52 3408202, fax: +48 52 3408245
e-mail:mateusz.wirwicki@utp.edu.pl

Abstract

Every engineer designer when designing the interior of a passenger car must obey certain norms and regulations. When engineer designer introduces innovative solutions of different equipment in the passenger car interior, he must create comfortable conditions for a driver. The article describes the applied issues concerning the interior ergonomics of a passenger car. A designer using CATIA type programs can put the designed model of car interior to work ergonomics analysis for basic service activities of a car driver. A male and female dummies from the European population were created for the purpose of conducting the analysis. The interior of a passenger car was designed and its most important elements were described. The engineer designer having general dimensions of the interior starts analysis which will be a base for the change in cabin dimensions. In this analysis two main positions of a driver were assumed: a sitting position with hands on steering wheel and a sitting position with a right hand holding gear shift stick. It was shown in which areas of the cabin of the passenger car changes in dimensions are necessary and then driver's comfort improvement was shown in percentage.

Keywords: car industry, ergonomics, CATIA, hybrid modeling, cabin interior ergonomics

1. Introduction

On the car market, one may find as many as 100 companies dealing with producing various kinds of cars. Car producing concerns try to lure customers by applying most advanced technologies. Currently, car designers are introducing innovative solutions as regards the placement of usable elements in the cabin of a passenger car. Because of ever increasing technological involvement in the interiors of passenger cars as regards the ergonomics of cabin equipment, the rules of designing such elements change in order to make them more comfortable and fulfill driver's needs. The interior must be designed in such a way that it should make the driver – no matter whether coming from Europe or Asia – feel well. [4]

A designer working with computer aided design programs (CAD) copes with the problem of an ergonomical placement of all elements. The designed machines and workplaces must meet not only the norms and requirements of the safety and hygiene regulations but also be ergonomic. In CATIA V5R19 program a designer may put into practice the above requirements by using *Human Builder* module. The module is used to check previously made three-dimensional model of workplace as regards its ergonomics for the person working there. The engineer designer, may creating a dummy with anthropometrical features in this program and import it into the tested workplace model. By using analysis tools, one may check the interior as regards ergonomics and visibility on the basis of such model. One can also analyze the dummy itself as regards the stress

of different body parts while performing such activities as raising/lowering or pulling/pushing of different objects [3].

2. The issues of ergonomics

Ergonomics in the car industry has a special meaning because comfort of a driver and his/her passengers while driving plays a crucial role in designing. Besides car performance, what really matters in this industry is users' comfort and their safety. One should also make sure that the interior equipment doesn't distract driver's eye attention while driving and was put in places that will not damage anybody in case of accident. Every designer must make use of norms and regulations when designing a car interior and by using them make the cabin also meet the user's needs. Figure 1 presents the suggested dimensions, from which a designer should start the process of designing. In the later stage of modeling, after conducting ergonomics analyses the dimensions will be changed. We should emphasize that the driver's chair – backrest should be 635mm long and the headrest – 275mm long. For passenger cars the angle of chair positioning amounts to 20° against the floor when this optimal value provides the driver a comfortable drive.

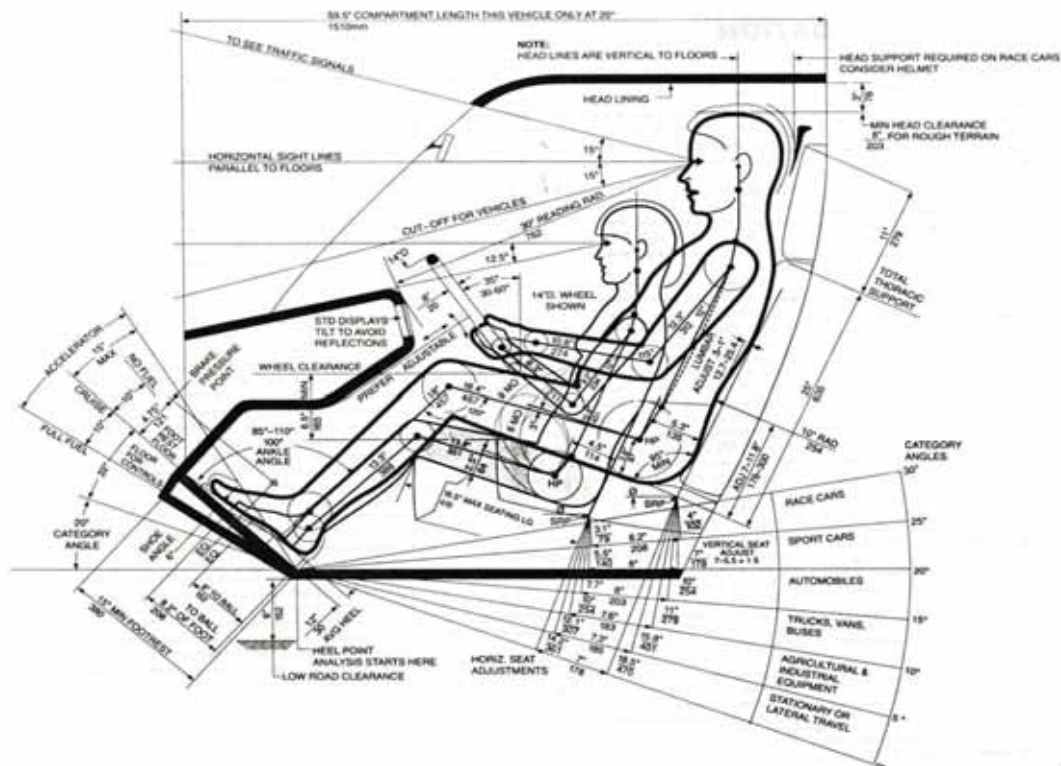


Fig. 1. Presentation of dimensions meeting the ergonomics conditions of a passenger car interior [5]

One should also take into account the distance of 76 mm between the car interior ceiling and the driver's head top. A correct distance between the chest and steering wheel should amount to 274 mm for men and 211 mm for women. The figure presents also visibility range that for both sexes should amount to 30° so that one could see a road lane and traffic lights. The steering wheel should be bent at 35° for a better comfort of a driver of a passenger car [5].

3. Elements and characteristic features of the tested construction

The test is carried out on the interior of a passenger car that was modeled in a hybrid way with the use of CATIA V5R19 program. The modeled cabin of the car corresponds to actual dimensions and placement of interior equipment elements. The elements include: car roof, dashboard, set of chairs, manipulators inside cabin, doors etc. [2].

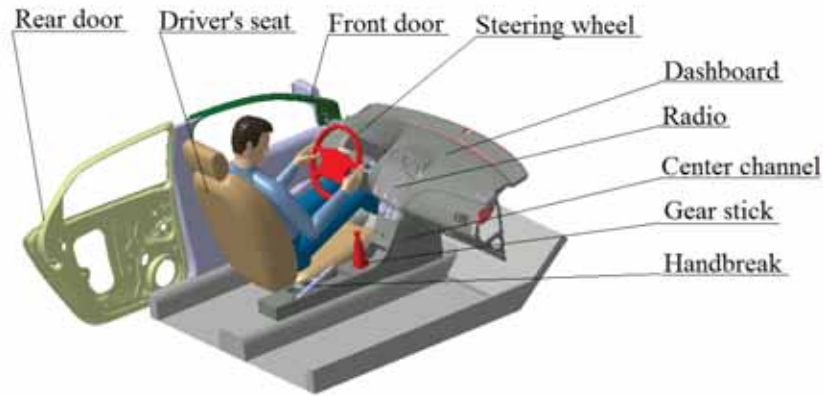


Fig. 2. The hybrid modeled car interior with the analyzed elements

When the designer models the cabin elements, s/he adopts supposed dimensions to place different elements and these dimensions are measured from some characteristic points assumed by the designer. Only at the later stage, after analysis, there occurs a change in basic dimensions and the adoption of placing such element to their usage. The dimensions that may be helpful in percentage analysis of movement range of body parts:

- a) the distance between steering wheel and the sitting driver: the distance will be measured from the centre of the steering wheel surface to the chest – dimension 1,
- b) distance of the chair in XY surface: the distance will be measured from the chair's edge to the sloped floor under pedals – dimension 2,
- c) height of the chair in XY surface: the distance from the chair to the floor – dimension 3,
- d) dimensions of the length and width of placing the gear shift stick: the distance measured from both edges of the floor – dimension 4,
- e) steering wheel leaning angle – dimension 5,
- f) a driver's chair leaning angle – the angle between the backrest and the seat surface – dimension 6.

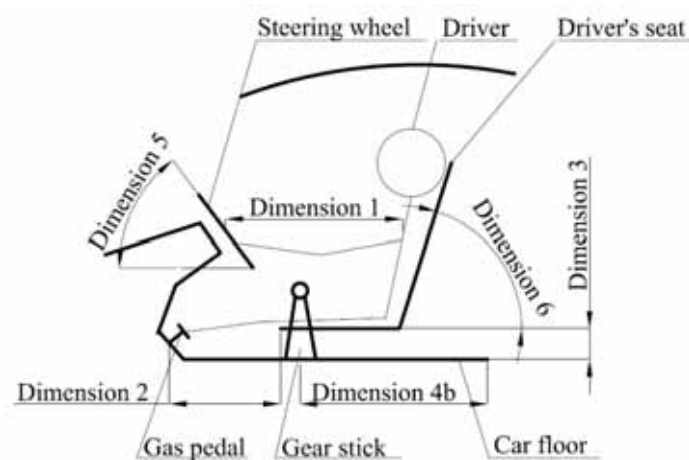


Fig. 3. The car interior dimensions taken for the analysis

Table 1 presents dimensions that were shown as a diagram on Figure 3 thanks to which we can characterize some elements of interior equipment. They play a crucial role in percentage use of a free body part movement. After conducting analysis, the designer should concentrate on these dimensions to create comfortable conditions of driving [3].

Tab. 1. A set of preliminary dimension values taken for the ergonomics analysis of the interior

Dimension number		Value of dimension
1		330 mm
2		518 mm
3		150 mm
4	a	747 mm
	b	807 mm
5		80°
6		70°

4. Analysis of the ergonomics of a car cabin

The analysis of work ergonomics in the interior of a passenger car was carried out on the basis of two imported dummies: male and female ones, whose body part dimensions were defined according to the statistical average of the population i.e. 50 centile dummies that are statistically most often met human dimensions in Europe. Centile measure is a set of statistical dimensions of a human body that reflects the size of a short person (5 centiles), middle-sized (50 centiles) and a tall one (95 centiles) [1].

In these tests the most important positions of the dummy were analyzed as well as the usable area of the car interior. Two tests were conducted after importing the dummy and placing it inside the car in a sitting position:

- a) dummy sitting on a driver's chair and holding steering wheel with both hands – position no 1,
- b) dummy sitting on a driver's chair and holding a gear shift stick with its right hand – position no 2.

During the ergonomics analysis of the cabin the following body parts were taken into account: 1) all levels of freedom 2) the lumbar region 3) chest region 4) neck region 5) thigh region 6) leg 7) toes 8) clavicular region 9) arm region 10) forearm region 11) whole hand (Fig. 4).

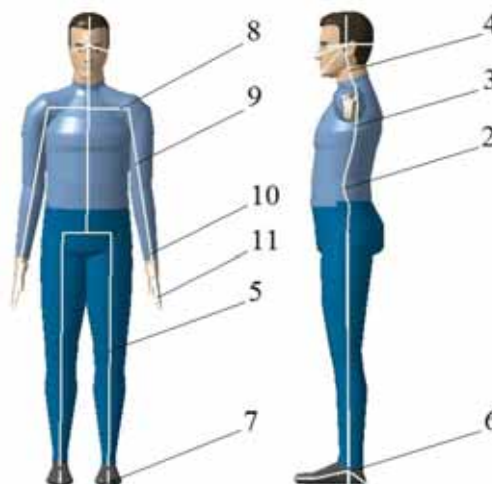


Fig. 4. Body parts taken for the analysis

Position no 1

The imported dummy in position no 1 is the most frequent position of a driver sitting inside a passenger car. According to the road code regulations, both hands should be placed on the upper part of the steering wheel, which was also included in the test and checked whether such position for a designed car is comfortable and ergonomic.

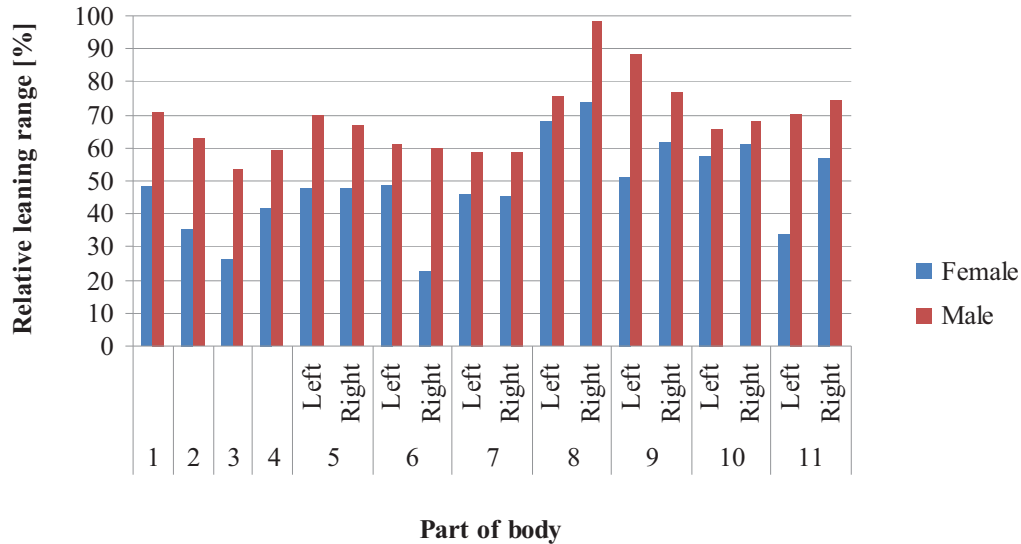


Fig. 5. A comparison of leaning range relative values for men and women for the position no 1

High per cent of the relative of the freedom angle as regards clavicular and arm region may mean that the car cabin was badly designed – the decrease of the usable space which results in lower comfort of the driver.

Position no 2

During driving a driver must take off one of his hands from the steering wheel to change into higher or lower gear. Such activity means also a temporary leaning of some body part that was analyzed for the position no 2.

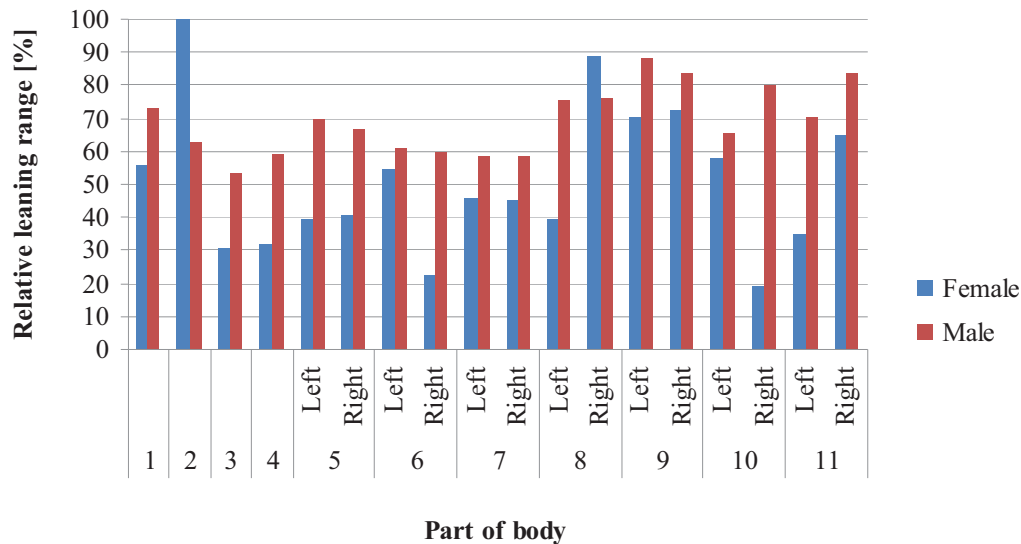


Fig. 6. A comparison of leaning range relative values for men and women for the position no 2

When analyzing the obtained results for the position no 2, one can notice that women show an extreme leaning of clavicular region which may result from bracing with all body. A similar

behavior but regarding whole hand can be observed among men, which probably is a result of grasping tight the gear shift stick and consequently gives a very high value of the relative degree of freedom.

5. Improving ergonomics in the modelled interior of a car cabin

When analyzing position no 1, one can see differences between percentage DOF range for men and women. By changing dimension no 1 by 50 mm, we can notice a percentage decrease of the angle range by 20% for clavicular and arm region. When we change dimension no 3 by 40 mm, we can observe a percentage decrease of angle range for clavicular region by 15%. If we change these two dimensions, we can achieve a considerable improvement of comfort for both sexes. If we change the leaning of the steering wheel by 5°, the designer will get a decrease of the angle range for clavicular region by 10%. When we change dimension no 1, dimension no 2 will get automatically adjusted by 30 mm as these two dimensions are correlated. To solve this problem, we may change dimension no 6 by 10° which will result in a better comfort for forearm and arm region.

Tab. 2. A set of final dimensions taking into account conducted analysis

Dimension number		Value of dimension
1		430 mm
2		548 mm
3		190 mm
4	a	767 mm
	b	877 mm
5		85°
6		80°

With women, the clavicular region is leant at 89%, which means that the gear shift stick is too far from the driver. They need to lean their bodies to reach it. The change of dimension no 4a by 70 mm and dimension no 4b by 20 mm will result in an automatic decrease of the percentage leaning of clavicular region by 15%. When analyzing angle range in percents for men at agreed changes, we can see a decrease of angle range by 10% for arm region and 20% for forearm region.

6. Summary

The present work presents modeled interior of a passenger car. Before starting the analysis, some selected elements from the car cabin were measured. Two analyses of work ergonomics for basic service activates of the driver of the car were conducted. The results obtained during the analysis shown that geometrical condition of car cabin are inadmissible as far as the driver's comfort is concerned. After the analysis, the cabin was remodeled and as a result a 15% decrease of the movement range for all body parts was achieved.

References

- [1] Buckland, K., *Słownik terminów statystycznych*, PWE, Warszawa, 1986.
- [2] Car Body Design, Automotive Design and Engineering [Online], [Access on June 9th 2010], Website: <http://www.carbodydesign.com>.

- [3] Ergonomics in Automotive Industry [Online], Ergonomic Technologies Corporation [Access on June 9th, 2010], Website: <http://www.ergoworld.com/ergonomics-industry-automotive.html>.
- [4] Ergonomics and Anthropometrics [Online], Car Design Online [Access on June 15th 2010], Website: <http://www.cardesignonline.com/design/ergonomics/index.php>.
- [5] Peacock, B., Karwowski, W., *Automotive ergonomics*, Taylor & Francis, London, 1993.



THE APPLICATION OF THE COMPUTER PROGRAMME TO THE ANALYSIS OF MICROSTRUCTURE OF THE MATRIX OF AUSTEMPERING DUCTILE IRON

Tomasz Giętka, Stanisław Dymski

*University of Technology and Life Sciences
al. Prof. S. Kaliskiego 7, 85-789 Bydgoszcz, Poland
tel.: +48 52 3408719, fax: +48 52 3408796
e-mail: tgietka@utp.edu.pl*

Abstract

In this work the attempt at quantitative evaluation of the microstructure of ADI cast iron matrix has been made. The automatic analysis of the image of the microstructure of austempered spheroidal cast iron has been used for the evaluation. The treatment variant was a two-phase austenitization. First phase was carried out at a temperature $t_\gamma = 950^\circ\text{C}$ and after cooling to a temperature $t_\gamma = 900^\circ\text{C}$. The isothermal process was carried out at a temperature $t_{pi} = 300$ and 400°C for $8 \div 64$ min. Ordinary cast iron was austempered. After it the microstructure images were recorded and subjected to automatic image analysis with the use of the NIS ELEMENTS 3.0 AR software.

Keywords: Image analysis, Isothermal process, Diffraction, ADI

1. Introduction

In the technology of high strength ADI cast iron grades the microstructure of matrix, consisting of austenite and ferrite [1-3] is significant.

In ADI iron cast production the austempering is used in order to produce high carbon austenite and rich in carbon ferrite in the matrix. Such composition of microstructure is called ausferrite and the isothermal process of over-cooled austenite – ausferritizing.

Research works over ADI cast iron concentrate mostly on ausferritizing process [3, 8, 9-13]. It is a rational approach, because shaping of strength, ductility and toughness as well as impact strength of the cast iron result mostly from the parameters of heat treatment. It is significant on account of the practical cast application in accountable machine parts.

Image analysis is considered to be significant in many fields of science connected to quantitative analysis of microstructure. Application of algorithms of automatic image analysis consists in processing the images of material microstructures in order to calculate statistic characteristics of the size and shape of the grains.

The microstructure which has been analysed in this way may be used to prepare a model of the material structure for simulation calculations with the use of Finite Element Method (FEM). In order to make the calculations reliable, the complex analysis of the input data basing on extraction of characteristic features like edges, inclusions and noise has to be carried out.

The microstructure image analysis is in many cases complex on account of the variety of shapes and sizes of grains, which in effect has an influence on the reliability of the results and the

later calculations [4,6-9]. The majority of accessible algorithms serving to edges detection cannot cope with the problem of occurring noise, treating it as a typical image element.

The aim of this work was to carry out a test of the ADI cast iron components qualitative evaluation with the use of automatic image analysis. The results of the quantitative microscopy have been compared to the X-ray diffraction analysis.

2. Material, programme and research object

The researched cast iron has been smelted in a hot blast cupola furnace. Balling of the cast iron was carried out with the use of magnesium alloy ML5, applying rod method in the container of the cupola. Cast iron has been cast to wet sand moulds. The casts had a shape of ingots YII according to (PN-EN 1563:2000). On the base of static tensile test the cast iron was qualified to the grade EN-GJS-500-7. Cast iron had ferritic- pearlitic (10 %) matrix structure and proper nodular graphite form (share 11,5 %, 112 rel./ mm² microsection surface).

Chemical composition and properties in the initial state of the ordinary cast iron are presented in the Table 1.

Tab. 1. The chemical composition and mechanical properties in ductile iron

Chemical element, % mas.					
C	Si	Mn	P	S	Mg
3.65	2.59	0.18	0.052	0.014	0.06
Mechanical properties					
R _m , MPa	A ₅ , %	H _v , HV10	KCG, J/cm ²		
507	12.1	156	106		

Before hardening the lower part of ingot YII were treated with two-phase ferritizing annealing. The first phase at the temperature of 1050⁰C for 4 hours and the second one after cooling to 680⁰C held for 6 hours. Cooling down of the cut ingots was carried out with the use of a furnace (Fig. 1).

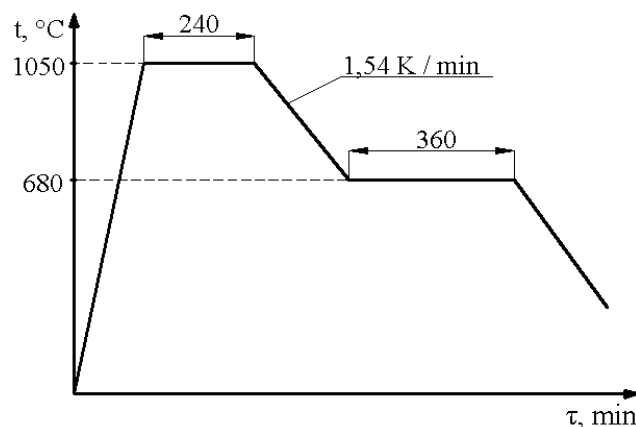


Fig. 1. The schema of dual-stage ferritizing annealing of the ductile cast iron

After that the ingots were cut into three flat bars. The flat bars were marked with the retaining of their previous location in the ingots and the tensile test samples, whose dimensions are depicted in the Figure 2, were made.

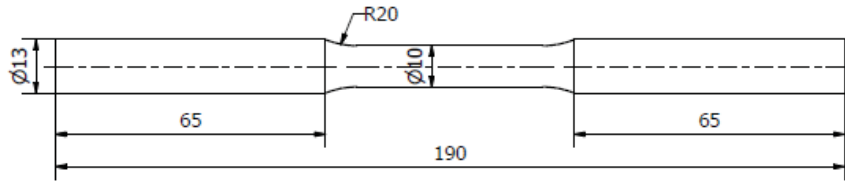


Fig. 2. Dimensions of the tensile test

Tensile test samples have been austempered according to the schemes shown by the Figure 3. For every treatment condition a set consisting of 3 samples, originating from 1 ingot YII, has been prepared.

From the gripping part of the samples after heat treatment the 11-millimetre-long specimens were taken, on which metallographic microsections were made. They served for the assessment of their microstructure under an optic microscope. The record of the microstructure images has been made with the use of scanning electron microscope (SEM) type JSM-50A made by company JEOL with the acceleration voltage 20 kV and absorptive current of the sample ca. $0,2 \cdot 10^{-10}$ A. The images have been registered on the enlargement scale $1000 \div 3000\times$.

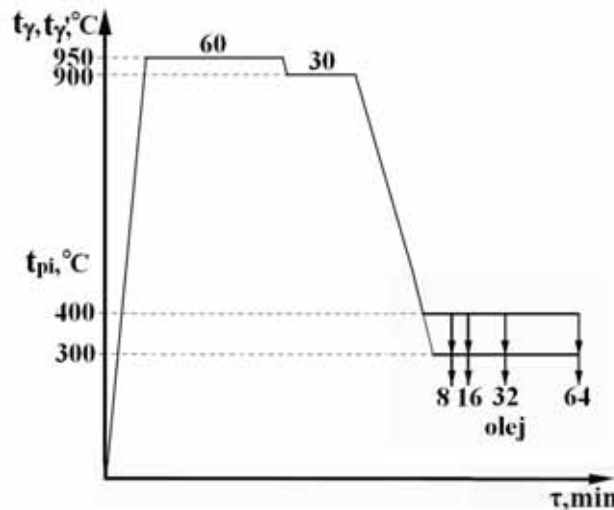


Fig. 3. Scheme depicting austempering of the ductile cast iron

Automatic image analysis has been made with the use of NIS ELEMENTS 3,0 AR software (Fig. 4). Its task was to calculate specially marked pixels of the image which was calibrated according to the enlargement. Halftone screen image received from the scanning microscope has been converted to the binary image, which explicitly determined the evaluated microstructure components. With the use of computer software the share of austenite and sizes of the ferrite needles have been determined.

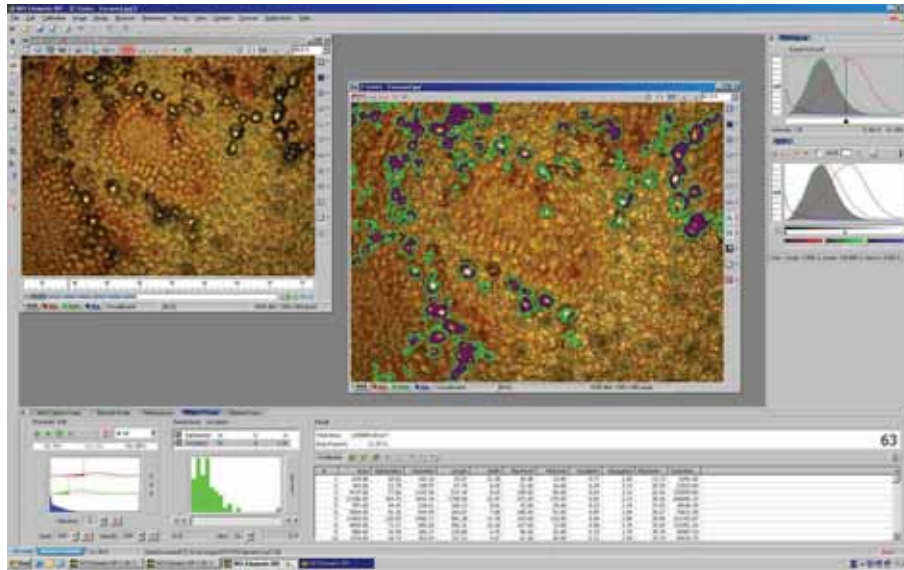


Fig 4. The window of the programme NIS ELEMENTS 3,0 AR

On the metallographic specimens also the x-ray diffraction analysis has been carried out. The research has been made on the diffractometer, using CoKa radiation and iron filtering. The following parameters of diffractometer's work have been assumed:

- lamp voltage 36 kV;
- lamp current 6 mA;
- the arrangement of collimating slits I – 2, II – 2, III – 2 mm, the Soller slits on the primary beam and on the diffracted beam;
- scintillation counter detector operated at 700 V.

Diffraction patterns have been recorded within the angular range 2Θ $49,5 \div 53,5^\circ$. Within this angular range, using step $0,01^\circ$, diffraction lines (110) phases α and (111) and phases γ have been recorded. Intensity of each interference line has been determined three times by planimetry of the field under the curve to the background level. Share of austenite (V_γ) from the formula 1 [17]:

$$V_\gamma = \frac{1}{1 + I_\alpha \cdot I_\gamma^{-1} \cdot R} \cdot 100 \% \quad (1)$$

where:

V_γ - share of austenite in the volume fraction,

I_α - relative intensity of diffraction line (110) phase α , planimetry on the X-ray photograph,

I_γ - relative intensity of diffraction line (111) phase γ , planimetry on the X-ray photograph,

R - value of the constant accepted to these measurements 0,85. mm

Averaging size of ferrite needles has been determined from the formula 2 [18]:

$$d = \frac{0,9 \cdot \lambda}{B \cdot \cos \Theta} \quad (2)$$

where:

d - average diameter of the crystal particle,

λ - wavelength in nm,

B - diffraction line broadening, measured in the middle of its maximal intensity in rad,

Θ - the angle of the interference line determined from the diffraction pattern in $^\circ$.

3. The results of the research and their analysis

The quantitative evaluation of the components of the austempered cast matrix microstructure has been carried out on 5 random chosen images, registered for each specimen which has been enlarged 2000x. The demonstration microstructures of the cast iron have been depicted in the Figures 5 ÷ 8.

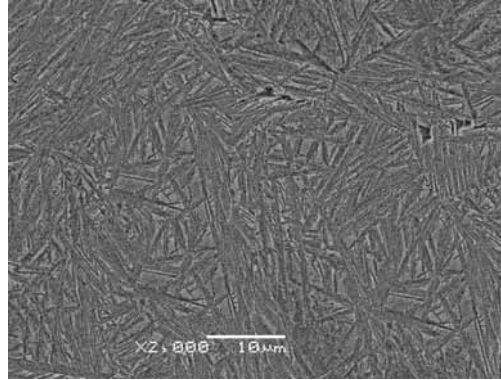


*Fig. 5. The microstructure of the cast iron austempered at a temperature $t_{pi} = 300^{\circ}\text{C}$, $\tau_{pi} = 8$ min.
Etched in nital, micr. surf. 2000x*

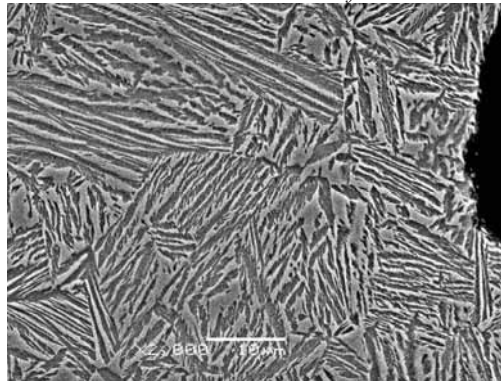


*Fig. 6. The microstructure of the cast iron austempered at a temperature $t_{pi} = 400^{\circ}\text{C}$, $\tau_{pi} = 8$ min.
Etched in nital, micr. surf. 2000x*

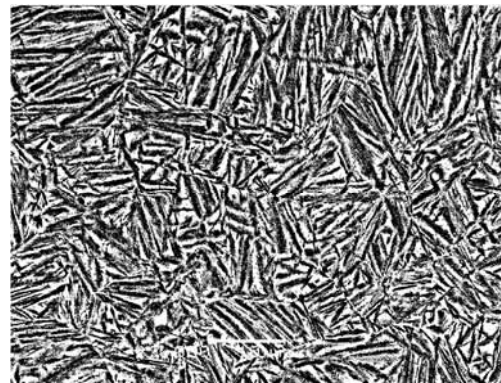


*Fig. 7. Binary image of the cast iron microstructure austempered at a temperature $t_{pi} = 300^{\circ}\text{C}$, $\tau_{pi} = 64$ min.
Etched in nital, micr. surf. 2000x*

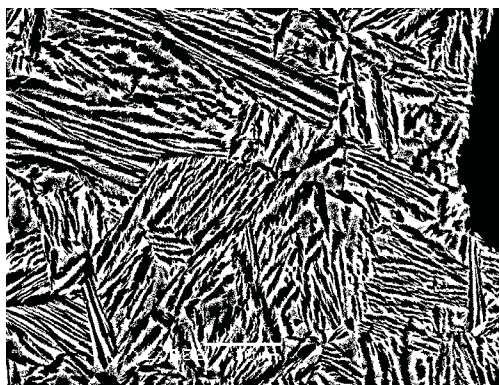


Fig. 8. Binary image of the cast iron microstructure austempered at a temperature $t_{pi} = 400\text{ }^{\circ}\text{C}$, $\tau_{pi} = 8\text{ min}$.
Etched in nital, micr. surf. 2000x

After austempering at temperature $t_{pi} = 300\text{ }^{\circ}\text{C}$ the matrix consisted of the lower ausferrite (Fig. 5, 7). While at a temperature $t_{pi} = 400\text{ }^{\circ}\text{C}$ upper ausferrite (Fig. 6, 8). The morphology of the components of ADI cast iron microstructure has been changing in the holding time function. For comparison the microstructure registered on (SEM) for the specimen austempered at a temperature $t_{pi} = 300\text{ }^{\circ}\text{C}$ for 8 minutes (Fig.5) as well as the binary image of the specimen austempered at the same temperature for 64 minutes (Fig. 7). With the elongation of the conversion time the ferrite needles have undergone the length change and the austenite plates have been evenly distributed. The conversion time affects the microstructure arrangement.

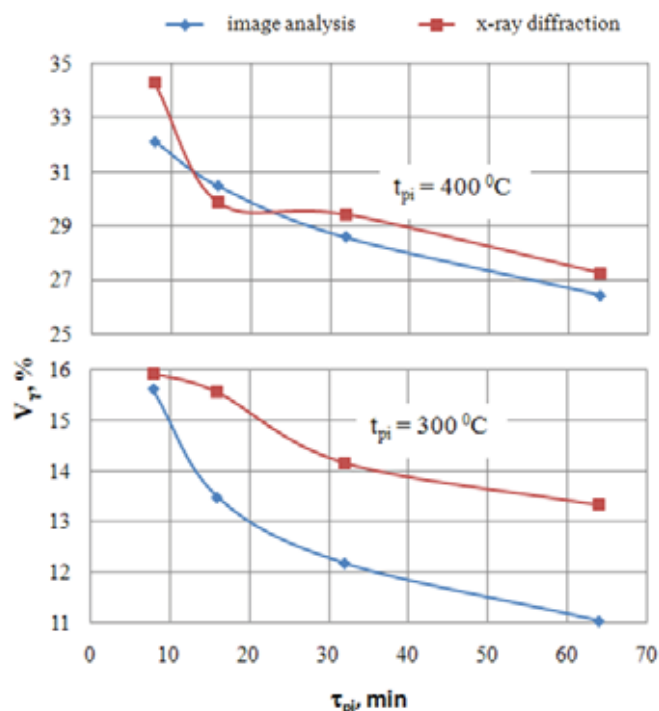


Fig. 9. Impact of the temperature and austempering time on the austenite share (V_{γ}) in the ADI cast iron matrix

On the base of image analysis the share of austenite in the microstructure has been determined. The microstructure of the ADI cast iron austempered at a temperature $t_{pi} = 400\text{ }^{\circ}\text{C}$ contained austenite in the range $32,1 \div 26,4\%$ while at a temperature $t_{pi} = 300\text{ }^{\circ}\text{C}$ - $15,6 \div 11,0\%$. The share of phase γ determined by diffraction was bigger for both temperatures (apart from $\tau = 16\text{ min}$ for $t_{pi} = 400\text{ }^{\circ}\text{C}$). The character of the chart lines was the same for both research methods. The growth of conversion time caused a decrease of the austenite share. The differences of the received results

depicting the austenite share in the cast iron matrix were bigger for the lower temperature of austempering. It results from finer microstructure of the matrix.

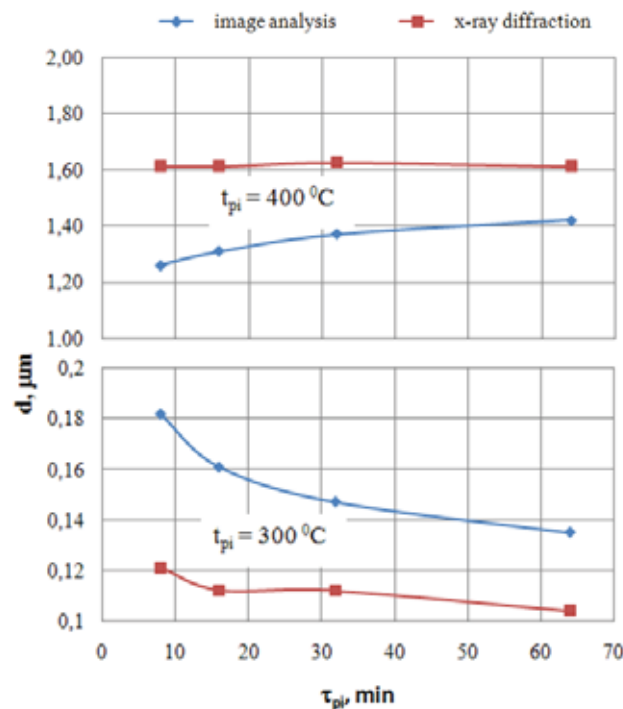


Fig. 10. Impact of the temperature and isothermal process time on the average diameter of the ferrite needles (d) in ADI cast iron matrix.

The diameter of the ferrite needles (Fig. 10) measured by image analysis is almost ten times, and with the use of diffraction thirteen times smaller at $300\text{ }^{\circ}\text{C}$ than at $400\text{ }^{\circ}\text{C}$. The little transverse size of the ferrite needles in lower ausferrite has contributed to registering low contrasted images. The result of it has been depicted in the figure 10 between the diameters at – values determined from the image analysis and the diameters at – values received from the rtg diffraction for $t_{pi} = 300\text{ }^{\circ}\text{C}$. Bigger diameters at – sizes received from the image analysis result from binary images which have been enlarged by noise and shadows. The change of the transverse sizes of the ferrite needles is connected to the conversion $\gamma \rightarrow \alpha$ mechanism.

The length of the ferrite needles in ADI cast iron under the influence of time decreased (Fig. 11). This relation is stronger in cast iron which has been hardened from the temperature $t_{pi} = 300\text{ }^{\circ}\text{C}$ than at $400\text{ }^{\circ}\text{C}$.

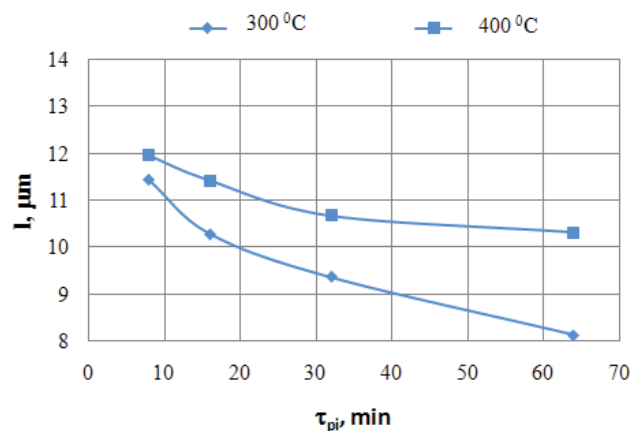


Fig. 11. Impact of the temperature and isothermal process time on the length of the ferrite needles determined with the use image analysis software

4. Conclusion

On the base of the research carried out and its results the following statements can be made:

1. The image analysis software NIS ELEMENTS 3,0 AR can be used to the quantitative evaluation of the components of ADI cast iron matrix microstructure.
2. From the comparison of methods to the evaluation of the percentage share of austenite in ADI it results that the computer image analysis can be used in the upper ausferrite examination. However, in the range of the lower ausferrite the measurement discrepancy between the methods rises to over 2%.
3. The evaluation of the sizes (diameters and length) of the ferrite needles in ausferrite has been treated as a pre-operation to the next research, although during the analysis of the received results the meaningful impact of the temperature and austempering time on these sizes has been noticed.

References

- [1] Pietrowski, S., *Żeliwo sferoidalne o strukturze ferrytu bainitycznego z austenitem lub bainitycznej*, Archiwum Nauki o Materiałach, t.18, pp. 253-273, 4/1997.
- [2] Guzik, S. E., *Żeliwo ausferrytyczne jako nowoczesne tworzywo konstrukcyjne*, Inżynieria Materiałowa, pp. 677-680, 6/2003.
- [3] Dymski, S., *Kształtowanie struktury i właściwości mechanicznych żeliwa sferoidalnego podczas izotermicznej przemiany bainitycznej*, Rozprawy nr 95. ATR Bydgoszcz, 1999.
- [4] Wojnar, L., Kurzydłowski, K., Szala, J., *The Practician of the Analysis of the Painting*, Publishing house Polish Company Stereology, Cracow, 2002.
- [5] Kovacs, B. V., *On the Terminology and Structure of ADI*, AFS Transactions, pp. 417-420, 102/1994.
- [6] Miernik, K., Bogucki, R., Gądek, A., Dziadur, W., *The Influence of Conditions of the Thermal Processing on Content of the residual austenite in Ductile Cast Iron of Isothermal Transformation (ADI)*, Conference Materials XXX the School Engineering Material, Kraków-Ustroń Jaszowiec, 2002.
- [7] Szala, J., *The computer analysis of the painting in metallography quantitative*, The Programmer in the Technology Metals, vol. 3, pp. 41-57, 1/2003.
- [8] Kowalski, A., Kuder, M., *Use of Computer Programme to the Analysis of Painting LUCIA to the Quantitative Opinion of the Structure of Cast Iron ADI*, Innovations in Founding, Part I, Cracow, pp. 281-290, 2007.
- [9] Rauch, Ł., Kusiak, J., *Automatic Analysis of Microstructure Photographs*, Scientific Works, Varsovian Engineering College z. 216, pp. 165–170, 2007.
- [10] Kilicli, V., Erdogan, M., *The Strain-Hardening Behavior of Partially Austenitized and the Austempered Ductile Irons with Dual Matrix Structures*, Journal of Materials Engineering and Performance, vol. 17, pp. 240-249, 2/2008.
- [11] Delia, M., Alaalam, M., Grech, M., *Effect of Austenitizing Conditions on the Impact Properties of an Alloyed Austempered Ductile Iron of Initially Ferritic Matrix Structure*, vol 7, pp. 265 – 272, 2/1998.
- [12] Grech, M., Young, J. M., *Effect of Austenitising Temperature on Tensile Properties of Cu-Ni Austempered Ductile Iron*, Materials Science and Technology, pp. 415-421 6/1990.
- [13] Mallia, J., Grech, M., *Efect of Silicon Content on Impact Properties of Austempered Ductile Iron*, Materials Science and Technology, pp. 408-414, 13/1997.
- [14] Ogi, K., Sawamoto, A., Jin, Y. C., Loper Jr. C. R., *A Study of Some Aspects of the Austenitization Process of Spheroidal Graphite Cast Iron*, AFS Transactions vol. 96 (1988).

- [15] Aranzabal, J., Gutierrez, I., Rodriguez-Ibabe J. M., Urcola J. J., *Influence of the Amount and Morphology of Retained Austenite on the Mechanical Properties of an Austempered Ductile Iron*, Metallurgical and Materials Transactions, pp. 1143-1156, 28A/1997.
- [16] Eric, O., et al., *The Austempering Study of Alloyed Ductile Iron*, Materials Design, pp. 617-622, 27/2006
- [17] Senczyk, D., *The Laboratory from X-Ray Structure Analysis*, Pub. School Engineering, Poznań, 1974.
- [18] Cullity, B. D., *Elements of X-Ray Diffraction*, State Scientific Publishing house, Warsaw, 1964



DOUBLE DYNAMIC VIBRATION ABSORBER

Henryk Holka

*University of Technology and Life Sciences in Bydgoszcz
 ul. Prof.S.Kaliskiego 7, 85-789 Bydgoszcz, Poland
 tel.: +48 52 3408292
 e-mail: holka@utp.edu.pl*

Abstract

The paper presents the analysis of object vibration (a rigid beam) with asymmetrically located central point of mass supported on two elastic springs. In order to eliminate the vibration of the main system the dynamic vibration absorber with two degrees of freedom has been joined. Results of calculation for specific data have been demonstrated on the diagrams.

Keywords: rigid beam, vibration damper, anti-vibration insulation

1. Introduction

One of the known dynamics problems is an issue with insulating selected construction elements from foundation vibrations.

In Fig. 1 a carrying element (beam) on which sensitive to vibrations, mechanical-electric subsystems are placed, can be seen. Notice that in general cases point s does not coincide with the mass centre m .

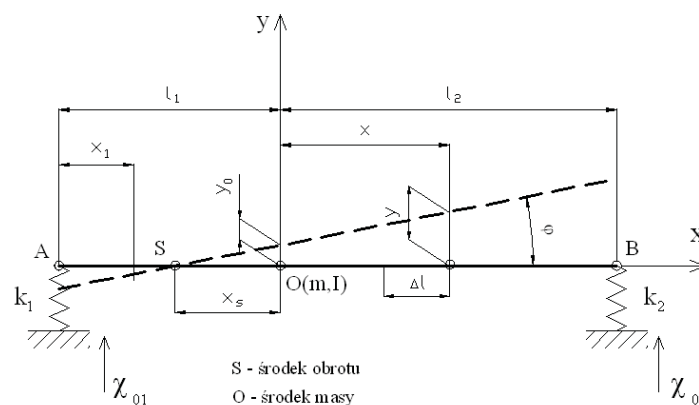


Fig.1. Beam supported on two springs

From the point of view of the designer a question arises considering the beam point's displacements and their values for specified excitation frequency.

The construction must meet the following condition: in certain beam segment the length Δl , vertical displacement y , velocity \dot{y} , and acceleration \ddot{y} must be always smaller from the threshold value defined as admissible for the construction elements placed on the beam.

There are two possible options for restraining the beam's movement:

- changing the beam parameters,
- applying a dynamic vibration absorber.

In the first case we notice that the beam's movement is planar and the description of displacement y of beam's optional point x is possible, if we know position of rotation centre s and the value of the angle $\varphi = \varphi(t)$

$$x_{1s} = \frac{y_1(t)}{\operatorname{tg} \varphi_1} = \frac{y_1}{\varphi_1}. \quad (1)$$

The values $y_1(t)$ and $\varphi_1(t)$ are determined from the beam's motion equations. The centre s depends from the system parameters and the excitation frequency. Defining of admissible beam vibrations is rather troublesome.

In the second case we receive good results by using a dynamic vibration absorber. Usually the vibration damper has one degree of freedom. In this particular problem a different solution has been applied – dynamic vibration damper with two degrees of freedom.

2. Motion equations

The following system is to be considered:

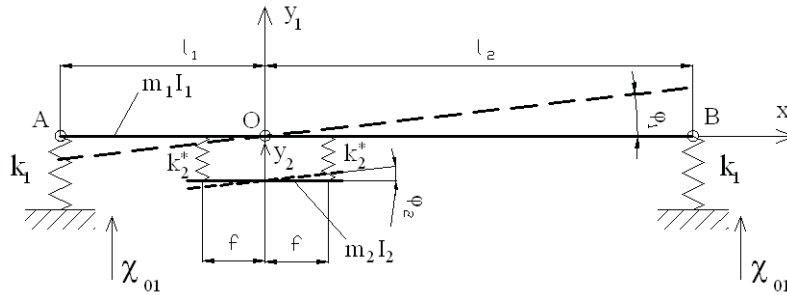


Fig. 2. Dynamic system with a double vibration absorber applied

As can be seen of the Fig. 2, an absorber with two degrees of freedom has been attached to the main beam. Hence the whole system has four degrees of freedom. In accordance to Fig. 2, the displacements of mass m_1 and m_2 are described by coordinates y_1 , φ_1 , y_2 , and φ_2 .

Equations of motion can be written in matrix form

$$[A] \begin{Bmatrix} \ddot{x} \end{Bmatrix} + [B] \begin{Bmatrix} \dot{x} \end{Bmatrix} + [C] \begin{Bmatrix} x \end{Bmatrix} = \{Q(t)\}, \quad (2)$$

where: A – inertia matrix, B – damping matrix, C – rigidity matrix, Q – excitation matrix, $k_2^* = k_2 + sc$, $s = i\omega$.

Equation (2) is transformed to:

$$\begin{aligned}
Z(s) \cdot X(s) &= Q(s) \\
x(s) &= \text{col}\{y_1(s), \varphi_1(s), y_2(s), \varphi_2(s)\} \\
Q(s) &= \text{col}\{F_1(s), F_2(s), 0, 0\},
\end{aligned} \tag{3}$$

where:

s – complex variable in Laplace transformation,
 $Z(s)$ – rigidity matrix containing matrixes A, B and C ,
 $F_1(t) = 2k_1\kappa_o \sin \omega t$, $F_2(t) = k_1(l_2 - l_1)\kappa_o \sin \omega t$.

System response can be derived from Cramer's rule

$$x_r(i\omega) = \sum_1^n (-1)^{r+n} \cdot \frac{z_{rn}(i\omega)}{|Z(i\omega)|} F(i\omega) = \sum_1^n \alpha_{rn}(i\omega) \cdot F(i\omega), \tag{4}$$

where: z_m is minor of matrix Z ,

$\alpha_{rn}(i\omega)$ – complex matrix of system receptance.

Matrix $|Z|$ has the form:

a_{11} $-m_1\omega_1 + 2k_1 + 2k_2^*$	a_{12} $-k_1(l_1 - l_2)$	a_{13} $-2k_2^*$	a_{14} 0
a_{21} $-k_1(l_1 - l_2)$	a_{22} $-I_1\omega^2 + 2k_2^*f^2 + k_1(l_1^2 + l_2^2)$	a_{23} 0	a_{24} $-2k_2^*f^2$
a_{31} $-2k_2$	a_{32} 0	a_{33} $-m_2\omega^2 + 2k_2^*$	a_{34} 0
a_{41} 0	a_{42} $-2k_2^*f^2$	a_{43} 0	a_{44} $-I_2\omega^2 + 2k_2^*f^2$

(5)

Next, in accordance to (4), x_I i φ_I can be transformed to

$$\bar{x}_1(i\omega) = \frac{1}{|Z|} \left(\begin{vmatrix} a_{22} & 0 & a_{21} \\ 0 & a_{33} & 0 \\ a_{42} & 0 & a_{44} \end{vmatrix} \cdot F_1(t) - \begin{vmatrix} a_{21} & 0 & a_{24} \\ a_{31} & a_{33} & 0 \\ 0 & 0 & a_{44} \end{vmatrix} F_2(t) \right), \tag{6}$$

$$\bar{\varphi}_1(i\omega) = \frac{1}{|Z|} \left(\begin{vmatrix} a_{12} & a_{13} & 0 \\ 0 & a_{33} & 0 \\ a_{42} & 0 & a_{44} \end{vmatrix} F_1(t) - \begin{vmatrix} a_{11} & a_{13} & 0 \\ a_{31} & a_{33} & 0 \\ 0 & 0 & a_{44} \end{vmatrix} F_2(t) \right). \tag{7}$$

From the relation of (6) and (7) can be seen, that coordinates $x_I(t)$ and $\varphi_I(t)$ will equal zero, when elements a_{33} and a_{44} of matrix Z will also have zero value

$$x_1(t) = \varphi_1(t) = 0 \quad \text{when} \quad a_{33}(i\omega) = a_{44}(i\omega) = 0. \tag{8}$$

Elements a_{33} i a_{44} have the form:

$$a_{33} = 2k_2 - m_2\omega^2 = 2k_2 \left(1 - \frac{m_2\omega^2}{2k_2} \right), \quad (9)$$

$$a_{44} = 2k_2f^2 - J_2\omega^2 = 2k_2f^2 \left(1 - \frac{J_2\omega^2}{2k_2f^2} \right). \quad (10)$$

Notice that:

$$\omega_{x2}^2 = \frac{2k_2}{m_2} \text{ i } \omega_{\varphi2}^2 = \frac{2k_2f^2}{J_2}, \quad (11)$$

where ω_{x2} i $\omega_{\varphi2}$ are free vibration of mass m_2 .

We tune both values to the same frequency $\omega_{x2} = \omega_{\varphi2}$

$$\frac{2k_2}{m_2} = \frac{2k_2f^2}{J_2}, \quad (12)$$

hence

$$J_2 = m_2f^2. \quad (13)$$

Eventually, by substituting (13) and (11) to (9) and (10), we get

$$a_{33} = 2k_2 \left(1 - \frac{\omega^2}{\omega_{x2}^2} \right), \quad (14)$$

$$a_{44} = 2k_2f^2 \left(1 - \frac{\omega^2}{\omega_{x2}^2} \right). \quad (15)$$

From equations (14) and (15) can be seen, that

$$x_1(t) = \varphi_1(t) = 0 \quad \text{when } \omega = \omega_{x2} = \omega_{\varphi2}. \quad (16)$$

The determined rule is valid for all beam excitation frequencies.

3. Example

In order to verify the correctness of introduced dependencies, calculations on numerical data have been performed.

Following data has been used:

$$m_1 = 25 \text{ kg}, \quad I_1 = 50 \text{ kgm}^2; \quad k_1 = 50000 \text{ N/m}, \quad l_1 = 3 \text{ m}, \quad l_2 = 1 \text{ m}, \quad \kappa_o = 0,001 \text{ m}.$$

Free vibrations of the main beam, without absorber has been calculated from the formula:

$$\omega_{1,2}^2 = \frac{1}{2} \left[\frac{2k_1}{m_1} + \frac{k_1(l_1^2 + l_2^2)}{J_1} \right] \pm \sqrt{\left[\frac{2k_1}{m_1} + \frac{k_1(l_1^2 + l_2^2)}{J_1} \right]^2 - \frac{4k_1(l_1^2 + l_2^2)}{m_1 I_1}}.$$

After substituting data we receive:

$$\omega_1 = 53,6 \text{ rad/s}; \quad \omega_2 = 105,4 \text{ rad/s}.$$

Assuming, that the ratio $\frac{m_2}{m_1} = 0,2$ then $m_2 = 5 \text{ kg}$.

From the system tuning conditions I_2 , k_2 can be determined,

$53,6 = \omega_{x2} = \omega_{\varphi2}$. (the system operates near the place of first resonance)

hence $\sqrt{\frac{2k_2}{m_2}} = 53,6 \quad i \quad k_2 = 7190 \frac{N}{m}$.

Assuming $f=0,25m$, we get $J_2=0,3125 \text{ kgm}^2$.

In the end we verify tuning conditions:

$$\omega = 53,6 = \omega_{x2} = \sqrt{\frac{2k_2}{m_2}} = \omega_{\varphi2} = \sqrt{\frac{2k_2 f^2}{J_2}}.$$

Calculation results are shown on Fig.3.

The presented curves confirm calculations. Amplitude $x_1 = f(\omega)$ with absorber is equal to zero for the resonance frequency $\omega = 53.6$ and $\varphi_1 = f(\omega)$ is also equal to zero for $\omega = 58$.

The Fig. 3d shows the curves for $k_2 = 5260$ (optimum stiffness), $c_2 = 0$. In this case amplitudes for the resonance frequency are not zero, but the scope of small amplitudes is wider.

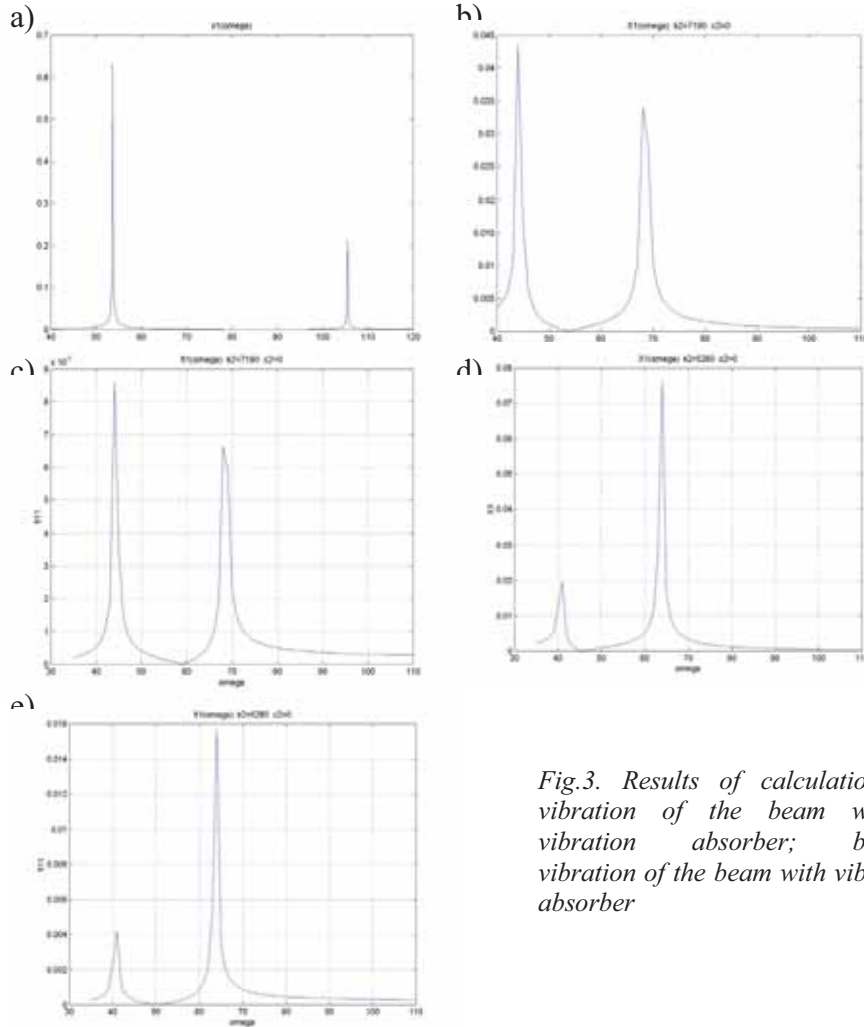


Fig.3. Results of calculation: a) vibration of the beam without vibration absorber; b,c,d,e) vibration of the beam with vibration absorber

4. Conclusions

1. The calculations confirm the analysis. Applying an absorber with two degrees of freedom eliminates main system vibrations.

2. If the foundation excitation frequency is changing, an absorber with damping should be used.
3. The presented solution may be applied in many designs: machine tools, damping pipeline vibrations, etc.

Reference

- [1] Radziszewski, B., Różycki, A., *Układ o dwóch stopniach swobody jako „Dynamiczny izolator drgań”*, Mechanika Teoretyczna i Stosowana, PWN, Warszawa 1978.
- [2] Holka, H.: *The dynamic vibration absorber for the main system with two degrees of freedom*. International Symposium on Design and Synthesis, Tokyo, 1984.



COMPARATIVE ANALYSIS OF THE BODY VIBRATIONS OF NEW CARS WITH A SPARK-IGNITION ENGINE WITH AND WITHOUT A SUPERCHARGER

Andrzej Kaźmierczak

Marek Reksa

Przemysław Moczko

Radosław Wróbel

*Wrocław University of Technology
Institute of Machine Design and Operation
I. Łukaszewicza Street 7/9, 50-371 Wrocław
Tel. +48713477918
e-mail: andrzej.kazmierczak@pwr.wroc.pl
marek.reksa@pwr.wroc.pl
przemyslaw.moczko@pwr.wroc.pl
radoslaw.wrobel@pwr.wroc.pl*

Abstract

The paper presents the results of tests carried out on two new cars: a Fiat Bravo (model 198, version 54A) with the 1.4BZ 90CV CD spark-ignition engine and the same Fiat Bravo model with the 1.4BZ 120CV CD spark-ignition engine equipped with a supercharging system. The car body vibrations experimentally determined in several specific repeatable points, i.e. behind the front side indicator and behind the passenger handle, were compared. A PSV-400 laser Doppler vibrometer made by Polytec was used to measure vibration velocities. The vibrometer directly measures two quantities: displacement and velocity. In the investigated case, vibration velocity turned out to be the variable supplying better diagnostic information. Vibrations were measured for the car standing on its wheels and for the car jacked up to reduce the influence of the car vibration damping systems on the measurement results. The latter are presented in the form of comparative diagrams. Moreover, the fast Fourier transform was used to determine the frequency distribution. Prior to that the signal was subjected to conditioning operations in time domain, such as parametric windowing and filtering. On the basis of the results the effect of the drive unit on the behaviour of the car body can be assessed for different engine types and rotational speeds. It is shown that the way in which the engine is mounted affects the vibrations of the car.

Key words: *Laser Doppler Vibrometry, vehicle body vibrations, vibration velocity, spark-ignition engine*

1. Introduction

Vibrations, particularly the ones which may affect human health or physical and mental state, are currently a topical issue which is widely discussed, unfortunately mainly in popular magazines. In specialist medical and telecommunications journals the focus is either on the health aspects [1] or the strictly vibrational ones [2] and no attempt is made to explore the phenomenon from the

mechanical or mechatronic point of view. Having the comfort of passengers in mind, the authors decided to comprehensively examine the problem.

2. Effect of vibrations on human organism

The effect of vibrations on the human organism has been widely described in the specialist literature [3], focusing on

- the values of the parameters (velocity, displacement, etc.) describing vibrations;
- the way in which vibrations are transmitted to the human body;
- the individual physiological characteristics;

The natural vibrations of most of the human organs range from 3 to 25 Hz. If such vibrations are transmitted to the human body, resonance may arise. This may result in the dislocation of an organ and in the extreme case, in its damage. The exposure of the human organism to general-impact vibrations can be assessed with regard to vibration parameters, such as acceleration, displacement and velocity, according to the criteria

- the harmfulness limit;
- the nuisance limit;
- the comfort limit;

Polish Standard PN-91/N-01354 “Vibrations – allowable accelerations of vibrations having a general impact on the human organism and methods of assessing exposure” sets the limits of vibrations to which the human organism can be exposed. Figure 1 shows vibration accelerations versus allowable exposure time.

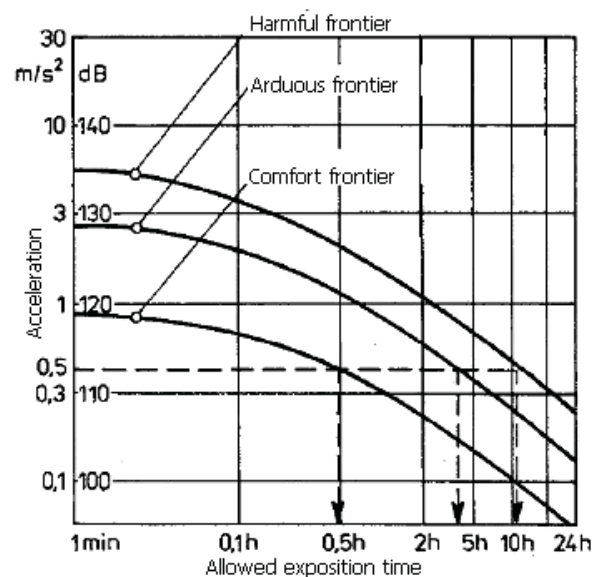


Fig. 1. Allowable acceleration values [3]

It is apparent from figure 1 that the comfort limit (the most representative quantity for the experimental results) is characterized by the lowest acceleration value which becomes extremely annoying after 10 hours. But this long journey by car is nothing extraordinary.

3. Investigated object in light of vibration transmitting components

The structure of a motor vehicle without its plating is shown in fig. 2. The crucial parts and the structure of the individual beams are shown in detail. Test results indicate that the side frame,

through which vibrations are transmitted to the measurement sites, is critical. The structure of the particular components is layered as shown in the figure.

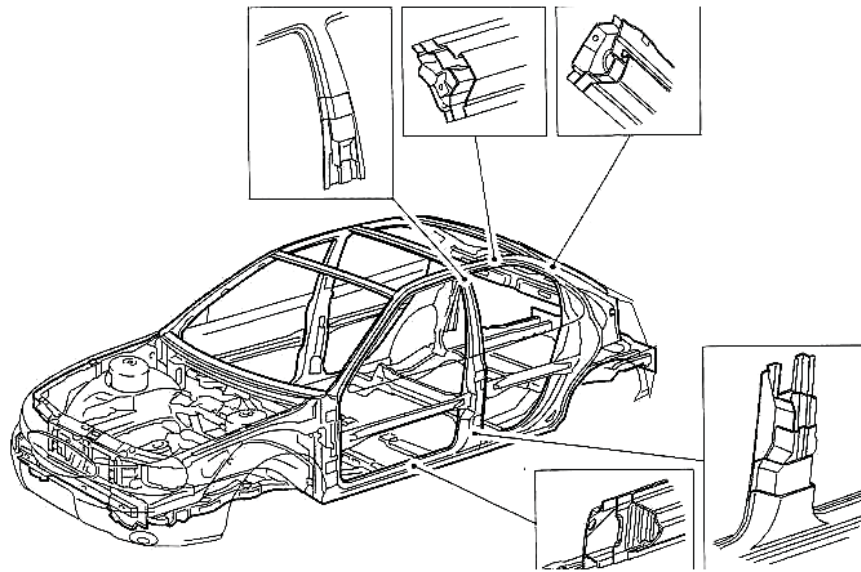


Fig. 2. Investigated object without plating

4. Measurement system and method

Laser Doppler vibrometry (LDV) was used for the investigations. LDV is based on the Doppler effect, which consists in a change in the length of the light wave received by the target if the latter is moving relative to the source.

A laser probe is the transmitting-receiving device. After it is reflected and returns to the scanning head the laser beam hits a lens. This measuring method allows one to directly measure velocity and relative displacement [4]. Any other parameter is a derivative of the above quantities. Velocity is converted into voltage proportional to frequency shift. Displacement is measured by counting the occurrences of areas generating specific wavelengths.

A diagnostic circuit consisting of a Polytec PSV-400 (PSV-I-400) vibrometric probe, an OFV-5000 controller and a PSV-W-400 supervision & acquisition system was used in the experiment. The controller and the supervision system were contained in a dedicated mobile enclosure. Vibration velocity was measured behind the side indicator and behind the rear passenger door handle. The measurements were performed in the neutral gear with and without forcing the crankshaft rotational speed of 2000 min^{-1} . The measurements were carried out for a jacked up car and a car standing on its wheels. The two cars were investigated in the same conditions. Figure 3 shows a photograph of the test rig and the place (behind the passenger handle) on which the laser beam falls.



Fig. 3. Test rig: 1 – place from which laser beam is reflected, 2 – method of isolating from base (jacking up), 3 – scanning probe

The results are shown in the form of diagrams in which the measured velocities of the vibrations generated by motor vehicles are compared. The waveforms were registered during 0.5 s long tests being part of the measurement lasting 2 s and involving 2048 samples in each case. Also frequency spectra (obtained through the Fourier transform) are shown in the figures.

5. Measurement results

Figure 4 shows the waveform and the frequency spectrum of engine vibrations measured at idle running behind the passenger handle.

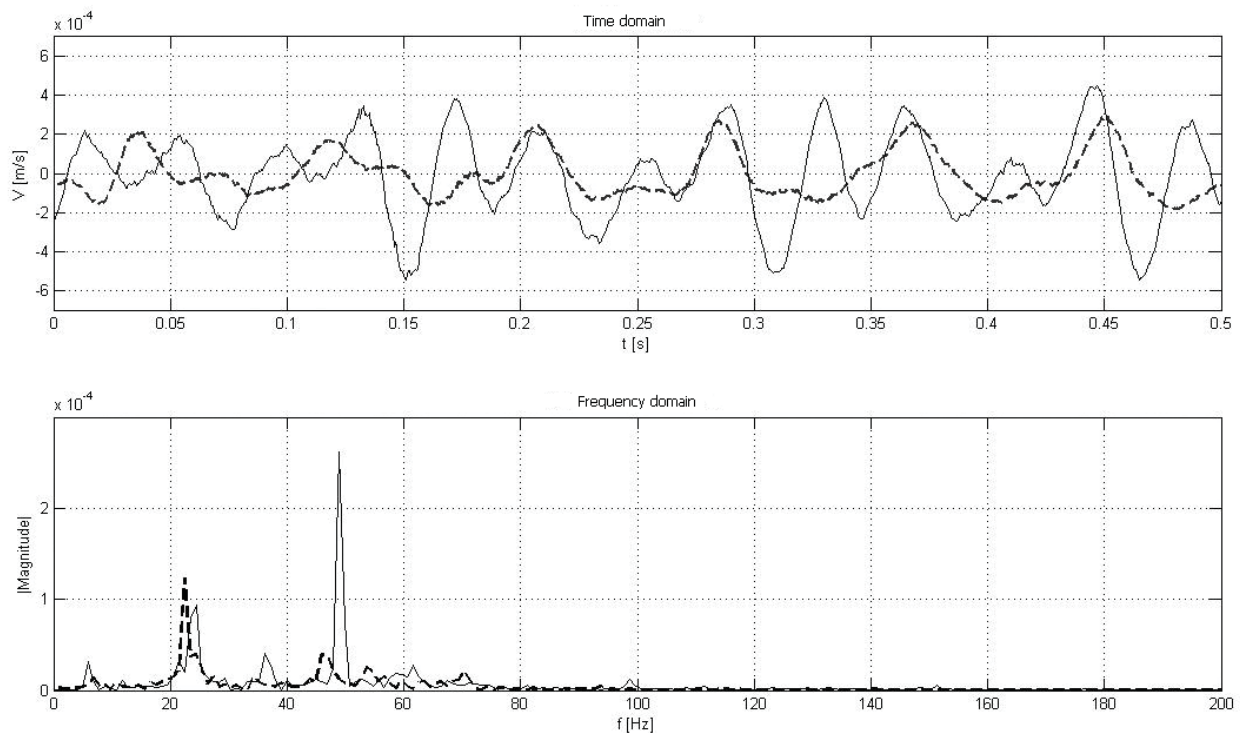


Fig. 4. Waveform and frequency spectrum of vibration velocities measured behind passenger handle for jacked up idle running car; solid line represents car having engine equipped with supercharger

The above analysis was performed for the two compared cars. It should be noted that the measurement of vibrations under the forced crankshaft rotational speed of 2000 min^{-1} carries an error due to the difficulty in maintaining constant speed during the measurement, especially in the case of the car whose engine is not equipped with a supercharger. This adverse phenomenon can be partially eliminated thanks to the fact that the Fourier transform does not preserve information about the phase of the measured signal [5]. The figure below shows the trace of vibration velocity measured behind the indicator of the car not isolated from the base for the crankshaft rotational speed of 2000 min^{-1} forced at idle running. It is clearly visible that vibration frequency and signal nonstationarity increase for both the car with an engine supercharger and the one without it.

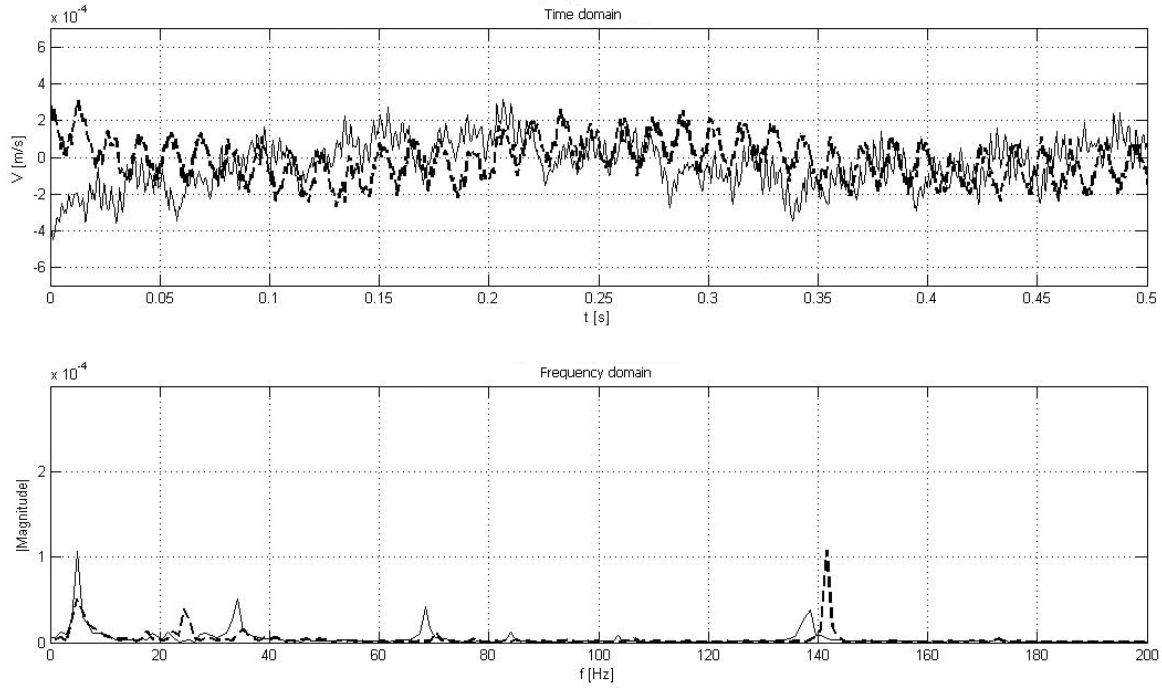


Fig. 5. Waveform and frequency spectrum of vibration velocities measured behind passenger handle for jacked up idle running (2000 rpm) car; solid line is for car having engine equipped with supercharger

The table below shows a comparison of average and maximum vibration velocities for the particular measurements.

Tab. 1. Maximum and average vibration velocities in different states

No.	Description	1,4BZ 90CV CD		1,4BZ 120CV CD	
		V_{\max} [m/s]	V_{av} [m/s]	V_{\max} [m/s]	V_{av} [m/s]
1.	Measurement behind handle, jacked up idle running vehicle	0.31	-0.0022	0.53	-0.017
2.	Measurement behind handle, jacked up idle running vehicle, forced 2000 min^{-1}	0.35	-0.0038	0.88	-0.019
3.	Measurement behind handle, jacked up idle running vehicle, no speed forcing	0.39	-0.0020	0.54	-0.018
4.	Measurement behind handle, jacked up idle running vehicle, forced 2000 min^{-1}	1736	-12.7	0.34	-0.020
5.	Measurement behind handle, not jacked up idle running vehicle, no speed forcing	0.46	-0.00023	0.55	-0.022
6.	Measurement behind handle, not jacked up idle running vehicle, forced 2000 min^{-1}	0.31	-0.0015	0.33	-0.030
7.	Measurement behind handle, not jacked up idle running vehicle, no speed forcing	0.48	0.0031	0.65	-0.017
8.	Measurement behind handle, not jacked up idle running vehicle, forced 2000 min^{-1}	0.41	-0.0046	0.60	-0.020

Measurement 4 (tab. 1) carries a large error due to the factors described earlier. For this reason the measured velocities in this case were not taken into account in the analysis.

6. Conclusions

The following conclusions emerge from the car vibration velocity spectra and waveforms and the values shown in tab. 1:

- the vibration velocities of the car whose engine was equipped with a supercharger are higher in each case;
- the vibration signal under forcing has a nonstationary character (fig. 4) and the signal without forcing is also nonstationary but no large fluctuation of peak values is observed in this case;
- the jacking up of the car, aimed at eliminating the effect of the base, has no methodological justification, as indicated by the properties of the transform and the high values of the dominant harmonics;
- it is very difficult to maintain the forcing, particularly in the case of the car without an engine supercharger. Such a measurement may carry a large error, of which one should be aware in order to avoid analytical errors;
- the two vehicles generate vibrations in the range of human internal organs natural vibrations. In the case of the car with a supercharged engine, the amplitudes of the vibrations are larger;

The aim of the research was to measure the velocities of the vibrations generated by a motor vehicle. The passenger comfort is greater in the case of the car whose engine is not supercharged. But the decision in this regard belongs to the owner since a car with an engine equipped with a supercharger is characterized by better driving properties, such as the ease of maintaining a constant driving speed.

References

- [1] AFFIRM Investigators, *A comparison of rate control and rhythm control in patients with atrial fibrillation*, N. Engl. J. Med., 2002; 347: 1825-1833.
- [2] De Silva, C., *Vibrations Fundamentals and Practice*, NY, CRC Press 2000.
- [3] Engiel, Z., *Protection of the environment against vibrations and noise (in Polish)*, PWN, Warsaw 1993.
- [4] *Measurement Solutions: Made Possible by Laser Vibrometry*, Polytec LM INFO Special, Issue 1/2003.
- [5] Kaźmierczak, A., Wróbel, R., *Vibroacoustic Diagnosis of EGR system*, Silniki Spalinowe, 3/2008.



COMPARATIVE ANALYSIS OF THE VIBRATIONS OF A SPARK-IGNITION ENGINE WITH AND WITHOUT SUPERCHARGING, MOUNTED IN NEW MOTOR VEHICLES

Andrzej Kaźmierczak
Marek Reksa
Przemysław Moczko
Radosław Wróbel

Wroclaw University of Technology
Institute of Machine Design and Operation
I. Łukasiewicz Street 7/9, 50-371 Wrocław
Tel. +48713477918
e-mail: andrzej.kazmierczak@pwr.wroc.pl
marek.reksa@pwr.wroc.pl
przemyslaw.moczko@pwr.wroc.pl
radoslaw.wrobel@pwr.wroc.pl

Abstract

The paper presents the results of tests carried out on two spark-ignition engines: 1.4BZ 90CV CD and 1.4BZ 120CV CD installed in new Fiat Bravo (model 198, version 54A) motor cars. The latter engine model (120CV) was equipped with a supercharging system. The investigations consisted in comparing engine vibrations measured in specific and representative points. In order to determine the vertical component vibrations, the measurements were performed via a mirror. A PSV-400 laser Doppler vibrometer made by Polytec was used to measure vibration velocities. The vibrometric system directly measures two quantities: displacement and velocity. In the investigated case, vibration velocity is the variable which supplies better diagnostic information. Vibrations were measured for the car standing on its wheels and for the car jacked up to reduce the influence of the car vibration damping systems on the measurement results. The latter are presented in the form of comparative diagrams. Moreover, the fast Fourier transform was used to determine the frequency distribution. Prior to that the signal was subjected to conditioning operations using parametric windowing and filtering. Interesting conclusions emerge from the obtained results and on their basis the effect of the drive unit on the behaviour of the car body can be assessed for different engine types and rotational speeds. It is shown that the way in which the engine is mounted affects the vibrations of the car.

Key words: *Laser Doppler Vibrometry, engine vibration, vibration velocity, spark-ignition engine*

1. Introduction

Mechanical vibration is a phenomenon consisting in the conversion of kinetic energy into potential energy, which is further converted into kinetic energy, etc., until the phenomenon dies out [1 - 3]. The measurement of mechanical vibrations depends on the system's number of degrees of freedom (DOF).

Since a mechanical system, such as the combustion engine, has an enormous number of DOFs, vibration diagnostics is highly complicated. In order to avoid a huge number of computations,

physical systems are interpolated to systems with a known number of DOFs. In such systems the components with the smallest mass are represented by deformable constraints while components with a larger mass are represented by material particles or rigid bodies [3].

For vibroacoustic vibration measurements the system is assumed to be continuous, which means that the number of freedom points is determinate and that it is necessary to change over from discretization based on differential equations to continuity based on integral calculus [4]. Therefore one can say that vibroacoustic vibration measurement is approximation already at the detection level where system discretization is approximated by continuity.

The aim of this research was to determine the effect of supercharging on combustion engine vibrations. It is obvious that the vibrations are transmitted to the rest of the vehicle and so affect the health and travel comfort of the driver and the passengers.

2. Description of investigated object

Two new Fiat Bravo Model 198 54A cars with respectively engine 1.4BZ 90CV CD and 1.4BZ 120CV CD were tested. The latter engine model was equipped with a supercharging system. The specifications of the tested cars with the two different engines are shown in the tab. below.

Tab. 1. Comparison of tested engines specifications

No.	Specification	Type of engine	
		1.4BZ 90CV CD	1.4BZ 120CV CD
1.	Engine cubic capacity	1368 cm ³	1368 cm ³
2.	Engine horsepower rating	90 hpm	120 hpm
3.	Engine mounting	front crosswise	front crosswise
4.	Type of camshaft	OHC	OHC
5.	Cylinders	bank	bank
6.	Number of cylinders	4	4
7.	Number of valves per cylinder	4	4
8.	Weight	1205 kg	1260 kg

In both cases the engine is mounted crosswise. The drive unit supports perform the function of a structural connection between the drive unit and the car body. The supports are suitably dimensioned to carry the drive unit weight and to withstand the loading with the torque transmitted from the engine. Each support has a rubber-metal shackle to dampen the vibrations generated by the engine. The shackle reduces most of the vibrations transmitted by the car body [5]. The drive unit support is of the centre of gravity type and consists of two shackles plus a reaction rod. The latter is a flexible connector in which the supports are aligned along the axis of gravity for the engine's centre of gravity in order to obtain a reactive force with a zero arm. The mounting is shown in fig. 1.

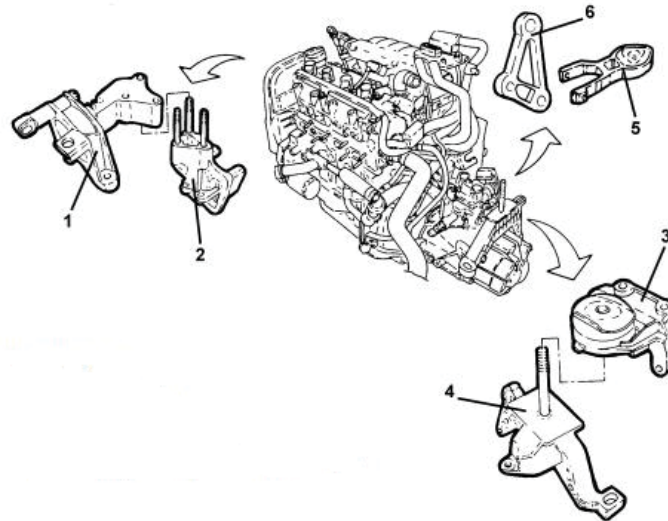


Fig. 1. Elements for mounting investigated object (1 - flexible connector on timing gear side, 2 - rigid support on timing gear side, 3 - flexible connector on gearbox side, 4 - rigid support on gearbox side, 5 - reaction rod on differential gear side, 6 - rod fixing support on differential mechanism side) [5]

3. Measuring system and method

Laser Doppler vibrometry (LDV) was used in the investigations. LDV exploits the Doppler effect, which consists in a change of the length of the light wave received by a target if the latter is moving relative to the source.

A laser probe is the transmitting-receiving device. After its reflection and return to the scanning head the light beam hits the lens. Thanks to this measuring method one can directly measure velocity and relative displacement [4]. Any other parameter is a derivative the above quantities. Velocity is converted into voltage proportional to frequency shift. The measurement of displacement consists in counting the occurrences of areas generating specific wavelengths.

A diagnostic circuit consisting of a Polytec PSV-400 (PSV-I-400) vibrometric probe, an OFV-5000 controller and a PSV-W-400 supervision & acquisition system was used in the experiment. The controller and the supervision system were contained in a dedicated mobile enclosure. Vibration velocity was measured behind the side indicator and behind the rear passenger door handle. The measurements were performed in the neutral gear with and without forcing the crankshaft rotational speed of 2000 min^{-1} . The measurements were carried out for a jacked up car and a car standing on its wheels. The two cars were investigated in the same conditions. In order to measure vertical-vector vibrations a mirror (fig. 2) reflecting the laser beam was used.



Fig. 2. Test rig: 1- laser probe, 2- mirror, 3- place of laser beam reflection

4. Measurement results

The results are presented in the form of diagrams in which the measured vibration velocities generated by the cars are compared. The waveforms were registered during 0.5 s long tests being part of the measurement lasting 2 s and involving 2048 samples in each case. Also frequency spectra (obtained through the Fourier transform) are shown in the diagrams.

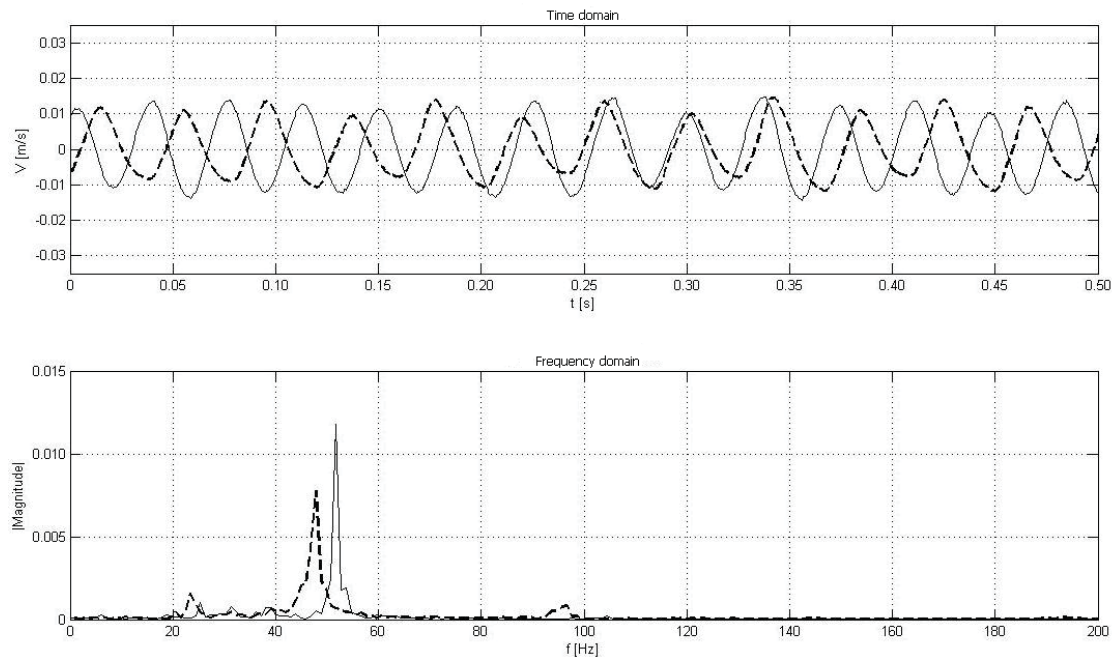


Fig. 3. Waveform and frequency spectrum of engine vibration velocity for not jacked up idle running car, solid line is for car with engine equipped with supercharger

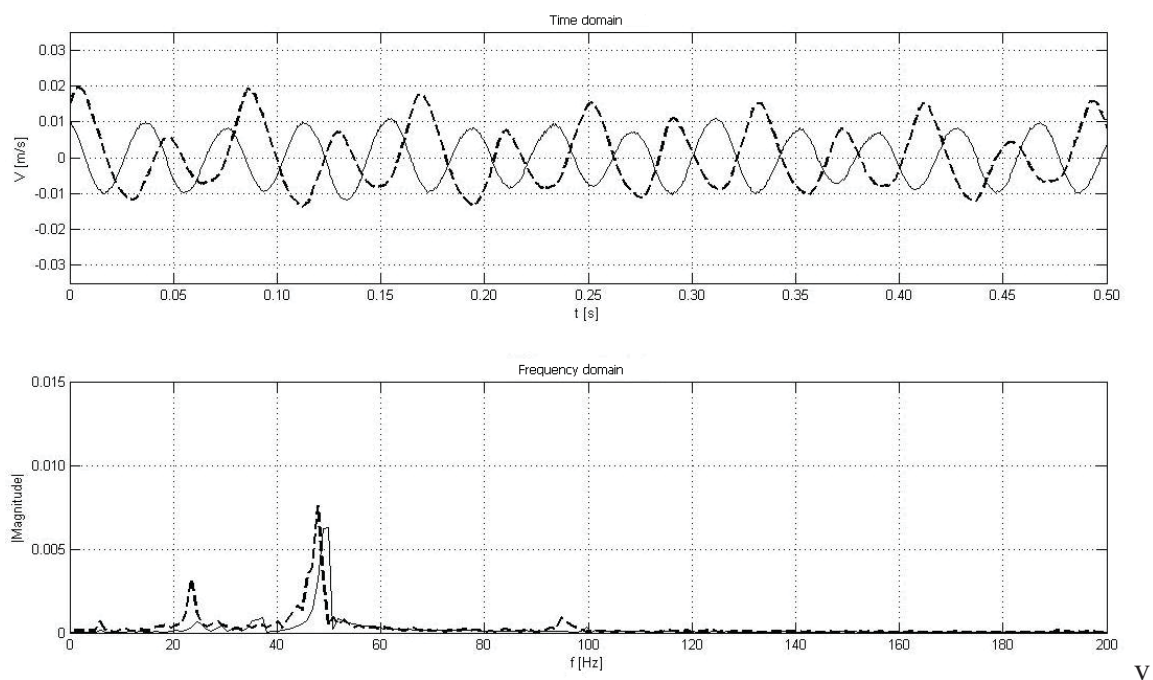


Fig. 4. Waveform and frequency spectrum of engine vibration velocities for jacked up idle running car, solid line is for car with engine equipped with supercharger

The measurement of the vibrations of the engine with forced crankshaft rotational speed is poorly repeatable, particularly for the engine without supercharging. In order to obtain reliable results, the measurements were performed several times. The average and maximum vibration velocities are compiled in tab. 2.

Tab. 2. Maximum and average vibration velocities in different states

No.	Description	1,4BZ 90CV CD		1,4BZ 120CV CD	
		V _{max} [m/s]	V _{av} [m/s]	V _{max} [m/s]	V _{av} [m/s]
1.	Idle running engine without forcing, car not jacked up	15.5	0.017	17.2	0.017
2.	Idle running car with forced 2000 min. ⁻¹ , car not jacked up	26.6	-0.041	27.6	-0.017
3.	Idle running engine without forcing, car jacked up	19.6	0.011	12.9	-0.018
4.	Idle running engine with forced 2000 min. ⁻¹ , car jacked up	23.5	-0.024	28.3	-0.010

5. Conclusions

The following conclusions can be drawn from the obtained characteristics and the vibration velocities measured by the laser vibrometer:

- the vibrations generated by the engine have a stationary character;
- the maximum vibration velocities are higher in the case of the engine equipped with a supercharger. Exactly the opposite was found for the average velocities;
- it is very difficult to maintain crankshaft rotational speed forcing and in order to obtain reliable results several measurements need to be performed, particularly in the case of the engine without a supercharger;
- the engine mounting system is highly effective in damping the vibrations transmitted to the rest of the car;
- the jacking up of the car does not affect the vibration frequency distribution, but it affects the amplitude of the individual harmonics. This means that it is not necessary to jack up vehicles for comparative analyses, provided the above measuring method is used.

References

- [1] De Silva, C., *Vibrations Fundamentals and Practice*, CRC Press, NY 2000.
- [2] Giergiel, J., *Mechanical vibrations (in Polish)*, University Scientific-Educational Publishers, Cracow 2000.
- [3] Kaźmierczak, A., Wróbel, R., *Detection of injection unit defects in Diesel engine through analysis of vibrations*, Journal of Kones, 2007.
- [4] Skalmierski, B., *Analytical mechanics and theory of vibrations*, Polytechnic Publishing House, Częstochowa 2001.
- [5] Fiat's technical information materials, www.fiat.com.



INFLUENCE OF UNBALANCE OF LOADS ON QUALITY OF ELECTRIC ENERGY IN A LOW VOLTAGE LINE

Piotr Kolber

*University of Technology and Life Sciences
ul. S. Kaliskiego 7, 85-796 Bydgoszcz, Poland
tel.: +48 52 3408297, fax: +48 52 3408495
e-mail: pkolber@utp.edu.pl*

Abstract

The paper presents results of investigations of deviations of voltage from rated value (δU) and the voltage unbalance coefficient (α_{U2}) at the rural consumers' sites supplied from the final section of a low voltage line under the load asymmetry conditions. Those parameters are one basic parameters describing quality of electric energy. A probabilistic model of the distinguished parameters, taking into account load unbalance, was built in scope of the investigations. A simulation programme enabling to determine voltage deviation and the voltage unbalance coefficient, among other things, for various variants of the cable cross-sections applied and various variants concerning the types of the consumers connected was elaborated on the basis of the model built; two essential types were distinguished here: living and production consumers characterised by different power consumption rate. The calculations were performed for a three-phase, four-cable airborne power line with flat arrangement of cables.

Keywords: low voltage line, single-phase receivers, load unbalance, voltage deviations, voltage unbalance

1. Introduction

Four-cable airborne power lines with flat arrangement of cables are the most frequent lines in the rural low voltage site networks. Consumers using three-phase and single-phase receivers for production and living purposes are supplied from those lines. Using those receivers is decisive for the line load rate. That load is unbalanced due to uneven division of power of the single-phase receivers into individual line phases and their random connecting to the network [5]. The unbalance is also influenced by: unequal phase mutual impedances of the electric power lines, unequal values of phase resistances and reactance of some receivers as well as unbalance of supply voltages. The effect of such unbalanced load is voltage unbalance – unequal values of voltages in the individual line phases. It deteriorates conditions of work of the receivers, particularly three-phase ones, e.g. engines. Moreover, the effect of unbalanced load are increased power and electric energy losses when compared to the losses which would occur in case of balanced load. Electric energy as goods must be characterised by appropriate values of the parameters. Keeping their admissible values is one of the conditions aimed at assurance of correct work of the receivers supplied by low voltage lines. From among various parameter describing energy quality one of the most significant is effective value and supply voltage unbalance. They are identified by deviation of voltage from rated value (δU) and the voltage unbalance coefficient: reverse sequence (α_{U2}) and

zero sequence (α_{U0}). Due to the fact that the standardised regulations concerning electric power refer to the two first parameters, the investigations were focused on them.

2. Selection and identification of the investigation object

The investigation object is a low voltage electric power line, with unbalanced load, supplying rural consumers.

Model of line of 2nd type with zero values of transverse parameters of an equivalent circuit (transverse parameters: unitary line conductance G_0 , unitary line susceptance B_0 are taken into account in the medium and high voltage lines) [1] has been adopted for the analysis. The considered line type is characteristic for rural areas: four-cable airborne power lines with flat arrangement of cables. This type, being the most common, is also the most favourable due to the mutual impedances of the lines in the aspect of load unbalance, and thus quality of energy supplied to the consumers. Unequal values of mutual impedances make that the line is unbalanced as a transmission element of electric energy.

Moreover, it has been assumed that the nature of the receivers is resistance-and-induction one.

Operation and maintenance tests in a real investigation object were performed in scope of the identifications. The investigation purpose was to determine load unbalance and related voltage conditions present in low voltage networks. The investigation programme consisted, among other things, of:

- determination of values of voltages occurring at the sites of the consumers, particularly the ones consuming energy supplied by the final section of the low voltage line,
- analysis of the values of voltage deviations from the rated value (230 V) including the tests to check, if those deviations exceeded the ranges specified by the standard,
- determination of the voltage unbalance level in a low voltage network.

The results of the performed investigations of the voltage conditions in a low voltage site network, referred to the voltage value and its unbalance are presented in the Tables 1 and 2

Tab. 1. Values of the voltage deviations at the sites of the consumers supplied by the final section of the low voltage line

Measurement method	Voltage deviation		
	Average value [%]	Value range [%]	Admissible value range [%]
Momentary measurements at 74 consumers' sites in the autumn-and-winter season, in the evenings:			
- with the receivers switched on	-2.48	-10.6 ÷ +5.13	-10 ÷ +10
- after switching on an additional 1 kW single-phase receiver	-2.47	-10.9 ÷ +4.83	
- after switching on an additional 2 kW single-phase receiver	-3.17	-12.2 ÷ +5.43	

Calculations of the value of the load deviations show that the average values are within the admissible range $-10 \div +10\%$, however exceeding the lower admissible limit was observed in 10% of cases. Growing the lower limit of the values going beyond the admissible range occurred together with an increase in power of the additional receiver being switched on.

At the investigation stage it was attempted to answer the question how the voltage conditions are changed when a rural consumer buys a new single-phase receiver, facilitating the work on the farm, and connects it to a single-phase network.

In many farms (19.8% of the consumers) the admissible value of the voltage unbalance coefficient (2%) was already exceeded with the current load (Table 2). After connecting a 1 kW receiver to a randomly selected phase, the number of the consumers with exceeded admissible value of the unbalance coefficient increased to 21,6%, and after connecting a 2 kW receiver to the same phase – as much as by 31%. It should be taken into account that connection of additional single-phase receivers improved voltage unbalance at some consumers' sites, however this state was worsened in a considerable part of cases.

Tab. 2. Voltage unbalance at the consumers' sites supplied by the final section of the low voltage line

Measurement method	Sample (consumers) number	α_{U2} [%]	α_{Uadm} [%]	Percentage of admissible value exceeded
- with the receivers switched on	69	1.29	2	19.8
- after switching on an additional 1 kW single-phase receiver	69	1.40	2	21.6
- after switching on an additional 2 kW single-phase receiver	69	1.79	2	31.0

Thus it was concluded that after introduction of new single-phase receivers improving technological processes in farms and used at households, taking into account the current state of the rural low voltage networks, exceeding the admissible values of the voltage unbalance coefficient should be expected.

Measurements of voltages at the medium voltage/low voltage stations were used to determine the voltage unbalance coefficient. It turned out that the phase voltages were practically balanced there, and the average value of the coefficient was around 0.02%.

The standard PN-EN 50160 specifies the limitations not only as to the admissible value for the parameters being the voltage deviation and supply voltage unbalance, but also admissible percentage number of exceeding those limiting values during a week time. Five-percent number of exceeding limiting values out of all weekly performances is admissible [7].

3. Probabilistic model to determine deviations and voltage unbalance coefficients in a low voltage line

The values of the voltage drops and consequently levels and unbalance voltage in a low voltage line are influenced by the parameters of the line as a transmission element, being its length, arrangement of cables, cross-sections of the cables, distribution of the receiving points as well the consumers through the value of the consumed power and unbalance of phase loads. Due to the quantity of those factors that are decisive for the level and voltage unbalance in the line and due to the difficulties related to performance of the complex investigations concerning loads of consumers as well as their cost, a model of simulation determination of the selected quality parameters of electric energy was elaborated. It facilitates to determine values of the voltage drops and deviations and voltage unbalance with various methods of distributing the consumers along the line, different values of the power consumed by the consumers and various levels of phase load unbalance. The input data refer to:

- length of the line l ;
- number of consumers n ,
- distance of the receiving points from the line beginning l_i ;
- cross-sections of the cables: phase s , neutral s_n ;
- distance between the cables $b_{AN}, b_{BN}, b_{CN}, b_{AB}, b_{BC}, b_{CA}$;
- value of the power consumed by the consumers P_i .

Topology was determined for the line, it means on the basis of once generated: length of the line l from Weibull distribution with the parameters $p=2, \lambda=0,8$, which corresponded to the data on the circuits gathered from the territory of Poland [2], determined number of receiving points n their distribution along the line l_i on the basis of the triangular distribution [3] was generated. Next, the phase line was specified randomly: the most, intermediately and the least loaded by a consumer at each i -th receiving point. The momentary loads for daily changes were generated from empiric distribution. In each generation point (time moment) the average value and standard deviation of load was taken from normal distribution on the basis of 14 days of daily changes at the consumer's site. Division of loads into phases was performed by generation of the value of the load unbalance coefficients in the particular receiving points on the basis of empiric distributions obtained from the load measurements performed at the consumers' sites. Those coefficients were defined as relations of respective phase loads [6]:

a) maximum load coefficient [4]

$$w_i = \frac{P_{\max i}}{P_i} \quad (1)$$

b) intermediate load coefficient

$$k_{1i} = \frac{P_{pi}}{P_{\max i}} \approx \frac{I_{pi}}{I_{\max i}}, \quad (2)$$

c) minimum load coefficient

$$k_{2i} = \frac{P_{\min i}}{P_{\max i}} \approx \frac{I_{\min i}}{I_{\max i}} \quad (3)$$

where:

$$P_i = P_{\max i} + P_{pi} + P_{\min i} \quad (4)$$

$P_{\max i}, I_{\max i}, P_{pi}, I_{pi}, P_{\min i}, I_{\min i}$ – power and phase current respectively for being the most, intermediately and the least loaded in particular receiving points

Mutual relation between the values of the coefficients is determined by the relation:

$$k_{1i} + k_{2i} = \frac{1}{w_i} + 1 \quad (5)$$

The value of the coefficient k_{2i} was determined on the basis of the relation (5) after prior generation of the values of the coefficients w_i and k_{1i} .

The admissible ranges of their values are presented in the Table 3.

Tab. 3. Admissible values of the coefficients of load unbalance

w_i	0.33	0.36	0.4	0.44	0.5	0.57	0.67	0.8	1
k_{1i}	1	0.875÷1	0.750÷1	0.625÷1	0.5÷1	0.375÷0.75	0.25÷0.5	0.125÷0.25	0
k_{2i}	1	0.875÷0.75	0.750÷0.5	0.625÷0.25	0.5÷0	0.375÷0	0.25÷0	0.125÷0	0

For balanced load those coefficients take the values: $k_{1i} = 1$, $k_{2i} = 1$, $w_i = 1/3$, however in case of an extreme unbalance, where the total power is taken by one phase, their values are as follows: $k_{1i} = 0$, $k_{2i} = 0$, $w_i = 1$. The momentary values of the coefficients of power - $\cos\varphi_{fi}$ for the receiving points were generated on the basis of the empiric distributions obtained from measurements performed at a medium voltage/low voltage station. The values of the phase loads and the phase coefficients of power made it possible to determine currents in the line (in the phase and neutral cables) between the receiving points. Those currents were the basis to determine drops of voltages, and thus values of phase voltages, deviation of phase voltages and coefficients of voltage unbalance in receiving points. The voltage deviation and coefficient of voltage unbalance are respectively defined by the following relations [5]:

$$\delta U_{fi} = \frac{U_{fi} - U_n}{U_n} \cdot 100\% \quad (6)$$

where:

U_n – rated voltage ($U_n=230V$),

U_{fi} – phase voltage.

$$\alpha_{U_{2i}} = \frac{U_{2i}}{U_{1i}} \cdot 100\% \quad (7)$$

where:

U_{2i} , U_{1i} – symmetrical components of phase voltages, respectively: of reverse and concurrent sequence in the i -th terminal

4. Selected results of simulation investigations

Due to performance of the simulation, a low voltage line with the length $l = 1048$ m, to which 15 consumers are connected, who are distributed in the following distances from the beginning of the line was, among other things, generated:

$l_1 = 82$ m, $l_2 = 92$ m, $l_3 = 105$ m, $l_4 = 284$ m, $l_5 = 296$ m, $l_6 = 301$ m, $l_7 = 312$ m, $l_8 = 368$ m, $l_9 = 495$ m, $l_{10} = 589$ m, $l_{11} = 663$ m, $l_{12} = 750$ m, $l_{13} = 795$ m, $l_{14} = 841$ m, $l_{15} = 1048$ m.

Calculations of the unbalance coefficient α_{U_2} were performed for different variants concerning the applied cross-section of cables and various variants concerning types of the connected consumers. Two types of consumers were considered: living and production ones. The obtained values of the coefficient for the performed simulations are presented in the Table 4 and as an example in the Fig.1.

The Fig.1 shows a histogram of values of voltage unbalance coefficients for the performed simulation in case of a supply line for the prevailing number of production consumers. Distinct fraction of values of the coefficient exceeding the admissible value of 2% may be noticed.

Tab 4. Selected results of simulation investigations of the voltage unbalance coefficient

Cross-sections of the cables		Percentage value of the exceeded admissible value of the coefficient		
phase	neutral	α_{U2}		
70	70	2.09	0.49	0.00
50	70	9.72	2.97	0.00
50	50	10.32	3.97	0.20
35	50	11.71	9.82	0.99
35	35	12.10	10.02	1.09
Number of living consumers		0	5	10

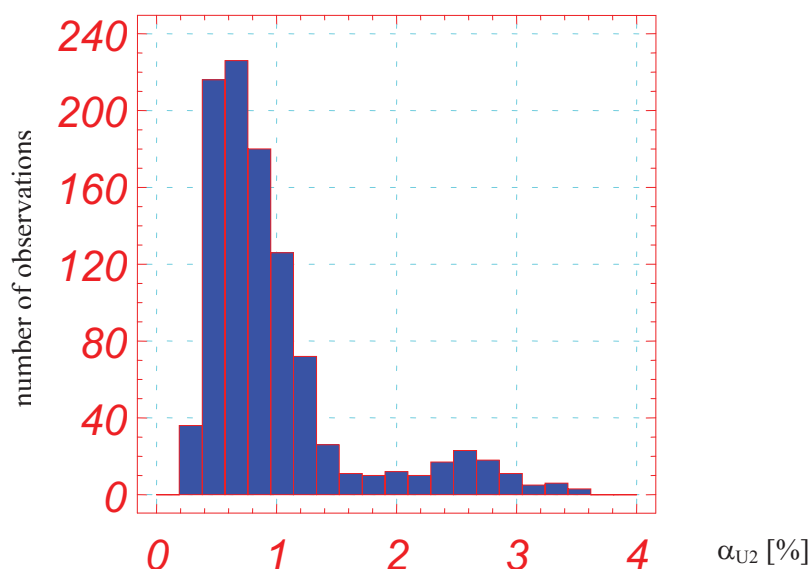


Fig.1. Histogram of values of the voltage unbalance coefficient, obtained as a result of the simulation, for the following parameters: c-section of phase cables - 35 mm², cross-section of the neutral cable - 35 mm², number of the living consumers – 5.

5. Summary

Performance of the simulation experiments with a probabilistic model allows to determine values of the selected parameters describing the low voltage line and consumers, for which there is a risk of exceeding admissible values of the selected items describing quality of the electric energy transferred. Risk of exceeding admissible values of the parameters of electric energy caused by the load unbalance is the larger the larger consumption of power in the line is. The length of the low voltage line with unbalanced consumption of power affects quality of electric energy, however significant deterioration of the parameters (δU , α_{U2}) appear at the clients' sites located within the final section of the line (e.g. more than 800 m for a line with about 1000 m length). Improvement of the values of the parameters δU , α_{U2} is obtained by increasing cross-sections of the phase and neutral cables, but it is related with bearing specific costs in order to assure adequate quality of electric energy supplied to the consumers – improvement from 25 to 40% of the values of the parameters for the simulation performed.

References

- [1] Bolkowski, St., *Elektrotechnika teoretyczna*, Tom 2., WNT, Warszawa 1986.

- [2] Gawlak, A., *Stan wiejskich linii niskiego napięcia w Polsce w 1991r.*, Energetyka, 10., 1992.
- [3] Hellwig, Z., *Elementy rachunku prawdopodobieństwa i statystyki matematycznej*, PWN, Warszawa 1993.
- [4] Kolber, P., *Wpływ wybranych czynników na nierównomierność obciążeń wiejskich elektroenergetycznych sieci niskiego napięcia* (rozprawa doktorska), Uniwersytet Warmińsko-Mazurski, Olsztyn 2006.
- [5] Kowalski, Zb., *Asymetria w układach elektroenergetycznych*, PWN, Warszawa 1987.
- [6] Kujszczyk, S., *Elektroenergetyczne sieci rozdzielcze, Cz.2.*, PWN, Warszawa 1991.
- [7] Polska Norma PN-EN 50160, *Parametry napięcia zasilającego w publicznych sieciach rozdzielczych*, 1998.



PARAMETERIZATION OF A TECHNICAL OBJECT IN SOLID EDGE

Bogdan Landowski, Rafał Poliński

*University of Technology and Life Sciences
Machine Maintenance Department
ul. Kaliskiego 7, 85-796 Bydgoszcz, Poland
tel.: +48 52 3408495, fax: +48 52 3408495
email: lbogdan@utp.edu.pl*

Abstract

This paper presents the core of the elaborated system of automatic generation of design documentation for a family of technical objects. An indispensable element of the system are commercial CAD 3D computer tools. The method of using parametric models of objects for automatic generation of the design and technological documentation (to the limited extent) of the modelled equipment has been presented. Implementation of the system made it possible to execute orders for production of the equipment submitted by the clients who require (other than standard) features of an object. All the considerations have been illustrated on the basis of the devices intended for the companies dealing with production and distribution of cables. Assumptions and design solutions for a cable rewinder have been elaborated. An algorithm of a process of preparation of the design documentation for various variants (series of types) for the designed equipment, on the basis of a prepared three-dimensional parameterized model of an object, has been elaborated. The suggested solutions and elaborated programming tools have been implemented in practical applications. Placing the consecutive variants of the equipment on the market, in the production system under analysis (a real enterprise), was connected with manual modification of recording the designs of most of the parts of the base MCAD (Mechanical Computer-Aided Design) model of the specific product. The above solution resulted in design- and technological errors, most of them being detected only at the production process stage. It was linked with longer term of execution of an order and with bearing additional costs. Implementation of the suggested system contributed to shortening order execution term, reduction of the equipment production costs and elimination of errors in the design documentation.

Keywords: *designing, parameterization, parametric modelling, computer aided design, automation of numerical design recording*

1. Introduction

Due to an increased demand for products having features imposed by a client, the production companies were forced to implement quick modifications of already existing products. 3D CAD programs became one of the tools allowing a quick modification of a product. Along with growing requirements, concerning shorter order execution terms and product production capabilities according to the individual clients' requirements, the companies started to parameterize their products in order to be able to modify them quickly.

The paper presents benefits resulting from applying parameterization of a model of a technical object during the equipment designing process dedicated to the companies dealing with production and distribution of cables. Assumptions and design solutions for a cable rewinder have been elaborated. A cable rewinder is a device intended for bundling wires being unwound from reels,

bobbins and bundles [1]. It is quite often that after removing the bundling reel they also make it possible to wind wire on commercial plastic bobbins. Solid Edge with Synchronous Technology (Solid Edge ST) was applied to support the design process. Basing on the adopted design assumptions a 3D (Three-Dimensional Graphics) model of a cable rewinder (Fig.1) has been created using this software.

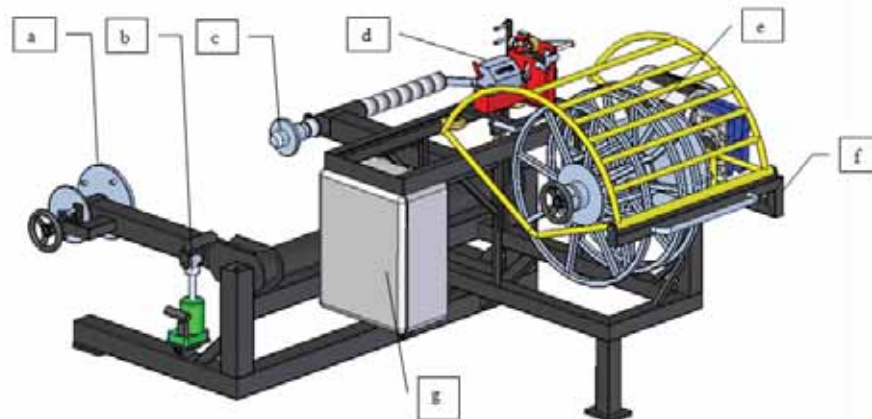


Fig.1. The most important subassemblies and components of a CAD model of a cable rewinder: a) unwinder journal with a brake, b) hydraulic jack, c) pressure journal, d) lying device with a measurement module, e) framework bobbin of a winder, f) supporting structure, g) electrical box (Source: own elaboration)

2. CAD model generation process for the specific product variant

Parameterization is a substitution of numerical dimensions of a 3D model with names of the variables (parameters) and a related possibility to apply equations and inequalities defining relations between those variables, and consequently automatic modification of a geometrical model. Parameterization is a kind of a span between a geometrical model and a mathematical model, and it assures mutual conformity of those models. Changing a value of one dimension in a design parametric record results in changing other resultant dimensions of the model [2]. By applying parameterization, a family of structures may be obtained very easily (including particularly series of types of standardised products) [4].

Two types of parameterized variables: geometrical and relational have been used to create a 3D parametric model of the rewinder. The geometrical parameters of the model may be edited by editing a sketch (a sketch in Solid Edge ST is a profile for extrusion and cutting commands made on a reference plane) from which it was created, or by changing the value of the parameters of the feature used to create it [3]. For instance it is possible to change the extrusion length for the extruded part, by entering new value for the item “extrusion” in the structural tree of the model. Relational parameterization allows to change the design record by changing the values of the dimensions obtained relationally for the specified independent variable, e.g. values of characteristic features, significant dimensions [2]. The relations between the independent variable and the values of the dimensions are recorded in an appropriate editor. After entering the specific value of an independent variable the dimension values are calculated, and then the existing records of the design are updated.

A producer offers several variants of a selected model of the cable rewinder to its clients, thus it may satisfy the needs appearing in the market. Placing the consecutive variants of the equipment on the market was connected with manual modification of recording the designs of most of parts of the base MCAD (Mechanical Computer-Aided Design) model of the specific product. The above solution resulted in design-and-technological errors, most of them being detected only at the

production process stage. It was linked with longer term of execution of an order and with bearing additional costs.

It was suggested to build a system of automatic generation of design documentation, and to the limited extend of technological documentation for a family of the equipment being analysed. Implementation of the system, apart from bringing economic benefits, eliminated the necessity to edit manually the design documentation and thus it limited the errors made at this stage of object production preparation.

In order to shorten the design and construction process, the structure of the base MCAD model of the analysed product [6] was reanalysed. Such items have been distinguished the values of which differ from one another in case of various variants of the product. Some variables were assigned to those items, the values of which are controlled by means of a generator written in Visual Basic language. New values on the basis of a choice made by a user (thus obtaining quite a new form of the product design record) may be assigned to the appropriate variables by means of the application. The procedure algorithm of a user of Solid Edge when working with parameterized model of the rewinder is presented in the Fig. 2.

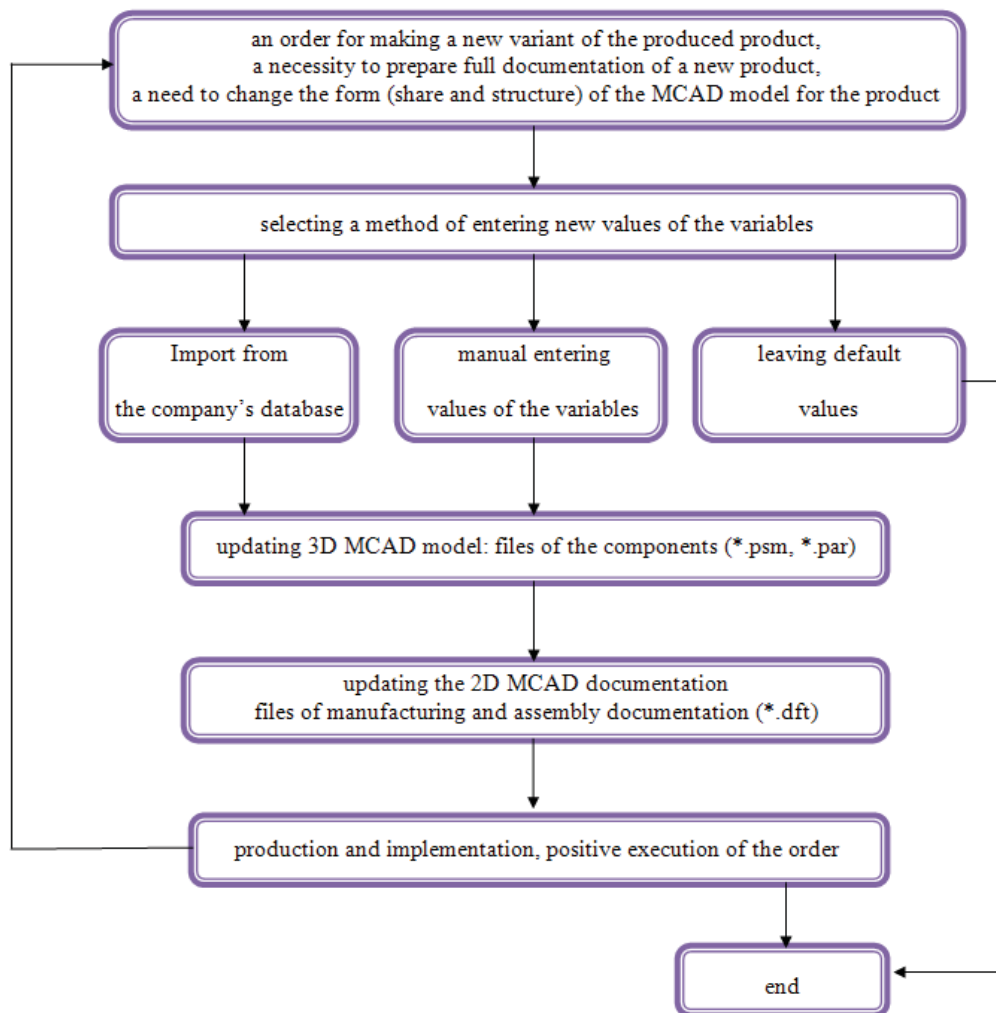


Fig. 2. Simplified algorithm of automation of the design documentation creation process (Source: own elaboration)

Two types of variables have been distinguished, to which new values may be assigned:

- logical variables:
 - a) presence of an automatic lying device (yes, no),

- b) presence of an electronic meter (yes, no),
- c) presence of a travelling device (yes, no);
- metrological variables:
 - a) dimensions of the winder,
 - b) dimensions of the unwinder,
 - c) dimensions of the structure,
 - d) dimensions of the cable lying device guide rail.

After geometrical transformation of the product model, for instance the following items are automatically updated:

- values of the features of a complete assembly (of the rewinder 3D model),
- assembly documentation of the product,
- detailed design documentation,
- database for production orders.

3. Controlling the values of the variables by means of the 3D CAD model generator

Before starting to parameterize each model the forms containing parameters have been prepared [5]. The parameters of the considered models may be divided into two groups:

- directly defined parameters,
- indirectly defined parameters.

The directly defined parameters are the ones which are directly defined by a user and do not depend on one another or on other parameters. The exemplary parameters being defined directly are presented in the Table 1.

Tab. 1. Exemplary parameters being defined directly (Source: own elaboration)

Parameter name	Unit
Reel diameter	mm
Reel width	mm
Core diameter	mm
Unwinder diameter	mm

The indirect parameters result from various dependencies between the parameters or they are an outcome of the design assumptions. The exemplary parameters being defined indirectly are presented in the Table 2.

Tab. 2. Exemplary parameters being defined indirectly (Source: own elaboration)

Parameter name	Unit
Retaining shield generator	mm
Retaining shield hoop	mm
Fixed reel shield generator	mm
Fixed reel shield hoop	mm
Length of the section fastening the guard	mm
Fixed reel core generator	mm

In order to illustrate considerations, the Fig. 3 shows how the geometrical form of the winder is changed (depending on modification requirements, both dimensions and geometrical form may get changed) after determining the input values of the parametric three-dimensional model of the rewinder. Values of such items as: reel external diameter, reel width and reel core diameter are

defined directly. Individual lengths of generators, a driver, bearing pipe, base ring etc. are defined indirectly based on dependencies between the specific elements of the structure.

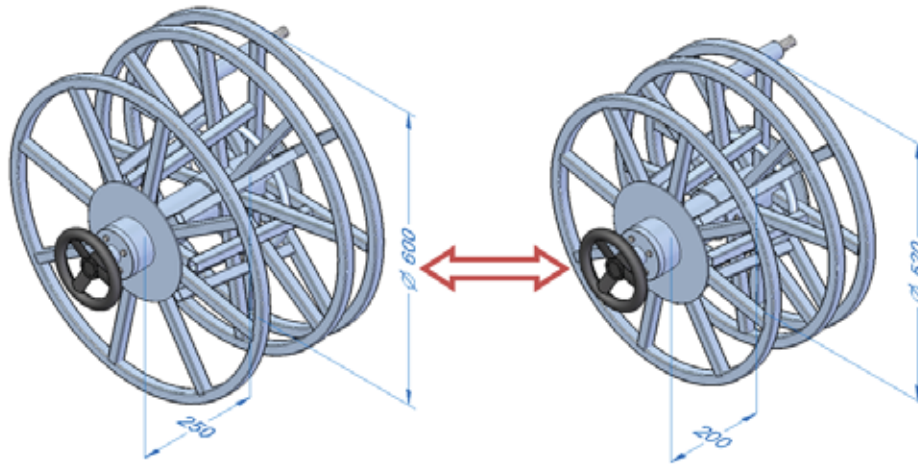


Fig. 3. An example of changing the values of the structure element features after changing the values of the model parameters (Source: own elaboration)

4. Transformation of a parametric model into a resultant design record

An element of the system of automatic generation of design documentation is a developed computer application executing the algorithm of transformation of a parametric model into a resultant design record of the specific variant of the modelled object. Implementation of the algorithm (Fig. 2) was performed in Visual Basic language, and then compiled into the executable form (the application is called “Generator v1.1”). The exemplary application window is shown in the Fig. 4.



Fig. 4. View of the “Generator v1.1” window program (Source: own elaboration)

After entering the numerical data in the “Winder” and “Unwinder” boxes the input data necessary to edit the model are defined. The next step is the user’s selection of the equipment variant (Table 3).

After filling in all the options, the model updating is confirmed by clicking the “Generate” button. The “Update drawings” button is to update the drawings of 2D documentation. The next “Save order” button allows to save the client’s data, as well as the parameters of the ordered equipment in a spreadsheet.

Tab. 3. Variants of the equipment selected by a user (Source: own elaboration)

Option	Variant
Automatic lying device	Yes, no
Measurement	Mechanical, electronic
Version	Stationary, moveable

5. Summary

All the fragmentary solutions elaborated if being combined together make a system of automatic generation of design documentation for a family of objects that may be represented by means of a parametric model.

The elaborated algorithm of the design documentation creating process for various variants (series of types) of the designed device on the basis of the elaborated three-dimensional parameterized model of the rewinder and the elaborated computer program (executing the algorithm built) significantly contribute to:

- shortening the order execution term,
- reduction of the equipment production costs,
- elimination of the design errors occurred when changing manually the equipment parameters.

On the basis of the presented possibilities to modify numerical records of the rewinder structure it may be stated the number of the product variants that may be modelled is in fact unlimited and depends on the individual clients’ needs.

The elaborated programming tools have been implemented and verified in a real system of production of products dedicated for the enterprises operating in the field of production and distribution of cables.

The decision makers of an enterprise in which the elaborated solutions are implemented have eliminated the errors occurring during traditional elaboration of new variants of a product. After implementing the design parameterization methods, described herein, and after expanding them additional, the equipment producer significantly increased the scope of its commercial offer and shortened the time to place new products on the market accompanied by simultaneous reduction of the total production costs.

References

- [1] Tyczyński, J., *Cable and wire picking and packing, Elektrosystemy*, No. 2 (85), p.66-67, 2007
- [2] Sydor, M., *Introduction to CAD. Basics of the computer aided design*, Polish Scientific Publishers, Warsaw 2009.
- [3] Luźniak, T., *Solid Edge ST. Step by step. Traditional drawing and modelling*, GM System Integracja Systemów Inżynierskich Sp. z o.o., Wrocław 2009.
- [4] Kazimierczak, G., Pacuła, B., Budzyński, A., *Solid Edge. Computer aided design*, Helion SA Publishing Group, Gliwice 2004.

- [5] Osyszka, A., Jankowski, R., Sklana, I., Krajewski, P., *Visual Basic for Applications*, Uczelniane Wydawnictwa Naukowo-Techniczne, Kraków 2006.
- [6] Budzyński, A., Bachan, M., Urbaś, Z., *Applying methods of advanced MCAD parameterization achievable in Solid Edge v19 system on the basis of the selected structure*, Bulletin GMView 10, p.5-6, Wrocław 2007.



GERALIZATION OF GOODMAN'S DIAGRAM ON THE HIGH-CYCLE FATIGUE RANGE

Bogdan Ligaj

*University of Technology and Life Sciences in Bydgoszcz
ul. Prof. S. Kaliskiego 7, 85-789 Bydgoszcz, Poland
tel.: +48 52 3408253, fax: +48 52 3408271
e-mail: bogdanj@utp.edu.pl*

Abstract

The calculations of fatigue life of the structural components in random load conditions are connected with many problems. One of them is taking into consideration the impact of the cycles of variable value of R coefficient, which is included in service load composition, on estimated value. This involves application of calculations of two-parametric fatigue characteristics in system S_m - S_a in time. There are many models of two-parametric characteristics. One of them is characteristics being a development of the Goodman's conception, the biggest value of which is undoubtedly a simple description requiring the knowledge of following properties: R_m , R_{-1} and m_0 . In order to evaluate the characteristics mentioned above, it was compared to two-parametric fatigue characteristics determined in experimental way. The results of the analysis have been presented in form of diagram, which reveals the differences between characteristics depending on the number of cycles and the cycle asymmetry coefficient.

Keywords: fatigue life, two-parametric characteristics, S355J0 steel

Nomenclature

- A_5 – elongation [%],
 N – cycle number - general notation (fatigue life),
 N_0 – cycle number – fatigue life corresponding with fatigue limit,
 $R = S_{min}/S_{max}$ – cycle asymmetry ratio,
 R_e – material yield point [MPa],
 R_m – material tensile strength [MPa],
 R_{-1} – fatigue limit under oscillating load ($R = -1$) for N_0 cycle number, [MPa],
 S – specimen stress – general notation, [MPa],
 $S_a = 0,5(S_{max} - S_{min})$ – sinusoidal cycle stress amplitude [MPa],
 $S_m = 0,5(S_{max} + S_{min})$ – mean sinusoidal cycle stress [MPa],
 S_{max} – maximum sinusoidal cycle stress [MPa],
 S_{min} – minimum sinusoidal cycle stress [MPa],
 Z – contraction [%],
 m_0 – exponent in formula describing Wöhler fatigue diagram for oscillating load ($R = -1$),
 ψ_N – factor of material sensitivity to cycle asymmetry, for $N \neq N_0$.

1. Introduction

One of the known forms of diagrams of maximum pressure is Haigh diagram. In the figure 1 the first quarter of co-ordinate system [1] has been depicted. There the diagram mentioned above has been marked with a full line (defined with points A and B). Point B in the figure corresponds to material tensile strength (R_m), whereas point A corresponds to fatigue limit under oscillating load (R_{-1}). The area marked with the points AB0 corresponds to unlimited fatigue limit. In the discussed figure the lines, along which the cycles of specified cycle asymmetry coefficient R value are distributed, have been placed. The point of intersection of the lines mentioned with the maximum pressure diagram determinates the fatigue limit for the optional value of the R coefficient.

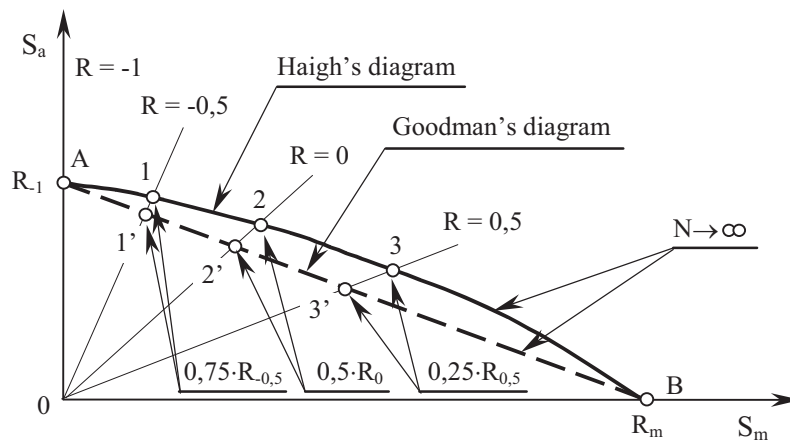


Fig. 1. Diagrammatic depiction of the maximum pressure diagram of Haigh and Goodman [1]

The simplification of the Haigh's diagram proposed by Goodman consists in replacing the curve with a straight line connecting points A and B. It influences the decrease of the fatigue limit for loads characterized by the cycle asymmetry coefficient from the range $-1 < R < 1$. The Goodman's diagram described with relation (1) has application in fatigue calculations within fatigue limit range, the result of which is the evaluation of factor of safety.

$$\frac{S_a}{R_{-1}} + \frac{S_m}{R_m} = 1,0 \quad (1)$$

In case of calculations of fatigue life in range of high-cycle fatigue the two-parametric fatigue characteristics, the example of which is known in the literature [1] Heywood's diagram, have application.

The development of the Goodman's conception is two-parametric fatigue characteristics proposed and published in work [2, 3, 5]. In the figure 2 the graphical form of the characteristics mentioned above, including the first and second quarter of co-ordinate system, has been presented. The simplification proposed by Goodman has been widened to the area of dominating compressive stress (second quarter). Point A in the figure concerns the fatigue limit under oscillating load (R_{-1}), whereas points B, C, K mean material tensile strength (R_m). The line JAEB divides the diagram into two areas: unlimited (described by JAEBKJ points) and limited fatigue life. By leading a line which crosses points B and M, where M is amplitude of fatigue limit under oscillating load $R = -1$ from the range of high-cycle fatigue, a contour line characterized by specified value of number of cycles N_j is determined. The lead contour line enables us to determine amplitude S_{aj} and average value S_{mj} of load characterized by specified value of cycle asymmetry coefficient R .

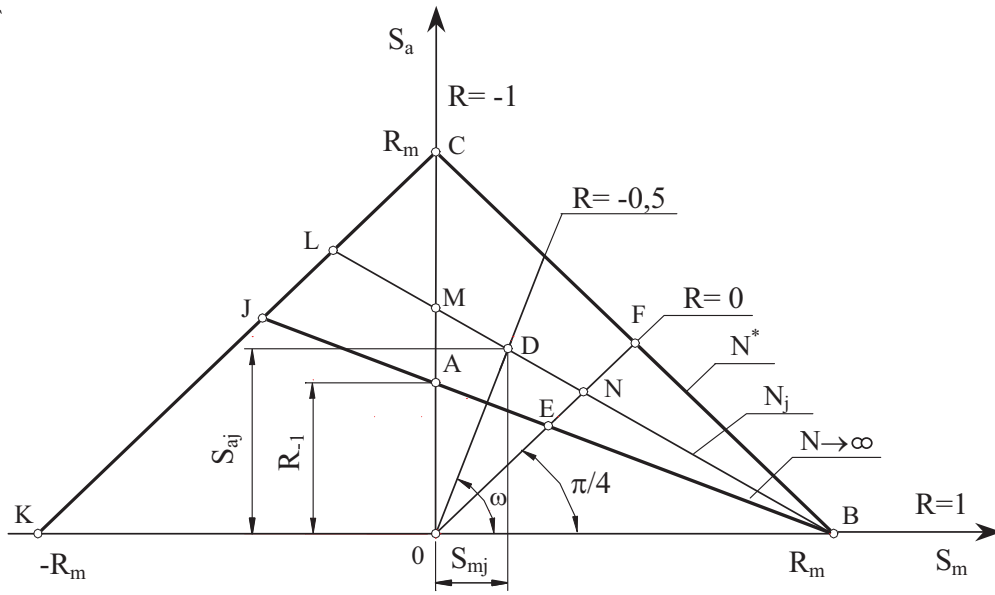


Fig. 2. Two-parametric fatigue characteristics [5]

The discussed fatigue characteristics is based on the use of relation describing the S-N curve for cycle asymmetry coefficient $R = S_{\min}/S_{\max} = -1,0$ in form:

$$S_a^{m_0} \cdot N = R_{-1}^{m_0} \cdot N_o = C_o \quad (2)$$

and formula (1). After appropriate transformations, depending on need, the following relations occur:

$$N = N_o \left[\frac{R_{-1}}{S_a} \left(1 - \frac{S_m}{R_m} \right) \right]^{m_0}, \quad (3)$$

lub

$$\frac{S_a}{R_m} = \frac{R_{-1}}{R_m} \left(\frac{N_o}{N} \right)^{\frac{1}{m_0}} \left(1 - \frac{S_m}{R_m} \right), \quad (4)$$

lub

$$N = \frac{2^{m_0} \cdot N_o \cdot R_{-1}^{m_0}}{[(1 + \psi_N) \cdot S_{\max} - (1 - \psi_N) \cdot S_{\min}]}. \quad (5)$$

The aim of this work is to compare two-parametric fatigue characteristics for S355J0 steel determined experimentally with two-parametric model of fatigue properties based on the conception of Goodman.

The scope of the work includes presentation of the empirical examination results for S355J0 steel in conditions of constant amplitude sinusoidal load of variable R coefficient value and elaboration on their base on two-parametric fatigue characteristics. The properties of the steel, which have been determined experimentally, enable us to elaborate on two-parametric fatigue characteristics described by formula (3). Then the specified characteristics are to be compared and the whole is to be ended by a summary.

2. Results of the empirical examinations of S355J0 steel

The research on static properties in conditions of tensile stress have been carried out on normalized fivefold cylindrical samples of circular intersection (fig. 3a) made according to PN-EN 10002-1 +AC1 standard, whereas in research on fatigue life in conditions of constant amplitude sinusoidal load the cylindrical samples of circular intersection (fig.3b) made according to PN-74/H-04327 standards have been used.

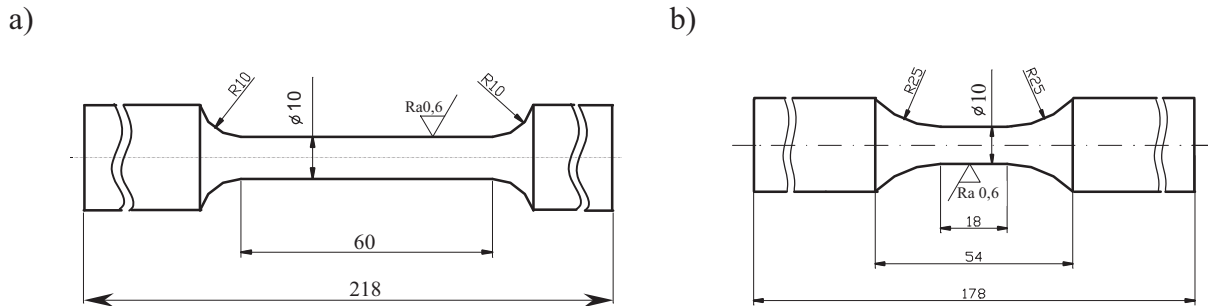


Fig. 3. Shape and measurements of samples for: a – statistical examinations, b – fatigue examinations

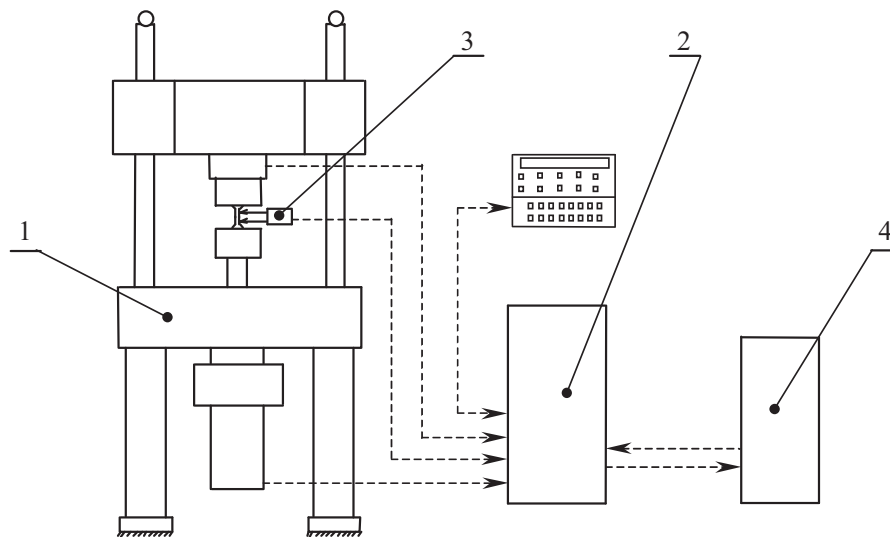


Fig. 4. Diagrammatic presentation of the construction of the test stand: 1, 2 – INSTRON 8501 testing machine with control and measurement system, 3 – extensometer, 4 – PC

The examinations have been carried out on test stand, the construction of which has been illustrated by figure 4. Our instrumentalism included: INSTRON 8501 testing machine with control and measurement system, extensometer and PC with software. During the examinations of properties in conditions of static loads extensometer of 50mm basis has been used, whereas in fatigue examinations extensometer of 10mm basis has been used.

The examinations of the static properties of steel have been carried out according to PN-EN 10002-1 +AC1 standard. The achieved results enabled us to determine the yield point, tensile strength, Young module, deformation and reduction of the sample. In table 1 the average values of the specified parameters have been depicted as well as standard deviation value has been given.

Tab. 1. Static strength properties of S355J0 steel [4]

	Static properties of S355J0 steel				
	R_e	R_m	E	A_5	Z
	MPa	MPa	MPa	%	%
Average values	499,9	678,0	208159	17,2	59,8
Standard deviation value	8,4	7,1	1306	0,99	0,9

Then the examinations in conditions of the constant amplitude sinusoidal load characterized by different cycle asymmetry coefficient value R have been carried out. The experiment has been carried out for 5 values of the coefficient R : 0, -0.5, -1.0, -1.25 and -2. For each load type the examination has been made on five levels of amplitude of nominal stresses, realizing three repetitions on each level. The acquired results enabled us to determine the fatigue life diagrams, which have been described by formula (6). The values of the slope and y-intercept for individual load types have been put together in table 2.

$$\log S_a = a \log N + b \quad (6)$$

Tab. 2. Values of the slope a and y-intercept b in formulas describing S - N curve of assumed values of cycle asymmetry coefficient R [4]

	Cycle asymmetry coefficient R				
	0	-0,5	-1,0	-1,25	-2,0
	1	2	3	4	5
a	-0,0628	-0,0528	-0,0811	-0,0709	-0,0592
b	2,7630	2,7810	2,9247	2,8894	2,8233

The empirical examinations which have been carried out enabled us to elaborate on two-parametric fatigue characteristics depicted in the figure 5. In co-ordinate system S_m/R_m – S_a/R_m the contour lines corresponding to specified number of cycles in range from 10^2 to 10^7 for assumed in examinations cycle asymmetry coefficient R have been marked by separate lines.

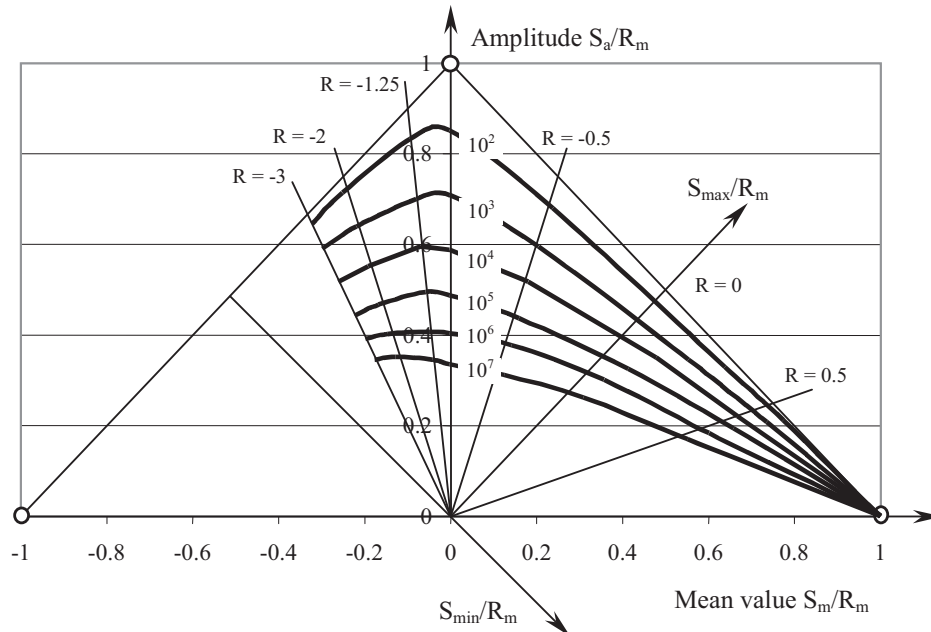


Fig. 5. Two-parametric fatigue characteristics determined experimentally [4]

3. Two-parametric fatigue characteristics

The experiment, conducted in static and variable load conditions, enabled us to determine parameters used in equation describing two-parametric characteristics. On the base of the slope in equation describing fatigue life diagram for $R = -1$ the value of the index exponent $m_0 = 12,33$ has been determined. The fatigue limit has been accepted as $R_{-1} = 274$ MPa for the number of cycles $N_0 = 10^6$. Material tensile strength R_m has been assumed according to the table 1.

The data mentioned enabled us to elaborate on two-parametric fatigue characteristics (fig.6) illustrated in the co-ordinate system $S_m/R_m - S_a/R_m$, similarly with characteristics determined experimentally.

Contour lines corresponding to specified number of cycles in range from 10^2 to 10^7 have been described by equation (7)

$$\frac{S_a}{678} = \frac{274}{678} \left(\frac{10^6}{N} \right)^{\frac{1}{12,33}} \left(1 - \frac{S_m}{678} \right). \quad (7)$$

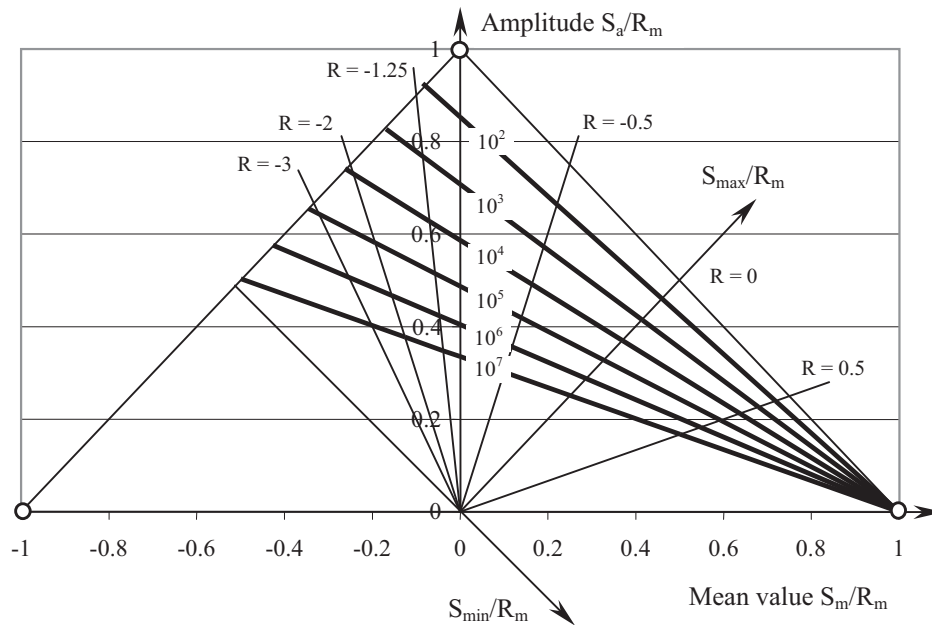


Fig. 6. Two-parametric fatigue characteristics elaborated on the base of the conception of Goodman

Two-parametric characteristics illustrated in the figures 5 and 6 differ from each other, especially in the range for negative average value. The Values of the differences are to be shown in the next point.

4. Comparison between research results

The conducted empirical examinations as well as calculation results enabled us to determine two-parametric models of fatigue properties of S355J0 steel. Characteristics illustrated by the figures 5 and 6 include contour lines corresponding to the defined number of cycles. Knowing the location of the contour lines, one can read the value of amplitude and average value which characterizes the point of intersection between the contour line and the line for cycles of stable value of R coefficient. Reading the amplitude value for examination results $S_{a_{ex}}$ and calculation results $S_{a_{ac}}$, the relative values of the differences δ can be calculated according to the formula (8)

$$\delta = \frac{S_{ac} - S_{a \text{ ex}}}{S_{a \text{ ex}}} \cdot 100\% \quad (8)$$

The calculated values of differences have been depicted on the bar chart (fig. 7).

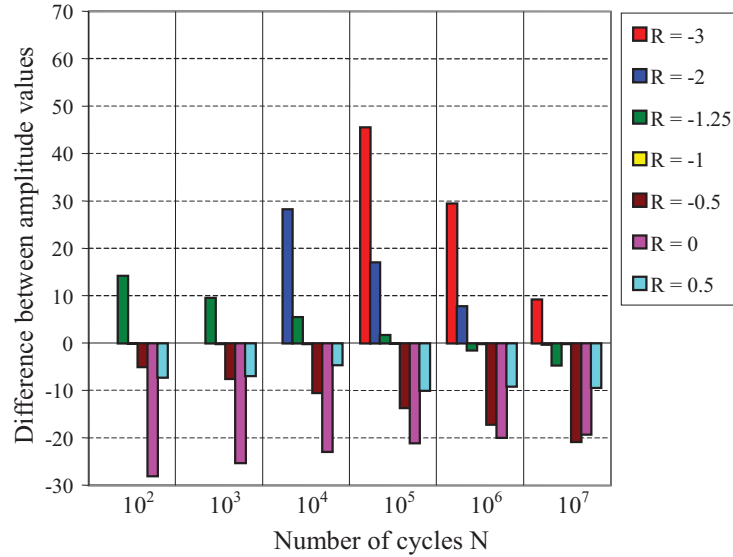


Fig. 7. Bar chart depicting the difference between amplitude values

For the range of the variability of coefficient $R > -1$ to $R = 1$ and the number of cycles from 10^2 to 10^7 the values of the amplitude which characterize the empirical examination results, were higher than the results determined on the base of two-parametric characteristics. For the cycle asymmetry coefficient $R = 0,5$ values of the differences range from $-4,5\%$ to $-9,4\%$. For the coefficient $R = 0$ divergences from the range $-19,2\%$ to -28% have been achieved. In case of coefficient $R = -0,5$ the values of the differences were increasing with the change of the number of cycles from $-4,9\%$ to $-20,7\%$.

In case of cycle asymmetry coefficient $R = -1$ the results of experiments and calculations are identical. It is connected to the fact that the elaborated characteristics is based on the fatigue properties determined in conditions of the oscillating loads.

In case of coefficient $R = -1,25$ for the number of cycles from 10^2 to 10^5 the results of calculations were higher than the examination results. The value of the differences for the mentioned range has been changing from $14,2\%$ to $1,8\%$. For the number of cycles 10^6 and 10^7 respectively the values $-1,5\%$ and $-4,6\%$ have been gained.

For the coefficient $R = -2$ for the number of cycles from 10^4 to 10^7 the gradual decline of the value of the differences between amplitudes from $28,3\%$ to $-0,2\%$ has been achieved. In case of the number of cycles 10^2 and 10^3 the maximal load value was higher than the material tensile strength ($S_{max} > R_m$).

Achieved research results point out that the biggest differences have been achieved for the coefficient $R = -3$. On account of the condition $S_{max} > R_m$ the analyzed range of the number of cycles has been limited to values 10^5 , 10^6 and 10^7 . For the range of the number of cycles mentioned above the following values of the amplitude differences have been achieved: $45,5\%$, $29,6\%$ and $9,2\%$.

5. Summary

The comparison between the empirical examination results and the calculation results points out a decline of the amplitude values in the first quarter of the co-ordinate system (for the range of the variability of the cycle asymmetry coefficient $-1 < R < 1$) for all numerals from 10^2 to 10^7 . In the second quarter for the mentioned values of the number of cycles the distinct increase of the amplitudes occurred, especially for coefficient $R = -2$ and $R = -3$. The occurring differences are connected to the shape of the contour lines on the analyzed diagrams, which result from the applied simplification in the two-parametric fatigue characteristics.

Application of the two-parametric fatigue characteristics based on the conception of Goodman during initial calculations, e.g. in machine design process, can be explained by the lack of precise data about cyclic properties of the material and about service load.

References

- [1] Kocańda, S., Szala, J., *Fundamentals of fatigue calculations, (in Polish)*, PWN, Warszawa, 1997.
- [2] Lipski, A., Szala, J., *Description of properties of fatigue materials with reference to changeability of cycle asymmetry coefficient at sinusoidal load*, Materiały XX Sympozjum Zmęczenia i Mechaniki Pękania, Bydgoszcz – Pieczyska, 2004.
- [3] Lipski, A., Szala, J., *Experimental examination of two – parametric fatigue characteristics*, Materiały XX Sympozjum Zmęczenia i Mechaniki Pękania, Bydgoszcz – Pieczyska, 2004.
- [4] Szala, G., *Empirical examination of the impact of the cycle asymmetry coefficient of the load on the fatigue life of S355J0 steel*, Journal of POLISH CIMAC, Gdańsk 2010.
- [5] Szala, J., Szala, G., *Two – parametric fatigue characteristics - formulating problem, (in Polish)*, Problemy Eksploatacji – Zeszyty Naukowe 3/2001 (42), Wydawnictwo Instytutu Technologii Eksploatacji (Publishing House of Operation Technology Institute), pp. 287-296, Radom 2001.

Note : This work has been elaborated in the frame of the project No. 0715/B/T02/2008/35 financed by Polish Ministry of Sciences and Higher Education.



IMPACT OF THE METHOD OF ELABORATION OF A LOAD SPECTRUM ON THE RESULTS OF THE CALCULATION OF S355J0 STEEL FATIGUE LIFE

Bogdan Ligaj

*University of Technology and Life Sciences in Bydgoszcz
ul. Prof. S. Kaliskiego 7, 85-789 Bydgoszcz, Poland
tel.: +48 52 3408253, fax: +48 52 3408271
e-mail: bogdanj@utp.edu.pl*

Abstract

The evaluation of fatigue life of the elements of machines which have been subjected to service load can be carried out through empirical examination or calculations. The calculations of fatigue life require the knowledge of fatigue characteristics, assuming the Palmgren-Miner rule and elaborating on the spectrum of the service load. The way of elaboration on the load spectrum is connected among other things with taking the appropriate normalization method into account. In this work the analysis of the influence of selected methods of normalization on the calculated fatigue life has been depicted. In the analysis the following methods have been applied: counting of local extrema, counting the branch span, pairs of spans and full cycles. The calculation has been done for exploitation loads run which was a result of measurements.

Keywords: fatigue life, random service load, normalization methods

Nomenclature

- A_5 – elongation [%],
 D_0 – value of the statistical parameter for the course in discrete form,
 L_0 – value of the statistical parameter for the course in local extrema form,
 N – cycle number – general notation (fatigue life),
 N_e – number of average value crossings through increasing and decreasing semicycles,
 N_{ij} – number of cycles to fatigue crack for values S_{aij} and S_{mij} ,
 N_0 – cycle number – fatigue life corresponding with fatigue limit,
 $R = S_{min}/S_{max}$ – cycle asymmetry ratio,
 R_e – material yield point [MPa],
 R_m – material tensile strength [MPa],
 R_{-1} – fatigue limit under oscillating load ($R = -1$) for N_0 cycle number, [MPa],
 S – specimen stress – general notation, [MPa],
 $S_a = 0,5(S_{max} - S_{min})$ – sinusoidal cycle stress amplitude [MPa],
 $S_m = 0,5(S_{max} + S_{min})$ – mean sinusoidal cycle stress [MPa],
 S_{max} – maximum sinusoidal cycle stress [MPa],
 S_{min} – minimum sinusoidal cycle stress [MPa],
 Z – contraction [%],

- m_0 – exponent in formula describing Wöhler fatigue diagram for oscillating load ($R = -1$),
- n_{ij} – number of cycles with variable values S_{aij} and S_{mij} ,

1. Introduction

Calculating of fatigue life of structural components which have been subjected in service conditions to random load concern three problems: description of fatigue properties of a structural component, Palmgren-Miner rule and elaborating the model of the service load.

The fatigue properties of elements can be described by relations in system $N(S_a)$ or $N(S_m, S_a)$. Assuming that cycles of values S_m and S_a from the wide range of inequalities belong to the composition of service load, more beneficial is (for the sake of calculation accuracy) application of two-parametric model of fatigue properties of element (two-parametric fatigue characteristics). The problems mentioned above have been described in details in references [7, 8].

Another element necessary to do the calculations is taking Palmgren-Miner rule as basis. The detailed characteristics of the methods has been described in the reference [3].

The third problem concerns the method of elaboration of the random load spectrum. The first stage in process of elaboration of the spectrum mentioned above is so called normalization, the main task of which is to substitute the course of loading being a record of subsequent extreme values (e.g. stresses) over time on set of sinusoidal cycles described with parameters S_m and S_a or S_{min} and S_{max} . The determined set of data enables us to elaborate on load spectrum, which may be: statistical function, block load spectrum or correlation table. Several methods of normalization are known, among which the most often applied are: peak counting method, range counting method, range pair count method, full cycles count method and rainflow count method. The detailed characteristics of the methods mentioned above has been described in references [2, 4, 5, 6]. On their basis it can be assumed that in the case of elaborating on random courses of a narrow spectrum the choice of the normalization method does not impact significantly on the calculated fatigue life. However, in case of courses of loads of a wide spectrum the methods leading to determination of the full sinusoidal cycles are recommended. To these methods belong: range pair count method, full cycles count method and rainflow count method.

The aim of this work is to compare the results of fatigue life received from calculations for load spectrums elaborated with use of various methods of normalization of the chosen operating course.

The range of this work includes presentation of service load, statistical evaluation normalization of loads and analysis of results of fatigue life calculations received for different methods of normalization.

2. Exploitation loads run

For the research purposes the course of stresses changes of a car steering spindle registered while driving forwards with speed of 30km/h on the straight road without elevations, on the concrete pavement (fig.1a) has been assumed. The registered changes of stresses have been depicted in relative values related to the maximum value present in the course. After that the course of loading has been divided into 20 ranges and the local extrema have been determined (fig. 1b). Figure1c and 1d depict short sections of courses in discrete form and form of local extrema, on which the values belonging to them have been marked with points. The course in form of local extrema is the simplified form of course registered during measurements. Its simplification is connected to determination of local extrema i.e. minima and maxima present in turns, situated in various class ranges.

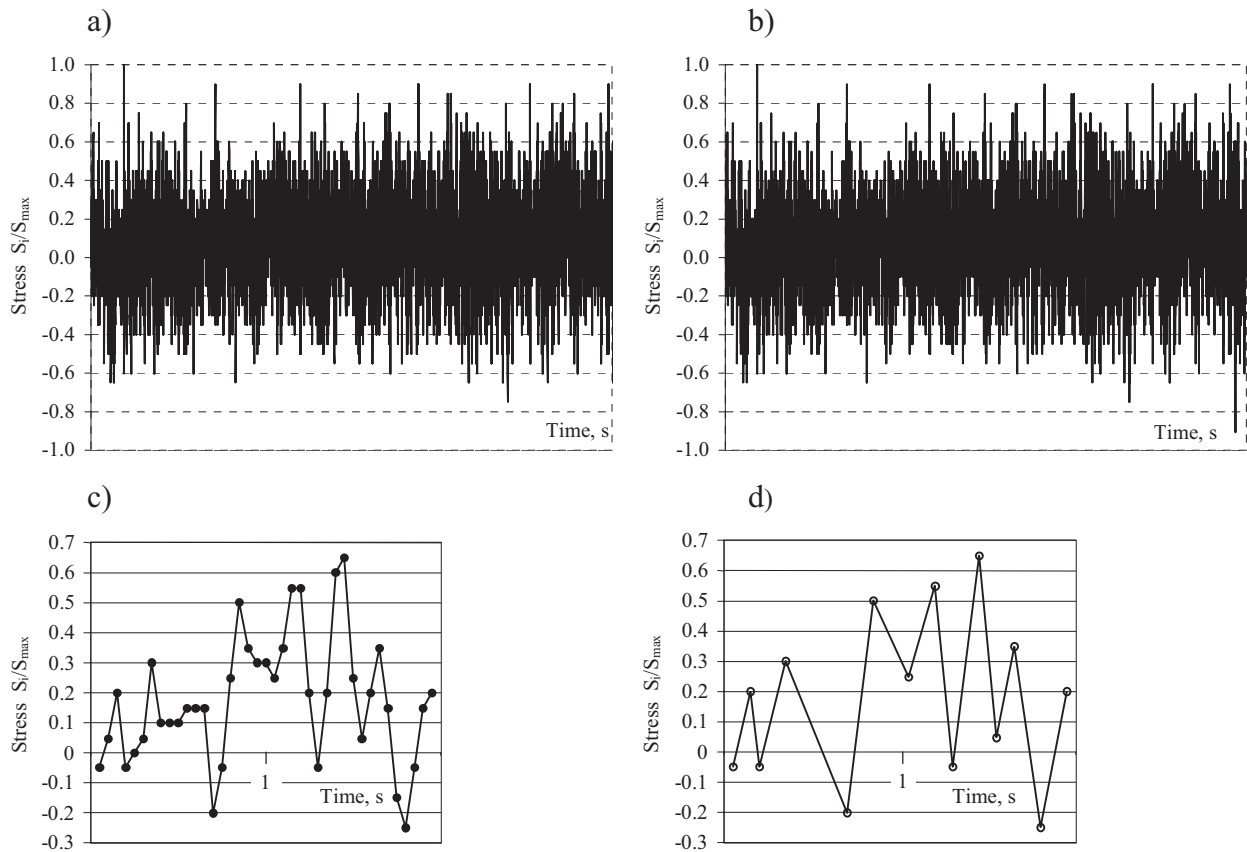


Fig. 1. Part of an exploitation course of loading for steering spindles registered during driving on concrete pavement: a – in discrete form, b – in form of local extrema, c – a short section of course depicted in the figure a, d – a short section of course depicted in the figure b

The forms of stress change course depicted above have been subjected to statistical evaluation, the aim of which was to determine: average value, variance, standard deviation, skewness, kurtosis and range. The results of the calculation have been depicted in the table 1.

Tab. 1. Statistical parameters of the loading course

Loading course in form	Statistical Parameters					
	Average Value	Variance	Standard Deviation	Skewness	Kurtosis	Range
Discrete	0.081	0.059	0.243	-0.0173	0.1825	1.97
Local extrema	0.076	0.089	0.298	0.0383	-0.4884	1.97
Difference between results δ , %	-6,2	50.8	22.6	321.4	-367,6	0.0

The calculated results differ from each other and difference values have been calculated from the relation (1)

$$\delta = \frac{L_0 - D_0}{D_0} \cdot 100\% \quad (1)$$

Cursory analysis of the examination results points at a small decline of the constituent statistical value of load in form of local extrema, which is described by the average value. In case of dynamical constituent for the course form mentioned above, described by a variance, the considerable increase 50,8% occurred. Significant differences concern the parameters

characterizing the probability density function. In case of discrete form course the skewness value points at asymmetrical distribution of values regarding its average value. The asymmetry of the distribution extends in the direction of negative values. The value of kurtosis points at the relative culmination of the values distribution in comparison with normal distribution. The skewness and kurtosis values determined for the course in form of local extrema are considerably different from the values for course in discrete form. The value of the skewness coefficient points at an asymmetrical distribution extending in the direction of positive values, whereas on the base of kurtosis coefficient value it can be concluded that in comparison with normal distribution this distribution was relatively flat.

The differences ensuing in the statistical parameters for loading course in discrete form and form of local extrema should be explained by simplification connected with determination of values of extrema. The following part of the work will be based on the course in form of local extrema.

A significant property of the loading course, e.g. on account of the choice of the normalization method, is width of the load spectrum, which can be evaluated with use of the simplified method based on coefficient I value, expressed by the formula (2)

$$I = \frac{N_i}{N_e} \quad (2)$$

The described method requires counting of local extrema, i.e. minimal and maximal values present in the course. Second element necessary to determine the coefficient I value is determination of the number of intersections of the average value level by ascending and diminishing high cycles. The average value for the course in form of local extrema has been depicted in table 1. As a result of calculations the number of intersections of average value level $N_i = 2115$ has been determined. The number of extrema in loading course totals $N_e = 2558$. By using the formula 2 the coefficient value $I = 0.827$ has been calculated. The value of the coefficient I enables us to qualify the analyzed course to wide-range loads. A detailed description of the method presented here can be found in reference [2].

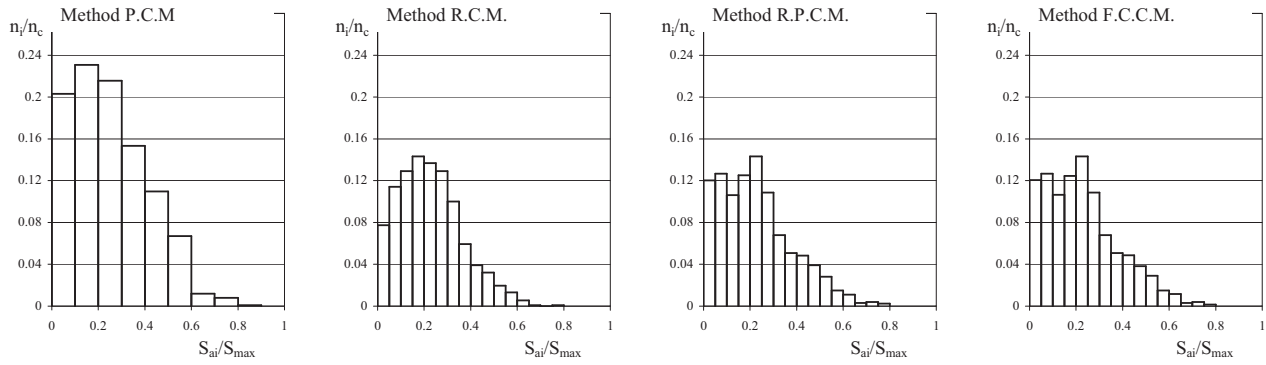
3. Service load spectrum

The elaboration on service load spectrum requires so called normalization. In this work 4 methods have been applied: peak counting method (P.C.M), range counting method (R.C.M.), range pair count method (R.P.C.M.) and full cycles count method (F.C.C.M.). On the base of received set of sinusoidal cycles the bar charts depicting frequency of appearance of the cycles of determinate amplitude values S_{ai}/S_{max} and average value S_{mi}/S_{max} have been depicted (fig.2).

Tab. 2. Statement of statistical parameters for distribution of average values and amplitudes

Distribution	Method of normalization	Statistic parameters values			
		Average value	Standard deviation	Skewness	Kurtosis
$\frac{S_{ai}}{S_{max}}$	P.C.M.	0.303	0.163	0.6190	-0.2284
	R.C.M.	0.252	0.135	0.6190	0.0647
	R.P.C.M.	0.252	0.155	0.7715	0.1918
	F.C.C.M	0.252	0.154	0.7572	0.1305
$\frac{S_{mi}}{S_{max}}$	R.C.M.	0.132	0.140	-0.3750	0.7905
	R.P.C.M.	0.132	0.118	-0.5654	1.8912
	F.C.C.M	0.132	0.118	-0.5443	1.8779

a)



b)

From the assumption of counting of the local extrema method results that there is a constant value for all cycles

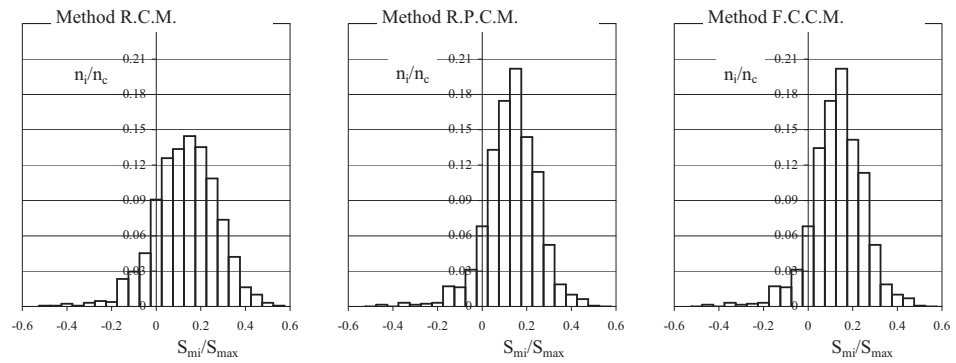


Fig. 2. Bar charts elaborated according to the data received as a result of normalization of service load:
a – for amplitudes S_{ai}/S_{max} , b – for average value S_{mi}/S_{max}

The analysis of the distribution of average values and amplitudes can be carried out on the base of statistical parameters depicted in table 2. Superficial evaluation of data shows that the parameters of distribution of the average value for all methods of normalization are close to the values for normal distribution, whereas amplitude distribution is close to Raleigh distribution.

4. Two-parametric fatigue characteristics

The sinusoidal cycles determined as a result of normalization belonging to the service load have different amplitudes and average values, which has been signaled in superficial analysis in point above. On this account the calculations of fatigue life of structural component require assuming the characteristics which determines the fatigue properties for two variable parameters: amplitude and average value.

There are many well-known descriptions of fatigue surface [2, 7]. From the analysis of the fatigue characteristics described in the references mentioned it turns out that in case of limited number of data from fatigue research the good conformity between calculation and examination results can be received through the application of characteristics according to model II [2].

Model II consists in accepting a plane crossing the branch of limited durability of Haigh diagram determined with $R = -1,0$ and point R_m or R_c on the axis S_m as fatigue characteristics. This plane is described by a relation:

$$N = N_o \left[\frac{R_{-1}}{S_a} \left(1 - \frac{S_m}{R_m} \right) \right]^{m_o} \quad \text{for} \quad S_{max} \geq Z_G. \quad (3)$$

5. Results of calculations and their analysis

The calculations of fatigue life have been carried out for S355J0 steel. On the base of the empirical examinations the properties in cyclic load and static load conditions, enabling us to elaborate on two-parametric fatigue characteristics, have been determined.

The strength properties of S355J0 steel received from the test of static tensile test are following: the yield point $R_{eL} = 499.9$ MPa (8.4 MPa), material tensile strength $R_m = 678$ MPa (7.1 MPa) and Young module $E = 208159$ MPa (1306 MPa). The standard deviation values for mentioned parameters have been given in brackets.

On the base of examination in constant amplitude load the S-N curve has been determined. The range of limited fatigue strength for oscilating load $R = -1$ is described by a relation:

$$\log S_{\max} = -0.0811 \log N + 2.9247 . \quad (4)$$

On the base of slope in formula (4) the value of index exponent $m_0 = 12,33$ has been determined. The fatigue limit of the material totals $R_{-1} = 274$ MPa for number of cycles $N_0 = 10^6$.

In calculations the Palmgren-Miner linear damage hypothesis has been used. The total fatigue failure caused by all the cycles of variable values S_a and S_m is described by the formula (5)

$$D = \sum_{i=1}^k \sum_{j=1}^p D_{ij} = \sum_{i=1}^k \sum_{j=1}^p \frac{n_{ij}}{N_{ij}} . \quad (5)$$

Fatigue life in number of cycles is calculated from:

$$N_c = \frac{1}{D} \sum_{i=1}^k \sum_{j=1}^p n_{ij} . \quad (6)$$

After replacing the formula (3) with the data the equation describing two-parametric fatigue characteristics has been received:

$$N = 10^6 \left[\frac{274}{S_a} \left(1 - \frac{S_m}{678} \right) \right]^{12.33} . \quad (7)$$

As a result of the calculations with application of two-parametric fatigue characteristics (7), Palmgren-Miner hypothesis (5) and loading spectra the diagrams of fatigue life for accepted normalization methods (fig. 3) have been elaborated. The received results have been depicted against the background of fatigue life in service load conditions.

Analyzing the received calculation results some divergences have been noticed. The lowest strength have been received for loading spectrum elaborated with the peak counting method, whereas the biggest for the range counting method. The strength results received for the loading spectrum elaborated with the range pair count method and the full cycles count method are close to empirical examination results in range from 400 to 550 MPa.

In order to determine the differences in calculated fatigue life the quotient of analytical durability and durability in service load conditions has been determined for chosen maximal stress intensity in spectrum (fig.4).

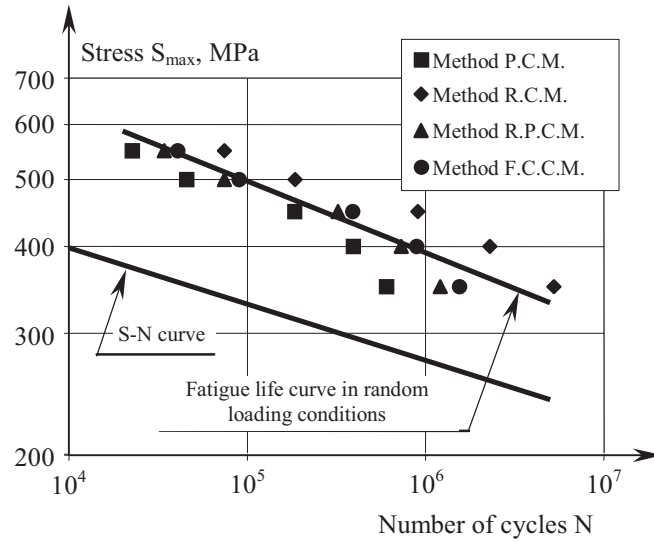


Fig. 3. The results of calculations of fatigue life

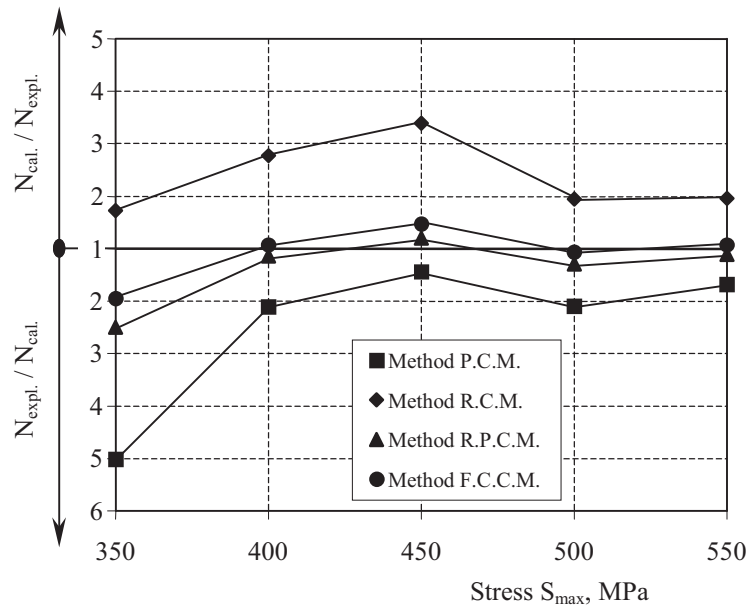


Fig. 4. Comparison of the durability results

Analyzing the examination results, shown in figure 4, good conformity between the calculation results and empirical examination results for the full cycles count method in the stress range from 400 to 550 MPa can be noticed. In the stress range mentioned above 1,5 growth of the analytical durability in comparison with experimental durability for value $S_{\max} = 450$ MPa has been noted down. In case of the lowest stress value (350 MPa) the double decrease of the analytical value has been noted down. The similar tendency of the distribution of the results has been received for the load spectrum elaborated with the range pair count method. The scope of variability of analytical durability, for stresses from $S_{\max} = 400$ MPa to $S_{\max} = 550$ MPa, did not cross the level of 1.2. Similarly to the full cycles count method the biggest result divergence has been noted town on the level of 350 MPa, which amounted to approximately 2.5. The results of calculations for load spectrums elaborated with the range pair count method and the full cycles count method. were closest to experimental results for the range $S_{\max} = 400 \div 550$ MPa.

In case of the peak counting method the calculation results are lower than empirical examination results for each stress intensivity. The scope of difference change totals from 1.4 (for

stresses $S_{\max} = 450$ MPa) to 5.0 (for stresses $S_{\max} = 350$ MPa). Ensuing differences are related with the load spectrum, the shape of which results in the hardest loading conditions.

For the spectrum elaborated with the range counting method the results were higher from the results of empirical examination data. The differences oscillated within 1.7 and 3.4.

6. Summary

The comparison between the calculation results with the empirical examination results has pointed out the impact of the normalization method on the fatigue life. On the base of the received results the biggest conformity has been achieved for the range pair count method and the full cycles count method. The results achieved for the load spectrum elaborated with the full cycles count method are the closest to the empirical examination results, but depending on the chosen stress intensity they are located on the left and right side (in the safe and hazardous area) of the life fatigue diagram for random load. In case of the results for the range pair count method the durability results are located in the safe area with the exception of the $S_{\max} = 450$ MPa. The close conformity of the results for the mentioned normalization methods is caused by a similar way of functioning. The differences in the sets of cycles have been visualized by small changes of the values of statistical parameters determined for distributions of average values and amplitudes. In case of the peak counting method, as expected, the lowest durability has been received, whereas in case of the range counting method the highest durability has been received.

References

- [1] Bendat, J. S., Piersol, A. G., *Methods of analysis and measurement of random signals*, [in Polish], PWN, Warszawa 1974.
- [2] Kocańda, S., Szala, J.: *Fundamentals of fatigue calculations*, (in Polish), PWN, Warszawa 1997.
- [3] Szala, J., *Hypotheses of fatigue damage accumulation*, (in Polish), Monographs, University of Technology and Agriculture, Bydgoszcz 1998.
- [4] *Standard Practices for Cycle Counting in Fatigue Analysis*, ASTM E 1049-85 (Reapproved 1990).
- [5] Szala, J., *Loads and fatigue life of machine elements*, University of Technology and Agriculture, Bydgoszcz 1989.
- [6] Szala, J., Lipski, A., Ligaj, B., *An influence of cycle counting method of random operating loading on calculated fatigue life*, (in Polish), Problemy Eksploatacji – Zeszyty Naukowe 4/2005 (59), Wydawnictwo Instytutu Technologii Eksploatacji (Publishing House of Operation Technology Institute), pp. 303-314, Radom 2005.
- [7] Szala, J., Szala, G., *Two – parametric fatigue characteristics - formulating problem*, (in Polish), Problemy Eksploatacji – Zeszyty Naukowe 3/2001 (42), Wydawnictwo Instytutu Technologii Eksploatacji (Publishing House of Operation Technology Institute), pp. 287-296, Radom 2001.
- [8] Szala, J., Szala, G., *Comparative analyses of two – parametric fatigue characteristic and their experimental verification*, (in Polish), Problemy Eksploatacji – Zeszyty Naukowe 3/2001 (42), Wydawnictwo Instytutu Technologii Eksploatacji (Publishing House of Operation Technology Institute), pp. 297-304, Radom 2001.

Note : *This work has been elaborated in the frame of the project No. 0715/B/T02/2008/35 financed by Polish Ministry of Sciences and Higher Education.*



TEM INVESTIGATIONS OF DAMAGE STRUCTURE OF PURE GOLD AFTER NITROGEN PLASMA IMMERSION ION IMPLANTATION (PIII) USING RF DISCHARGES

Zdzisław Ławrynowicz

*University of Technology and Life Sciences,
ul. S. Kaliskiego 7, 85-796 Bydgoszcz, Poland
Department of Materials Science and Engineering
Mechanical Engineering Faculty
e-mail: lawry@utp.edu.pl*

Abstract

The paper presents experimental results concerning microstructural changes caused by PIII. Thus, the main aim of these experiments was to make preliminary investigations of structural damage introduced by N^+ PIII into gold in such circumstances where precipitation processes are not available and structural damage only exists. After electropolishing Au foils with a [100] preferred orientation were PIII implanted to a total dose of $2 \times 10^{17} N^+$ ions/cm². Gold was used in the present study for three reasons: first, the noble character of gold will minimize contamination problems, second, thus far there are no definite evidence about gold nitride formation even when the dose was as high as $2 \times 10^{18} N^+$ /cm², and third, theoretical calculations give for this metal the highest interstitial and substitutional solubility. It has been observed that pure gold after nitrogen PIII contains a great deal of small gas bubbles. These bubbles can grow as a result of their migration, consequent collision and coalescence. It may be assumed that bubble creation, migration, coalescence and growth can best be reduced by the introduction of stable precipitates into the metal.

Keywords: *plasma immersion ion implantation, damage structure*

1. Physical aspects of ion - surface interaction

An ion of energy greater than a few keV striking a solid surface at normal incidence has a probability approaching unity, of entering that surface.

On its way to its final resting place however, the incoming particle will lose typically 70% of its energy in a series of collisions with lattice atoms. If such atoms receive energy greater than a threshold displacement energy E_d of order 20-50 eV they will be recoiled from their normal lattice site to leave a vacancy at their original position and form an interstitial elsewhere.

When the energy transfer is large, these displaced atoms can cause further displacements to form a cascade of recoils. The cascade mechanism depends mainly on the nature of the metal, the bombarding particle and the energy, but is relatively insensitive to other factors if the temperature is below that at which clusters are stable [5,25].

The situation is far removed from that found in conditions of thermal equilibrium. Since the incorporation of a foreign species into a solid by ion implantation is not constrained by equilibrium

considerations, non-conventional near-surface alloys can be formed [22,23].

Seeger first reviewed the nature of a displacement cascade (DC) in irradiated crystalline materials and the concepts of displacement spikes, replacement collision sequences (RCS), "diluted" or depleted zones, and thermal spikes which are all individual aspects of a DC [18].

The ideas embodied in Fig. 1 are still qualitatively correct, and they have allowed researches to understand many of the effects of DC on properties.

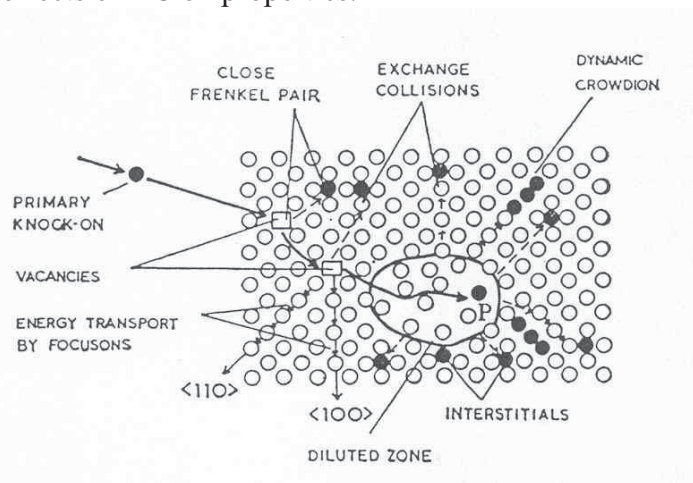


Fig. 1. Schematic two-dimensional representation of the depleted zone and its environment in a face-centred cubic crystal. A primary knock-on impinges from the left and comes to rest on the site P [18]

The core of a DC is void-like in nature, and the missing atoms (self-interstitial atoms (SIA)) reside on the periphery of the DC. This was supported by the results of Calder et al [4] who observed that loops in gold were only formed in the core of cascades in the thermal spike phase (10^{-11} - 10^{-12} s) of cascade evolution. Since in cascades which do collapse, most vacancies retained in the resulting loops, thereby suggesting that interstitials were effectively separated from vacancies in the collision phase of cascade formation. It was found that collapse occurs even at 4.2K and must therefore take place in the thermal spike phase. To the same conclusion came Jäger et al [2,11] who found that vacancy clusters in gold formed as the dominant cluster type as a result of vacancy rearrangements in depleted zones, both in individual cascades and after cascade overlap at higher doses.

Displacement spike is a very large numbers of atoms displaced in a small volume of material. There is possible to focus energy along close-packed crystallographic directions in a crystalline material, this phenomenon is called a focuson. The focusons along the [110] directions in a f.c.c. lattice could lead to the production of what Seeger termed, "dynamic crowdions". When a "dynamic crowdion" runs out of energy an SIA is deposited at the end of the track, thus creating a Frenkel pair with a large separation between the vacancy and the SIA. It is now common to call a "dynamic crowdion", a replacement collision sequence (RCS) [19]. The region denoted as the "diluted zone" is now called a DC.

This vacancy rich core in the ion track may subsequently collapse to form a vacancy dislocation loop. Experiments have shown that, in many cases, the vacancy rich regions collapse within the cooling phase of the cascade to form vacancy dislocations loops [4,19]. They are usually Frank loops on (111) habit planes, with $b = a/3$ (111) [11,19].

The mechanisms which lead to recovery by collapse are not yet understood, but their importance is undoubted because they provide a means by which the vacancy component of implantation damage is retained within the microstructure [4]. Likewise the interstitials can migrate to form interstitials loops [5]. Under such conditions, conventional metallurgical phase relations can be violated as shown by Marwick et al [15].

All these processes occur within about 10^{-11} - 10^{-12} s from the impact of the ion. There is thus a

short lived hot spike of material which can promote so-called radiation induced segregation as seen by Marwick et al above [15], or, can encourage diffusion to form equilibrium phases, the process being referred to as radiation enhanced diffusion within the volume of the DC [19].

However, only heavy ions deposit enough energy in the stopping volume to produce a "depleted zone" and hence lattice collapse into a vacancy cluster. When the damage density is lower (light ions), the local vacancy density is insufficient to produce a vacancy cluster [17]. Thermally activated mobile interstitials may, however, form interstitial clusters. Thus, the nature of the defect clusters depends on the mass and energy of the incoming ion [17]. Generally at implantation energies of 50-150 keV, the nature of observed defect clusters depends on the mass of the implanted ion: light ion (atomic number A below 85) irradiations created interstitial loops, while heavier ion implantation created vacancy loops [17].

Transmission electron microscopy (TEM) may be used successfully to characterize stable defect-cluster configurations resulting from energetic displacement cascade damage in metals and to determination of the phase composition after ion implantation. The objective of such studies is, besides fundamental aspects, an understanding of defect production during neutron irradiation in reactor materials and of modifications in structure and composition of materials by ion implantation.

2. Structural changes and depth profile of implanted layer

Ion implantation possesses several distinct advantages over other techniques for the surface treatment of materials. These are:

1. The ability to introduce any ion into the surface region of any substrate without the constraints of thermodynamic phase equilibrium. The optimum effects were obtained by nitrogen implantation with energies of 40-80 keV and optimum ion dose was found at $4-8 \times 10^{17}$ ions/cm².

Lower doses produce no visible effect and higher doses sometimes result in a change of the initial state for the worse. The implanted layer only reaches a thickness of about 100-200 nm but the effect often considerably exceeds this range.

The thickness of a developed dislocation structure in the near-surface layer exceeds the ion range by several orders of magnitude. The thickness of the layer with developed dislocation structure was found greater than 100 μm .

2. The ability to perform the implantation at a low process temperature. But it is ineffective for all applications involving high process temperatures. This is because of the instability at higher temperatures of the nitrogen induced defects and precipitates formed in the surface layer during implantation which are thought to be responsible for the beneficial influence.

3. The ability to perform the treatment without further need of annealing or refinishing.

4. The absence of coating adhesion problems.

The implantation depth decreases with increasing ion mass and increasing the energy results in an increase of the penetration depth.

It is known that particle implantation causes damage in crystals which appears on the transmission micrographs in general as "black dots" or "black spots" with diameters $d \leq 100 \text{ \AA}$, i.e. small compared with the extinction length ζ_g of the operating diffraction vector \mathbf{g} .

The sputtering factors for Cu, Ag and Au are high and the saturation values remain low, which, in turn, means that no blister formation can occur [1,25]. However, if higher bombarding energies were used, the blister formation could also occur in Cu, Ag, Au elements [13], and the number of blisters was evidently proportional to the range of the implanted ions. Accordingly, if no nitrogen migration occurs during treatment, with its relatively low solubility, the nitrogen dose should be selected precisely to avoid blister formation [1,13,25].

3. Precipitation processes in implanted materials

Ion implantation is a non equilibrium process. There is possible to implant materials with impurities to concentration levels which far exceed the solid solubility. The return of the system to thermodynamic equilibrium is often accomplished by precipitation of the implanted species or a compound involving atoms of both the host and the implanted species. This process may involve very long time scales when taking place at room temperature or it may take place dynamically during the implantation.

Precipitates which are formed during implantation depend on the alloying elements. The kind of nitride produced depends of course on the different affinities of the alloying elements for nitrogen.

Ion implantation with interstitial species, such as nitrogen, can have a major influence on surface related mechanical properties in a wide range of ferrous alloys. The formation of numerous small sized precipitates, high densities of dislocations and martensitic transformation are supposed to be favorable factors for hardening the outermost layer.

Many metal nitrides, such as TiN, ZrN etc., belong to the category of easily produced nitrides [12,20]. However, noble metal nitrides are difficult to form or even not obtainable under implantation conditions. In recent years, AgN₃ and CuN₃ phases were observed by TEM pattern after implantation to a dose 2×10^{18} Ncm⁻² [17]. Yet, for nitrogen implantation into Au films, no definite evidence was obtained about gold nitride formation even when the dose was high as 2×10^{18} N cm⁻² [38]. Kelly [12,20] suggested, that failing to appear of gold nitride could be explained by N loss at the surface.

Antila [1,24] attributed the failure of the formation of noble metal nitride to the high sputtering yield of nitrogen ion-noble metal partners, which prevented the average nitrogen concentration in the implanted layer from reaching the required stoichiometry. Surface recession due to sputtering seems to be played important role on nitride formation but it needs further study.

Yet, the precipitated phases can have an effect on the actual shape of the implantation profiles. It was found that second phase precipitation however does not affect the total retained dose of the implanted species very much since the precipitated region is away from the surface and the loss due to sputtering is not modified. The effects become more significant if the implanted species are highly mobile during the implantation process.

4. Plasma immersion ion implantation (PIII)

Conventional ion implantation is a line-of-sight process in which ions are extracted from an ion source, accelerated as a directed beam to high energy and then raster scanned across the target. If the target is nonplanar, target manipulation is required to implant all sides of the target. The necessary target manipulation adds complexity and reduces the size of the target which can be implanted.

Thus, the main disadvantages are the relatively high process costs and the restriction to visible areas because it is a line-of-sight process. This precludes ion implantation treatment of parts with obscured or re-entrant features.

These all disadvantages are overcome in a new technique for the ion implantation of materials which has been reported by Conrad et al. [2,3,6,7,8], Tendys et al. [14,21], and Hossary et al. [9]. This technique has been named plasma immersion ion implantation (PIII or PI³), or plasma source ion implantation (PSII). PIII is a non-line-of-sight technique [6,10]. In PIII, the target is placed directly in plasma source and pulsed to high negative potential relative to the chamber walls. Ions are accelerated normal to the target surface, across the plasma sheath, thus eliminating not only the line-of-sight problems of conventional ion implantation but also the retained dose problem. The pulse amplitude, width and spacing are independently and continuously variable. The temperature

of the sample can be controlled by using a pulsed discharge which can be varied in both frequency and amplitude [9]. All advantages of PIII over conventional ion implantation have been discussed widely by Conrad et al. [6,10].

Up to now any experimental results have not been published concerning microstructural changes caused by PIII. Thus, the main aim of these experiments was to make preliminary investigations of structural damage introduced by N^+ PIII into gold in situation where precipitation processes are not available and structural damage only exists.

5. Experimental procedures

Air-cleaved NaCl (100) surfaces were used as substrates, heated at 450°C on Mo resistively heated strip. NaCl was cleaved immediately before loading into the vacuum system. The substrate temperature was measured by 0.2 mm wire chromel-alumel thermocouple touched to the Mo strip. A spiral-type W wire source was used to evaporate gold. The thickness of the films (60, 85, 100 and 125 nm) and the evaporation rate were controlled. The single crystal Au films were floated from the NaCl crystal in distilled water and supported on a copper microgrids.

Specimens of polycrystalline gold foil, 0.065 mm thick were annealed in vacuum at 980°C for four hours and furnace cooled, prior to electropolishing to produce foils with large electron transparent regions. The foils after this treatment had a [100] preferred orientation. The specimens were thinned in a bath of 200 ml water, 14g potassium cyanide, 6g potassium ferrocyanide, 6g potassium sodium tartrate (solution A), and 0.8 ml ammonia, 4 ml phosphoric acid, and 20 ml H₂O (solution B). The solutions A and B were mixed immediately before use. The samples were also electropolishing in 1 mol-LiCl-methanol at 245 K ($I=0.25A$, $V=9.5V$) but the foils had strongly ununiform final thickness. The specimens were washed in water and methanol after electropolishing.

After electropolishing Au foils were PIII implanted to a total dose of $2 \times 10^{17} N^+$ ions/cm². Gold samples were examined in a JEOL 2000FX microscope at an accelerating voltage of 200 kV.

Gold was used in the present study for three reasons: first, the noble character of gold will minimize contamination problems, second, thus far there are no definite evidence about gold nitride formation even when the dose was as high as $2 \times 10^{18} N^+$ /cm², and third, theoretical calculations give for this metal the highest interstitial and substitutional solubility. In the case of low solubility, for instance of helium solubility in nickel the helium tends to precipitate, forming blisters on the surface or gas filled bubbles in the bulk which preferentially nucleate at inhomogeneities like grain boundaries, dislocations or precipitates and cause a significant loss of ductility.

Despite the laboratory experiments of ion implantation using RF [9,14,21] or microwave discharges, little is known of the microstructural effects of these processes. Thus choice of optimum parameters for ion implantation has almost always been made by trial and error.

The present work is an attempt to improve the understanding of the basic processes of structural damage in f.c.c. substance (gold) taking place during PIII.

6. Results

Figures 2 and 3 are micrographs of typical areas, in the single crystal and in the polycrystal foil unimplanted gold specimens. Unfortunately, the all single crystals were damaged during implantation and for further investigations only the polycrystal specimens could be used.

Fig. 3b shows area of a specimen after nitrogen implantation with lots of white circles. There is the possibility that these effects were caused by crystallographic etching or by surface craters produced during implantation [1,24].

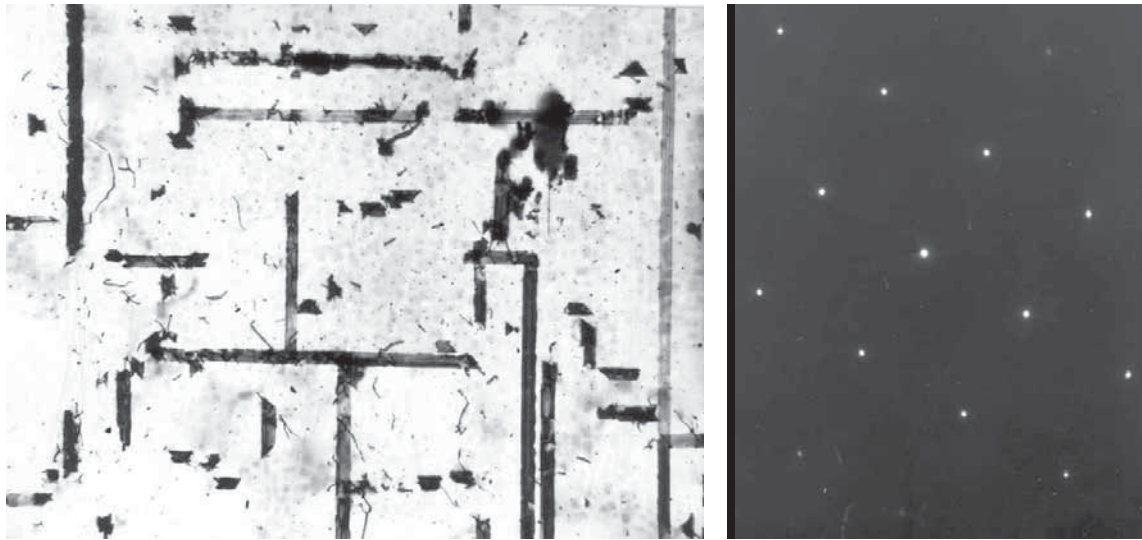


Fig. 2. Micrograph of the single gold crystal. Diffraction pattern with zone axis [100] is inserted

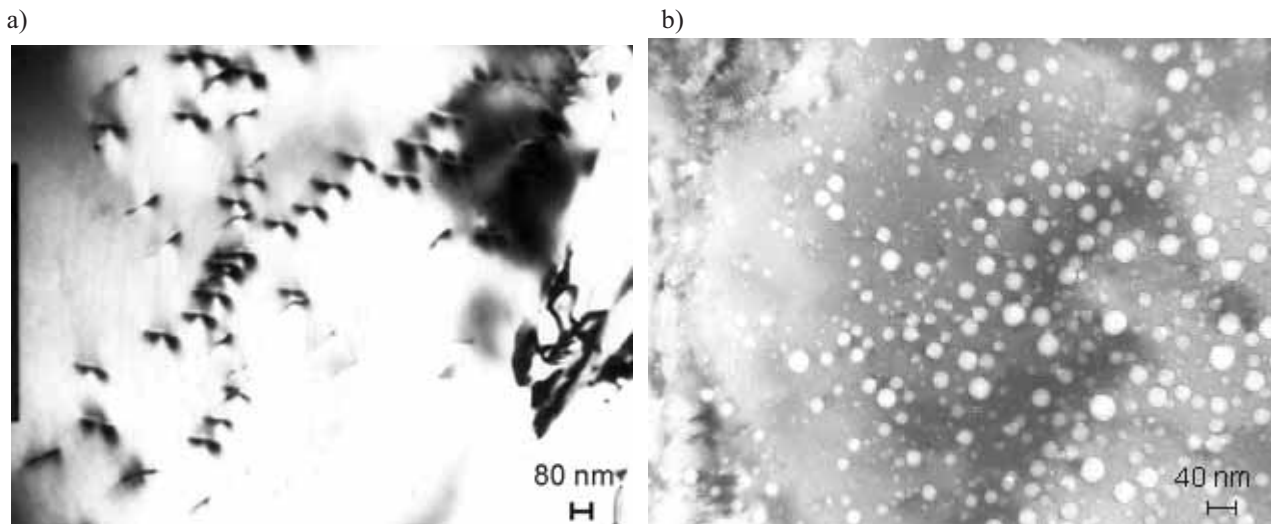


Fig. 3. a) Typical microstructure of polycrystalline unimplanted gold foil, b) micrograph of the implanted polycrystalline gold foil

In this case the contrast of the brighter circles would in general be light, relative to the background and fringes parallel to the edges of the pit or crater would be expected. However, the experimental observations show that the contrast is always bright relative to the background and there are no fringes. Furthermore no trace of these circles has been observed in unimplanted specimens (Fig. 2 and 3a). As the bright circles are found in specimens of gold only if they have been implanted, it is thought that they raised during implantation.

Figure 4 shows the electron micrograph of the typical structure formed by nitrogen ion implantation in a near perforation region of gold foil. The left part of the micrograph, which corresponds to the near-perforation area (the thinnest region of the foil) is without bright circles. In the middle part could be noted increasing amount of small circles. The right part (the thicker region) contains lots of big circles. In other words the bigger the foil thickness the greater bubbles, of course to some extent. The bright circles having obtained a certain limit size stop its growth regardless to the thickness of the foil (Fig. 3b and 4).

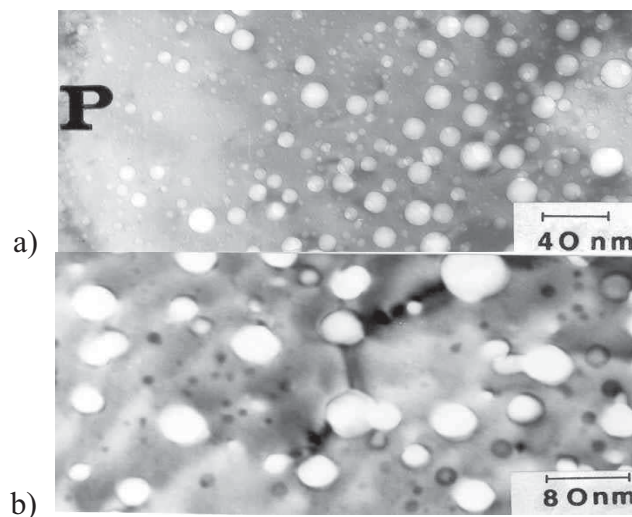


Fig. 4. Micrograph of the structure in a near perforation region of gold foil (perforation is noted P), a) bubbles and dislocation loops in implanted gold foil, b) coalescence of the bubbles

In addition to bright circles there are also observed a background of damage consisting of numerous black dots roughly 8 Å in diameter and bigger dislocation loops 20-50 Å in diameter (Fig. 4b).

Probable when implanted nitrogen has exceeded their solubility limit in gold begins to precipitate into tiny gas bubbles which coarsen on heating (temperature of foils was 245°C during implantation). This coarsened upon heating and tiny bubbles appeared inside the grains and upon the grain boundaries and dislocation lines (Fig. 3b and 4). These latter bubbles grew larger but became fewer in number upon further heating. The bubbles in the dislocation lines tend to be larger than those in the neighboring area. It can be assumed that the nitrogen might however diffuse along dislocation "pipes", and that this explains the growth of bubbles which have been shown to lie on dislocation lines in Fig. 4b.

Quite frequently bubbles disappeared because they came into contact and coalesced to form a larger bubble; e.g. bubbles in Fig. 4b.

If there would be strain field around the bubble it is insufficient to produce a diffraction contrast effect. It is thought, however, that same strain field does exist, because on several occasions small bubbles have been seen closely associated with larger bubbles; e.g. Fig. 4, where they remained apparently touching without coalescing during heating. Such observation suggest that a short-range repulsion does exist between these bubbles.

Conclusions

It has been observed that pure gold after nitrogen PIII contains a great deal of small gas bubbles. These bubbles can grow as a result of their migration, consequent collision and coalescence.

It may be assumed that bubble creation, migration, coalescence and growth can best be reduced by the introduction of stable precipitates into the metal.

References

1. Anttila, A. et al., *Nitrogen implantation of metals*, J. Appl. Phys., 57, pp. 1423-1425, 1985.
2. Baragiola, Ra, A., *Invited review: Some challenging unsolved problems in atomic collisions in solids*, Nuclear Instruments and Methods in Physics Research B 237, pp. 520-524, 2005.

3. Bogaerts, A., Neyts, E., Gijbels, R., Joost van der Mullen, *Gas discharge plasmas and their applications*, Spectrochimica Acta Part B 57, pp. 609–658, 2002.
4. Calder, A.F., Bacon, D.J., Phythian, W.J., English, C.A., *Collapse of cascades produced by low-energy ion irradiation of gold*, Vacuum, vol.39, pp. 1115-1118, 1989.
5. Colligon, J.S., *Surface modification by ion beams*, Vacuum, vol.36, pp. 413-418, 1986.
6. Conrad, J. R. et al., *Plasma source ion-implantation technique for surface modification of materials*, J. Appl. Phys., vol. 62, pp. 4591-4596, 1987.
7. Conrad, J.R., *Plasma Source Ion Implantation: A New Approach to Ion Beam Modification of Materials*, Materials Science and Engineering, A116, pp. 197-203, 1989.
8. Conrad, J.R. et al., *Plasma source ion implantation dose uniformity of a 2x2 array of spherical targets*, J. Appl. Phys., vol. 65, pp. 1707-1712, 1989.
9. El-Hossary, F. et al., *Plasma nitriding of stainless steel using continuous and pulsed rf glow discharge*, Surface Engineering, vol.4, pp. 150-154, 1988.
10. Hanley, L., Sinnott, S. B., *The growth and modification of materials via ion-surface processing*, Surface Science 500, pp. 500–522, 2002.
11. Jäger, W., Merkle, K.L., *Defect-cluster formation in high-energy-density cascades in gold*, Philosophical Magazine A, vol.57, pp. 479-498, 1988.
12. Kelly, R., *Factors determining the compound phases formed by oxygen or nitrogen implantation in metals*, J. Vac. Sci. Technol., 21, pp. 778-789, 1982.
13. Kiss, A.Z. et al., *Avoidance of blister formation in targets backings during alfa-particle bombardment*, Nuclear Instruments and Methods, 203, pp. 107-108, 1982.
14. Lopez-Heredia, M.A., Legeay, G., Gaillard, C., Layrolle, P., *Radio frequency plasma treatments on titanium for enhancement of bioactivity*, Acta Biomaterialia, 4 pp. 1953–1962, 2008.
15. Marwick, A.D., Pilier, R.C., Sivell, P.M., *Mechanisms of radiation-induced segregation in dilute nickel alloys*, Journal of Nuclear Materials, vol. 83, pp. 3541, 1979.
16. Nono, M.C.A., Corat, E.J., et al, *Surface modification on 304 SS by plasma-immersed ion implantation to improve the adherence of a CVD diamond film*, Surface and Coatings Technology 112, pp. 295–298, 1999.
17. Ruault, M.O., Bernas, H., Chaumont, J., *Transmission electron microscopy study of damage by ion implantation in gold . Evidence for a spike threshold*, Philosophical Magazine A. vol.36, pp. 757-783, 1979.
18. Seeger, A., *Radiation Damage in Solids*, vol. 1, IAEA, Vienna, 1962.
19. Seidman, D.N., Averback, R.S., Benedek, R., *Displacement Cascades. Dynamics and Atomic Structure*, Phys. Stat. Sol.B, 144, pp. 85-103, 1987.
20. Tan, L., Crone, W.C., *Surface characterization of NiTi modified by plasma source ion implantation*, Acta Materialia 50, pp. 4449–4460, 2002.
21. Tendys, J., Donnelly, I.J., Kenny, M.J., Pollock, T.A., *Plasma immersion ion implantation using plasmas generated by radio frequency techniques*, Appl. Phys. Lett., 53, pp. 2143-2145, 1988.
22. Tian, X.B., Chub, P.K., Fub, R., Yang, S.Q., *Hybrid processes based on plasma immersion ion implantation: A brief review*, Surface & Coatings Technology, 186, pp. 190– 195, 2004.
23. Williams, J.S., Poate, J.M., *Ion Implantation and Beam Processing*, Academic Press, Sydney, New York, London, 1984.
24. Yankov, R.A., Shevchenko, N., et al, *Reactive plasma immersion ion implantation for surface passivation*, Surface & Coatings Technology 201, pp. 6752–6758, 2007.
25. Zhu, S., Huang, N., Shu H., Wua, Y., Xu, L., *Corrosion resistance and blood compatibility of lanthanum ion implanted pure iron by MEVVA*, Applied Surface Science, 256, pp. 99–104, 2009.



RELATIONSHIP BETWEEN BMD, APPARENT AND ASH DENSITY OF HUMAN TRABECULAR BONE

Adam Mazurkiewicz, Tomasz Topoliński

*University of Technology and Life Sciences
ul. Kaliskiego 7, 85-789 Bydgoszcz, Poland
tel.: +48 52 3408446
e-mail: adam.mazurkiewicz@utp.edu.pl*

Abstract

Trabecular bone is one of components of bone which quality is responsible for strength whole human bone. It is a porous structure, which change with age. In medical practise for estimation quality of bone the most often is used dual energy x-ray absorptiometry (DEXA). For scientific investigation of bones are often used apparent density and ash density. In the work presented results comparison values BMD, apparent and ash density obtained from measurement samples of human trabecular bone. Obtained values coefficient of determination R^2 for relationship between this densities were in range $0,28 \div 0,62$.

Keywords: trabecular bone, BMD, apparent density, ash density

1. Introduction

Trabecular bone is one of components of bone which quality is responsible for strength whole human bones. It is a porous structure, which change with age. In medical practise for estimate quality trabecular bone most often is used dual energy x-ray absorptiometry (DEXA) [1-3]. Result of the measurement is value of BMD density selected part of bone. In scientific investigation trabecular bone mostly is used apparent density App.D [4,5] or ash density Ash.D [6,7].

The aim of the work is to determine relationship between BMD, apparent and ash density for human trabecular bone.

2. Materials and methods

Material to the investigation were 42 samples of human trabecular bone. Samples were collected from 21 osteoporotic and 21 coxarthrotic femoral heads gained in result of hip arthroplasty. The samples used to investigation have cylindrical shape about diameter 10 and height 8,5 mm. Manner of collecting sample is presented in fig. 1 [8].

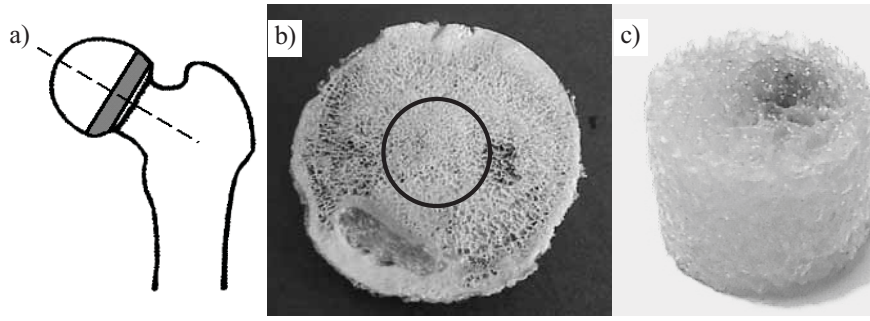


Fig. 1. Manner of collecting sample: cutting slice a), cutting sample b), sample c)[8]

The age of the patients ranged from 50 to 91 with an average of 73 years. The samples were stored in 10% formalin solution at the room temperature.

BMD density was performed with scanner Lunar Expert, General Electric Company. Apparent density obtained by dividing mass of sample by its volume. In the aim obtain ash density samples were burning in temperature 500°C by 15 hours [9]. Ash density Ash.D was calculated by dividing mass burned sample by its volume before burning.

3. Results

In Tab. 1-2 presented minimal, maximal and mean values, standard deviation and relative standard deviation for BMD, apparent and ash density for coxarthrotic and osteoporotic samples respectively. For both investigated group values RSD are on the similar level only for BMD. For App.D and Ash.D differences are 8% and 13% respectively.

Tab. 1. Values of densities for coxarthrotic samples

	min	max	mean	SD	RSD
BMD, g/cm²	0.135	0.396	0.285	0.077	27 %
App.D, g/cm³	0.504	1.148	0.919	0.162	18 %
Ash.D, g/cm³	0.174	0.512	0.341	0.089	26 %

Tab. 2. Values of densities for osteoporotic samples

	min	max	mean	SD	RSD
BMD, g/cm²	0.134	0.343	0.209	0.055	26 %
App.D, g/cm³	0.734	1.120	0.910	0.090	10 %
Ash.D, g/cm³	0.113	0.592	0.251	0.097	39 %

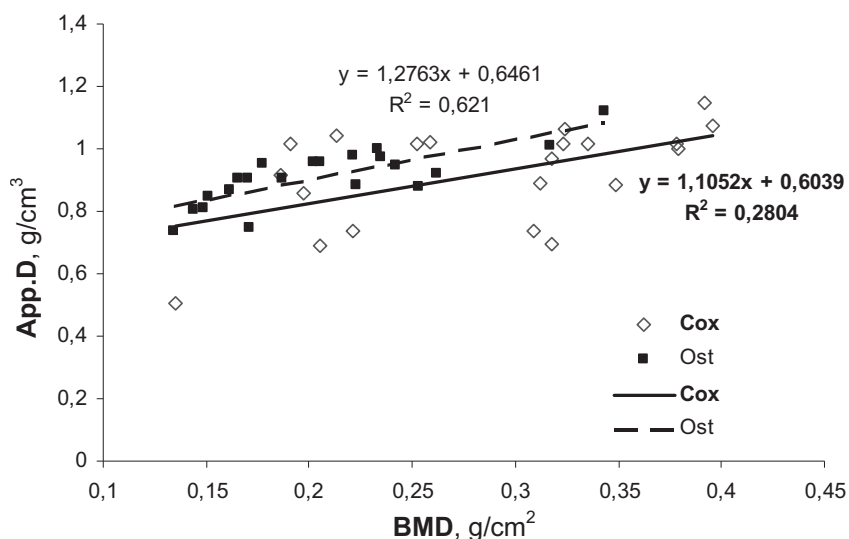


Fig. 2. Relationship between BMD and apparent density

In Fig. 2–4 presented relationship between BMD–App.D (Fig. 2), BMD–Ash.D (Fig. 3) and Ash.D–App.D (Fig. 4). For osteoporotic samples the relationships between the densities are similar $R^2=0,53\div0,62$. For coxarthrotic samples relationship BMD–App.D and Ash.D–App.D are clearly weakly $R^2=0,28\div0,29$. For relationship BMD–Ash.D coefficient of correlation $R^2=0,52$.

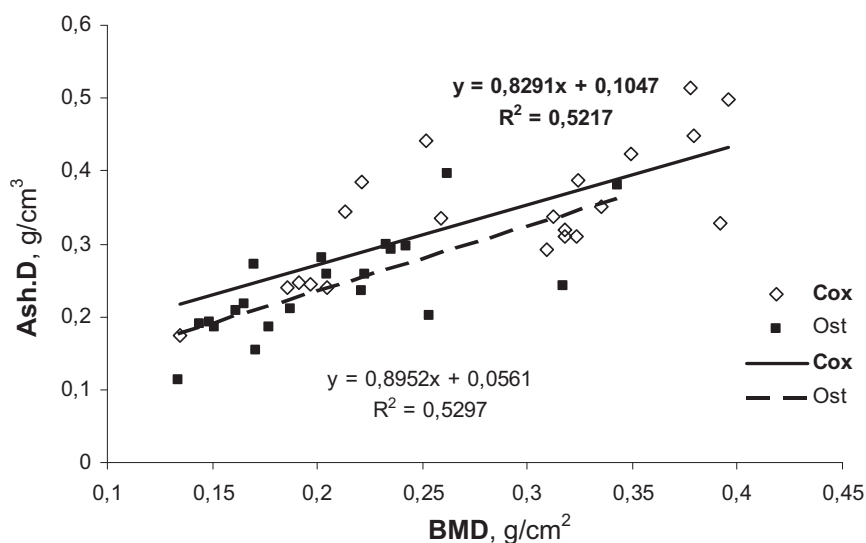


Fig. 3. Relationship between BMD and ash density

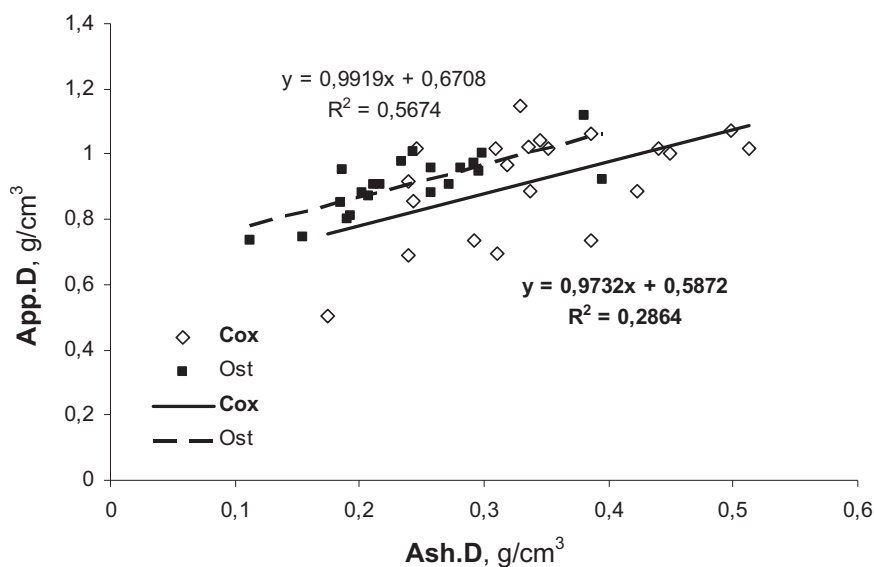


Fig. 4. Relationship between ash and apparent density

4. Conclusions

Analysis results densities measurement for both group of samples are visible significant differences in mean values for BMD and Ash.D. For this indices higher values were obtained for coxarthrotic samples. For App.D mean value is similar in both groups.

Obtained values of coefficient of determination only for relationship BMD-Ash.D are similar in both groups and contain in range $R^2=0,52\div0,53$. For relationships BMD-App.D and Ash.D-App.D values R^2 are higher in osteoporotic group ($R^2=0,62$ and $R^2=0,57$). The same relationship in coxarthrotic group were $R^2=0,28$ and $R^2=0,29$.

Measurement BMD and Ash.D are based on measurement mineral of phase of bone. App.D was calculated by dividing mass of sample by its volume. Trabecular bone is porous structure, therefore mass include marrow, blood or formalin (samples were stored in formalin) in pores of sample. It would be reason of errors in estimating the parameter. In result relationships App.D with BMD and Ash.D values wouldn't give satisfying values R^2 . Lower values R^2 in coxarthrotic group for relationship BMD-App.D and Ash.D-App.D probably are caused character of coxarthrotic disease. One of results the disease is hypertrophy articular cartillage in pores of trabecular bone. It would be influence on result measurement apparent density in this group of samples.

Acknowledgements

This work by supported by The State Committee for Scientific Research (KBN) under grant No. N N501 308934.

References

- [1] Lespessailles, E., Jullien, A., Eynard, E., Harba, R., Jacquet, G., Ildefonse, J., Ohley, W., Benhamou, C., *Biomechanical properties of human os calcanei: relationships with bone density and fractal evaluation of bone microarchitecture*, J Biomech., Vol. 31(1998), pp. 817-24.
- [2] McDonnell, P., McHugh, P., O'Mahoney, D., *Vertebral osteoporosis and trabecular bone quality*, Ann Biomed Eng., Vol. 35(2007), pp. 170-89.

- [3] Keyak, J., Rossi, S., Jones, K., Skinner, H., *Prediction of femoral fracture load using automated finite element modeling*, J Biomech., Vol. 31(1998), pp. 125-33.
- [4] Rice, C., Cowin, S., Bowman, J., *On the dependence the elasticity and strength of cancellous bone on apparent density*, J. Biomech., Vol. 21 (1988), pp. 155-168.
- [5] Ciarelli, M. J., Goldstein, S. A., Kuch, J. L., Cody, D. D., *Evaluation of orthogonal mechanical properties and density of human trabecular bone from the major metaphyseal regions with material testing and computer tomography*, J. Ortop. Res., Vol. 9 (1991), pp. 674-682.
- [6] Mosekilde, L., Danielsen, C., *Biomechanical competence of vertebral trabecular bone in relation to ash density and age in normal individuals*, Bone, Vol. 8 (1987), pp. 79-85.
- [7] Goulet, R. W, Goldstein, S. A., Ciarelli, M. J., Kuhn, J. L., *The relationship between the structural nad orthogonal compressive properties of trabecular bone*, J. Biomech., Vol. 27 (1994), pp. 375-389.
- [8] Mazurkiewicz, A., Topoliński, T., *The relationship between structure, density and strength of human trabecular bone*, Acta of Bioengineering and Biomechanics, Vol. 11 (2009), pp. 55-62.
- [9] Yuehuei, H., Draughn, R., *Mechanical testing of bone and the bone-implant interface*, CRC Press, New York 1999.



RELATIONSHIP BETWEEN FATIGUE LIFE AND STRUCTURAL INDICES OF HUMAN TRABECULAR BONE

Adam Mazurkiewicz, Tomasz Topoliński, Artur Cichański, Krzysztof Nowicki

*University of Technology and Life Sciences
ul. S. Kaliskiego 7, 85-789 Bydgoszcz, Poland
tel.: +48 52 3408446
e-mail: adam.mazurkiewicz@utp.edu.pl*

Abstract

Trabecular bone is one of components of human bone. It is a porous structure which strength has principal influence on strength whole bone. In the study has been presented results investigation relationship between fatigue life (loading with stepwise increasing amplitude) and structural indices of human trabecular bone. Dependencies were described by determination coefficient R^2 . Obtained values the coefficient were contained in range 0,50÷0,69.

Keywords: trabecular bone, fatigue life, structure trabecular bone

1. Introduction

Trabecular bone is one of components of human bone. It is a porous structure which strength has principal influence on strength whole bone. A typical loading for bones, eg. during gait is the cyclic loading variable in time, and thus behaviors under such loading are fatigue behaviors [1-2]. Thus, besides bone tests exposed to static compression, bending or torsion, research is carried out under cyclic variable loadings. It investigation covers both the cortical bone parts [3] and the trabecular bone parts [4-5].

The aim of the work is estimation relationship between fatigue life under cyclic loadings with stepwise increasing amplitude and structural indices of human trabecular bone.

2. Experimental methods

Material to the investigation were 61 samples of human trabecular bone. Samples were collected from osteoporotic and coxarthrotic femoral heads gained in result of hip arthroplasty. The samples used to investigation have cylindrical shape about diameter 10 and height 8,5 mm – Fig.1 [6].

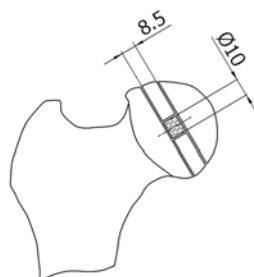


Fig. 1. Test sample obtained from the femoral head

The age of the patients ranged from 46 to 88 with an average of 73 years. The samples were obtained from 40 women and 21 men and were stored in 10% formalin solution at the room temperature. Samples were examined at microCT device (μ CT80) with resolution $36\mu\text{m}$ (parameters: 70kV, $114\mu\text{A}$, 500 projections/ 180° , 300ms integration time). In result the investigation were obtained values 11 structural indicators of samples e.g. trabecular number Tb.N, trabecular thickness Tb.Th as well as bone volume fraction BV/TV.

Fatigue tests were carried out under compression with stepwise increasing loadings using the testing machine INSTRON 8874. The frequency of sinusoidal loading was 1 Hz, the minimum loading for all the loading layers was 5-7N. The maximum loading started from 20N with a gain every 10N at successive steps. Each level of load maintained 500 cycles, realized under constant-amplitude loadings.

Fatigue life was determined by estimation the median of the values of deformation increment and then considering the value of the first loop for which the deformation gain exceeded the value of the median by 10% (to be the fatigue life).

3. Results

Fatigue tests with stepwise increasing loading demonstrated the fatigue life of the trabecular bone samples between $3,75 \cdot 10^3$ cycles and $5,02 \cdot 10^4$ cycles (time of test between 1,04 h and 13,95 h). In Fig. 2 presented values of fatigue life versus maximal compression stress achieved in test.

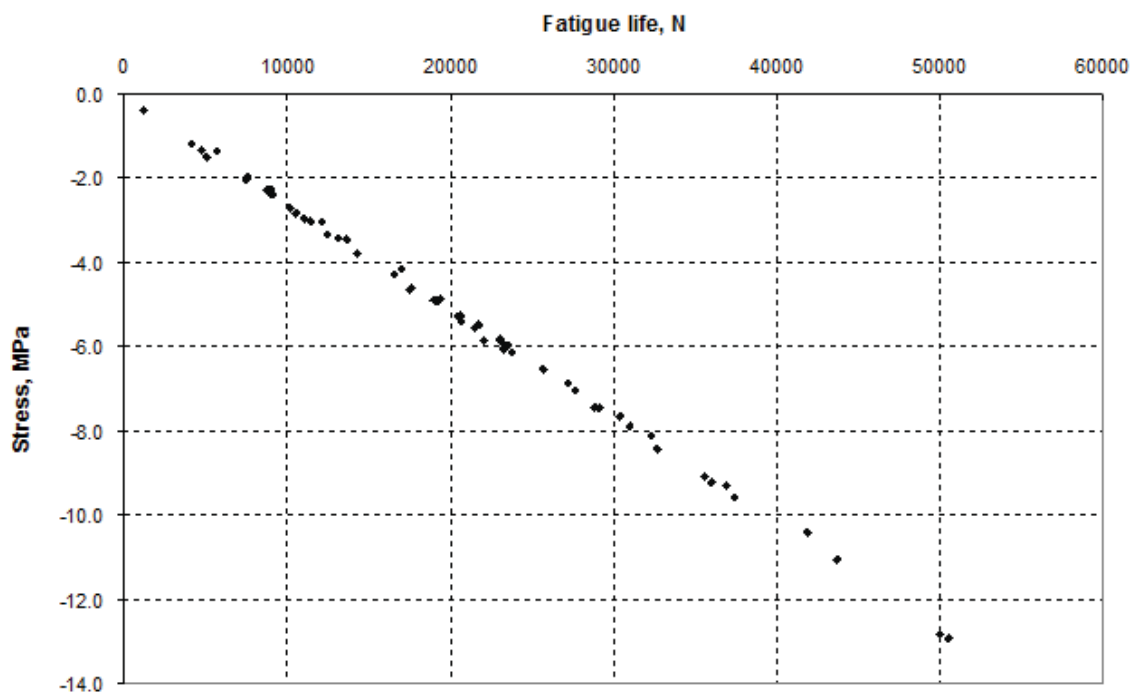


Fig. 2. Fatigue life versus maximal compression stress

In Tab. 1 presented values of selected indices structure of trabecular bone obtained from microCT investigation. The table includes minimal, maximal and mean values as well as standard deviation SD and relative standard deviation RSD.

Tab. 1. Values of selected indices structure of trabecular bone obtained from microCT investigation

Indicator	min	max	mean	SD	RSD
BV/TV, -	0.0759	0.4595	0.2049	0.0747	36 %
Tb.Th, mm	0.1053	0.2677	0.1714	0.0354	21 %
Tb.N, 1/mm	0.5109	1.5435	1.1329	0.222	20 %
BS/BV, 1/mm	5.2056	18.995	11.997	2.7467	23 %

In Fig. 3-6 presented relationship between fatigue life and BV/TV, Tb.Th, Tb.N and BS/BV respectively. Obtained values coefficient of determination R^2 for this relationship were in range $0,5 \div 0,69.R^2$

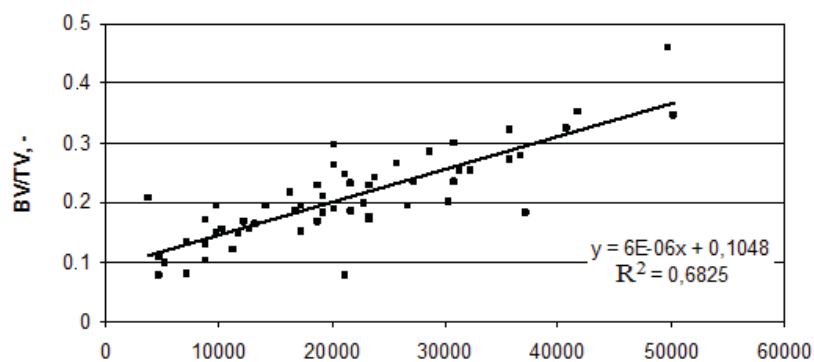


Fig. 3. Relationship between fatigue life N and bone volume ratio BV/TV

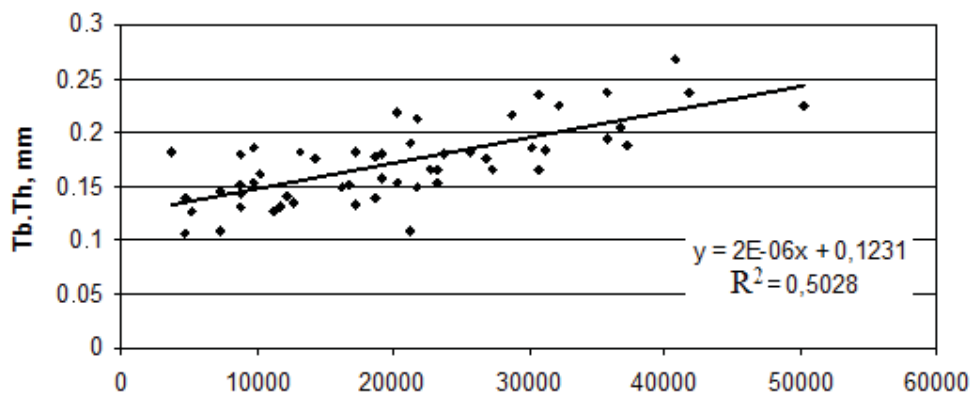


Fig. 4. Relationship between fatigue life N and trabecular thickness $Tb.Th$

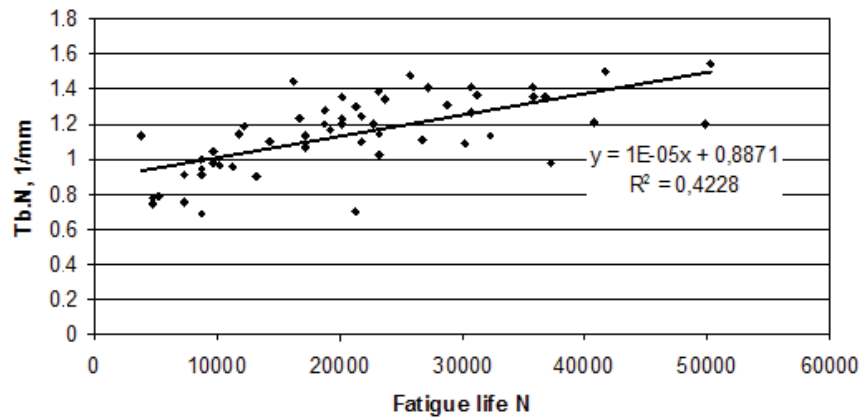


Fig. 5. Relationship between fatigue life N and trabecular number Tb.N

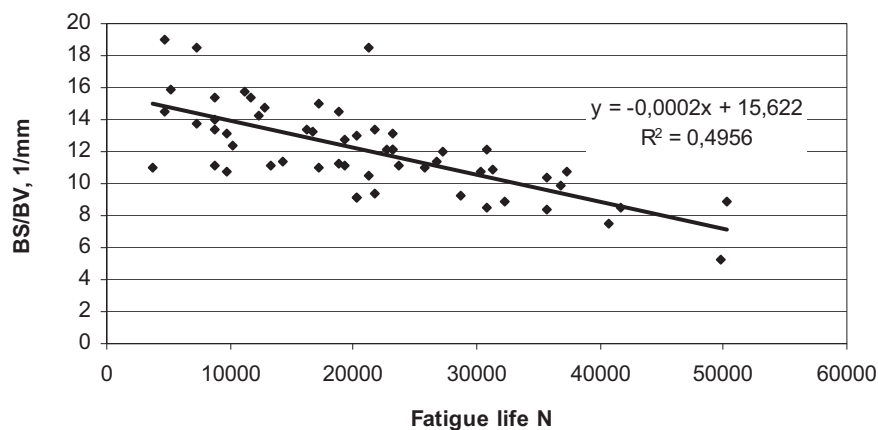


Fig. 6. Relationship between fatigue life N and BS/BV

4. Conclusions

From microCT investigation obtained wide range of values structure indices and significant values SD or RSD. It point out significant differences in structure samples of trabecular bone.

Obtained values R^2 for relationship structure indices and fatigue life contained in range (0,5÷0,69). Values R^2 is the highest for BV/TV. To tell about existence strong relationship between BV/TV and fatigue life. For the other investigated indices values R^2 are similar – about 0,5.

In spite of differences in structure trabecular bone obtained values of coefficient of determination for relationship between structure indices and fatigue life point out existence relationship between structure of trabecular bone an its fatigue life.

Acknowledgements

This work by supported by The State Committee for Scientific Research (KBN) under grant No. N N501 308934.

References

- [1] Taylor, M., Tanner, K. E., *Fatigue failure of cancellous bone: a possible cause of implant migration and loosening*, Journal of Bone and Joint Surgery, Vol. 79-B (1997), pp. 181-182.
- [2] Martin, R. B., *Fatigue Microdamage as an Essential Element of Bone Mechanics and Biology*, Calcif Tissue Int., Vol. 73 (2003), pp. 101-107.
- [3] Evens, F. G., Riolo, M. L., *Relations between the fatigue life and histology of adult human cortical bone*, The Journal of Bone and Joint Surgery, Vol. 52-A (1970), pp. 1579-86C.
- [4] Benhamou, C. L., Poupon, S., Lespessailles, E., Loiseau, S., et. al., *The influence of boundary conditions and loading mode on high-resolution finite element-computed trabecular tissue properties*, Bone, Vol. 44 (2009), pp. 573-578.
- [5] Ding, M., Odgaard, A., Hvid, I., *Changes in the three-dimensional microstructure of human tibial cancellous bone in early osteoarthritis*, J Bone Joint Surg., Vol. 85-B (2003), pp. 906-912.
- [6] Mazurkiewicz, A., Topoliński, T., *The relationship between structure, density and strength of human trabecular bone*, Acta of Bioengineering and Biomechanics, Vol. 11 (2009), pp. 55-62.



ROBOT APPLICATION TO SURFACE FINISH MACHINING

Tadeusz Mikołajczyk

*University of Technology and Life Sciences
ul. Prof. S. Kaliskiego Str. 7, 85-796 Bydgoszcz, Poland
tel.: +48 52 3408743, fax: +48 52 3408743
e-mail tami@utp.edu.pl*

Abstract

The paper describes the robot equipped with tool using to surface finish machining. Presented examples of robots using to: milling, grinding, polishing. Showed example of CAD/CAM system to robot machining. Idea of surface machining based on adaptation of tool position to unknown surface shape. Presents modernized system to robot control by PC. To support its position was developed in VB6 environment RoboCAM special software. Video optical systems for the surface geometry scanning is presented. The worked out system software is recognizing surface profile and changing position of robot head equipped with tool.

Keywords: robot machining, system control, surface scanning, milling, grinding

1. Introduction

Industrial robots are used in many ranges of contemporary manufacturing [1-4, 8, 9, 11]. The kinematics possibilities of robots [1, 3] and applied software [10] make possible their use in the different jobs. Industrial robots in manufacturing processes are most often practiced in: welding, the assembly, manual works, painting, surface machining [1-4, 9-12].

Cutting processes are used to rough machining [1, 4, 9] (Fig. 1a). To finishing [3, 9, 11] (Fig. 1b, 1c) grinding process was used. These solutions are more cheap as conventional numeric control machine using. Amongst directions of the development whereas machining tools increasing them are important versatility by applying geometric and kinematics flexibility tools (Fig. 1) [3-6, 8]. Kinematics possibilities of robots, frequently equipped in more than 5 axes machine-tool, enabled its geometric and kinematics flexibility tools for shaping and finishing. Wide possibilities of industrial robot kinematics made possible use geometric and kinematics flexibility tools idea in surface shaping [2, 4, 6, 8].



Fig. 1. Robot machining: a) milling [9], b) grinding [9], polishing [11]

Surface processing with robots are programmed using CAD model of its geometry [9, 10]. For example IRBCAM [10] converts the APT-CL or ISO G-code formats to the ABB robot language RAPID and supports the robot controllers S4C+ and IRC5. IRBCAM supports 3- and 5-axis machining operations and is suited for rapid prototyping, cutting, milling, grinding, surface finishing or mould production of wood, foam and ceramic materials and light metals (aluminum). In addition to traditional machining, the IRBCAM software can also be used for water jet, plasma and laser cutting, gluing, as well as painting. Typical accuracies that can be achieved with an ABB IRB-type robot is 0.3mm, a repeatability of 0.1mm and a workspace volume with radius up to 3.9 m. IRBCAM supports external axes linear and rotational), which can extend the workspace and enables an object to be machined from all sides in one setup. Very large objects can be machined this way, for example moulds and plugs for marine applications (Fig. 3).

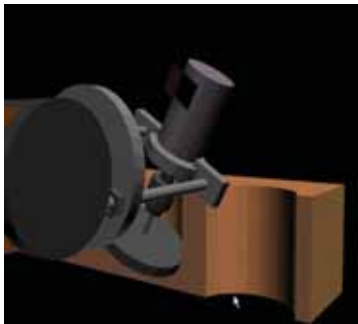


Fig 2. Using idea of EGK tools in robots machining [6]

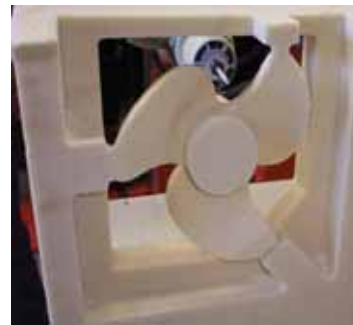


Fig. 3. Example of milling mold surface [10]

This paper describes the intelligent system to surface machining with robot equipped in modernized control system and the reverse engineering system to surface scanning and analysis.

2. Machining with active surface shape control idea

New idea of robot machining is using it to cutting unknown surface geometry [8]. This system has been worked out in Department of Production Engineering University of Technology and Life Science (Bydgoszcz, POLAND). Idea of surface machining based on adaptation of tool position to unknown surface shape. This process is similar to surface finishing by human worker. To realization this idea was build special on-line reverse engineering system which can analyses surface inclination or profile [8]. Profile of this surface can be use with interpolation system to robot tool system controlling (Fig. 4). When profile of surface is known, system can change tool position according best machining criteria. This adaptation of machining system can process with unknown geometry surface.

3. Surface scanning system using robot

3D scanning system was developed based on a synthesis of the surface points (x, z) coordinates from the scanner intersections and the coordinates x, y, z reading from robot kinematics. Reading of the IRb60 robot coordinates is possible by using the special PC robot control system developed by the Department of Production Engineering UTP Bydgoszcz [7] (Fig. 5).

Modern technology allows you to create simple scanning system [8]. To measure the coordinates of the surface a robot control system is associated with video optical scanner (Fig. 6) working in planar mode. Was used a red laser (wavelength 660 nm) with a flat stream system which generates a surface profile.

Trace of laser light on the analysed surface is captured using a USB digital camera VGA (640 * 480 pixels), which is focused in the beam plane.

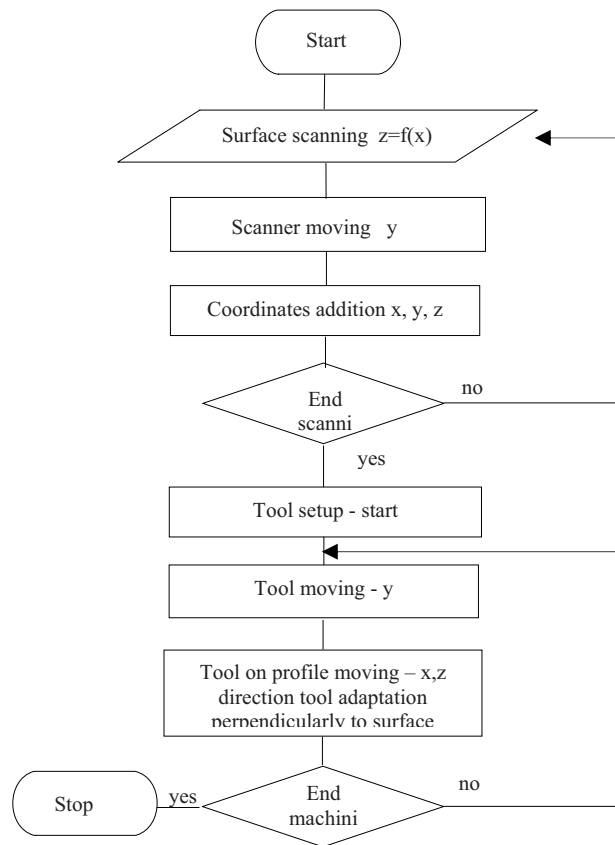


Fig. 4. Scheme of intelligent finish machining system of unknown shape surface

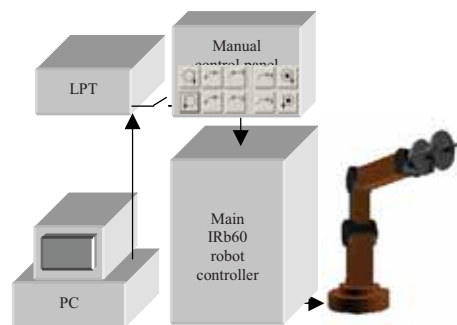


Fig. 5. IRb60 robot control system using PC [7]

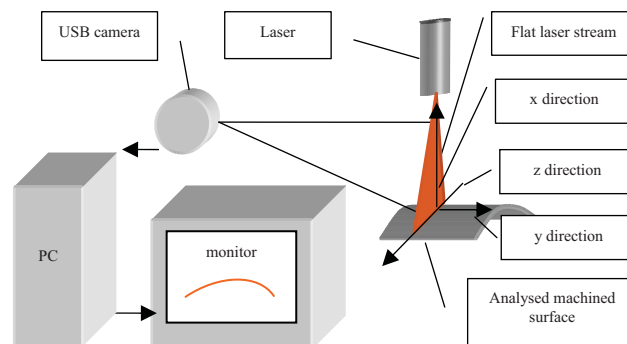


Fig. 6. Surface scanning system idea

To support its position RoboCAM special software has been developed in VB6 environment (Fig. 7).

Developed software in the field of the scanner ensures:

- support for digital cameras,
- periodic image capture,
- automatically determined coordinates of the analysed profile,
- synthesis of coordinates from the scanner system and control system robot,
- surface curvature visualization,
- record the coordinates of the scanned area to a file.

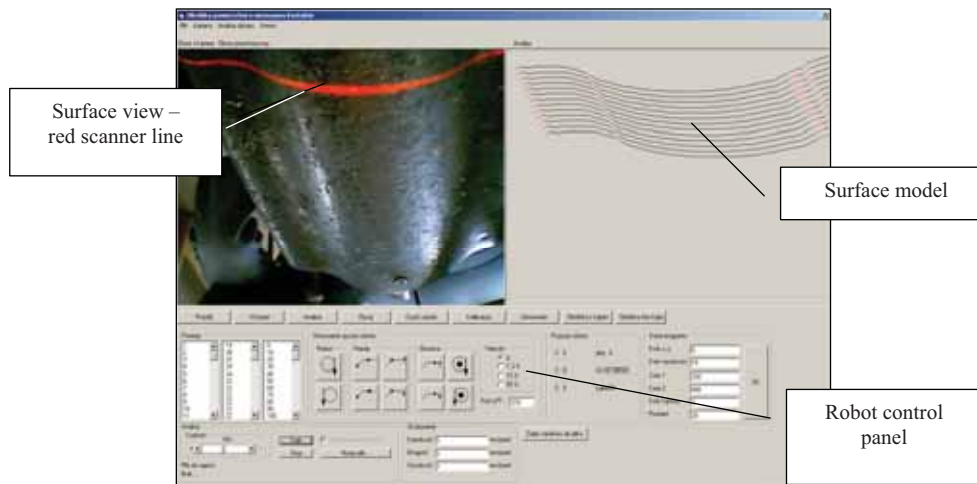


Fig. 7. Main form of RoboCAM software

Profile coordinates are determined using a specially developed procedure, which analyses the image to find points of parameters as much as saturated red - R. Due to the time of analysis, the software scans every tenth of a vertical line in search of a pixel with high density of red.

Based on the results of the search algorithm attempts to set points on the analysed surface. The R pixel readout parameter (default $R = 100$) has been used as a criterion surface point. The program allowed to change this value. In order to guard against erroneous readings, the software is equipped with intelligent analysis modul, together with a filter capturing interference.

4. Surface finish machining

Developed system was verified in trials, where treatment was carried out cylindrical surface profiling (Fig. 8). The robot system in addition to the scanner is equipped with tool mounted on a flexible elastic disc drive. The shield with Velcro mounted disc abrasive cloth. RoboCAM software (Fig. 7) was equipped with a data analysis module of the scanner and control functions in accordance with recognized surface gradient (Fig. 3).

During the first transition system automatically analysed the surface curvature. In the second pass, at the next positions of robot's head automatic adaptations of the robot axis tool positioning surface shape was done. Under current gradient surface mounted tool spindle axis of the robot's head change the position to normal the surface while maintaining a constant distance from tool axis machined surface (Fig. 8). There was a necessity of corrective tool head movements in the direction of x and z.



Fig. 8. View system in surface finish machining

Position of the axis were determined using the software based on previously defined space coordinates. With the flexibility of tool surface in machining followed adaptation tool curvature to the local surface curvature (Fig. 8).

In those trials the correctness of the system scan has been verified, even under a certain distortion of external lighting. Positioning system to the surface shape tools adaptation also work correctly.

5. Conclusions

The results of this work shows the possibility to equip the robot in own surface scanning system with using low-cost USB camera. It may be useful to create virtual models of large objects and analysis of surface shape in the process of finishing. Initially verified the accuracy of the surface coordinates reading systems indicates the possibility of it practical application. In trials carried out verified the correctness of the system scan, even under a certain distortion of external lighting. Positioning system to adapt to the shape of the surface of tools also work correctly.

Developed solution to the scanner and the software can also be convenient to draw 3D surfaces. Cloud of points obtained by scanning should be sent to CAD such as Solid Edge.

Initial positive verification system developed intelligent finish machining using a robot equipped with a tool for self-propelled, makes it advisable to continue the research work developed concept.

In further work it is advisable to use active control of surface condition, especially non-contact. This will create the possibility of finishing the surface with a given parameter of roughness. Reflectometry technique seems to be convenient. It is appropriate also to develop procedures for ensuring EGK adaptive mapping tool, using the possibility of kinematics robot. Convenient for this purpose is to use assumed in the work spindle positioning tool in relation to the robot head.

References

- [1] Chen, Y. H., Hu, Y. N., *Implementation of a robot system for sculptured surface cutting. Part 1. Rough machining*. International Journal Advanced Manufacturing Technology, v. 15, 1999, pp. 624-629.
- [2] Honczarenko, J., *Roboty przemysłowe. Budowa i zastosowanie*. WNT, Warszawa, 2004.

- [3] Hu, Y. N., Chen, Y. H., *Implementation of a robot system for sculptured surface cutting. Part 2. Finish machining*. International Journal Advanced Manufacturing Technology, v. 15, 1999, pp. 630-639.
- [4] Latoś, H., Mikołajczyk, T.: *Surface shaping with industrial robot*. 1st International Conference "Optimization of the Robots and Manipulators" OPTIROB-2006, Predeal, Romania, University "POLITEHNICA" of Bucharest, Faculty IMST, Department MSP, 2006, pp. 265-269.
- [5] Latoś, H., *Elastyczność geometryczno-kinematyczna narzędzi skrawających*. Wydawnictwo Uczelniane Akademii Techniczno-Rolniczej, Bydgoszcz, 1997.
- [6] Latoś, H., Mikołajczyk, T., *Virtual aid design of geometric and kinematics flexible tools*. XII Workshop on Supervising and Diagnostics of Machining Systems. Virtual Manufacturing, Karpacz, Poland, 2001, pp. 145-152.
- [7] Mikołajczyk, T., *Modernisation of IRb60 industrial robot steering system*. The 2nd edition of the international conference Optimization of the Robots and Manipulators, OPTIROB'2007, Predeal, Romania, University "POLITEHNICA" of Bucharest, Faculty IMST, Department MSP, 149-152.
- [8] Mikołajczyk, T., *The robot machining system with surface shape active control*. The second edition of the international conference The 2nd edition of the international conference Optimization of the Robots and Manipulators, OPTIROB'2007, Predeal, Romania, University "POLITEHNICA" of Bucharest, Faculty IMST, Department MSP, pp. 205-209.
- [9] www.delcam.com/powermill/simulation.htm.
- [10] www.irbcam.com.
- [11] www.robots.com.contacts.htm.



MODELLING OF WASTE-PAPER STOCK TREATMENT PROCESS IN DISC REFINERS

Adam Mroziński

*University of Technology and Life Sciences
Faculty of Mechanical Engineering
ul. S. Kaliskieg. 7, 85-796 Bydgoszcz, Poland
www.amrozinski.utp.edu.pl
adammmroz@utp.edu.pl*

Abstract

In the article problem of modelling and simulation in the range of refining devices of waste-paper industry were presented. Author have proposed own method of modelling of disc refiner work.

Keywords: disc refiner, modelling of beating process, waste paper

1. Introduction

The refining stage in stock preparation plays an important role in developing the properties of stock for paper production [4, 5]. Appropriate fiber treatment in the refiner greatly affects the runnability of the paper machine and quality of the end product. On the Figure 1 was presented mechanical treatment of fibers inside disc refiner.

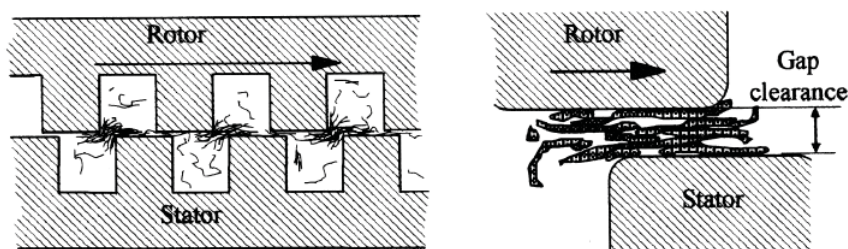


Fig. 1. Mechanical treatment of fibres inside a refiner[1, 3]

Bar configuration in refiner is probably the most important factor to achieve pulp properties. We have following plate design parameters, which are the key components of a refiner plate [1, 4]:

- Bar edge: Major working point of fibrillation (peeling action or pulling back of the primary wall along the fiber length) that increases fiber flexibility.
- Bar width: Narrower bars yield more bars for a given size plate which increases the total available bar edges and frequency of bar crossings, leading to a higher degree of fiber development while minimizing fiber shortening.

- Groove width and depth: Groove width determines flow through the refiner. Decreased groove width and depth brings the fibers to the bar edges, promoting refining action, restricting flow rate, and reducing hydraulic capacity. Excessive groove depth results in more stock passing through the refiner untreated.
- Bar angle: Increased bar angle gives more bar edge length, leading to enhanced refining and fiber development. This also increases pumping action, yielding more throughput capacity and higher pressure build-up, which uses more energy and lowers efficiency.
- Dams: Prevents the water-slurry mixture from channeling through the plate without being passed over the bar edges, but dams reduce throughput capacity. They are seldom used in low consistency refiners.
- Plate clearance: Distance between the refiner plates determines the amount of fiber cutting, as well as affects plate wear.

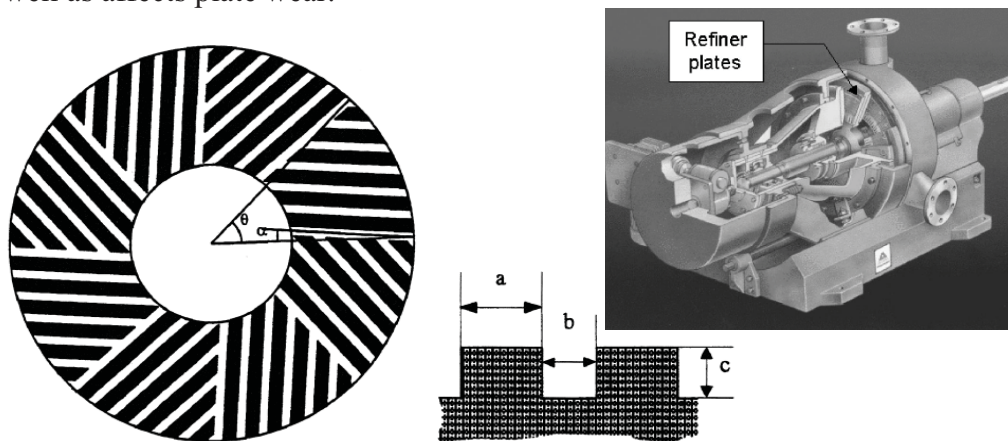


Fig. 2. Geometrical parameters of refiner fillings: a - width of bars; b - width of grooves; c - depth of grooves; θ - sectorisation angle; α - grinding angle [1]

Beating process, like in any other complex technological processes, depends on many factors, which we can divide into construction and system factors (connected with beating system and with its equipment) and technological factors. In the first group of factors there belong: using refining system (periodic, continuous), number of refining devices and their division into units (refining, proper beating, post refining), system of refiners connections and chests and characteristics of the used devices (kind, type, rotary speed, refining elements etc). We cannot change these factors during the exploitation of refiner or these changes would be complicated in practical realization.

To the most essential parameters of the second group (technological) we can accept [1, 3, 6]: properties of waste paper stock before refining, flow intensity by refiner, distance between disc, stock consistency and stock temperature.

2. Modelling of waste-paper stock treatment process in disc refiner

During the last two decades refining processes and the pulp produced with the refiners has been studied very intensively. However in many presented papers the refiner itself has been treated like a macro scale black box [5, 6]. In these studies, the effect of the major operating or input parameters such as refining consistency, refining pressure and production rate have been studied with different refining processes. The refiner mechanical pulps have also been categorized by the type of refiner used to produce them and in many cases it has been possible to differentiate between double disc, single flat disc and conical disc pulps [5]. At present, new refining processes employing high operating pressures and high refiner rotational speed are being compared to conventional refiner operation. A process model is a mathematical representation of an existing or

proposed industrial (chemical) process. Process models normally include descriptions of mass, energy and fluid flow, governed by known physical laws and principles. In process engineering, the focus is on processes and on the phenomena of the processes and thus: A process model is a representation of a process. The relation of a process model and its structure to the physical process and its structure can be presented on the Figure 3 [5, 6].

Why modelling? Models, simulation and optimization in waste paper treatment are important because of the following [1, 5]:

- reduce manufacturing costs, reduce research, development and engineering times,
- increase efficiency of paper production,
- greater understanding of the waste paper stock treatment problem,
- decision support in production, knowledge management,
- ability to handle complex problems,
- improve the safety of the plants,
- bring new products to market faster,
- reduce waste in process development,
- improve product quality of paper.

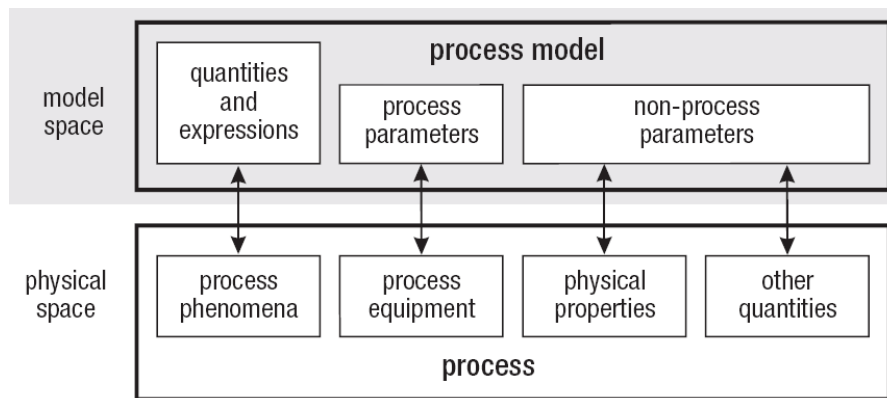


Fig. 3. Process and process model [1, 2, 3]

Different steps in the modelling of disc refiner unit processes can be presented in the following way:

- 1) **Identification of the main purpose of the model.**
- 2) **Identification of different phenomena in the beating process:**
 - stock refining, fibers cutting, proper beating,
 - mixed friction (beating friction and metallic friction of knives),
 - procesy dodatkowe zakłócające (ciepło, drgania, zużycie itp.).
- 3) **Identification of the most important phenomena and planning their experimental research:**
 - refining - mutual fibers friction and friction between fibers and working surfaces of knives,
 - proper beating - treatment on the frontal surfaces of working discs,
 - cutting - decohesion on the knife edges,
 - mixed friction on the working surfaces of discs.
- 4) **Selection of the theoretical basis from several competitive theories:**
 - friction theory,
 - specific edge load theory,
 - specific surface load theory.
- 5) **Formulation of power consumption equations:**
 - balance of power consumption [4]:

$$N_c = \begin{cases} \text{for } x = x_4 : & N_j + N_r + N_t + N_{esz} \\ \text{for area IV : } x_4 < x < x_3 : & N_j + N_r + N_t + N_{sz} \\ \text{for area III : } x_3 < x < x_2 : & N_j + N_r + N_b + N_t \\ \text{for area II : } x_2 < x < x_1 : & N_j + N_r + N_b \\ \text{for area I : } x_1 < x : & N_r + N_j \end{cases} \quad (1)$$

- cutting index, index of beating and refining, index of quality of paper stock,
- treatment intensity of fibers equations, component powers equations:

Power consumed on beating [4]:

$$N_b = k_b \cdot n \cdot p \cdot (D_z^3 - D_w^3), \quad (\text{kW}) \quad (2)$$

where:

k_b - solidity coefficient of beating,

n - rotational speed (rev/min),

p - beating pressure (Pa),

D_z - outside diameter of disc (m), D_w - inside diameter of disc (m).

Power consumed on refining [4]:

$$N_r = k_r \cdot n^3 \cdot (D_z^5 - D_w^5), \quad (\text{kW}) \quad (3)$$

where:

k_r - solidity coefficient of refining.

Power consumed on fibers cutting [4]:

$$N_t = P_t \cdot z_1 \cdot z_2 \cdot l \cdot k \cdot \tau \cdot n \cdot d_w, \quad (\text{kW}) \quad (4)$$

where:

P_t - elementary cutting force (on knives length unit) (N/m),

l - average length of movable and non-movable discs knives,

z_1 i z_2 - knives number of movable and non-movable discs,

k - coefficient of length using of intersecting knives on cutting process,

τ - intensity of cutting,

d_w - width of fiber cutting layer (m).

Power consumed on metallic friction [4]:

$$N_e = \frac{\pi^2 \cdot b^2 \cdot p \cdot \alpha_t \cdot \sigma \cdot n \cdot (D_z^3 - D_w^3)}{6 \cdot t^2}, \quad (\text{kW}) \quad (5)$$

where:

α_t - coefficient of knives metallic friction,

σ - summary coefficient of irregularity of frontal surface of knives, mechanical damages, angle of knives setting and knives material,
 b - width of knives (m),
 t - knives pitch (m).

6) Solution of the model

The solution of the model can be carried out in three basic ways: simulation, design and parameter estimation (Table 1). Optimization and experimental design could also added to the table. Process parameters refer to the parameters that are specific to the process. Non-process parameters refer to the parameters that are not specific to the process.

Tab. 1. Three ways to the solution of models

Solution mode	Calculated	Specifications
Simulation	output variables	input variables process parameters non-process parameters
Design	process parameters	input variables output variables non-process parameters
Parameter estimation	non-process parameters	input variables output variables process parameters

On the Figure 4 was presented example of disc refiner work simulation: dissipation of energy in disc refiner (application of J&L Fiber Services Inc.).

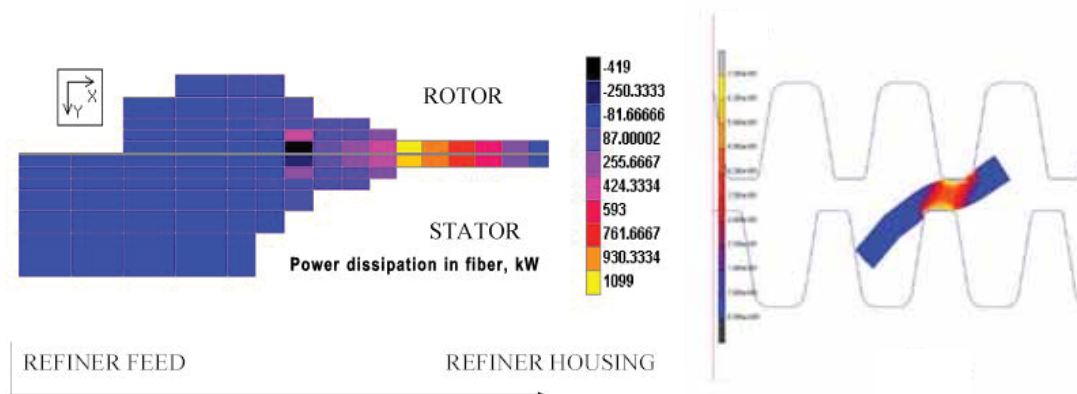


Fig. 4. Simulation: dissipation of energy in disc refiner - J&L Fiber Services Inc. [5]

7) Presentation and interpretation of the results

Parameter estimation and model validation based on experimental data, experimental data should be obtained using experimental design methodologies. On the Figure 5 was presented chart of total power consumption in function of the slot - x for disc refiner with regard of composition powers.

Beating of paper stock is one from basic processes of paper treatment and also is one from most energy-consuming processes. Power delivered on engine shaft in the time of beating changes in dependence on many factors. And in peculiarity from slot between discs refiner - x and from each composition powers. These powers are consumed on different processes, which occurred in

disc refiner during beating. Total power consumption we can show by formula, in which are the basic processes [4]:

$$N_t = N_b + N_r + N_t + N_{sz}, \text{ (kW)} \quad (6)$$

where:

N_b - power consumed on beating,

N_r - power consumed on refining,

N_t - power consumed on cutting of fibers,

N_{sz} - power consumed on metallic friction between beating surfaces.

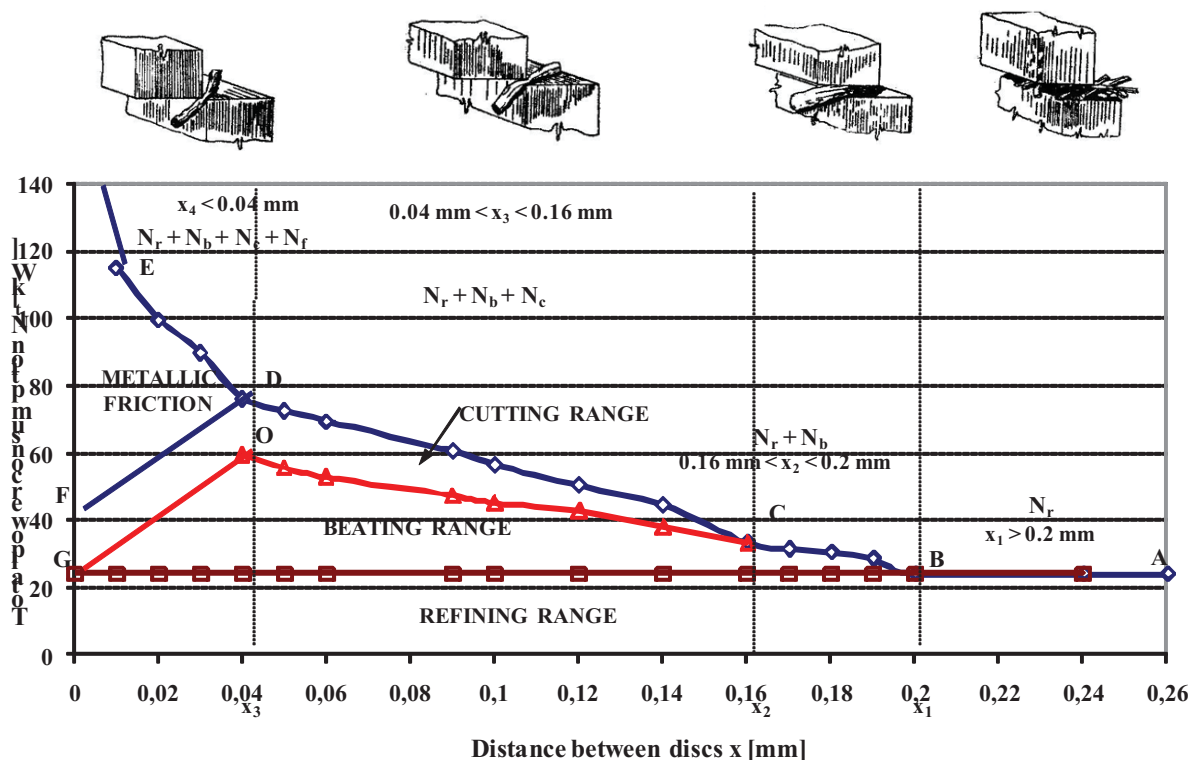


Fig. 5. Chart of total power consumption in function of the slot - x for disc refiner with regard of composition powers

Process powers were qualified by theoretical analyses of refining process [4, 5]. These powers are as follows:

- N_c - Total power consumption, which depends on x – distance between disc, refiner construction and stock kind. This power is measured on engine shaft, which drives refiner;
- N_j - Power consumed on idle run without stock for slot size greater than 0.2 mm;
- $N_{jr} = N_j + N_r$ - Power consumed on refining with power consumed on idle run (with stock) for slot size $x > 0.2$ mm;
- $N_r = (N_j + N_r) - N_j$ - Power consumed on refining, $N_{jr} - N_j = N_r$;
- N_b - Power consuming on beating;
- N_t - Power consuming on fibers cutting;
- N_e - Power consuming on metallic friction (friction between frontal surfaces of knives);
- N_{sz} - Power consumed on mixed friction (mixed friction consist of metallic friction and friction, which is connected with beating process): $N_{sz} = N_{msz} + N_{esz}$;
- N_{msz} - Power consumed on beating which is a part of power consumed on mixed friction;

N_{esz} - Power consumed on metallic friction, which is a part of power consumed on mixed friction.

- 8) **Documentation of the model**
- 9) **Integration of the model to the whole system or process**
- 10) **Further development of the model.**

4. Conclusion

Presented conception of mathematical models elaboration enabled the comprehensive solution of the problem of mutual relations of power consumption components in relation to working conditions of investigated refiner grinding unit. Accepted assumptions and methods of logical proceeding resulted in elaboration of original work algorithm and finally led to the elaboration of the unique graph: $(N_c, N_b, N_t, N_r) = f(x)$.

References

- [1] Hietanen, S., Ebeling, K., *Fundamental aspects of the refining process*, Paperi ja Puu – Paper and Timber, Vol. 72, No 2, 1990, p. 158-170.
- [2] Mroziński, A.: *Power consumption investigation in disc refiner at waste paper treatment*. Journal of POLISH CIMAC nr 3/2009, Vol. 4, str. 91-98
- [3] Mroziński, A.: *Podstawy rozwoju przetwarzania mas makulaturowych w młynach*. Ekologia i Technika, Vol. 101, nr 4 (2009), str. 151-158
- [4] Mroziński, A.: *Badanie poboru mocy przez zespół rozdrabniający makulaturową masę włóknistą w warunkach zmiennej szczeliny roboczej młyna tarczowego*, Rozprawa doktorska, ATR Bydgoszcz, Wydział Mechaniczny, 25 styczeń 2005.
- [5] Mroziński, A., Kikiewicz, Z.: *Modelowanie i symulacja przetwarzania mas papierniczo-makulaturowych*. Inżynieria i Aparatura Chemiczna, Nr 1/2007, Vol. 46 (38), str. 97-99
- [6] Waterhouse, J.F.: *Whither refining?* Refining 97, 4th International Refining Conference, Palazzo della Fonte, Fiuggi, Italy, March 18-20, 1997



PROPERTIES AND MICROSTRUCTURE OF BRASS UNDER VARIABLE LOADING

S. Mroziński ¹, S. Dymski ²

¹ University of Technology and Life Science
Department of Machine Design, Mechanical Engineering Faculty
ul. Prof. S. Kaliskiego 7, 85-789 Bydgoszcz, Poland
e-mail: stmpkm@utp.edu.pl

² University of Technology and Life Science
Department of Materials Science and Engineering, Mechanical Engineering Faculty
ul. Prof. S. Kaliskiego 7, 85-789 Bydgoszcz, Poland
e-mail: dysta@utp.edu.pl

Abstract

In the paper there were presented changes of properties and microstructure in the specimens made of CuZn37 brass under fatigue test. During the analysis there were used parameters of hysteresis loop and microstructure changes for different levels of fatigue damage, that were registered during the tests. Basing on the analysis of three hysteresis loop parameters: stress amplitude σ_a , plastic strain amplitude ε_{ap} and plastic strain energy ΔW_{pl} , it has been found that the smallest changes are observed for the energy ΔW_{pl} . Microstructure observations of brass specimens for various damage levels showed that fatigue damage cumulation is also visible in the grains of α phase. Plastic strain of the brass was characterized by the presence of creep strands inside the grains.

Keywords: damage, cyclic properties, failure, creep, brass

1. Introduction

Variable loadings generate in the material of the construction units specific changes and fatigue phenomena. If these loadings are high enough they may locally cause the plastic strains (for example in the notch areas). During fatigue life calculations of the construction units containing areas of the plastic – elastic strains there are used material data defined in the low-cycle fatigue tests [1]. Experimental conditions in this fatigue area are defined i.e. in the standards [2,3]. The characteristic feature of the low-cycle fatigue area is forming, in every cycle of variable loading, of hysteresis loop (Fig. 1).

Characteristic loop parameters i.e. are: total strain amplitude ε_{ac} , plastic strain amplitude ε_{ap} , stress amplitude σ_a and ranges of the mentioned parameters, that is: $\Delta\varepsilon_{ac}$, $\Delta\varepsilon_{ap}$, $\Delta\sigma_a$. The area enclosed by the loop is the measure of the energy dissipated in the material during one loading cycle. This energy is also called the plastic strain energy ΔW_{pl} . Analysis of the mentioned parameters in the function of the loading cycles number enables the description of changes of the cyclic properties of the material and also the course of the damage cumulation. Cyclic strains in

metals and their alloys result in the processes of hardening or softening of the material. They are undoubtedly extraordinary phenomena among many processes that accompany the low-cycle fatigue of metals. At the present moment there is a number of hardening or softening hypotheses. Some of these hypotheses are in connection with hypotheses elaborated for the static loading or they directly result from them. Changes of cyclic properties observed during low-cycle tests are the consequence of the various phenomena and processes which occur in the microstructure of the metals. Description of these processes is possible on the base of analysis of microscopic tests results with the use of dislocation theory.

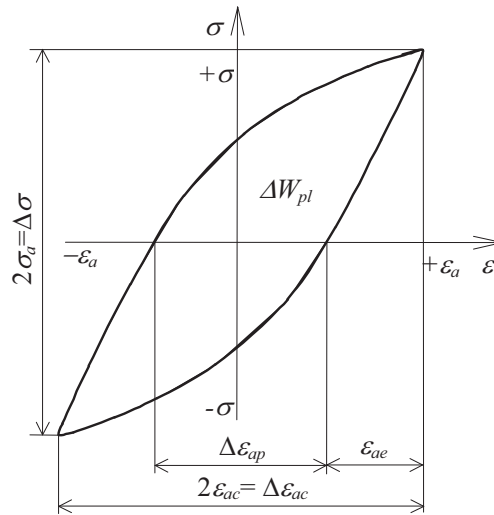


Fig. 1. Characteristic of hysteresis loop parameters

The aim of the paper was analysis of the course changes of the basic hysteresis loop parameters under cyclic loading of one phase alloy - brass with considering metallographic tests.

2. Description of the tests

Fatigue tests were carried out under constant amplitude loadings. They were preceded by the static tests aimed at defining the levels of variable loading. Fatigue tests were performed on six levels of controlled total strain $\varepsilon_{ac(1)}=0.35\%$, $\varepsilon_{ac(2)}=0.5\%$, $\varepsilon_{ac(3)}=0.65\%$, $\varepsilon_{ac(4)}=0.8\%$, $\varepsilon_{ac(5)}=1.0\%$, $\varepsilon_{ac(6)}=1.2\%$. Fatigue tests were performed with the use of the Instron 8501 strength machine. Loading frequency applied in the tests was 0.2 Hz. During the tests momentary values of the loading force and strain of a specimen for chosen loading cycles were registered. Tests parameters were accepted according to directions in the standard [1]. Specimen accepted in the fatigue tests were made of CuZn37 brass. There were two kinds of these specimens: smooth (without a notch) and notched ones. The shape of specimen used in the tests is presented in Fig.2

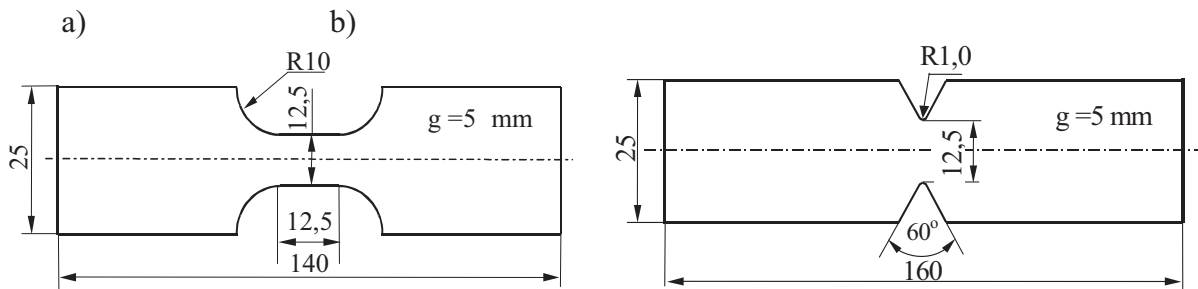
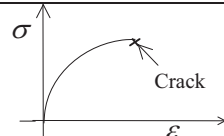
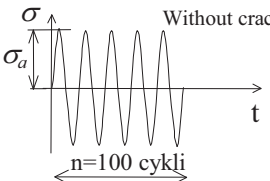
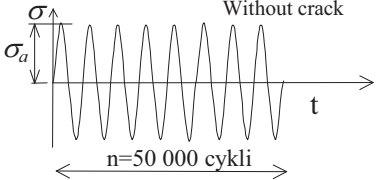
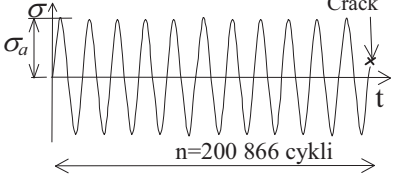


Fig. 2. Specimen used in fatigue tests: a) smooth, b) with a notch

Observations concerning the surface microstructure of specimens were made during the fatigue tests. During microstructure analysis of the fatigue cracks, prof. Kocańda's experiences were widely used [6]. Observations were made for various degrees of fatigue damage. Fatigue damage was defined with the use of so called relative life n/N , where n is the current number of loading cycles and N is the number of cycles until fatigue failure. After realization of the defined number of n cycles for a given loading level the test was stopped and specimens underwent a microscopic examination. Specimens were given this examination in the following situations:

- 1) after static tensile test,
 - 2) after 100 cycles of variable loading ($\sigma_a = 86.4$ MPa), $n/N = 0.002$,
 - 3) after 50 000 cycles of variable loading ($\sigma_a = 86.4$ MPa), $n/N = 0.25$,
 - 4) after 200 866 cycles of variable loading ($\sigma_a = 86.4$ MPa), $n/N = 1$ - failure of the specimen.
- In Tab. 1 there were shown loading diagrams of specimens 1-4 and the ranges of observations.

Tab. 1. Loading diagrams and range of the microscopic observations

Specimen	Scheme of loading	Description of observations
1		Crack and surface of a specimen
2		Surface of a specimen
3		Surface of a specimen
4		Crack and surface of a specimen

Specimens destined for microscopic examinations were specially treated. Their side surfaces in the notch zone were grinded and then polished. After static and fatigue tests there were performed observations of specimen surfaces with the use of light metallographic microscope and scanning electron microscope (SEM). On the specimens there were also taken hardness measurements. Hardness tests were performed with use of the Vickers method under loading of 0.49 N. At each measuring point there were made minimum 5 measurements of hardness. The points of measurement on the specimen were shown in Fig. 3.

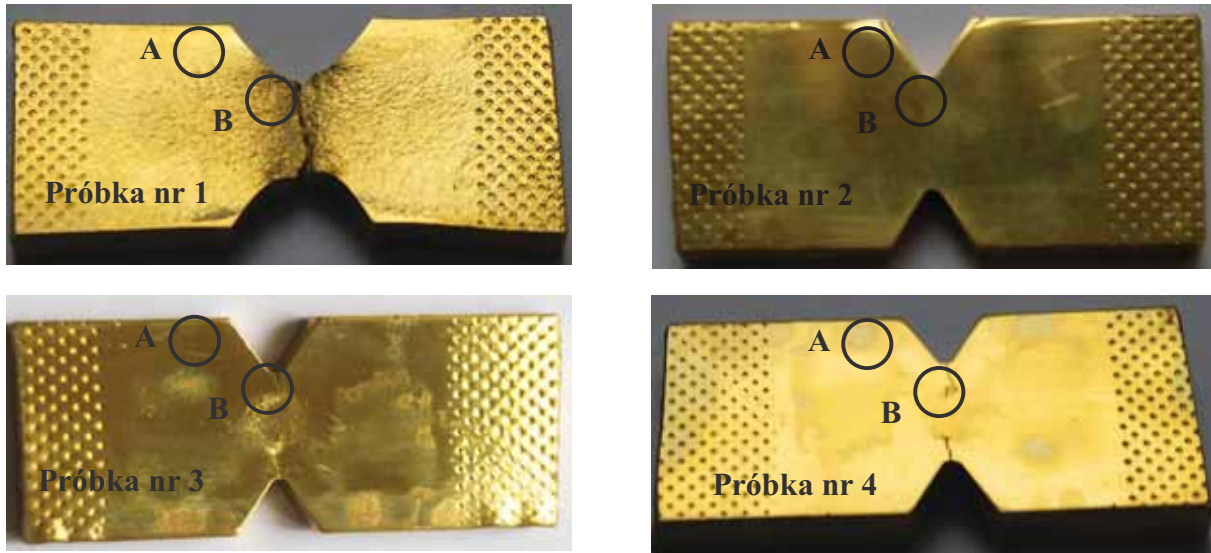


Fig. 3. Points of hardness measurements on the specimens. A – strained zone, B – not strained zone

3. Test results

3.1. Static tests

Static test results were presented in the form of static tensile diagrams of the relation stress σ - relative strain ε . Stress σ values were determined by dividing the momentary loading value of the specimen during the test by its initial cross-section area. An example of the full tensile diagram was shown in Fig. 4a. In Fig. 4b there was shown an initial fragment of this diagram limited to the strains $\varepsilon < 2\%$. In Fig 4b there were also drawn strain amplitude levels accepted during fatigue tests of the specimens.

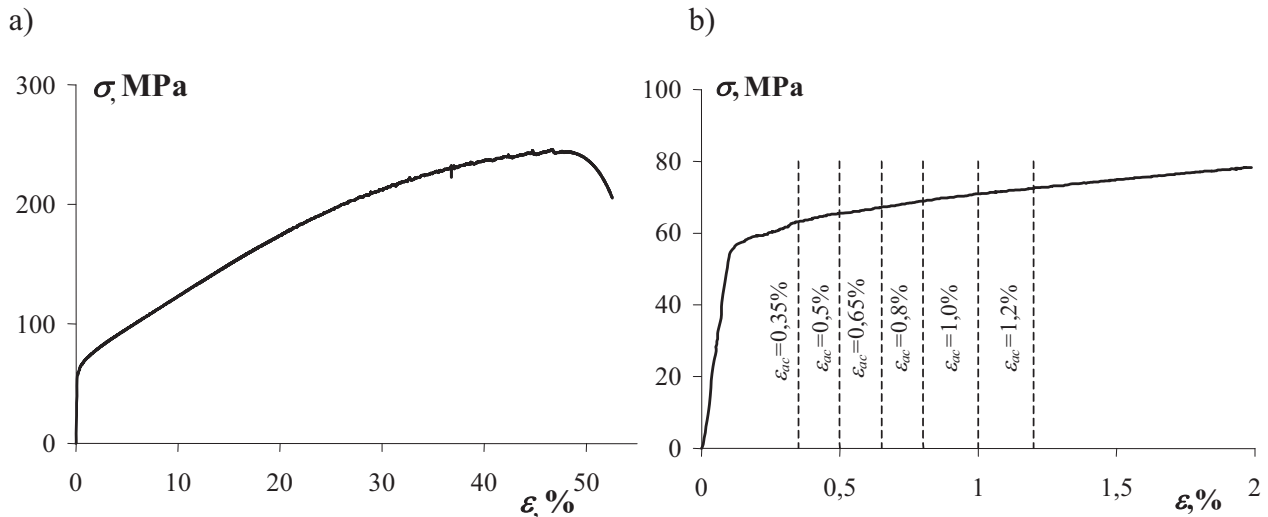


Fig. 4. Static tensile diagrams: a) full diagram, b) initial fragment of the diagram (for $\varepsilon < 2\%$)

3.2. Fatigue tests

During fatigue tests there were observed changes of cyclic properties of tested metal. In order to illustrate the nature of these changes in Fig. 5 there were shown examples of the hysteresis loop

registered during the test at the strain level $\varepsilon_{ac}=0.5\%$. Cycles numbers corresponding to the registered hysteresis loops were marked with figures (in the right top of the diagram).

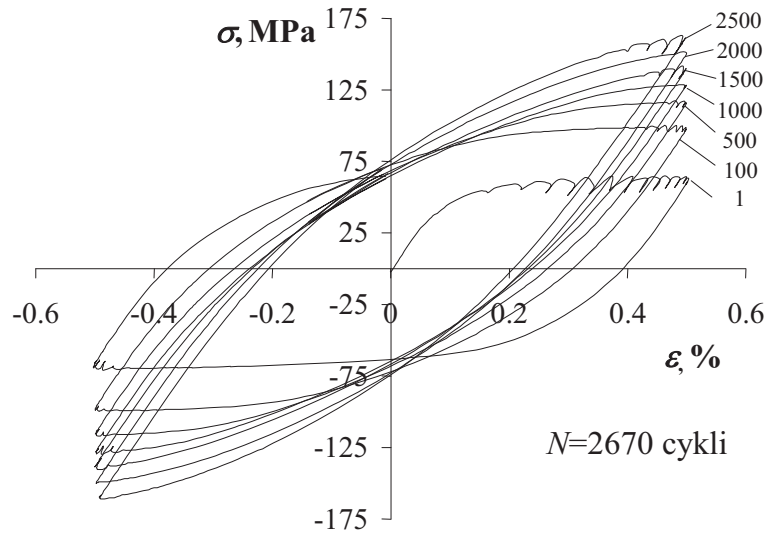


Fig. 5. Hysteresis loops at the strain level $\varepsilon_{ac}=0.5\%$

3.3. Microscopic examinations and hardness tests

Surface observations of the 1st specimen in the area of mild plastic strain showed the occurrence of multisystem creeps in grains of α phase. Strain twins were also visible in some grains (Fig. 6a). Specific arrangement of the creep strands in grains determines their boundaries. The arrangement of the creep strands was in agreement with their crystallographic orientation and they had an adequate direction in comparison to the direction of the shear stress action.

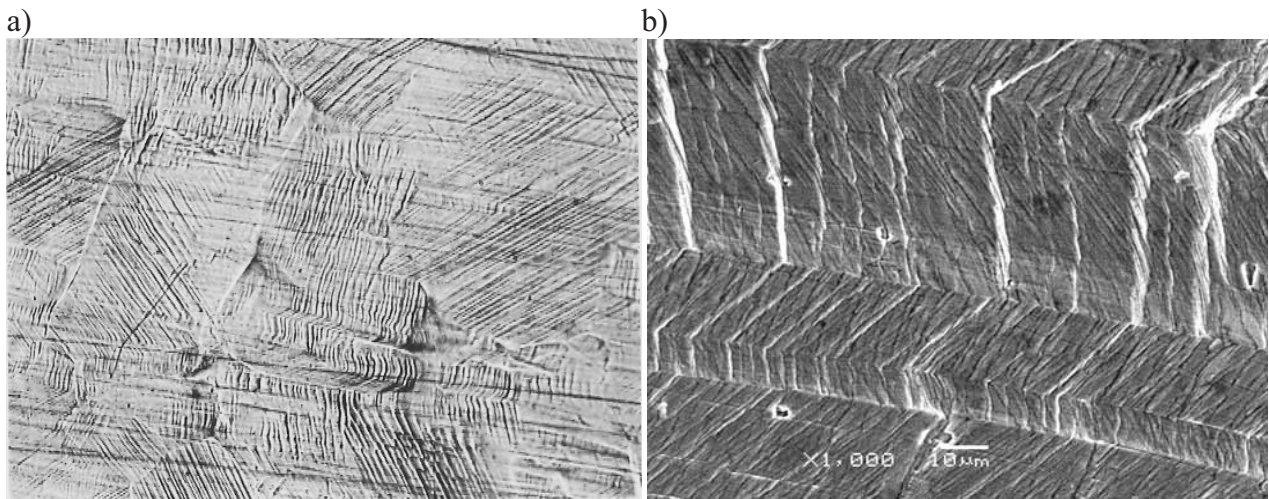


Fig. 6. Microscopic examinations results: a) Multisystem creep in the grains of α phase on the surface of 1-st specimen. 200x magnification, b) Strain twins and permanent creep strands on the surface of the 1st specimen (SEM)

Surface morphology of the 1st specimen next to its crack was shown in Fig. 6b. In grains with very high plastic strain there were found twins and permanent creep strands, i.e. in the form of long filaments – cords [6].

Fatigue failure was initiated on the bottom of the notch near the specimen edge, with significant surface relief. The line of the cracking was orientated at an angle of 90° towards the

loading direction and side surface of specimen. In the initiation zone of the fatigue failure there was observed local plastic strain and it was characterized by the presence of the creep strands in the grains of α phase (Fig. 7a).

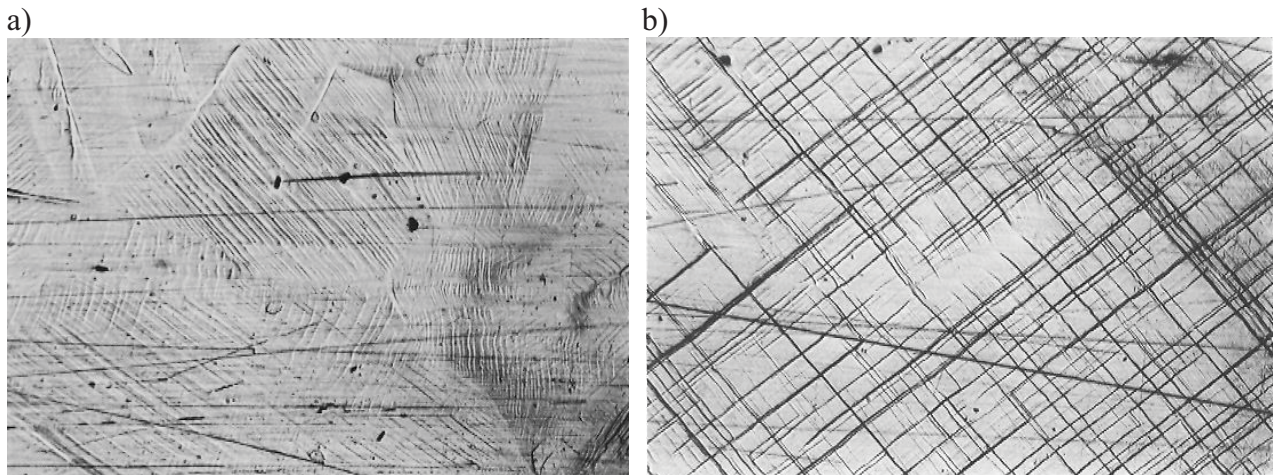


Fig. 7. The strands and creeping lines: a) The creep strands in the grains of α phase on the surface of the 2nd specimen in the initiation zone of failure. 200x magn. ,b) Creeping lines on the surface of the 2nd specimen. 200x magn.

Basing on the microscopic observations along the straight line, connecting notches on the 2nd specimen (Fig. 3), there were found surface irregularities similar to those found on the surface of the 1st specimen in the zone with lower degree of the plastic strain.

On the one of surfaces of the 2nd specimen, near the bottom of the notch, there was found singular set of creeping lines. These lines intersected at an angle of 90° (Fig. 7b). And in relation to the direction of the shear loading, stretch loading and compression loading they were bended down at an angle of about 45° .

On the crack surface of the 4th specimen there were found fatigue stripes that were connected with the creep strands (Fig.8). On the surface of the specimen, just above the edge line and under the second edge of crack, there were visible, beside the creep strands, the extrusions and protusions. However just below the edge of the crack (in the middle of the picture) on its surface there were found the fatigue stripes.

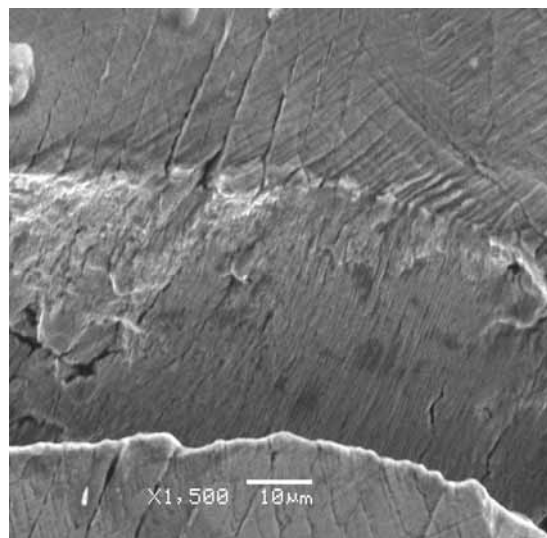


Fig. 8. Microstructure of the fatigue crack and surface of the 4th specimen (SEM)

Hardness measurements results according to the Vickers Method were presented in Tab 2. Measurements were taken in the plastic strain zone – fatigue (A) and in not strained zone (B) (Fig. 3).

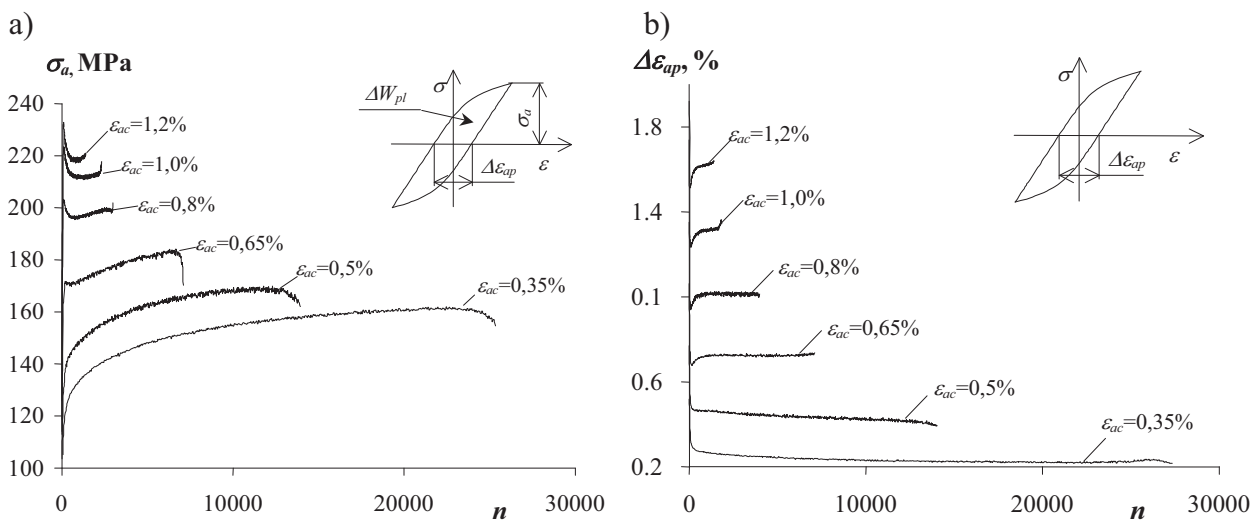
Tab. 2. Hardness of CuZn37 brass on the surface of specimens under static and fatigue tests

Specimen	Measuring point in the zone	Hardness according to Vickers, HV 0.05		
		Measurements	Gap	Arithmetic mean
1	Not strained	119, 117, 122, 119, 122	5	120
	Strained at the edge of the notch	127, 122, 126, 130, 124	8	125
2	Not strained	100, 117, 107, 117, 112	17	115
	Fatigue	127, 120, 120, 127, 124, 143, 124, 136, 128, 126 130	23	128
3	Not strained	133, 137, 130, 136, 130	7	133
	Fatigue	101, 101, 101, 112, 101	11	103
4	Not strained	136, 138, 150, 161, 146	25	136
	Fatigue	114, 105, 107, 107, 107	7	103

Results of hardness measurements show that specimen 2 hardened in the fatigue zone after $n=100$ cycles of loading. Its hardness increased by 13 HV 0.05. And in specimens 3 and 4 in the result of variable loading respectively: $n=50\ 000$ and $n=200\ 866$ cycles hardness decreased by 30 and 33 HV 0.05.

4. Analysis of test results

Analysis of hysteresis loops presented in Fig. 5 shows that at the strain level $\varepsilon_{ac}=0.5\%$ primary loop parameters such as stress amplitude σ_a , plastic strain range $\Delta\varepsilon_{ap}$ and plastic strain energy ΔW_{pl} undergo changes. The shape of the loop and value of its characteristic parameters in the following loading cycles are the proof of brass hardening at this strain level. The momentary values of the loading force and strain registered during the tests at the remaining strain levels were used for calculation of the earlier mentioned hysteresis loop parameters for all strain levels. Their example courses in the function of the loading cycles number were shown in Fig. 9.



c)

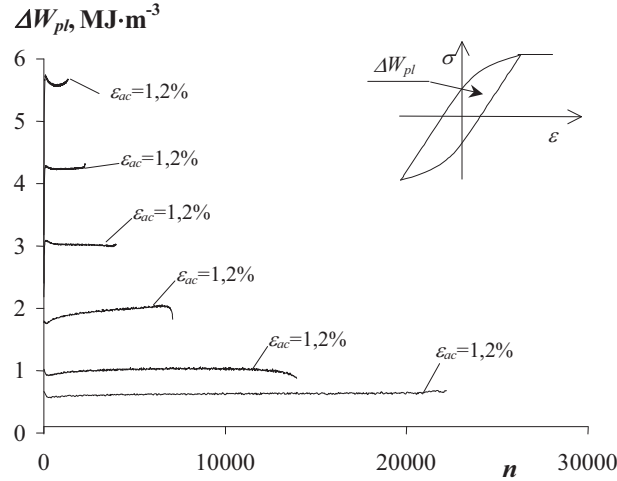


Fig. 9. Changes of hysteresis loop parameters in the function of loading cycles number n for: a) $\sigma_a=f(n)$, b) $\varepsilon_{ap}=f(n)$, c) $\Delta W_{pl}=f(n)$

The course analysis of σ_a , $\Delta \varepsilon_{ap}$ and ΔW_{pl} parameters (Fig. 9) shows that cyclic properties of single-phase brass undergo changes at all levels of strain. For all strain levels cyclic hardening is visible. From the analyzed parameters the least changes in the function of the loading cycles number are observed in the case of the plastic strain energy ΔW_{pl} .

Confirmation of cyclic hardening of brass during variable loading is the mutual position of cyclic and static strain diagrams. Cyclic strain diagram is obtained by approximation of the hysteresis loop apexes at all strain levels with a suitable equation. The most often applied description in the design fatigue analysis is the proposal of the equation given by Ramberg-Osgood [7] in the form :

$$\varepsilon_{ac} = \frac{\sigma_a}{E} + \left(\frac{\sigma_a}{K'} \right)^{\frac{1}{n'}} \quad (1)$$

where:

E - modulus of elasticity, MPa,
 n' - exponent of the cyclic hardening of the material,
 K' - cyclic life coefficient, MPa.

Cyclic strain diagram describing hysteresis loops apexes at all strain levels was presented in Fig. 10.

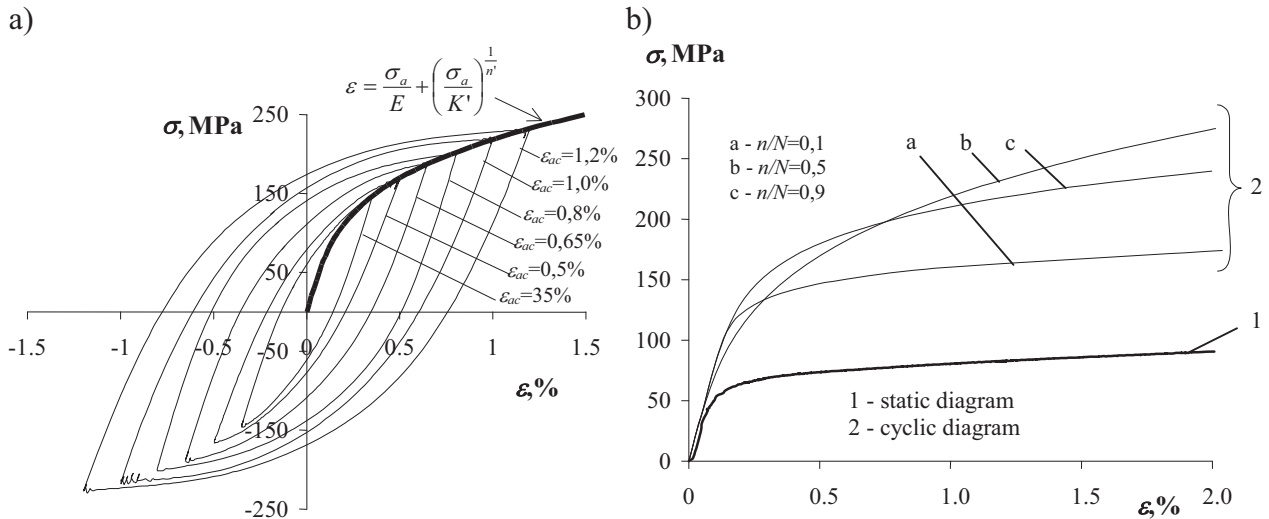


Fig. 10. Investigations results: a) Hysteresis loops from the half-life period ($n/N=0.5$) and cyclic strain diagram, b) Diagrams of static tension (1) and cyclic strain (2)

Hysteresis loops presented in Fig. 12 refer to the damage level corresponding to relative life $n/N = 0.5$. In order to illustrate the scale of changes of cyclic properties of brass during variable loading with the use of the equation (1) in Fig. 13 there were shown diagrams of cyclic strain obtained for the hysteresis loops from various periods of n/N life. There was also shown diagram of the static tension. Position of 2a, b and c curves of the cyclic strain above the diagram of the static tension (1) is the proof of proceeding changes of cyclic properties and the process of metal hardening.

Microscopic tests of specimen surfaces after static and fatigue loading showed microstructure features accompanying fatigue cracking areas. Their characteristic feature is the presence of the creep lines. Detailed analysis of these areas under variable loading enabled the probability valuation of the occurrence and then development of fatigue cracks.

Basing on the microstructure comparative analysis of the specimens under variable and static loading the presence of the similar plastic strain elements was found. Their feature was system of the creep lines originated in the grains of α phase, in agreement with their crystallographic configuration.

Gradual increase of stress during static tensile test resulted in originating, besides the creep systems, the strain twins of α phase (A1 network type). This strain system was also present during fatigue test, but in less degree.

It is given in literature [6] that plastic strain originates in grains with crystallographic orientation in agreement with the direction of easy creep and close to the notches. Therefore a creep in the grains under fatigue test proceeded in the same crystallographic systems as during plastic strain.

Variable loading with participation of plastic – elastic strains brought about the increase of dislocation density in α phase. This in turn resulted in cyclic hardening of the material. As far as crack initiation and development are concern, these processes proceeded under higher loadings.

Brass hardening (Fig. 11) observed in the courses of changes of hysteresis loop parameters was reflected in the results of hardness measurements. On the base of these measurements it was found that in the initial period of life ($n/N < 0.25$) with the increase of loading cycles number hardness of the specimen near the bottom of the notch increased. In this period there also took place the increase of the dislocation density, which in turn resulted in hardening of the material. Further increase of the loading cycles number resulted in insignificant decreasing of specimen hardness in the analysed area in comparison to the initial hardness. It can be the result of the softening of α phase, but only on the surface of specimens. Yet from fatigue tests resulted brass hardening.

Decreasing of the material hardness in the crack area on the stage of its development, demands further investigations based upon the stability of dislocation structure, originating during fatigue failure.

5. Summary

Changeability of the hysteresis loop parameters in the function of the loading cycles number causes that the values of the material data used during fatigue life calculations depend on the life period in which they were determined. In consequence the methods of fatigue life calculations based on the assumption of cyclic properties stabilization during variable loadings raise doubts.

The small changes of the plastic strain energy ΔW_{pl} in the function of loading cycles number observed during the tests are the confirmation of the literature data [3]. It results from them that energy parameter is the least sensitive to the changes of cyclic properties of material. It is motivated by the fact that the energy parameter takes into account mutual interactions of both stress and strain. Because of that fact it is believed that an energy approach to fatigue process is more complete than strain or stress description.

Changes of material properties under variable loading are influenced by dislocation structure. With the increase of fatigue damage degree dislocation density increases too, which results in cyclic hardening.

Presently there exist many models of the course of material hardening mechanism. One of the best known is the Granato-Lücke mechanism [5]. Analysis of this mechanism and obtained tests results allow to conclude that observed cyclic hardening of brass specimens was the result of creating the obstacles for dislocation movement, with their mutual interaction.

Obtained results confirm literature reports that pure metals and one-phase alloys after annealing can undergo cyclic hardening [6]. Hardening of α phase was confirmed by the fatigue tests (Fig. 13).

In the boundary layers of the specimens with the increase of the loading cycles number the creep lines turn into so called permanent creep strands which are different from the creep strands originating during static plastic strain. Permanent creep strands in the grain structure placed themselves on the surface of the specimen. Formation of the permanent creep strands resulted in the change of properties, decreasing of the plasticity limit also included, since inside of them intensive irreversible softening took place [6].

In literature there are also reports stating that plastic strain amplitude in the permanent creep strands is higher than in groundmass. It is the proof of existing diversified dislocation structure in the permanent creep strands and groundmass.

Decreasing of the dislocation density in the permanent creep strands results in the softening of the material under cyclic loading. So the explanation of the softening can refer only to the sub-boundary layer of the specimen, to the depth of only one or several grains. Performed investigations proved that all specimens under fatigue tests underwent the process of hardening in the whole cross-section.

On the base of the performed analysis of obtained results the following conclusions were formulated:

1. The course of the chosen hysteresis loop parameters in the fatigue test depends on the strain level. The values of these loop parameters, in turn, depends on the degree of fatigue damage.
2. Plastic strain energy ΔW_{pl} in the function of the loading cycles number is the least sensitive parameter to the changes of cyclic properties of CuZn37 brass.
3. Microstructure of the surface of the fatigue specimens presented the features of the plastic strain.
4. Acceptance in the tests of one – phase brass contributed to the partial explanation of the phenomena taking place during fatigue tests of the material with the use of light microscope and scanning electron microscope (SEM).

References

- [1] Tucker, L.E., *A Procedure for Designing Against Fatigue Failure of Notched Parts*, Society of Automotive Engineers, Inc., SAE Paper No 720265, New York 1972.
- [2] PN-84/H-04334: *Badania niskocyklowego zmęczenia metali*.
- [3] Kocańda, S., Kocańda, A., *Niskocyklowa wytrzymałość zmęczeniowa metali*, PWN Warszawa 1989.
- [4] Kocańda, S., *Zmęczeniowe pękanie metali*. WNT, Warszawa 1985.
- [5] Kocańda, S., Kocańda, D., *Fraktografia. Badania mikrobudowy przełomów zmęczeniowych w latach 1954-2004*, Przegląd mechaniczny R.LXIV, Z1 (2005).
- [6] Wyrzykowski, J.W., Pleszakow, E., Sieniawski, J., *Odkształcenie i pękanie metali*, WNT, Warszawa 1999.
- [7] Ramberg, W., Osgood, W.R., *Description of stress-strain curves by three parameters*, NACA, Tech.Note, No. 402, 1943.

The paper was elaborated on the base of the research studies BS-4/2002 under the title "Experimental methods in the fatigue tests of the materials and construction elements" which were carried out in the Faculty of Mechanical Engineering in 2009.



NUMERICAL SIMULATION FOR ECM MACHINING OF NONLINEAR SHAPED SURFACES

Tomasz Paczkowski

*University of Technology and Life Sciences in Bydgoszcz
Faculty of Mechanical Engineering
ul. Prof. S. Kaliskiego 7, 85-789 Bydgoszcz, Poland
tel.: +48 52 3408747, fax: +48 52 3408245
e-mail: tompacz@utp.edu.pl*

Abstract

In this work there has been presented a theoretical analysis of ECM machining curvilinear surfaces. Electrochemical machining with the use of a tool electrode (ECM.S) is one of the basic and most widely used electrochemical technological operations for machining tools and machine parts.

Physical phenomena occurring in the inter electrode gap have been described with partial differential equation system resulting from the balance of mass, momentum, and energy of the electrolyte flowing in the gap.

The equations formulated in the work describing the curvilinear surface shape evolution and the electrolyte flow (mixture of liquid and gas) in the gap, were simplified and then solved in part analytically, in part numerically. For complex machining parameters there have been performed calculation illustrated with distribution charts: volume fraction, temperature, gap thickness, mean flow velocity, pressure and current density.

Keywords: computer simulation, electrochemical machining, electrolyte flow

1. Introduction

Electrochemical machining with the use of a tool-electrode is today one of the basic operations of electrochemical machining technology for machine elements and other mechanical devices.

In the constant process the tool-electrode (TE) performs most often a translatory motion towards the machined surface. Electrolyte is supplied to the inter electrode gap with high velocity causing carrying away erosion products from the inter electrode space. These are mainly particles of hydrogen and ions of the digested metal. Thus, in such conditions we obtain multi-phase, in general, three dimensional flow [7].

Hydrodynamic parameters of the flow and the medium properties determine the processes of mass, momentum and energy exchange within the inter electrode gap. Properly matched they prevent from occurrence of cavitation, critical flow and volume fraction [1,6,8,9].

The above mentioned processes have significant influence on the electrochemical machining velocity and application properties of the machined surface [3,4,11].

Modeling of ECM involves: determination of the inter electrode gap thickness changes, the machined surface shape evolution in time, and distribution of physico-chemical conditions in the machining area, such as: static pressure distribution, electrolyte flow velocity, temperature and volume fraction [3,10].

The purpose of this work is a theoretical analysis of ECM of curvilinear surfaces on the example of a forming surface a turbo machine blade (Fig.1).

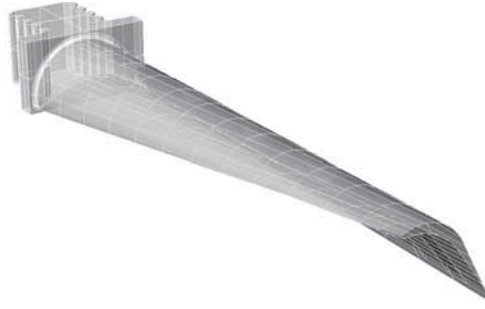


Fig. 1. Turbo machine blade

2. Mathematical model of the ECM process

2.1. Equation describing real shape change of the machined surface

The shape change of the machined surface caused by ECM machining can be described by an equation [3,5]:

$$F_t + k_v J_{A_i} F_i = 0, \quad (1)$$

with an initial condition $F(i, j, 0) = F_0$

here: $J_A = J(i_A, j_A, t)$ - current density distribution on the work piece (WP)-anode,

k_v - coefficient of electrochemical machinability

$F_0(i, j) = 0$ - equation describing the shape of the WP-anode in the initial time of machining

$F(i, j, t) = 0$ - equation describing the actual anode surface.

Current density is described by Ohm's law [3,5]:

$$J_i = -\kappa \left(u|_A \right)_i, \quad (2)$$

here: u - electrical potential,

κ - electrical conductivity.

The movement velocity of the anode surface points described in an open way by the equation $y = Y_A(i, t)$ is expressed by the formula:

$$v_j = Y_{A,t} = \frac{-v_n}{\cos(n_A, y)}, \quad (3)$$

here:

$$\frac{1}{\cos(n_A, j)} = \sqrt{1 + (Y_{A,i})^2}. \quad (4)$$

The anode velocity v on the basis of Faraday's law is equal :

$$v_{ni} = k_v J_{A,i}. \quad (5)$$

After introducing dependences (4), (5) and (2) to the equation (3) the equation describing the surface shape change assumes a form:

$$Y_{A,i} = \kappa k_v (u|_A)_i \sqrt{1 + (Y_{A,i})^2} . \quad (6)$$

In the inter electrode gap the electrical field is quasi – stationary, time functions as a parameter, thus, the potential distribution can be described by the following equation:

$$(\kappa u_{,i})_{,i} = 0 \quad (7)$$

with boundary conditions:

- on the tool - cathode $j = f(i) + V_f t ;$
- on the WP - anode $y = F(i, t); u(F) = U - E$
- on the insulator surfaces $u_{,n}|_{GI} = 0$

Assuming linear distribution of the electrical field potential along interelectrode gap (IEG) the current density in the anode, in a locally orthogonal coordinate system (Fig.3) is expressed in the following way [3]:

$$j_A = \kappa_0 \Phi_{TG}^{-1} \frac{U - E}{S} . \quad (8)$$

Function Φ describes changes of the electrolyte conductivity in the inter electrode gap and is determined from the balance of voltage fall along the path h (Fig.2) [3,4]:

$$\Phi_{TG} = \frac{1}{h} \left[\int_0^h \frac{dy}{(1 + \alpha(T - T_0))(1 - \beta)^{3/2}} \right] , \quad (9)$$

where: h - is the smallest distance of a given A point on WP from TE surface.

Introducing the dependency (8) to the equation (6) in an orthogonal kartezyan system (Fig.1) the searched for velocity of the anode points movement is now described by the dependency:

$$\frac{\partial Y_A}{\partial t} = k_v \kappa_0 \Phi_{TG}^{-1} \frac{U - E}{h} \sqrt{1 + \left(\frac{\partial Y_A}{\partial X} \right)^2 + \left(\frac{\partial Y_A}{\partial Z} \right)^2} . \quad (10)$$

With the initial condition $y = Y(x)$ for $t = 0$

In order to describe the work piece shape evolution on the basis of the equation (10) it is necessary to specify the temperature rise distributions and the volume fraction in the electrolyte.

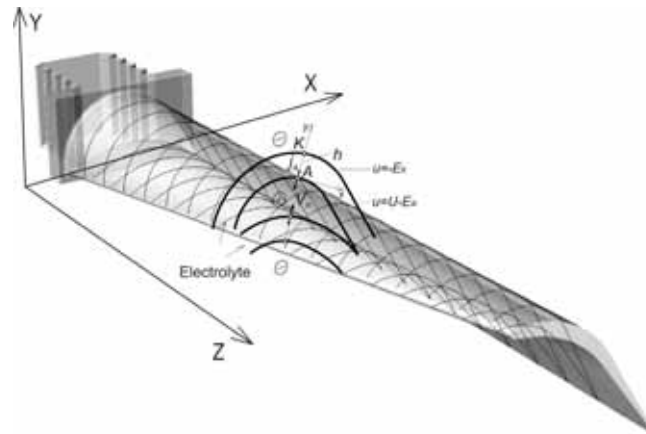


Fig. 2. Scheme of electrochemical machining

2.2. Mixture flow equations in the inter electrode gap

In order to determine the temperature distribution in the inter electrode gap and the volume fraction there have been formulated motion equations resulting from the mass, momentum and energy conservation laws for the considered mixture:

Equations of the flow continuity, respectively, for the electrolyte and hydrogen:

$$\rho_e v_{i,t} + (\rho_e v_i)_{,i} = 0, \quad (11)$$

$$\rho_h v_{i,t} + (\rho_h v_i)_{,i} = J \eta_H k_H h^{-1}, \quad (12)$$

where:

- $\rho_e = (1 - \beta) \rho_e^0$ - electrolyte density,
- $\rho_h = \beta \cdot \rho_h^0$ - hydrogen density,
- v_i - velocity of components,
- k_H - electrochemical equivalent of hydrogen,
- η_H - current efficiency of the hydrogen generation,
- β - volume fraction.

In the equation (11) the erosion products have been neglected assuming that they are negligibly small [2].

Equations of the momentum for the hydrogen and the electrolyte have the form:

$$\rho_e (v_{i,t} + v_j v_{i,j}) = -p_{e,i} + \tau_{ij,j}, \quad (13)$$

$$\tau_{ij} = \mu_e (v_{i,j} + v_{j,i}), \quad (14)$$

$$\rho_H (v_{i,t} + v_j v_{i,j}) = -p_{H,i} + \tau_{ij,j}, \quad (15)$$

$$\tau_{ij} = \mu_H (v_{i,j} + v_{j,i}), \quad (16)$$

here:

- p_e - electrolyte pressure,
- p_H - gas pressure,
- μ_e - dynamic electrolyte viscosity,
- μ_H - dynamic hydrogen viscosity.

The equation of energy for the electrolyte has the form:

$$(\rho_e T_e)_{,i} + (\rho_e T_e v_i)_{,i} = a T_{,ii} + \frac{Q}{c_p}, \quad (17)$$

where:

- T_e - electrolyte temperature,
- $a = \frac{\lambda}{\rho c_p}$ - thermal diffusivity,
- $Q = \frac{j^2}{\kappa}$ - Joule's heat, $j = \frac{\kappa \cdot U_c}{h}$,
- U_c - potential difference.

In order to solve the equation system (11)÷(17) the following simplifying assumptions have been introduced :

- the electrolyte flow is stationary, two-dimensional and laminar
- pressure $p_e = p_H = p$,
- volume fraction $\beta = \beta(x)$
- gap thickness is small in comparison with the inter electrode gap length ($h \ll L$).

Adding the sides of motion equations of both phases, neglecting the flow inertia forces and terms containing ρ_H/ρ_e ($\rho_H/\rho_e \ll 1$), the mixture motion equation system (13)÷(17) in a two-dimensional orthogonal coordinate system is now as follows :

$$\frac{\partial}{\partial x}(\rho_e v_x) + \frac{\partial}{\partial y}(\rho_e v_y) = 0, \quad (18)$$

$$\frac{\partial}{\partial x}(\rho_h v_x) + \frac{\partial}{\partial y}(\rho_h v_y) = j \eta_H k_H h^{-1}, \quad (19)$$

$$\frac{\partial^2 v_x}{\partial y^2} = \frac{1}{\mu} \frac{\partial p}{\partial x}, \quad (20)$$

$$\frac{\partial p}{\partial y} = 0, \quad (21)$$

$$v_x \frac{\partial T}{\partial x} + v_y \frac{\partial T}{\partial y} = a \frac{\partial^2 T}{\partial y^2} + \frac{Q}{\rho_e c_p}. \quad (22)$$

Equations (18, 22) should meet the following boundary conditions :

- for velocity
 $v_x, v_y = 0$ for $y = 0, y = h$
- for pressure
 $p = p_o$ for $x = x_o$
- for temperature
 - on the walls:
 $T = T_0$ for $x \geq x_i$ i $y = 0$ i $y = h$
 - on the inlet:
 $T = T_i$

where:

x_i - the coordinate of IEG inlet,

x_o - the coordinate of IEG outlet,

T_0 - electrode temperature, T_i - temperature on the inlet.

Solving the equation system (18)÷(21) there have been received distributions of velocity, pressure, and volume fraction in the inter electrode gap in the following form:

$$v_x = \frac{6Q_v}{h^3} (y^2 - yh), \quad (23)$$

$$p = p_w - 12\mu_e Q_v (A(x) - Aw), \quad (24)$$

$$A(x) = \int \frac{dx}{h^3}, \quad (25)$$

$$\beta = \frac{\eta_H k_H R_H}{\mu_H} \frac{\kappa_0 \Phi_{TG}^{-1}(U - E)}{Q_V h} \frac{T}{p} x, \quad (26)$$

$$\mu_e = \mu_0 (1 + \beta m) e^{-b(\Delta T)}, \quad (27)$$

here: Q_V – volume rate.

The equation (22) describing the temperature distribution in the gap has been numerically solved with the use of finite difference methods and with the use of the above specified formulas.

3. Numerical model of the ECM process

Determination of the machined surface shape evolution (anode) in time is described by equation (10) describing the real shape evolution of the machined surface.

For numerical calculations there have been performed WP and TE digitization for the cases:

- shaping surface in a global system of perpendicular coordinates described in the following way:

$$x_i = x_0 + i \Delta x,$$

where:

$$i = 0, 1, 2, \dots, I,$$

$$\Delta x = \frac{L}{i},$$

L – WP length towards x axis,

- turbo machine blade through approximation of the surface by curves. In this way a set of TE_k , WP_k curve pairs was received which later were described with assigned accuracy in a global coordinate system by points (Fig. 3),

$$x_i = \sum_{i=1}^i \Delta x_i, \quad (28)$$

where: $i = 0, 1, 2 \dots I$.

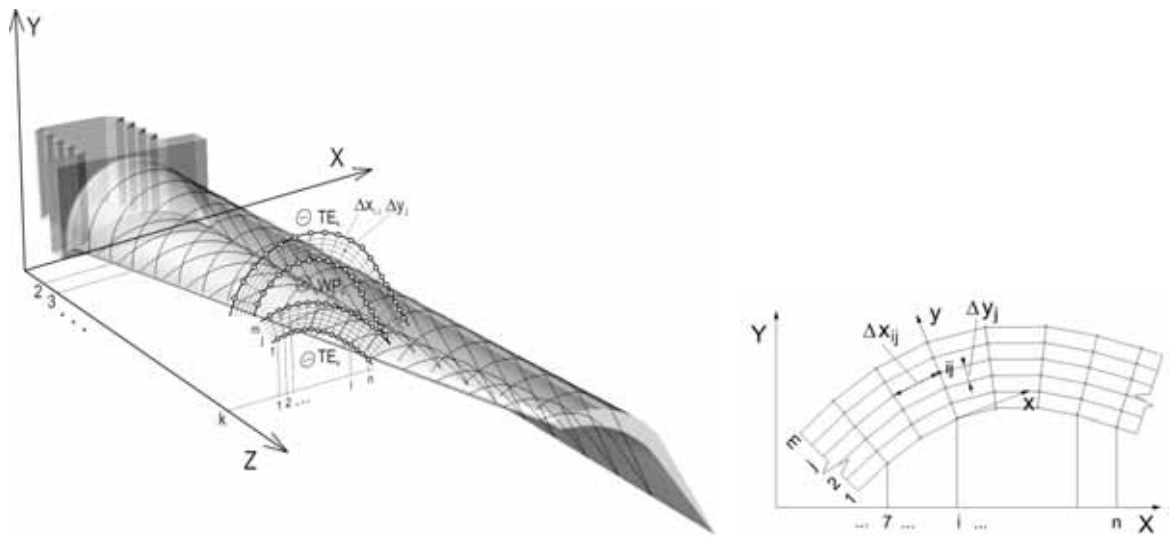


Fig. 3. Digitization IEG

After digitization of the TE and WP surfaces the demanded solution of the equation system describing the mathematical model of the turbo machine blade shape is presented by the computer simulation algorithm of the ECM process (Fig. 4)

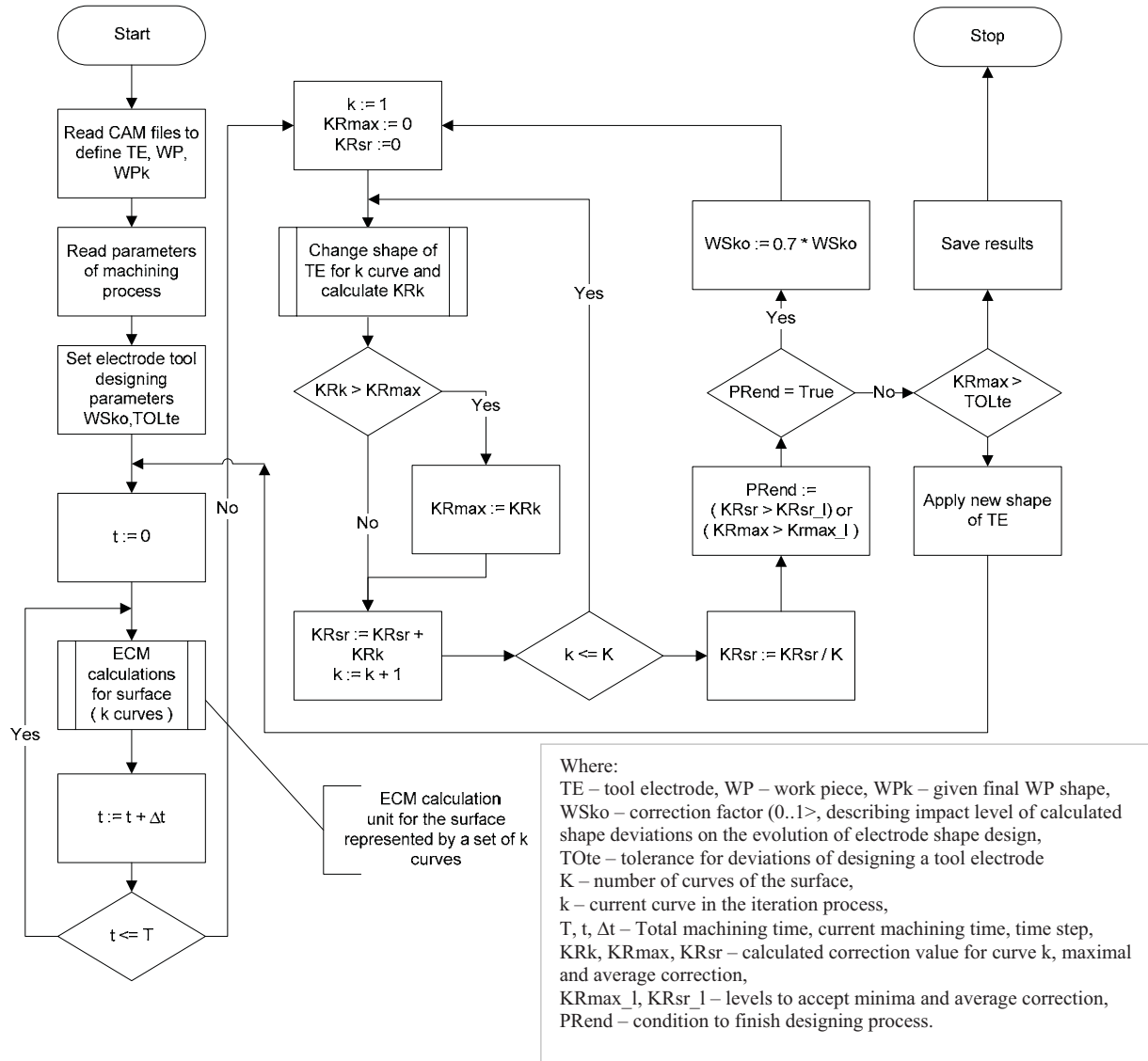


Fig.4. Numerical algorithm simulation of ECM with the ER shape designing procedure

4. Result study

In the calculations it was accepted that the inter electrode gap would be supplied with a constant value of the electrolyte flow volume and the electrolyte would be passivating. calculations were performed until obtaining a stationary state.

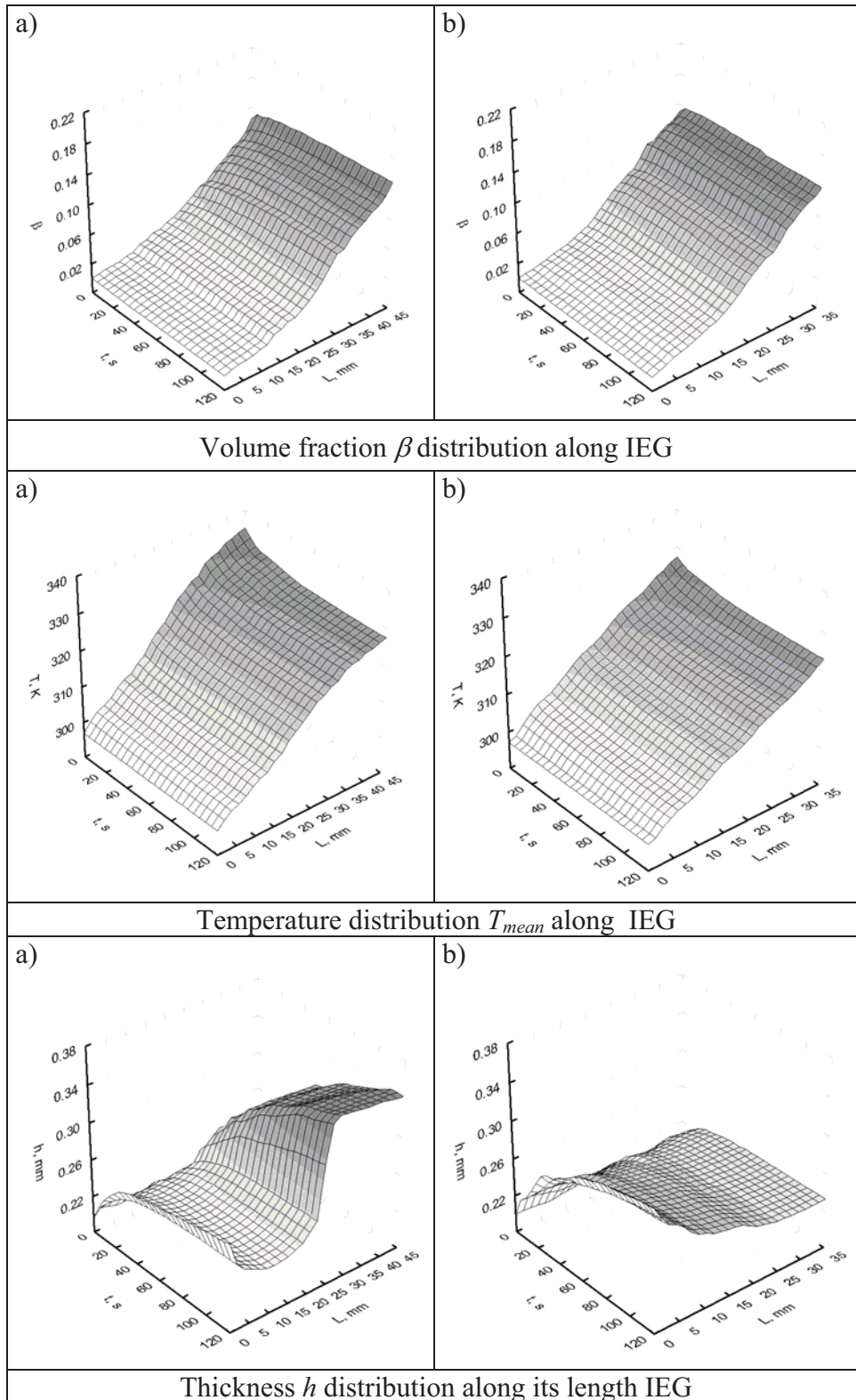
More important machining parameters:

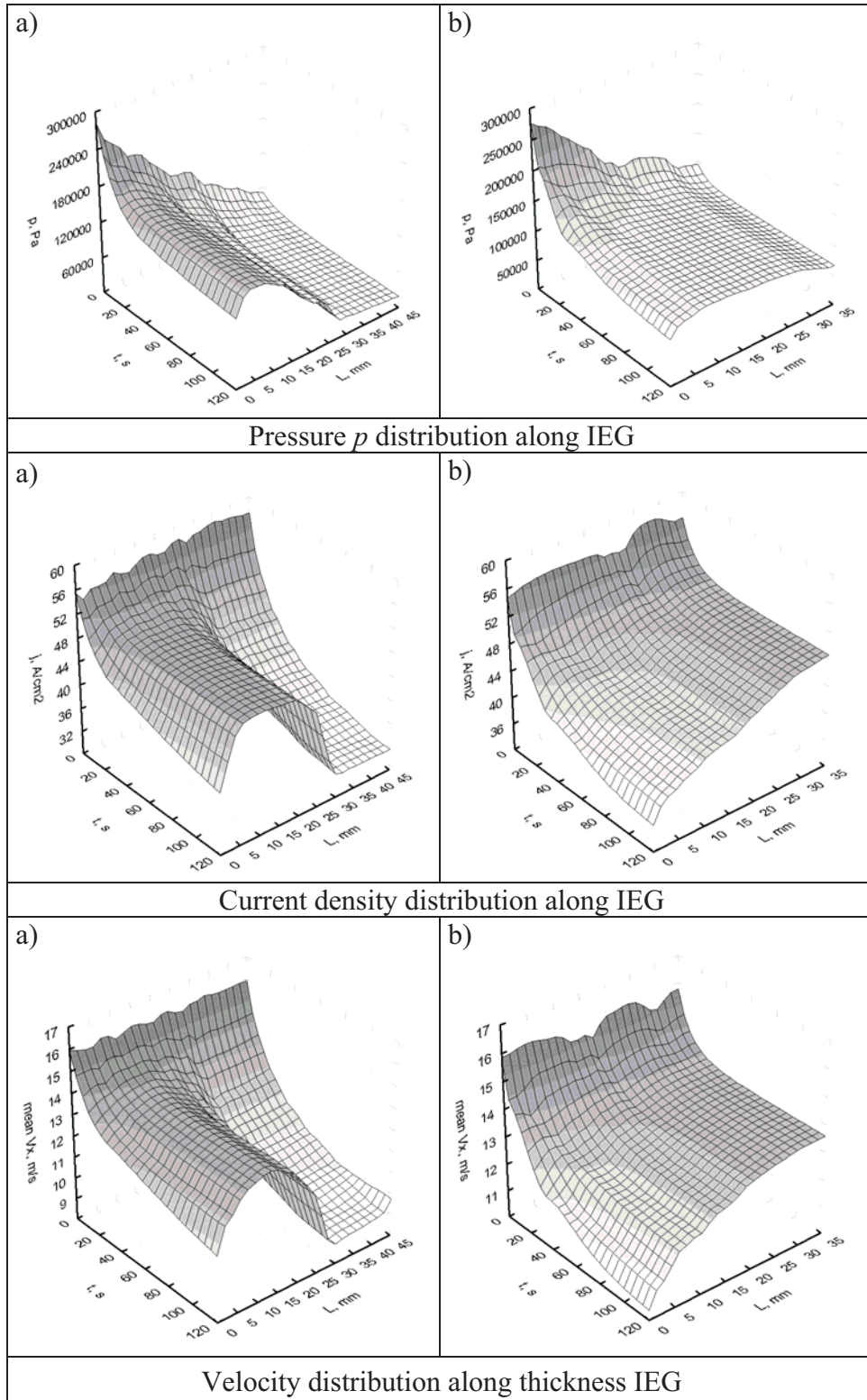
- initial gap - 0.2 mm,
- feed motion velocity TE - 0.0125 mm/s,
- interelectrode voltage - 15 V,

- material WP - WNL,
- material TE - 0H13N9.

Received numerical calculation results have been illustrated in charts of pictures in Tab. 1.

*Tab.1 Distributions of selected physical quantities for:
a) blade upper profile, b) blade lower profile*





In charts of Tab. 1 there have been shown calculation results of the volume fracture, temperature inter electrode gap thickness, pressure, flow density and mean flow velocity distributions for the upper and lower blade profiles of a turbo machine (Fig.1) as well as for the forming surfaces.

From the included charts the following conclusions generally correct for both analyzed curvilinear surfaces can be formulated:

- distribution of filling the inter electrode gap with gas is non-linear,

- the temperature of electrolyte and hydrogen mixture rises gradually along the interelectrode gap in a given machining time,
- local thicknesses of the inter electrode gap for the upper and lower blade profiles are changing. It results from the erosion velocity variability, TE profile angle of inclination to the machining direction and the physical conditions variability in the inter electrode gap
- distributions of pressure, flow density, and mean velocity along the gap result from the gap thickness changes and differ qualitatively for both surfaces of the blade profiles.
- Distributions of physical quantities and the length IEG for both blade profiles differ significantly from each other. Thus mathematical modeling of the ECM process seems to be essential for selection of similar conditions for the blade upper and lower profiles.

It should be emphasized that the solutions have been obtained through analytical and numerical integration of complex partial differential equations.

Further simulation and experimental tests will allow for quantitative verification of the accepted mathematical model.

References

- [1] Davydov, A.D., Kozak, J., *Wysokoskorostnyje elektrochimicheskoje formoobrazowanie*, Nauka, Moskwa, 1990.
- [2] Dąbrowski, L., *Podstawy komputerowej symulacji kształtowania elektrochemicznego*, Prace Naukowe, Mechanika z. 154, Wydaw. Politechniki Warszawskiej, Warszawa, 1992.
- [3] Kozak, J., *Kształtowanie powierzchni obróbką elektrochemiczną bezstykową (ECM)*, Pr. Naukowe PW, Mechanika nr 41, Wydawnictwo Politechniki Warszawskiej, Warszawa. 1976.
- [4] Kozak, J., *Mathematical Models for Computer Simulation of Electrochemical Machining Process*, Journal of Materials Processing Technology, Vol. 76, 1976.
- [5] Kozak, J., *Zagadnienie geometrii elektrod w procesie kształtowania elektrochemicznego*, Arch. Bud. Maszyn, t.XIV, z.2, 1967.
- [6] Łubkowski, K., *Stany krytyczne w obróbce elektrochemicznej*, Prace naukowe, Mechanika, z.163, Oficyna Wydawnicza PW, Warszawa, 1996.
- [7] Ruszaj, A., *Niekonwencjonalne metody wytwarzania elementów maszyn i narzędzi*, IOS Kraków 1999.
- [8] Paczkowski, T., Sawicki, J., 2003, *Wpływ koncentracji wodoru w elektrolicie na ewolucję kształtu przedmiotu obrabianego*, Wybrane zagadnienia obróbek skoncentrowaną wiązką energii, Praca zbiorowa pod red. Michała Styp-Rekowskiego, BTN, Bydgoszcz.
- [9] Paczkowski, T., Sawicki, J., *Modelowanie ewolucji kształtu powierzchni łopaty w obróbce elektrochemicznej elektrodą drgającą roboczą*, Przepływowe maszyny wirnikowe, zbiór prac IX konferencji pod red. E. Oczosia, Rzeszów 2003.
- [10] Paczkowski, T., *Modelowanie obróbki ECM powierzchni o zarysie krzywoliniowym*, Inżynieria Maszyn, zeszyt 2-3, 2009 s. 64-73.
- [11] Paczkowski, T., Zdrojewski, J., *System komputerowy dla obróbki ECM krzywoliniowych powierzchni kształtowych*, Inżynieria Maszyn, zeszyt 2-3, 2009 s. 74-81.



ANSYS-POLYFLOW SOFTWARE USE TO SELECT THE PARISON DIAMETER AND ITS THICKNES DISTRIBUTION IN BLOWING EXTRUSION

Karol Pepliński, Arkadiusz Mozer

*University of Technology and Life Sciences
ul. S. Kaliskiego 7, 85-789 Bydgoszcz, Poland
tel.: +48 52 3408224, fax: +48 52 3408222
e-mail: karolpep@utp.edu.pl*

Abstract

The blowing extrusion in mould is one of the most widely used techniques for the production hollow plastic product example: bottle, cosmetics container, fuel tanks etc. A significant factor in the design stage of new blowing product is the selection initial parison shape in order to obtain the best distribution of final wall thickness in bottle. In this case using Ansys-Polyflow software is very helpful. This paper presents the blowing container Polyflow simulation with high-density polyethylene (Borealis, BS 2541) under isothermal and non-isothermal conditions. In the present work was showed the impact of the initial parison diameter and their geometry distribution onto final wall thickness in the sample container. This series of numerical simulation with parison optimization was showed that initial parison diameter and geometry have crucial importance for uniform final wall thickness distribution and minimal bottle mass. Eleventh cases of blowing parison were considered. Initial parison diameter was 14 mm and final 34 mm (step 2 mm). Optimizing the thirty milimeters diameter parison profile thickness for allowed to eliminate excessive thinning in the corners of container wall and get minimal container weight. An established criterion for a minimum wall thickness (1 mm) in the final product was achieved.

Keywords: *blowing extrusion, non-isothermal conditions, optimization the parison profile thickness, Ansys-Polyflow simulation, minimal container weight*

1. Introduction

One of the areas of technique characterized the last three decades the dynamic development is the containers manufacturing technology using plastics. Result of this development is to significantly increase the production quantity of containers, including large blowing parts [13]. Already in 2000, the number of blown bottles to beverage industry in the world has exceeded 10 billion units [10]. Currently, this number is much higher. In 2008 in Europe processed 60 million tones of plastics, including up to 38% in the production of packaging [15]. These data show that the manufacturing of packaging technology, in particular extrusion blow molding process, is an important direction of development of polymer processing. Blowing extrusion in the mold are the basic plastics processing methods used to manufacturing packaging polymer, such as: beverages, cosmetics, chemical products or more complex structures such as tanks for liquid fuels [11].

In order to maintain the required mechanical properties and the criterion of a minimum plastic consumption for blowing product requires close monitoring in many aspects. One of the final aspect is the ending wall thickness distribution in the product which depends primarily on the

geometry and thickness distribution of the parison or pre-container [2,7]. Typically in industrial conditions required distribution of parison thickness is obtained by the trial and error method. However, this process is tedious and its results largely depend on the experience of workers. Moreover, the time and cost of obtaining satisfactory results is usually very high. Helpful solution is to use CAE software Ansys-Polyflow. The software makes it possible to determine the behavior of the plastics during the process, identify areas where there may be the biggest container wall thinning, which reduce the mechanical properties of the product and ultimately to suggest the appropriate geometry and parison thickness distribution in order to obtain a product of given parameters [3–5].

This article is a continuation of the research presented in [10], where for a given parison geometry were done two simulations under isothermal conditions, including one optimization of initial parison profile thickness.

2. Research aims

The information contained in the literature [1,6,8,9,12] shows that there are not possible to obtain extrusion blowing products with a uniform wall thickness distribution on the basis of parison with constant thickness. Additionally parison diameter influence on final product feature. In this case, the selection of parison diameter and wall thickness distribution was to be the most equitable form. It is not possible to do intuitively, but it can be done with available Polyflow software.

The aim of this paper is to stage a series of CAE simulations of blowing parison in non-isothermal conditions. The final effect will be to find parison diameter and geometry, providing the product of a minimum wall thickness 1 mm, while consuming minimal plastics to final product. Also determine the impact temperature distribution along the variable thickness parison on the final bottle thickness is taken into account. Simulations are carried out using Ansys-Polyflow 12.1 software.

3. Process description

The object considered in the Polyflow simulation is axially symmetric bottle, whose shape and dimensions are discussed in the publication [10]. Due to the complexity of the modeling process, blowing in the environment Polyflow, assumptions and methodology of the procedure was described in general terms. Figure 1 illustrated the initial configuration of extruded parison and mold cavity position adopted for the simulation run. It was assumed that the parison material is extruded, while the mold is still open. Both halves of the mold are located $s = 36$ mm to each other (Fig. 1 a,b). Parison height is $H = 154$ mm and initial thickness is $g = 2$ mm. Diameters in following simulations changed every $d = 2$ mm to $D = 14 \div 34$ mm. Material used in the simulations is high density polyethylene HDPE, which have a temperature of $T = 190$ °C, viscosity $\mu = 6622$ Pa•s and density $\rho = 0.96$ g/cm³ [14]. Due to the symmetry of the analyzed container, blow simulations can be carried out for the geometry quarter (Fig. 1c). This significantly cut down the time of calculation. The mold and parison model has been imposed on the finite element mesh in ANSYS Meshing module. The run of the whole process starts with the closure of the mold, where the final stage of closing the parison and plastic is welded only in at the bottom or top and bottom parts. It depends on the diameter of the parison. The two mold halves are moving with a velocity $v = 50$ mm/s, and the final welding of parison is followed with slow motion mold. Then blowing pressure is accompanied with a value of $p = 0.9$ MPa and running until the bottles is blown. Total time blowing process simulation is 1 second. More data on the assumptions for the simulation are contained in table 1.

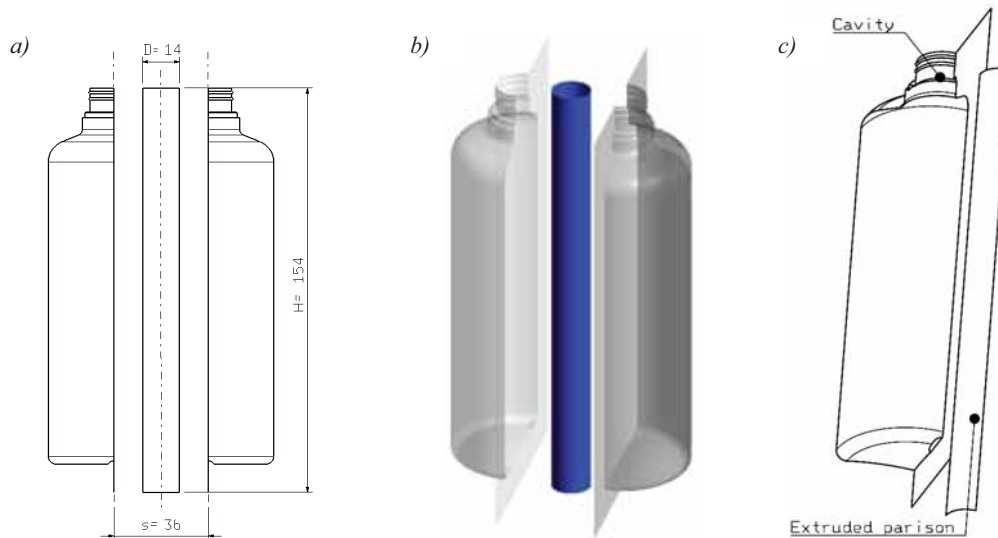


Fig. 1. Considered model: a) mold and parison position, b) CAD model, c) quarter of the mold and parison

4. Simulation results and their analyses

Realized simulations generated series of results, which the selected part is presented below. Figure 2 shows a comparison the distribution of thickness bottles obtained from the parison with a diameter 14 mm in isothermal and non-isothermal conditions, along a given line of measurement. Performed simulations for the initial constant parison thickness with and without taking into account non-isothermal conditions showed no significant differences in the value of the bottle wall thickness distribution. Significant differences were not observed also for the optimized parison, but there is a visible improvement the distribution of wall thickness in bottom area of container compared to the constant initial thickness of parison.

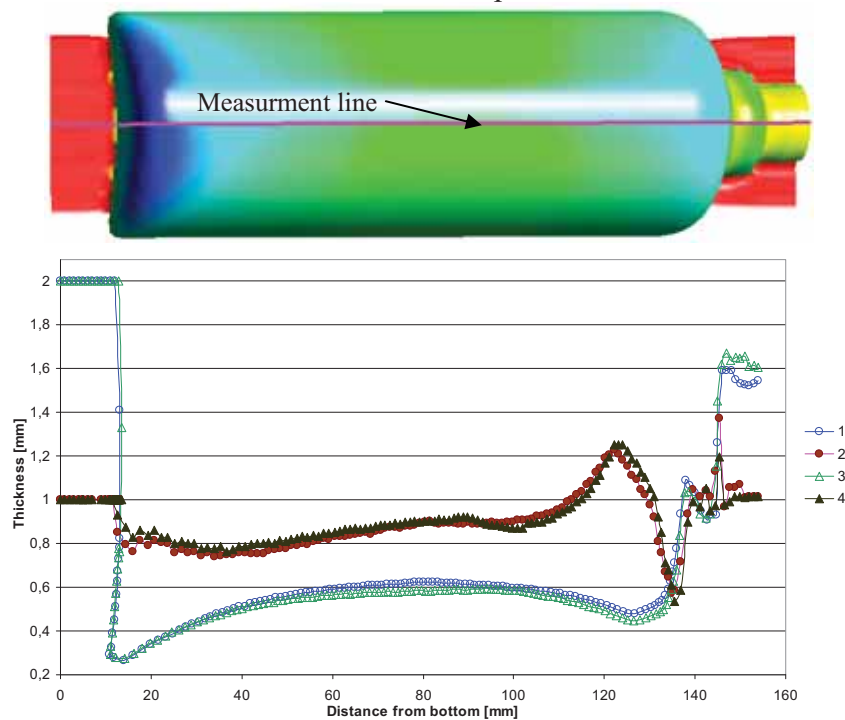


Fig. 2. Comparison part thickness distribution along the measurement line: 1 – initial part thickness under isothermal conditions, 2 – optimized part thickness under isothermal conditions, 3 – initial part thickness under non-isothermal conditions, 4 – optimized part thickness under non-isothermal conditions

As a result of simulation research for exploration in diameter and profile parison thickness satisfies the posed conditions (minimum thickness of wall container is 1 mm at the smallest consumption plastic for the bottle) was obtained in a large number of results. Selected summary is shown in table 1. It is visible percentage distribution of wall thickness obtained for selected diameters of parison, and also gained bottle weight. The posed condition – minimum thickness of wall container 1 mm – fulfill only the simulations with number 12, 15 i 18, for which the initial distribution of parison thickness has been obtained by simulation optimization. Of the three cases, the smallest mass consumption of plastic for blow product obtained for the case of 12 (weight is 27.31 g). Analyzing the obtained results it can observe some dependence. With the increase parison diameter, the percentage bottle wall thickness of less than 1 mm, progressively decrease in subsequent simulations (1 const., 2–3 opty.). In turn, reverse trends reveal the results obtained by weight of bottles, whose value increases in subsequent simulations (1 const, 2-3 opty.), except that the diameters of (30, 32 and 34) mm. An exception may arise from the relationship between the parison diameter and the material waste obtained in the upper and lower zone of the bottle and also minimization the product thickness in these areas through optimizing simulation, where instead parison with a thickness of 2 mm in the lower zone of waste is a minimum thickness of 1 mm.

Tab. 1. Summary of the results obtained for the simulation for the variable diameters of parison: D = 14, 20, 26, 30 and 34 mm, where: const – initial constant thickness of parison g = 2 mm, 2 (opty.) – the first simulation using the optimized parison, 3 (opty.) – second simulation using the optimized parison

Name	Parison diameter [mm]	Type of simulation	Percentage distribution of bottle wall thickness [%]			Weight [g]
			Above 1 mm	Belowe 1 mm	Equal 1 mm	
1	14	1 (const)	17,14	80,44	2,42	13
2	14	2 (opty.)	30,03	58,26	11,71	20,96
3	14	3 (opty.)	41,98	28,18	29,84	22,53
4	20	1 (const)	21,5	77,32	1,18	18,58
5	20	2 (opty.)	34,88	47,84	17,28	23,29
6	20	3 (opty.)	33,9	8,36	57,74	24,69
7	26	1 (const)	39,51	27,35	33,14	24,15
8	26	2 (opty.)	39,76	14,88	45,36	24,83
9	26	3 (opty.)	38,65	1,47	59,78	25,14
10	30	1 (const)	80,6	11,42	7,98	27,87
11	30	2 (opty.)	44,49	3,39	52,12	27,45
12	30	3 (opty.)	44,41	0	55,59	27,31
13	32	1 (const)	85,63	7,57	6,8	29,73
14	32	2 (opty.)	46,48	3,02	50,5	29,14
15	32	3 (opty.)	45,27	0	54,73	29,07
16	34	1 (const)	88,62	6,34	5,04	31,58
17	34	2 (opty.)	52,75	2,86	44,39	30,32
18	34	3 (opty.)	52,07	0	47,93	30,28

Figure 3 summarizes the results of selected simulation blowing plastic parison with diameters 14 and 30 mm. Simulations were carried out in non-isothermal conditions for a parison with a constant thickness and optimized. It is noticeable here resolution to improve the distribution of bottle thickness after the optimization for parison diameter of 30 mm. Graphical display blowing container for two diameters is shown in Figure 4. For parison diameter 30 mm achieved the most desirable distribution of wall thickness in the final container. It was noted, however, double-wall thickening at the bottom of the container in the parting line (Fig. 4d).

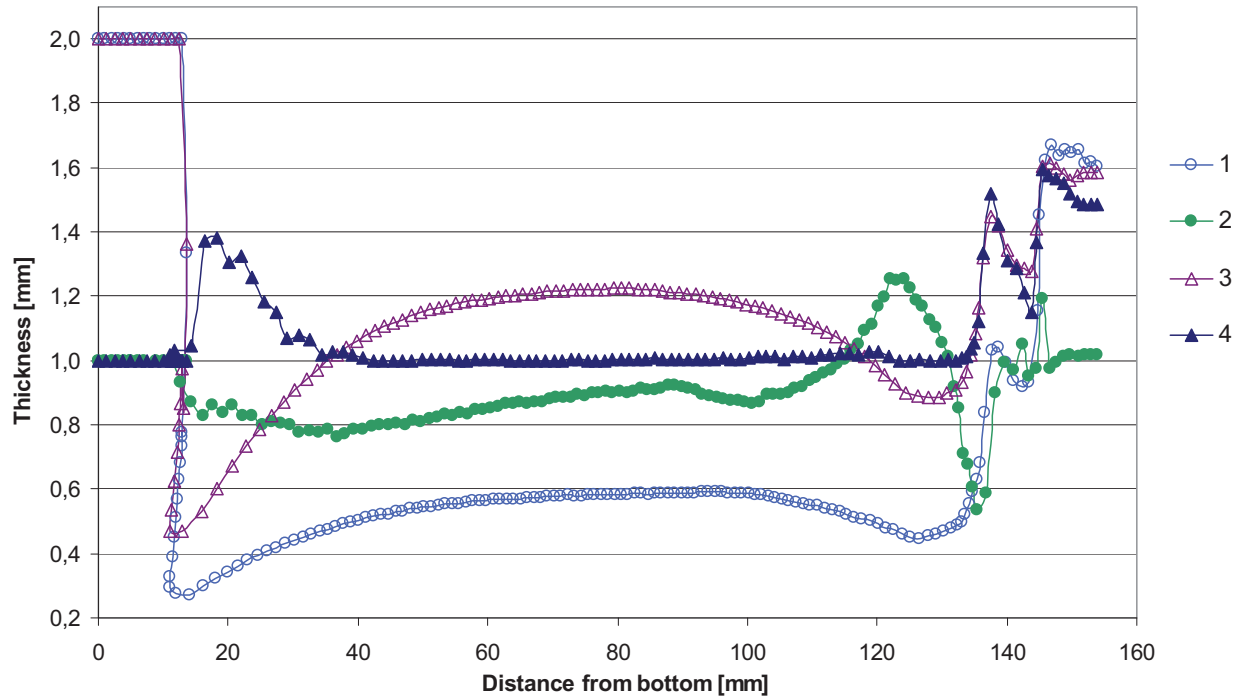


Fig. 3. Comparison part thickness distribution along the measurement line for three cases: 1 – parison with diameter 14 mm, 2 – optimized parison with diameter 14 mm, 3 – parison with diameter 30 mm, 4 – optimized parison with diameter 30 mm

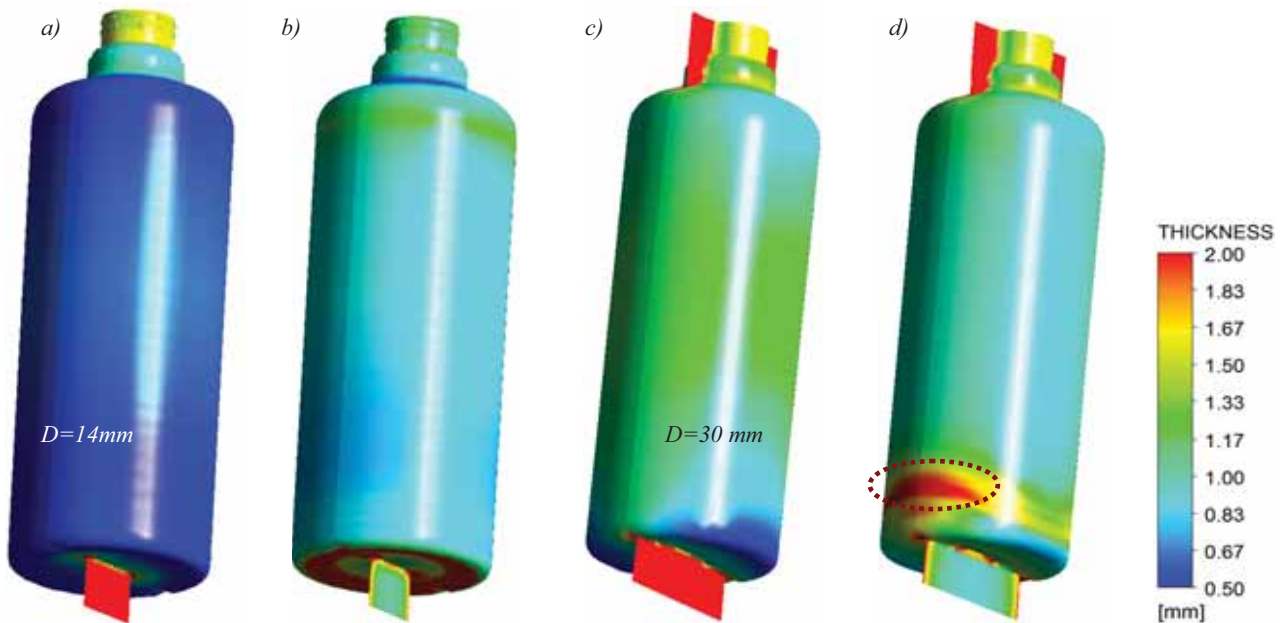


Fig. 4. Final part thickness distribution for parison with diameter 14 and 30 mm a) c) before optimizing, b) d) after optimizing

5. Final consideration and summary

For test cases most thin wall was observed in the final product of the edge bottle areas and the bottom, which is associated with the longest time parison wall deformation in these areas, also the largest plastic stretching in circumferential and longitudinal directions. It follows from this that the bottle wall thickness depends primarily on the shape and dimensions of the cavity mould and

varying degrees of individual areas stretching of parison and at different times of contact parison with the mold. Because that the shape of cavity mold is limited desired shape of the product, adjusting the final thickness profile of the container is only possible by obtaining appropriate parison thickness profile.

Performed blow molding simulation in the Polyflow environment allow creations container with improved performance characteristics, obtained as a result of a more even wall thickness distribution in the container. This is possible due to the selection of the proper parison diameter and their profile thickness. Polyflow simulation allows for minimizing the consumption of plastic on the product while retaining some structural assumptions such as the minimum wall thickness of container. Simulation could even be much more effective for blowing products with complex geometry.

References

- [1] Attara, A., Bhuiyan, N., Thomson, V., *Manufacturing in blow molding: Time reduction and part quality improvement*, Journal of materials processing technology, pp. 284–289, 2008.
- [2] Glenn, L. B., James, L., *Hollow Plastic Parts: Manufacture & Design*, Hanser Publisher, Munich 2004.
- [3] Huang, H.-X., Liao, M. *Prediction of parison swell in extrusion blow molding using neural network method*, Antec, pp. 745–749, 2002.
- [4] Huang, G.-Q., Huang, H.-X. *Optimizing parison thickness for extrusion blow molding by hybrid method*, Journal of Materials Processing Technology 182, pp. 512–518, 2006.
- [5] Huang, H.-X., Miao, Y.-S., Li D. *Numerical prediction and experimental validation of viscoelastic annular swell*, Advances in Polymer Technology, 25, pp. 259–269, 2006.
- [6] Norman, C. L., *Practical guide to blow moulding*, Smithers Rapra Technology, 2006.
- [7] Pepliński, K., *Badania wpływu warunków przetwórstwa na cechy wytworów wytłaczanych z rozdmuchiwaniami*, Rozprawa doktorska, UTP Bydgoszcz 2008.
- [8] Pepliński, K., Bieliński, M., *Ocena rozkładu grubości ścianki i odwzorowania powierzchni formy w pojemnikach wytłaczanych z rozdmuchiwaniami*, Inżynieria i Aparatura Chemiczna. 3, pp. 8-10, 2008.
- [9] Pepliński, K., Bieliński, M., *Ocena wybranych właściwości przetwórczych i użytkowych wytworów wytłaczanych z rozdmuchiwaniami*, pp. 115–118, Polska Akademia Nauk oddział w Lublinie, Komisja Budowy i Eksploatacji Maszyn, Elektrotechniki i Budownictwa, Tom II, Lublin 2008.
- [10] Pepliński, K., Bieliński, M. *Polyflow software use to optimize the parison thickness in blowing extrusion*, Journal of Polish CIMAC, 4, Gdańsk 2009.
- [11] Pepliński, K., Bieliński, M., *Processing and functional properties of the containers prepared by blowing extrusion in variable processing conditions, and evaluation of yield and quality of the process*, Polimery, 54, nr 6, pp. 448–456, 2009.
- [12] Tanifuji, S.-I., Kikuchi, T., Takimoto, J.-I., Koyoma, K. *Overall numerical simulation of extrusion blow molding process*, Polymer Engineering and science, 40, 2000.
- [13] Żenkiewicz, M. *Metody wytwarzania pojemników rozdmuchiwanych z tworzyw wielkocząsteczkowych*, Polimery, 39, pp. 74–81, 1994.
- [14] www.borealisgroup.com.
- [15] www.plasticseurope.org, The Compelling Facts About Plastics 2009, Plastics Europe, Brussels – Belgium 2009.



DRY CONSTANT-LOAD STEEL ALUMINA GRINDING ENERGY PARTITION

Robert Polasik

*University of Technology and Life Sciences in Bydgoszcz
ul. Prof. S. Kaliskiego 7, 85-789 Bydgoszcz, Poland
tel.: +48 53 3408743
e-mail: robpol@utp.edu.pl*

Abstract

The paper deals with the new, original model of energy partition in dry constant-load steel grinding. Experimental setup, experiment conditions and analyses were shown and discussed in this article. New findings are presented for energy flux distribution and energy partition ratios. Energy partition ratios, determined during experiments were compared with theoretical values for constant, maximum energy carried away by the grinding chips e_{cc} , approximately 6 J/mm^3 . Original model, based on grinding chips stream temperature measurements was used for chips energy partition ratio R_c evaluation. Measurements were made using high-class testing equipment, e.g. Kistler 9257B dynamometer and Minolta-Land Cyclops optical pyrometer. A case study based on constant-load grinding C45 (AISI 1045) with alumina grinding wheels is used to illustrate the variability of energy carried away by the grinding chips. Developed model of grinding energy partition can be useful for on-line grinding control systems, especially for low specific grinding energy and high efficiency grinding processes.

Keywords: grinding, alumina, dry machining, energy, modeling

1. Introduction

Grinding requires higher specific energy than other conventional machining processes like milling, shaping, turning, etc. There is a long history of calculation of grinding energy partition ratios and temperatures of workpiece, grinding wheel, coolant, grinding chips and environment. Most important key findings in the development of grinding processes thermal modeling [2,5,6,7,9,10,11,12,13,14,17] are listed in Tab. 1.

Tab. 1. Chosen key findings in the development of grinding processes thermal modeling

Author, year of publ.	Model description
Jaeger (1942)	Sliding (moving) heat source
Outwater (1952)	Shear plane partition model
Hahn (1962)	Partition between workpiece and grain
Makino (1966)	Real contact length l_e tool with workpiece grater than geometrical contact length l_g
Des Russeaux (1970)	Fluid convection model
Malkin (1971/1974)	Limiting chip energy; $e_{cc} \cong 6 \text{ J/mm}^3$, energy partition models

Shafto (1975)	Coolant film boiling, coolant energy limitation
Snoyes (1978)	Triangular heat flux distribution
Werner (1980)	Energy flux to: wheel-workpiece-coolant-chips
Howes (1987)	Fluid film boiling (in contact zone)
Pettit (1988)	Energy partition between wheel and workpiece
Lavine (1989)	Conical (one dimensional) grain model
Rowe (1991)	Transient contact (heat transfer) model
Qi (1993)	Contact length based on contact forces
Rowe (1993)	Force/contact length model
Ueda (1993)	Active grains temperature
Rowe (1994/95)	Critical temperature (of thermal damage)
Tönshoff (1995)	Critical temperature for tensile
Rowe (1996)	Effective grain thermal properties
Rowe (2001)	Inclined heat source model – conditions of e_c value reduction

Most analyses were made for constant, maximum specific energy carried away by the grinding chips $e_{cc} = \text{const} \cong 6 \text{ J/mm}^3$. Rowe suggested [12] lower maximum chip energy for cast iron at 1500°C ; approx. $5,28 \text{ J/mm}^3$. Tso et al. [18] determined minimum specific chips energy $e_{cc} \cong 2 \text{ J/mm}^3$. Chips specific energy also as chip energy partition coefficient R_{chips} is important component of total grinding energy partition flux distribution, especially when grinding at low specific energies. Examples of workpiece energy partition coefficient, as other way of total energy partition, R_w values, determined by researchers was shown in Tab. 2.

Tab. 2. Examples of workpiece energy partition R_w values

Author, year of publ.	R_w values	Grinding conditions
Rowe, Pettit (1988) [14]	$\sim 52 \div 75 \%$	dry, for v_w $0,1 \div 0,9 \text{ m/s}$
Rowe (1995) [10]	$\sim 75\%$ for Al_2O_3	a_e $0 \div 14 \text{ }\mu\text{m}$, $v_c = 30 \text{ m/s}$, $v_w = 0,3 \text{ m/s}$, CCS
Shaw (1994, 1996) [15]	$\sim 80\%$ for Al_2O_3 or SiC $\sim 50\%$ for Al_2O_3 or SiC $\sim 5\%$ for Al_2O_3 or SiC	Dry form and finish grinding (FFG) FFG with coolant v.coarse, dry stock removal grinding (SRG)
Chang, Szeri (1997) [1]	$\sim 5\%$ for Al_2O_3 $\sim 30\%$ for Al_2O_3	creep-feed, water, $v_c = 18 \text{ m/s}$, $v_w = 1,2 \text{ mm/s}$, $a_e = 0,5 \text{ mm}$ creep-feed, oil, $v_c = 18 \text{ m/s}$, $v_w = 1,2 \text{ mm/s}$, $a_e = 0,5 \text{ mm}$
Wang, Fuh (1998) [19]	$\sim 25\%$ for Al_2O_3 , when $(v_s/v_w)^{0,5} > 100$	creep-feed, steel, oil, $v_c = 18 \text{ m/s}$, $a_e = 1 \text{ mm}$
Rowe (2001) [3]	$\sim 5 \div 75 \%$, Al_2O_3	Deep grinding, $v_c = 55 \text{ m/s}$, a_e $0,4 \div 1 \text{ mm}$, v_w $0,2 \div 0,3 \text{ m/s}$
Jin, Stephenson (2003) [4]	$\sim 5 \div 35 \%$, CBN	HEDG, steel, $v_c = 150 \text{ m/s}$, $a_e = 3 \text{ mm}$, oil, Q'_w $0 \div 1000 \text{ mm}^3/\text{mm s}$

2. Experimental

Experimental, original set up is illustrated schematically in Fig. 1.

Main testing equipment were:

- Kistler dynamometer 9257B connected with amplifier 5017 for grinding force components measurements,
- Cyclops 152A Minolta-Land pyrometer for grinding chips temperature measurements,
- Metex M-3860M multimeter for power consumption measurements.

Equipment listed above and other instrumentation were connected with AD/DA PCI1710 card (through connecting interface PCLD-8710) for signals values acquisition and grinding system control. Original software was made.

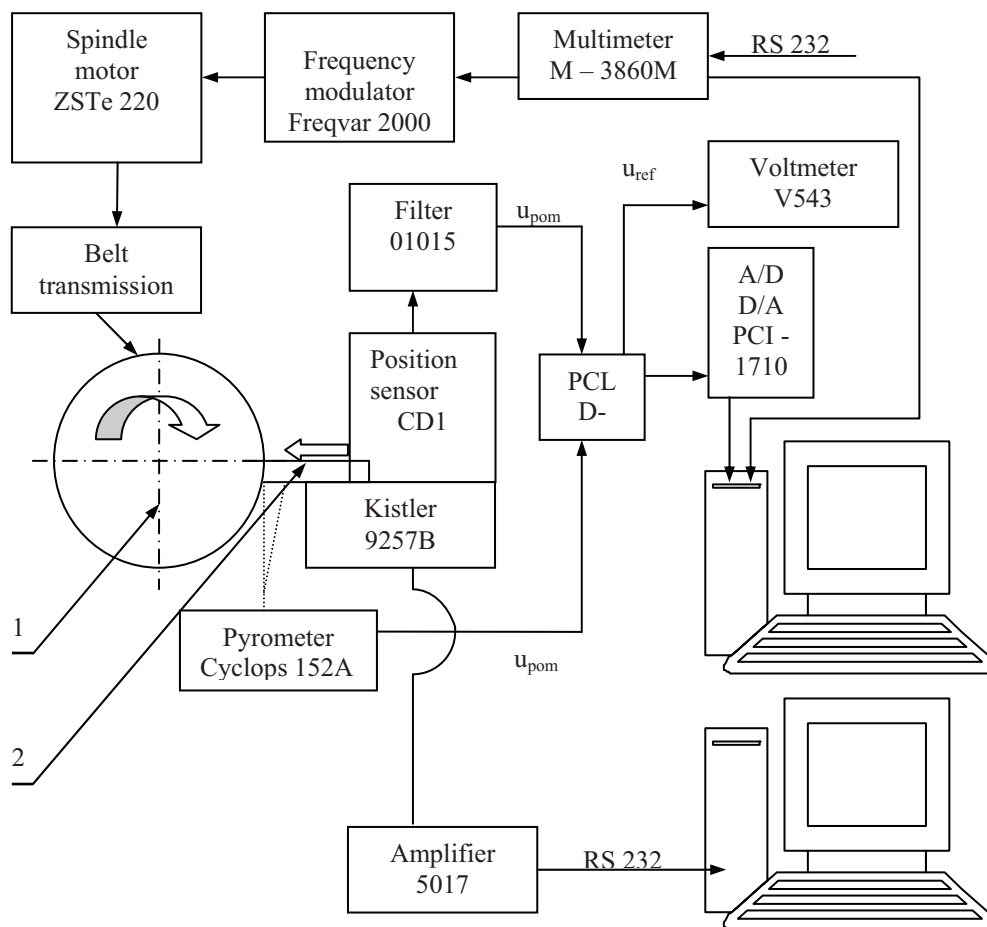


Fig. 1. Experimental set up schematic diagram; 1 – grinding wheel, 2 – workpiece

Experimental conditions:

- grinding wheels characteristics: 1-250x25x76 99A, 24 or 46 or 60, V or B or B10, example of full characteristic; 1-250x25x76 99A 24 M5 B10 50,
- grinding speed v_c : (12, 25 and 38) m/s,
- quasi constant-load force: (34,4 or 51 or 57,7) N as force used for workpiece-to-grinding wheel clamp,
- workpiece material: plain carbon steel C45 (AISI 1045), section dimensions: 10 x 10 mm,
- dry grinding.

Measured values: grinding force components, grinding sparks stream temperature, workpiece linear wear (for workpiece speed v_w evaluation), power consumption.

3. Results and analysis

Specific grinding energy can be determined from active grinding power consumption or tangential grinding force component:

$$e_c = \frac{F_t \cdot v_c}{Q'_w} = \frac{P'_{sc}}{Q'_w} \quad [\text{J/mm}^3], \quad (1)$$

where:

- $F_t \cdot v_c = P'_{sc}$ – specific active grinding power; F_t – tangential grinding force component,
- $v_w \cdot b \cdot a_e = Q'_w$ – specific volumetric removal rate.

Chips energy partition coefficient R_{chips} is a part of grinding chips specific energy $e_{cc}=6 \text{ J/mm}^3$ in total specific grinding specific energy e_c :

$$e_{cc} = R_{chips} \cdot e_c \quad [\text{J/mm}^3]. \quad (2)$$

There is no possibility for measure grinding chips („made” from workpiece material), grinding wheel grains and bond temperatures in contact area without invasion in workpiece-grinding wheel set-up. Thus temperature of grinding spark stream as calorimetric measurement was made for grinding sparks specific energy evaluate. The total grinding spark stream energy can be calculated from :

$$E_{tot} = E_{kin} + E_{ter} \quad [\text{J}], \quad (3)$$

where:

- E_{tot} – total grinding spark stream energy,
- E_{kin} – total spark stream particles kinetic energy,
- E_{ter} – total spark stream particles thermal energy.

$$E_{tot} = \frac{m_{parts} \cdot v_c^2}{2} + R_{chips} \cdot e_c \cdot v_w \cdot a_e \cdot b \cdot t_c \quad [\text{J}], \quad (4)$$

$$m_{parts} = \rho_{temp} \cdot v_w \cdot a_e \cdot b \cdot t_c \quad [\text{g}], \quad (5)$$

where:

- ρ_{temp} – transient workpiece material density in $\text{g} \cdot \text{mm}^{-3}$, calculated in spec. temperature [8],
- v_w – workpiece linear speed in mm/min,
- a_e – grinding depth in mm,
- b – active grinding width in mm,
- t_c – contact time in min,
- m_{parts} –workpiece removed mass in g.

Grinding chips specific energy e_{cc} (based on thermal material properties):

$$e_{cc} = \rho_{temp} \cdot c_{p_temp} \cdot \Delta T \quad [\text{J/mm}^3], \quad (6)$$

where:

- ΔT – measured chips (spark stream) temperature increase (from normal environment temperature),
- c_{p_temp} – transient workpiece material specific heat in J/kgK [8].

After transfiguration total E_{tot} can be found from:

$$E_{tot} = \rho_{temp} \cdot v_w \cdot t_k \cdot b \cdot a_e \cdot \left(\frac{v_c^2}{2} + c_{p_temp} \cdot \Delta T \right) [J], \quad (7)$$

and total chips energy partition coefficient R_{chips} :

$$R_{chips} = \frac{[\rho_{temp} \cdot (\frac{v_c^2}{2} + c_{p_temp} \cdot \Delta T)] \cdot v_w \cdot b \cdot a_e}{v_c \cdot F_T} \quad (8)$$

Values of chips energy partition coefficient R_{chips} determined for: theoretically constant grinding chips specific energy $e_{cc} \cong 6 \text{ J/mm}^3$ and differential values of e_{cc} calculated with spark stream temperature and tangential grinding force are illustrated in Fig. 2. Statistic based models and parameters are presented in Fig. 2.

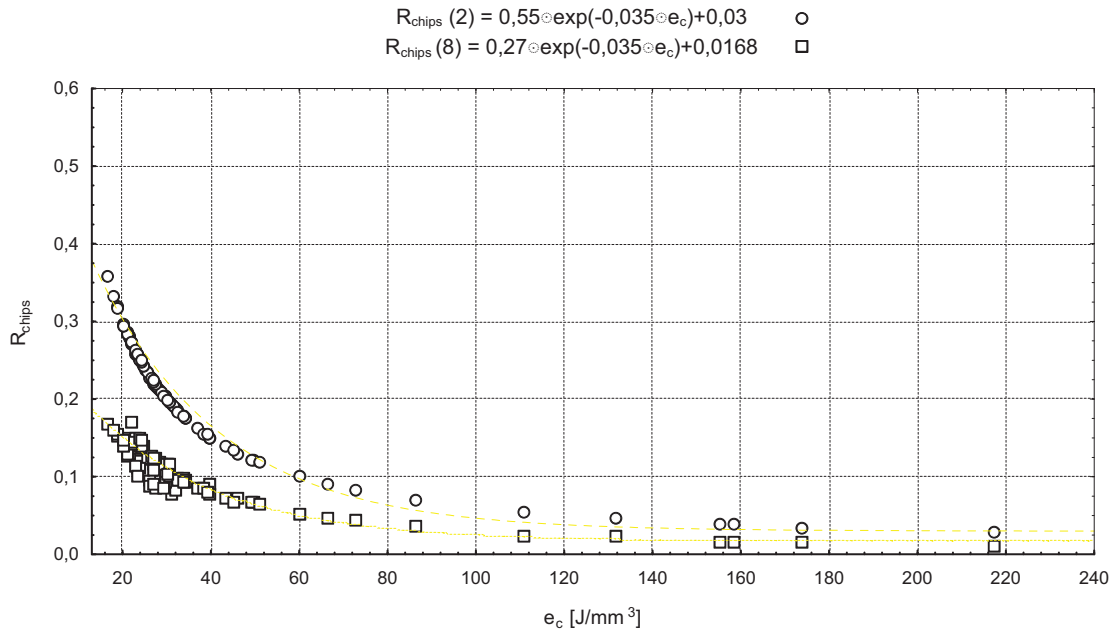


Fig. 2. Chips energy partition coefficient R_{chips} values for different specific grinding energy:

- for $e_{cc} = \text{const} = 6 \text{ J/mm}^3$, determined from eq. (1) and (2)- upper line;
 statistical parameters: $e_c: R_{chips}: R = -0,806, \alpha = 0,00; y = 0,267 - 0,0016 \cdot e_c$
- for e_{cc} determined from eq.(8), based on thermal spark stream measurements – lower line;
 statistical parameters: $e_c: R_{chips}: R = -0,797, \alpha = 0,00; y = 0,135 - 0,00082 \cdot e_c$.

Analyzing Fig. 2. one very important finding can be made; a part of grinding energy is not fully dissipated to grinding chips as follows from previous theoretical analysis. Depending on specific grinding energy difference can exceed 50% for low specific grinding energy techniques. A part of grinding energy, previously calculated as distributed to chips can be dissipated to other places; workpiece, wheel or environment.

4. Conclusions

- Grinding energy dissipated to grinding spark stream was reaching differential values; lower than theoretically constant grinding chip formation specific energy $e_{cc} \cong 6 \text{ J/mm}^3$.
- Chips energy partition coefficient R_{chips} , determined for differential values of e_{cc} calculated with spark stream temperature and tangential grinding force had always lower values than coefficient R_{chips} calculated in the same experiment point for theoretical chip formation specific energy.

- Developed model, based on spark stream temperature, tangential grinding force or power consumption measurements and workpiece thermal properties, can be useful for on-line grinding control systems. The best application for described model should be systems dedicated for low specific grinding energy processes.

References

- [1] Chang, C. C., Szeri, A. Z. *A thermal analysis of grinding*. Wear 216, 1998, pp. 77÷86.
- [2] Howes, T. D., Neailey, K., Harrison, A. J. *Fluid film boiling in shallow cut grinding*. Annals of the CIRP 36/1/1987, pp. 223÷226.
- [3] Jin, T., Rowe, W. B., McCormack, D. *Temperatures in deep grinding of finite workpieces*. Int. J. of Machine Tools & Manufacture 42, 2002, pp. 53÷59.
- [4] Jin, T., Stephenson, D. J. *Investigation of the heat partitioning in high efficiency deep grinding*. Int. J. of Mach. Tools & Manufacture 43, 2003, pp. 1129÷1134.
- [5] Malkin, S., Anderson, R. B. *Thermal aspects of grinding Part 1. Energy partition*. J. Eng. Ind. Trans. ASME B 96, 1974, pp. 1177÷1183.
- [6] Malkin, S., Anderson, R. B. *Thermal aspects of grinding Part 2. Surface temperatures and workpiece burn*. J. Eng. Ind. Trans. ASME B 96, 1974, pp. 1184÷1191.
- [7] Outwater, J.O., Shaw, M.C. *Surface Temperatures in Grinding*. Trans. of the ASME 74, 1952, pp. 73÷85.
- [8] Richter, F. *Die wichtigsten physikalischen Eigenschaften von 52 Eisenwerkstoffen*. Stahleisen – Sonderberichte Heft – 8, 1973, Verlag, Stahleisen M. B. H., Düsseldorf.
- [9] Rowe, W. B. *Temperature case studies in grinding including an inclined heat source model*. Proc. Instn. Mech. Engrs. Vol. 215, part B, 2001, pp. 473÷491.
- [10] Rowe, W. B., Black, S. C. E., Mills, B., Qi H. S., Morgan, M. N. *Experimental investigation of heat transfer in grinding*. Annals of the CIRP 44/1/1995, pp. 329÷332.
- [11] Rowe, W. B., Morgan, M. N., Allanson, D. A. *An advance in the modeling of thermal effects in the grinding process*. Annals of CIRP 40/1/1991, pp. 339÷342.
- [12] Rowe, W. B., Morgan, M. N., Black, S.C.E., Mills, B. *A simplified approach to control of thermal damage in grinding*. Annals of CIRP 45/1/1996, pp. 299÷302.
- [13] Rowe, W. B., Morgan, M. N., Qi H. S., Zheng, H. W. *The effect of deformation on the contact area in grinding*. Annals of the CIRP 42/1/1993, ss. 409÷412.
- [14] Rowe, W. B., Pettit, J. A., Boyle, A., Moruzzi, J. L. *Avoidance of thermal damage in grinding and prediction of the damage threshold*. Annals of the CIRP 37/1/1988, pp. 327÷330.
- [15] Shaw, M. C. *Energy Conversion in cutting and grinding*. Annals of CIRP 45/1/1996 pp. 101÷104.
- [16] Snoyes, R., Maris, M., Peters, J. *Thermally induced damage in grinding*. Annals of the CIRP 27/2/1978, pp. 371÷581.
- [17] Tönshoff, H. K., Wobker, H. G., Brunner, G. *CBN grinding with small wheels*. Annals of the CIRP 44/1/1995, pp. 311÷316.
- [18] Tso, P.-L., Wu, S.-H. *Analysis of grinding quantities through chip sizes*. Journ. of Materials Processing Technology 95, 1999, pp. 1÷7.
- [19] Wang, S.-B., Fuh, K.-H. *The workpiece temperature, fluid cooling effectiveness and burning threshold of grinding energy in creep feed grinding*. Proc. Instn. Mech. Engrs. Vol 212, part B, 1998, pp. 383÷391.



THE CONCEPTION OF DECISION-MAKING SUPPORT SYSTEM FOR COMPLEX ENERGETIC SYSTEM ON EXAMPLE OF SHIP PROPULSION SYSTEM

Jacek Rudnicki

*Gdansk University of Technology
ul. Narutowicza 11/12, 80-233 Gdańsk, Poland
tel.: +48 58 3472973, fax: +48 58 3471981
e-mail: jacekrud@pg.gda.pl*

Abstract

In paper, the conception of decision-making support system for complex energetic system on example of ship propulsion system has been presented. Diversity of conditions, information overload and very often contradiction of decision-making criteria and time constraints result in difficulties in making right (rational) decision without using more or less expanded information processing systems (eg. database systems, expert systems, programs dedicated to particular situations, etc.)

Using that systems undoubtedly increases the probability of making a good decision and efficiently decreases the time of its development. Following analysis relates to the test program implementation of exploit decision-making support system, which was developed in Department of Ship Power Plants in Gdansk University of Technology.

Keywords: *decision making, exploitation, operation, ship power plants*

1. Introduction

During exploitation of every power plant, its functional subsystems are affected by different external and internal factors, which are reasons for irreversible degradation processes, causing changes in technical state and usually gradual deterioration of its exploit characteristics. In those subsystems, damages to their components will appear inevitably.

The intense development of marine transport, increasing number of ships, enhancing marine traffic and diversity of realized tasks creates a real danger for people and natural environment.

Taking into consideration also the fact of significant complication of functional and structural ship energetic system (mostly main propulsion system), proper analysis of decision-making situation, which results directly influence ship's safety becomes particularly important problem.

Diversity of conditions, information overload and very often contradiction of decision-making criteria and time constraints result in difficulties in making right (rational) decision without using more or less expanded information processing systems (eg. database systems, expert systems, programs dedicated to particular situations, etc.)

Using that systems undoubtedly increases the probability of making a good decision and efficiently decreases the time of its development. Following analysis relates to the test program implementation of exploit decision-making support system, which was developed in Department of Ship Power Plants in Gdansk University of Technology.

2. General description of the application

The developed application, in present version, is designed to work off-line and works in interactive mode with user, requiring from him input from keyboard data essential for analysis, including:

- operative characteristics of analysed propulsion system (main engine + hull + propeller)
- conditions of task's realization
- results of exploit tests concerning reliability characteristics
- chosen values connected with reserves state and realization of preventive inspections of analysed system elements

The application consists of 4 main parts that realize analysis in sphere shown below and presents its results and possible conclusions. Its general scheme is presented in Fig. 1.

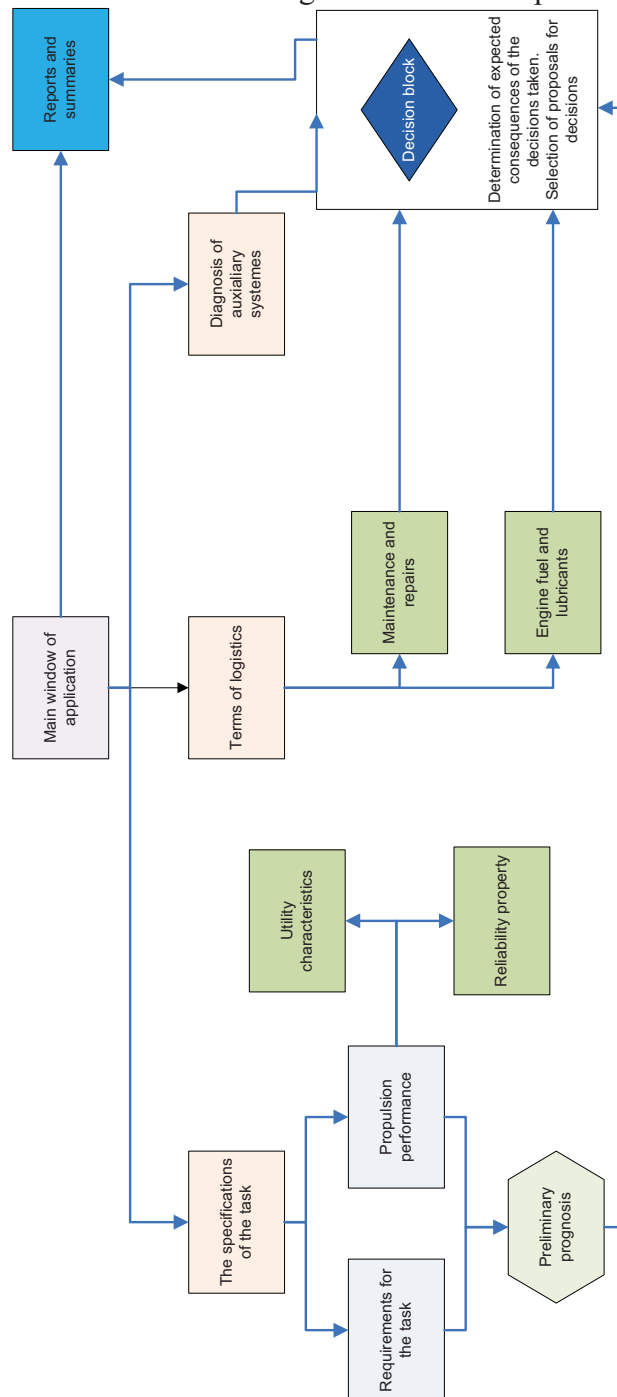


Fig.1. Block diagram of the application

First of all, the beginning of working with the application requires input the analysed system's characteristics data and specification of task realisation requirements. Realisation of those two conditions is possible by next choice of two options in programme's main window: "Entrance data input" and "Result of exploit tests".

3. General task realisation assumptions

After choosing the "Entrance data input" option, a transition to next part of the programme approaches, in which:

- provide general transport task realisation data (distance, required realisation time),
- by choosing buttons: "Engine's characteristics", "Propeller characteristics" and "Resistance characteristics" input the description of individual elements of propulsion system.

Example of main engine window is presented in Fig. 2.

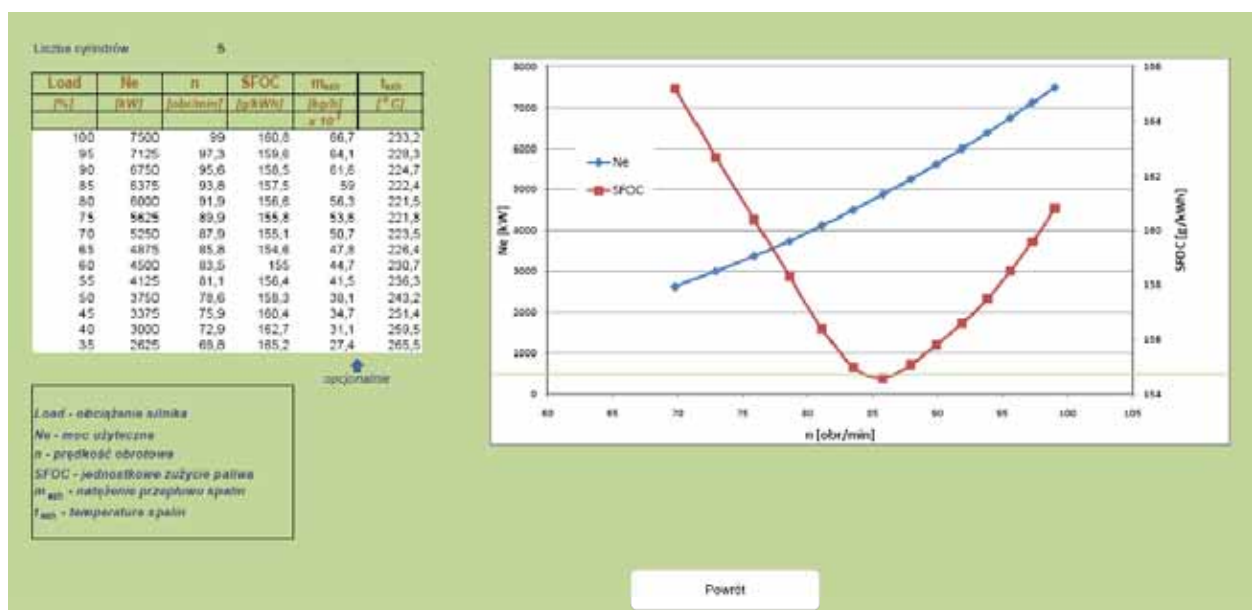


Fig.2. Description of main engine's operative characteristics.

Really expanded part of this application block is description of propeller operative characteristics. In this part were implemented algorithms of propeller hydrodynamic characteristics determination that were developed in Wageningen Institute, where pressure and moment indexes values depend on advance index value – J, jump index – H/D, surface index – S0/S, number of wings – Z and Reynolds number – Re [1]. Results of calculations are presented as it is on Fig. 3.

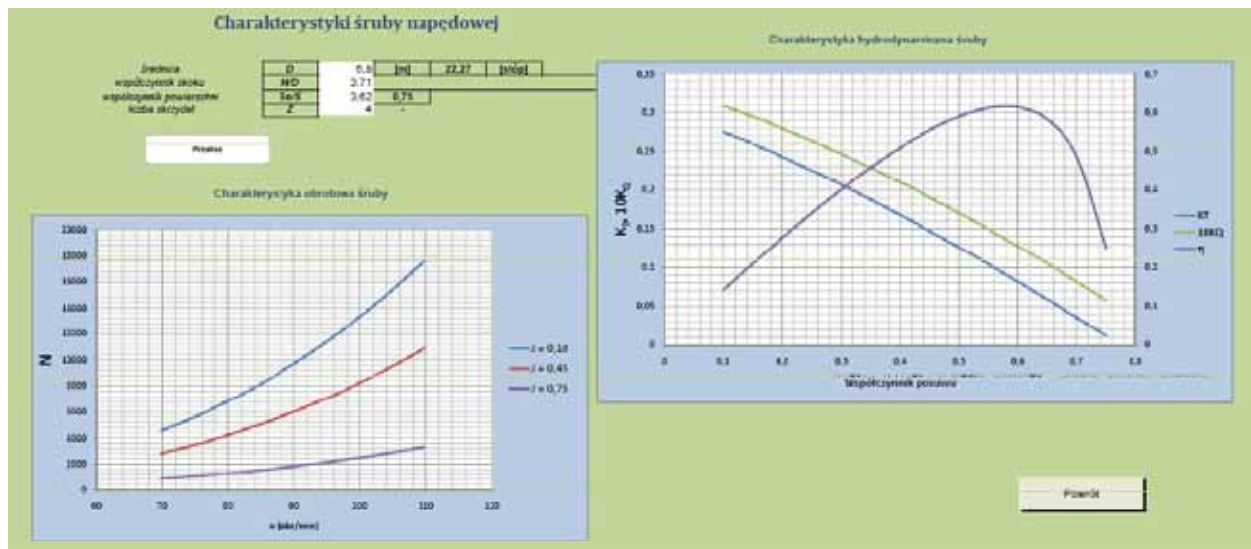


Fig. 3. Characteristics of propeller.

Input of all required data and return to data input window enables generating preliminary predictions and their explanation (Fig. 4.)

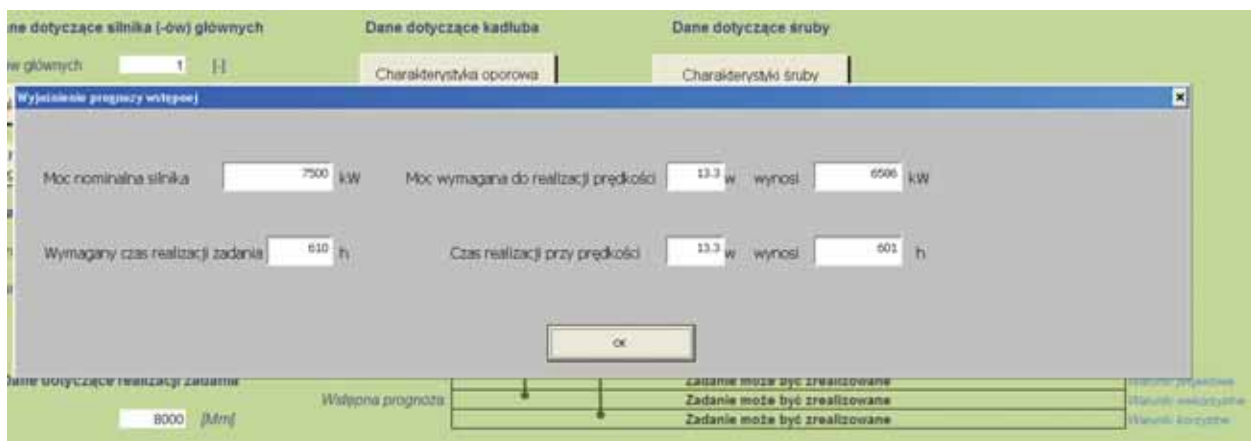


Fig. 4. Explanation of preliminary prediction

as well as presentation of optimised variants of power transmission system operation in disadvantageous, project and advantageous conditions when taking consumption of fuel during realisation of the transport task into consideration.

4. Assignment of reliability characteristics of power transmission system.

During exploitation of vessels, usage and operative for power plant devices decisions are made permanently – mainly about power transmission system. The choice of the decision, necessary for determination of right exploit strategy, is possible after taking many different information into consideration, but it will never be right choice without accounting power transmission system or its basic elements reliability data and indexes.

Amongst nowadays used reliability models of complex technical objects, we can distinguish two groups [2, 3, 5]:

- two-state models – in case of using this type of model, the process of technical state changes is binary – in particular moment the device is either serviceable or not,
- multi-state models – the process of technical state changes is constant in time and unobtrusive in states – the number of distinguished states is unrestricted.

The described application uses both groups of presented models, in order to get fuller description of analysed system reliability characteristics. The effect of that choice is window presented in Fig. 5.

Definition of reliability characteristics using classical methods of reliability theory and two-state probabilistic models.

Realisation of calculation based on conventional models is possible after choosing one of three buttons in "A" part presented in Fig. 5.

That kind of choice results in transfer to appropriate distinguished elements power transmission system sub-programmes (engine, propeller, shafting elements) considered as their serial reliability structure.

Interface managing this part of the application is presented in Fig. 6.

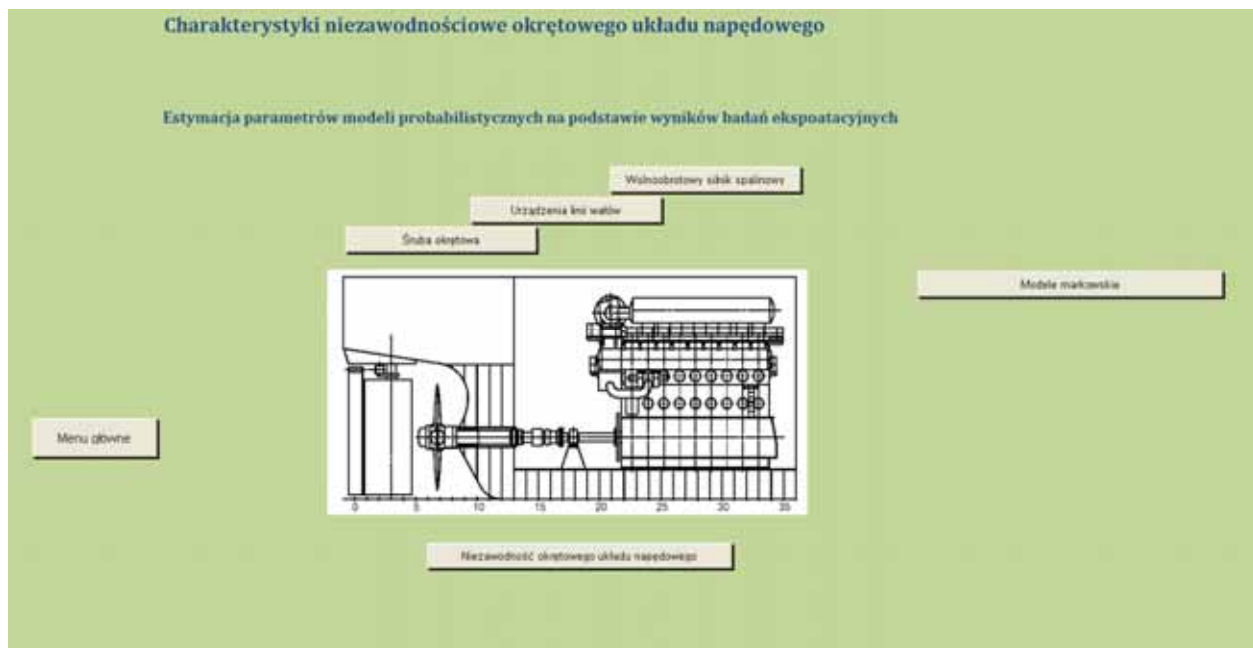


Fig.5. The choice of procedures making reliability calculations.

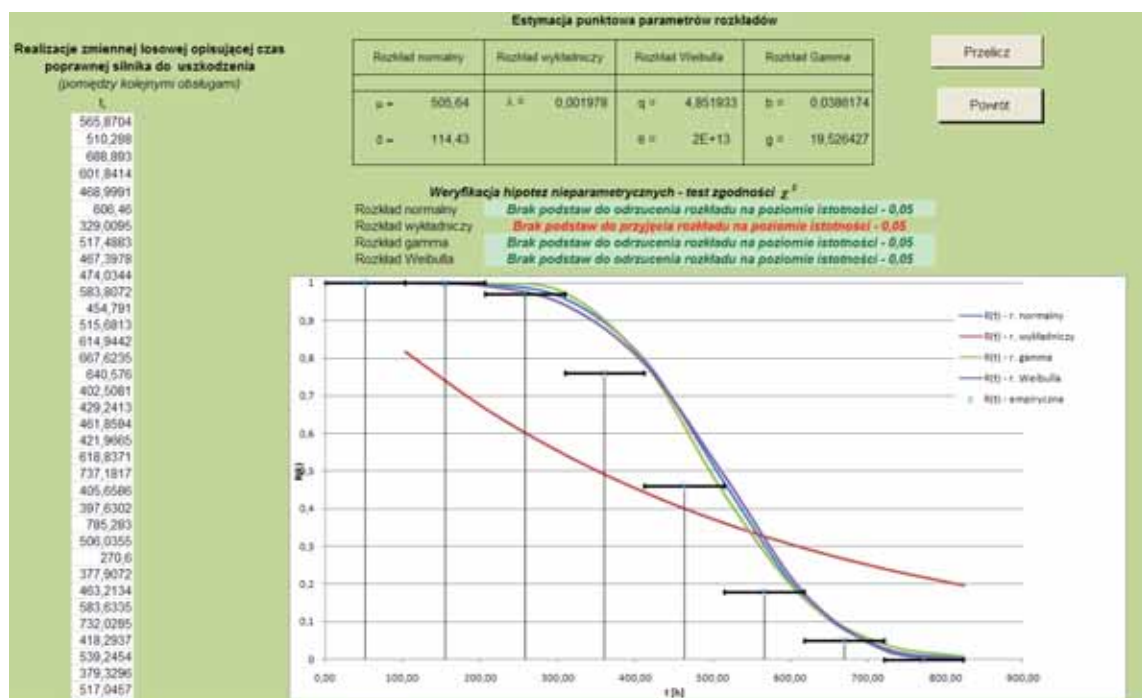


Fig.6. Interface of unit realising reliability calculations.

The algorithms implemented in this part of the programme require user to input up to 100 values of random variable realisation describing the time of main device correct functioning between subsequent main operations (in present version, it is assumed that realisation of main operation brings values of reliability functions to 1) and then the programme realises actions as follows:

- assignation of empiric reliability characteristics – presented as graphics,
- empiric distributions of particular random variables are used to check the function form of their distribution by verifying following statistical hypotheses with empiric and theoretical distributions compatibility [3].

The results of carried calculations are presented in table seen in window in that part of the application.

5. Use of Markov's processes theory in estimation of reliability indexes values

The use of stochastic processes theory in description of reliability enables giving up an bistativity assumption of technical, reliability and exploit states changes process and composing into the model a very important feature characterising mechanical machines and devices – renewal. In case of ship devices it is particularly important, because as complicated and complex technical objects they can be damaged in many ways, with different probability and consequences corresponding to their task reliability.

Reliability model are in this case stochastic processes with unobtrusive set of distinguished states and constant duration.

In researches in reliability of complicated technical objects, which power transmission systems definitely are, so far generally semi-Markov stochastic processes theory and Markov's processes have found their use.

In present version of the described application so far only Markov model has been implemented (mostly because of calculation complexity of semi-Markov model – calculation of Volterra integral equation of second type) with all its limitations [2, 3] but eventually it is planned to implement semi-Markov model as well.

In proffered functional – reliability model from the set of all possible reliability states of power transmission system, 7 classes (subsets) were distinguished, described as states s_i ($i=1, 2, \dots, 7$):

- s_1 state – the state of power transmission system's complete task ability. System in this technical state is capable of fulfilling all tasks it was designed and made for.
- s_2 state – the state of system's incomplete task ability due to partial capability of engine, which can happen eg. when:
 - it's impossible to achieve all the parameters in engine's work field;
 - all the parameters in field work are achieved, but SFOC and/or $SL_{ub}O_{il}C$ are increased.
- s_3 state – the state of system's complete inability due to complete engine's incapability, which precludes using the engine as intended.
- s_4 state – the state of system's incomplete task ability due to partial capability of shafting elements caused by eg. excessive vibration entailed by radial bearings emaciation
- s_5 state – the state of system's complete inability due to complete incapability of power transmission line.
- s_6 state – the state of system's incomplete task ability due to partial capability of propeller, eg. in case of mechanical damaging one of propeller's blades, which interferes its balance.
- s_7 state – the state of system's complete inability due to complete propeller's incapability, which precludes using the propeller as intended eg. in case of wide mechanical damage to the propeller.

The graph of states-transitions can be presented as follows:

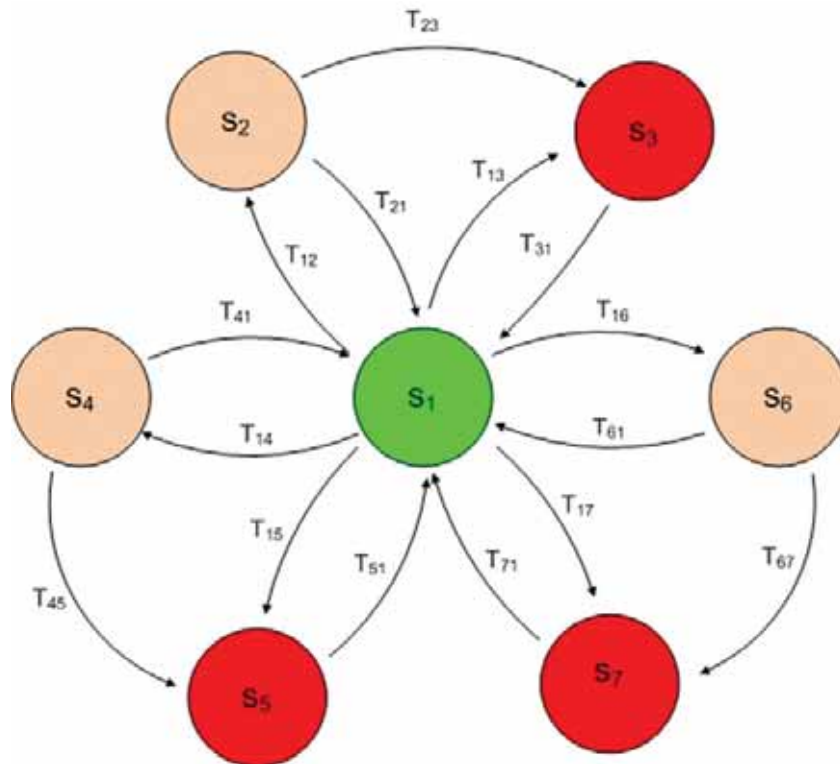


Fig.7. The graph of states-transitions of implemented Markov model.

The window of Markov model is presented in Fig.8.

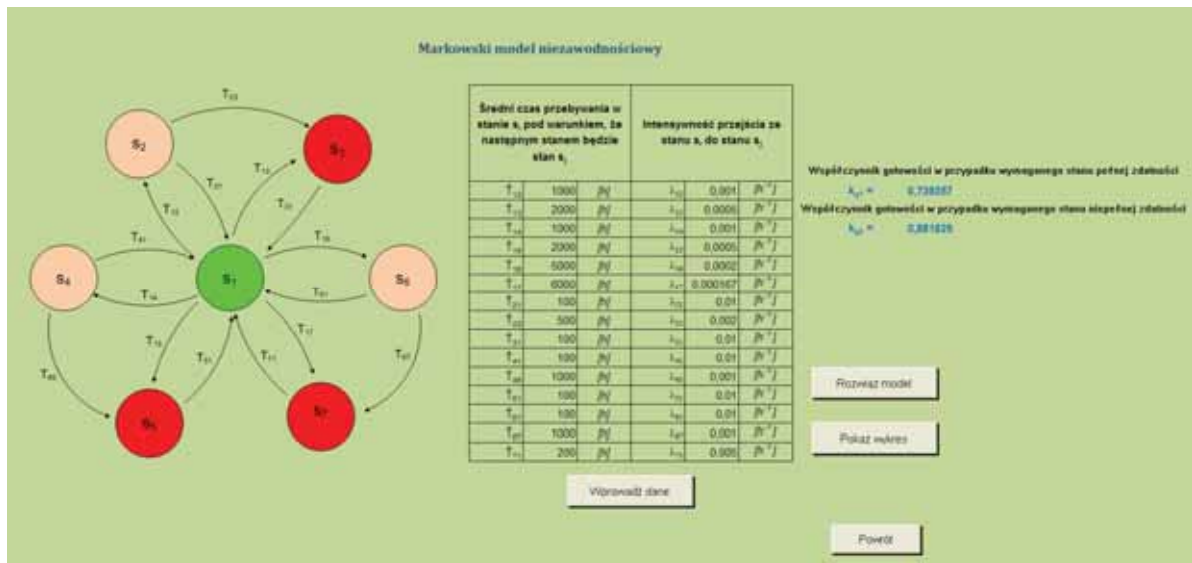


Fig.8. Markov model's window.

The window requires input of s_i state average time data, provided that the next state is s_j state. To enhance the clarity of input data it's done in additional form that includes proper explanations. The results of calculations are kept in the programme and presented as graphics.

6. Generation of decision-making situation solution's proffer.

Obtained in previously described parts of the application number values of particular indexes are used in exploit decision proffer generation mode. Access to this part of the application is possible from the main window level by the "Decision-making trees" reference.

The decision-making procedure is presented in one of most popular structural forms – decision-making tree.

In 1st step two decision-making trees are analysed, as shown in Fig.9.



Fig.9. The window of analysed decision-making trees.

The criteria function for shown tree I maximisation of expected consequence value $c(d_j, s_i)$ which for individual tree's nodes symbolising making particular d_j decision can be described as [9]:

$$E(c/d_j) = \sum_{i=1}^k [p(s_i)/d_j \cdot c(d_j, s_i)] \quad i = 1, 2, \dots, k \quad j = 1, 2, \dots, n \quad (1)$$

User is obliged only to estimate the consequence of particular state to occur.

In case of contradictory decision proffers communicated by the programme, it is possible to use additional procedure using evaluative description of operation, which was described wider by the author inter alia in papers [7, 8].

This option becomes active right at the moment of described contradictory of proffered decisions ascertainment by programme and access to that is available by “Additional criteria” overlap – Fig.10.

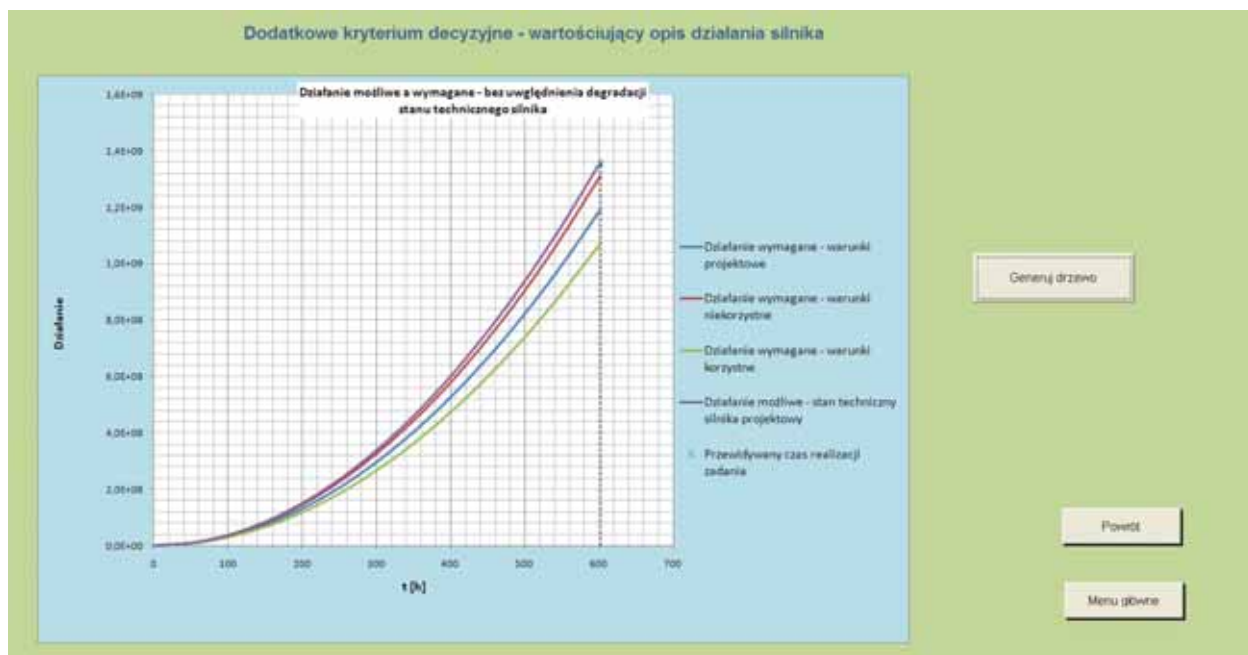


Fig.10. The window of additional decision-making criteria.

Model's calculation ("Tree's generation" button) results in generated decision-making tree display – Fig. 11.

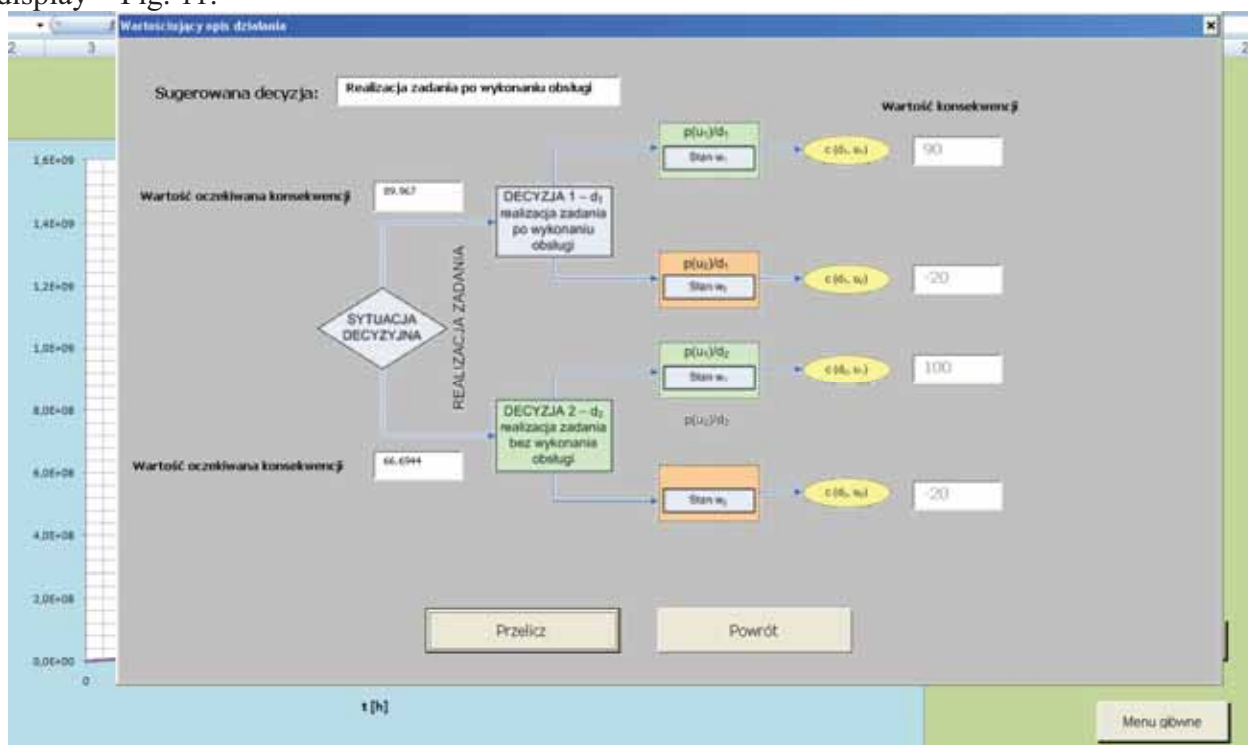


Fig.11. Generation of decision-making tree based of evaluative operation description.

as well as decision proffer, which possibly predominates on one of two generated in previous stage.

7. The application's extension – power plant's additional installations neuron state classifiers

The additional mode of the application is its part that is additional installations that secure main power transmission system functioning state classifier. The idea of neuron system of damages

detection is described in many thesis inter alia, [4, 10] and the described solution is based on author's experience described in inter alia [6].

A choice of analysed installation accessible from the application's main window. - Fig.12.

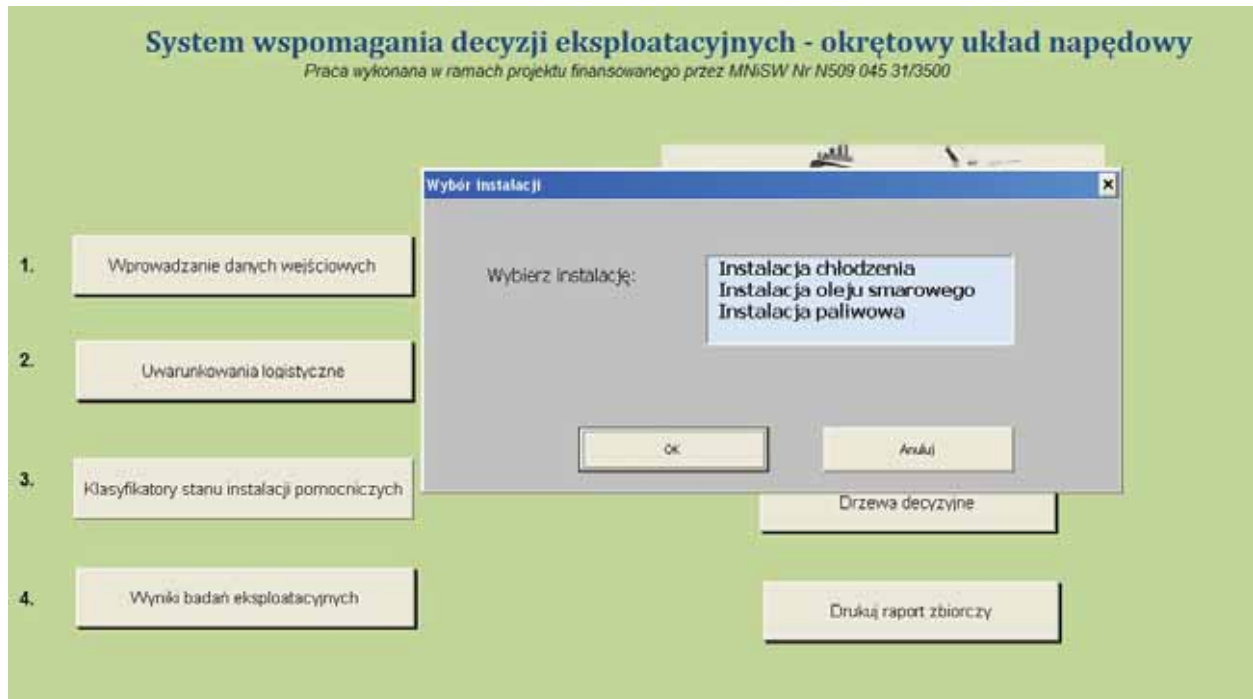


Fig.12. The form of classified additional installation choice

followed by particular classifier window's opening – Fig.13.

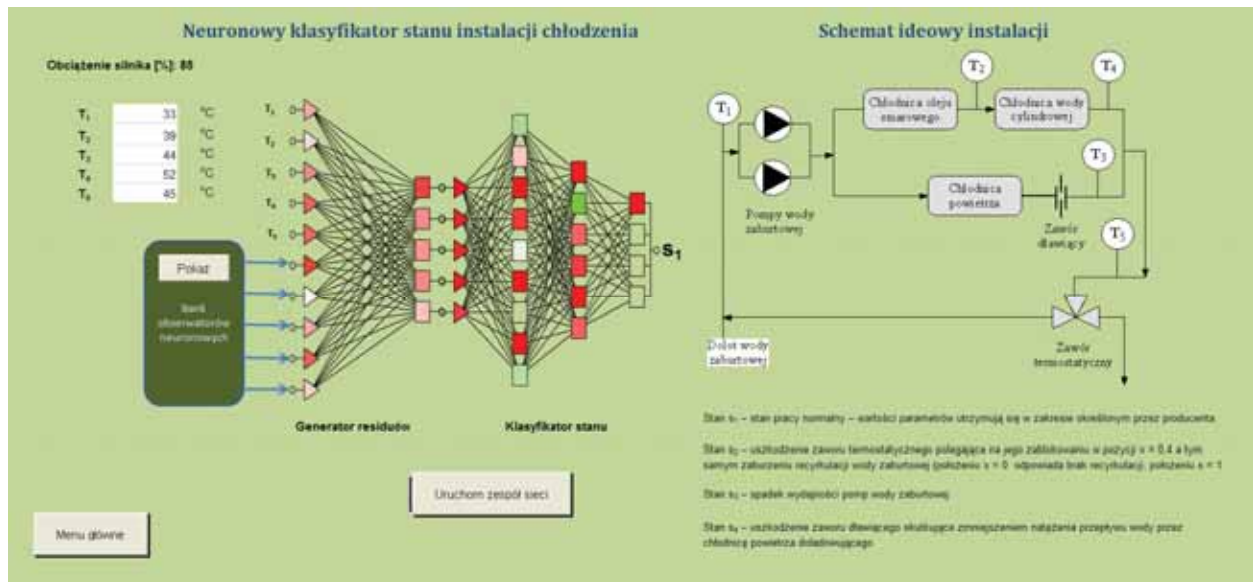


Fig.13. Cooling installation state classifier

in which user inputs basic parameters characteristic for chosen installation, and then properly trained system of neuron networks does the proper classification.

8. Summary

The process of making that kind of decision (amongst all possible) that in particular conditions

will be thought to be the best, should be based on as many accessible in that conditions data as possible. But even in the (practically unparalleled) case of having all device's exploit data, the nature of decision-making process is a choice of criteria that enables appraising and comparing consequences of making different decisions. In case of complex technical systems realising particularly important tasks connected to both expected profit and creating significant danger to the environment (including the exploitation object), two main, equal criteria are:

- maximisation of profit value (minimisation of loss),
- minimisation of danger situation chance.

Therefore, besides multiplicity of conditionings in the reality, a natural contradictory between presented criteria occurs – maximisation of security level decreases profits and vice versa – and existing formal regulations in the field of security determine some minimal, required level, the realisation of the decision-making process is rather diverse, very often intuitive, even when according to the same objects, exploited in similar conditions.

The described conjuncture in specific way affects the situation of ship energetic systems (especially ship power plant and ship power transmission system) as they realise tasks that influences natural environment, as well as human health and life.

Amongst tools enhancing the probability of the right decision choice and being available for decision maker, should be tools basing on decision-making models created basing on mathematical models of exploitation process.

Modulation of exploit reality is always a simplification of existing state, which means it's impossible to create one, universal model that in full way would reflect the complexity of structure and processes going on during that part of power plant existence.

The multiplicity of information about conditions of making and verifying different types of models useful during decision-making process can be found in literature and thesis. The more does seem strange the fact of their sporadic use in exploit practice of complex technical systems, especially power plant and its elements.

This gap in ready-made tools enabling practical use of developed models section can be up to some level program tools developed and improved basing on available software, which is proved by this application, developed in this thesis and presented in test version.

9. Bibliography

- [1] Chachulski K., *Metody i algorytmy rozwiązywania problemów eksploatacyjno-ruchowych okrętowych układów napędowych*, Wydawnictwo WSM Szczecin, Szczecin 1992.
- [2] Gercbach I.B., Kordonski Ch.B., *Modele niezawodnościowe obiektów technicznych*, WNT, Warszawa 1968.
- [3] Girtler J., *Modele matematyczne w badaniach niezawodności silników o zapłonie samoczynnym*, Konferencja Naukowo-Techniczna "Utrzymanie silników o zapłonie samoczynnym w ruchu" EXPLO-DIESEL'98, Instytut Technicznej Eksploatacji Siłowni Okrętowych WSM w Szczecinie, Szczecin 1998.
- [4] Korbicz J., Kościelny J.M., Kowalczyk Z., Cholewa W., *Diagnostyka procesów. Modele. Metody sztucznej inteligencji. Zastosowania*, Warszawa, WNT 2002.
- [5] Rudnicki J., *Detekcja uszkodzeń instalacji rurociągów okrętowych z wykorzystaniem sztucznych sieci neuronowych*, XXVII Sympozjum Siłowni Okrętowych, [Szczecin 16-17 listopada 2006] / red. R. Michalski, W. Zeńczak, S. Żmudzki. / Wydaw. Politechniki Szczecińskiej, 2006.
- [6] Rudnicki J., *Identyfikacja procesu eksploatacji okrętowych urządzeń i systemów energetycznych w aspekcie potencjalnych możliwości opracowania jakościowych i ilościowych*

modeli matematycznych tego procesu, Praca wykonana w ramach projektu finansowanego przez MNiSW Nr N509 045 31/3500, Projekt badawczy pt., „Kształtowanie bezpieczeństwa działania systemów energetycznych środków transportowych na przykładzie systemów okrętowych”, Gdańsk, 2007.

- [7] Rudnicki J., *Działanie systemu energetycznego w ujęciu wartościującym z uwzględnieniem jego struktury niezawodnościowej oraz stopnia zużycia potencjału użytkowego*, Praca wykonana w ramach projektu finansowanego przez MNiSW Nr N509 045 31/3500, Projekt badawczy pt., „Kształtowanie bezpieczeństwa działania systemów energetycznych środków transportowych na przykładzie systemów okrętowych”, Gdańsk, 2008.
- [8] Rudnicki J., *Model niezawodnościowo – funkcjonalny okrętowego, tłokowego silnika spalinowego*, 2000, Rozprawa doktorska (11.03.2000). Politechnika Szczecińska, Wydział Techniki Morskiej.
- [9] Sadowski W., *Teoria podejmowania decyzji*, Państwowe Wydawnictwo Ekonomiczne, Warszawa 1976.
- [10] Tzafestas S.G., Dalianis P.J., *Fault Diagnosis in Complex Systems using Artificial Neural Networks*, 3rd IEEE CCA, 0-7803-1872-2/94 © 1994 IEEE.



ECM MACHINING OF CURVILINEAR ROTARY SURFACES

Jerzy Sawicki

*University of Technology and Life Sciences
Faculty of Mechanical Engineering,
ul. Kaliskiego 7, 85-796 Bydgoszcz, Poland
tel.: +48 52 3408277
e-mail: Jerzy.Sawicki@utp.edu.pl*

Abstract

The paper deals with a theoretical analysis of curvilinear rotary surface machining (ECM) by a shaping electrode tool. An equation describing the curvilinear rotary surface shape evolution, and an equation of the electrolyte and gas mixture flow through the gap between curvilinear rotary surfaces, have been formulated. Calculations have been performed for the assumed machining parameters, depicting calculation results along the interelectrode gap. Distributions of: gap thickness, current density, void fracture, temperature, electrolyte flow rate and pressure have been presented in charts.

Keywords: *electrochemical machining, electrolyte flow, mathematical model,*

1. Introduction

Nowadays electrochemical machining by a tool shaping electrode is one of the basic operations of electrochemical technology for machining mechanical devices and tools. ECM machining has been developed as a machining method for alloys of high strength and temperature resistant whose machining used to be extremely complicated using other available methods (Wilson [1]); McGeough [2]).

During a constant process, the tool electrode (TE) usually performs a translation towards the machined surface. Electrolyte is supplied to the interelectrode gap, causing that the dissolution products are carried away from the interelectrode gap (IEG). These are mainly hydrogen atoms and ions of the dissolved metal. In such conditions, a multi-phase and three-dimensional flow [3] is obtained.

Hydrodynamic parameters of the flow and the medium properties determine the processes of mass, momentum and energy exchange in the interelectrode gap. Properly matched, they prevent from formation of cavitation zones, a critical flow, circulation, excessive rise of the electrolyte temperature and void fracture [4].

The above mentioned processes have a significant influence on the electrochemical dissolution velocity and applicability of the machined surface [5].

ECM modeling involves: determination of the interelectrode gap thickness, the machined surface shape evolution in time, and distributions of physical-chemical conditions within the machining area, such as: distributions of pressure, electrolyte flow rate, temperature and void fracture.

Many authors have dealt with the mathematical description of ECM machining, including: Tipon [8], Fitzgerald, McGeough and Marsh[9], Alkire[10], Davydov, Kozak[11], Sautebin[12], Jain and Pandey[13], Prentice, Tobias,[14], Bialecki[15], Hume [16], Zouh [17], Prentice and Tobias [18] and Dukovic [19] and others.

This paper is a theoretical analysis of ECM machining of curvilinear, rotary surfaces.

2. Mathematical model of ECM process

Figure 1 shows the area of electrolyte flow inside the interelectrode gap (IEG), between curvilinear, axially symmetrical surfaces.

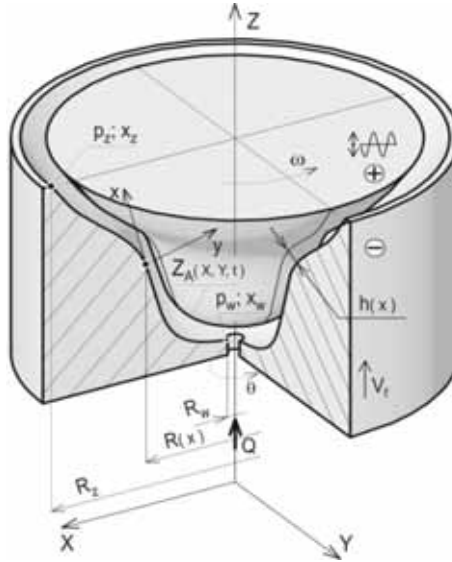


Fig.1. Area flow of electrolyte in interelectrode gap IEG

A general differential equation describing shape evolution of the surface machined by anode dissolution according to ECM dissolution theory, has the form [4,5,6,7]:

$$\frac{\partial F}{\partial t} + k_v \vec{j}_A \text{grad} F = 0 \quad (1)$$

with initial condition $F(X, Y, 0) = F_0$

where:

$\vec{j}_A = \vec{j}(X_A, Y_A, t)$ - distribution of current density on the machined surface,

k_v - coefficient of electrochemical machinability

$F_0(A, 0) = 0$ - an equation describing the initial workpiece (WP),

$F(A, t) = 0$ - an equation describing the anode surface in time t.

Current density results from Ohm's law [4,5,6,7]:

$$\vec{j} = -\kappa \text{grad} u \big|_A \quad (2)$$

where: u - potential of the electrical field between the electrodes,

κ - conductivity.

In rectangular axis X, Y, Z connected with the immovable anode, the anode surface equation has the form:

$$Z = Z_a(x, y, t) \quad (3)$$

Introducing equation(3) into dependence (1), one obtains:

$$\frac{\partial Z_A}{\partial t} = k_v j_A \sqrt{1 + \left(\frac{\partial Z_A}{\partial X} \right)^2 + \left(\frac{\partial Z_A}{\partial Y} \right)^2} \quad (4)$$

where: k_v - coefficient of electrochemical machinability

for $t=0$ $Z_A=Z_o(X,Y)$.

Assuming linear distribution of the electrical field potential along IEG the current density in the anode, in a locally orthogonal coordinate system x,y (Fig.1) is expressed in the following way [6,7,20,21].

$$j_A = \kappa_0 \Phi_{TG}^{-1} \frac{U - E}{h} \quad (5)$$

Function Φ_{TG} describes the influence of conductivity changes within the interelectrode gap (IEG) and is determined in the following way:

$$\Phi_{TG} = \frac{1}{h} \left[\int_0^h \frac{dy}{(1 + \alpha(T - T_0))(1 - \beta)^{3/2}} \right] \quad (6)$$

In order to close equation system (4),(5) and (6) it is necessary to determine temperature rises $\Delta T=T-T_o$ and the distribution of void fracture β . This requires definition of pressure, speed and temperature distributions within the curvilinear interelectrode gap.

Mathematical modeling of the electrolyte flow through the interelectrode gap has been performed in a curvilinear, locally orthogonal coordinate system connected with immobile surface [4].

Having accepted for consideration a model of two phase, anti-slide flow, the mixture movement equations resulting from laws of mass, momentum and energy preservation in curvilinear locally rectangular axis, are in the form [20]:

$$\frac{1}{R} \frac{\partial (\rho_e R v_x)}{\partial x} + \frac{\partial (\rho_e v_y)}{\partial y} = 0 \quad (7)$$

$$\frac{1}{R} \frac{\partial (\rho_H R v_x)}{\partial x} + \frac{\partial (\rho_H v_y)}{\partial y} = j \eta_H k_H h^{-1} \quad (8)$$

$$-\rho_e v_\theta^2 \frac{R'}{R} = -\frac{\partial p_e}{\partial x} + \mu_e \frac{\partial^2 v_x}{\partial y^2} \quad (9)$$

$$\frac{\partial^2 v_\theta}{\partial y^2} = 0 \quad (10)$$

$$0 = -\frac{\partial p_e}{\partial y} \quad (11)$$

here: v_x, v_θ, v_y - components of velocity vector,

p_e - electrolyte pressure,

$\rho_e = \rho_{eo} (1 - \beta)$ - electrolyte density,

$\rho_H = \rho_{Ho} \beta$ - hydrogen electrolyte,

μ_e - dynamic coefficient of electrolyte viscosity,

μ_H - dynamic coefficient of hydrogen viscosity,

β - void fraction,
 j, η_H, k_H - are, respectively, current density, current efficiency of hydrogen emission,
hydrogen electrochemical equivalent,
 R - tool electrode surface radius.

Energy equation for the considered flow, taking into consideration Joule's heat, emitted during the current flow, forced heat convection caused by the electrolyte flow, heat exchange by electrodes and negligence of the dispersed energy, has now the form:

$$v_x \frac{\partial T}{\partial x} + v_y \frac{\partial T}{\partial y} = \frac{1}{R} \frac{\partial}{\partial x} \left(a R \frac{\partial T}{\partial x} \right) + \frac{\partial}{\partial y} \left(a \frac{\partial T}{\partial y} \right) + \frac{j^2}{\rho_e c_p \kappa} \quad (12)$$

here: a - coefficient of electrolyte thermal diffusivity,
 κ - electrolyte conductivity,
 T - electrolyte temperature,
 c_p - specific heat with constant pressure,

Formulated equation system (7)-(12) is the principal system of equations for the analysis of an axially-symmetrical flow of the electrolyte and hydrogen mixture flow through the interelectrode gap.

The solution of equation system (7)-(12) will enable to define distributions of velocities, pressures and temperature in the interelectrode gap. The obtained formulas defining the temperature distribution in the gap will be utilized for determination of the workpiece (WP) shape evolution (anode) on the basis of equation (4).

Solutions of equations (7)-(12) should satisfy boundary conditions with regard to :

- pressure and velocity components:

$$\begin{aligned} v_x = v_y = 0 \quad dla \quad y = 0, \\ v_x = v_y = 0 \quad dla \quad y = h, \\ v_\theta = 0 \quad dla \quad y = 0, \\ v_\theta = \omega_\theta R(x) \quad dla \quad y = h, \\ p = p_z \quad dla \quad x = x_z \end{aligned} \quad (13)$$

-for temperature:

$$\begin{aligned} - \text{on the walls: } T = T_s \quad dla \quad x \geq x_w \quad i \quad y = 0 \quad \text{oraz } y = h \\ - \text{on the inlet: } T = T_w \end{aligned} \quad (14)$$

here: p_z – pressure on the interelectrode gap outlet,
 x_z – coordinate of the interelectrode end
 x_w - coordinate of the interelectrode beginning
 T_s - temperature of electrodes, T_w – temperature on the inlet,
 A – vibration amplitude,
 ω_z - vibration frequently,
 ω_θ - angular velocity.

When integrating motion equations (9) – (10), one can obtain formulas defining velocities and pressures within the interelectrode gap.

$$v_x = \frac{3Q}{\pi R h^3} (hy - y^3) + \frac{\rho}{\mu} \left[\frac{1}{12} \frac{\omega^2 R R}{h^3} (y^4 - h^3 y) \right] \quad (15)$$

$$v_y = \frac{V}{h^3} (3hy^2 - 2y^3) \quad (16)$$

$$v_\theta = \omega R \frac{y}{h} \quad (17)$$

$$p(x) = \frac{6\eta_\theta Q}{\pi h^3} (A_x - A_z) + p_a, \quad A_x = \int_R^x, \quad A_z = \int_{R_z}^x \quad (18)$$

Dependencies (15)-(18) describe velocity and pressure distributions in the mixture laminar flow through the gap, with a random profile of surfaces limiting the flow. The assumption of specific geometry of the axially-symmetrical surface leads to accurate definition of velocity and pressure distributions.

Distribution of void fracture β was determined from the mass balance of hydrogen, given off on the cathode.

When integrating equation (8) across the gap

$$\frac{1}{R} \frac{\partial}{\partial x} \left(\rho_H R \int_0^h v_x dy \right) + \rho_H v_y \Big|_0^h = j \eta_H k_H \quad (19)$$

and, next, accepting the assumption that $\beta = \beta(x)$ one can obtain, after transformations:

$$\frac{\partial}{\partial x} \left(\frac{x}{L} \beta \right) = \frac{2\pi \eta_H h k_H}{\mu_H Q} j R \quad (20)$$

whereas: β - void fracture, $\rho_{H_2} = \frac{\mu_H P}{R_H T}$ - hydrogen density, η_H - current efficiency of gas emission, k_H - hydrogen electrochemical equivalent, R_H - hydrogen gas constant, μ_H - hydrogen molar mass.

Solution to equation of the machined surface shape evolution (4) was based on the method of successive approximations in combination with the time step method [6,7,20,21].

3. Numerical model of ECM process

This problem is accounted for according to a successive approximation method for all used numerical schemes using at the same time the time steps method [6,7,20,21].

Energy equation (12) has been solved numerically with the use of finite difference method replacing the temperature derivatives with algebraic expressions.

Simplified algorithm of a mathematical model solution is presented in fig. 2.

4. Conclusions

Calculations were performed for shaping rotary electrodes with spherical surface profiles. The supply system ensures the electrolyte fixed flow rate in the interelectrode gap. Passivating electrolyte was accepted for calculations. Calculations had been performed until a quasi – stationary state was reached.

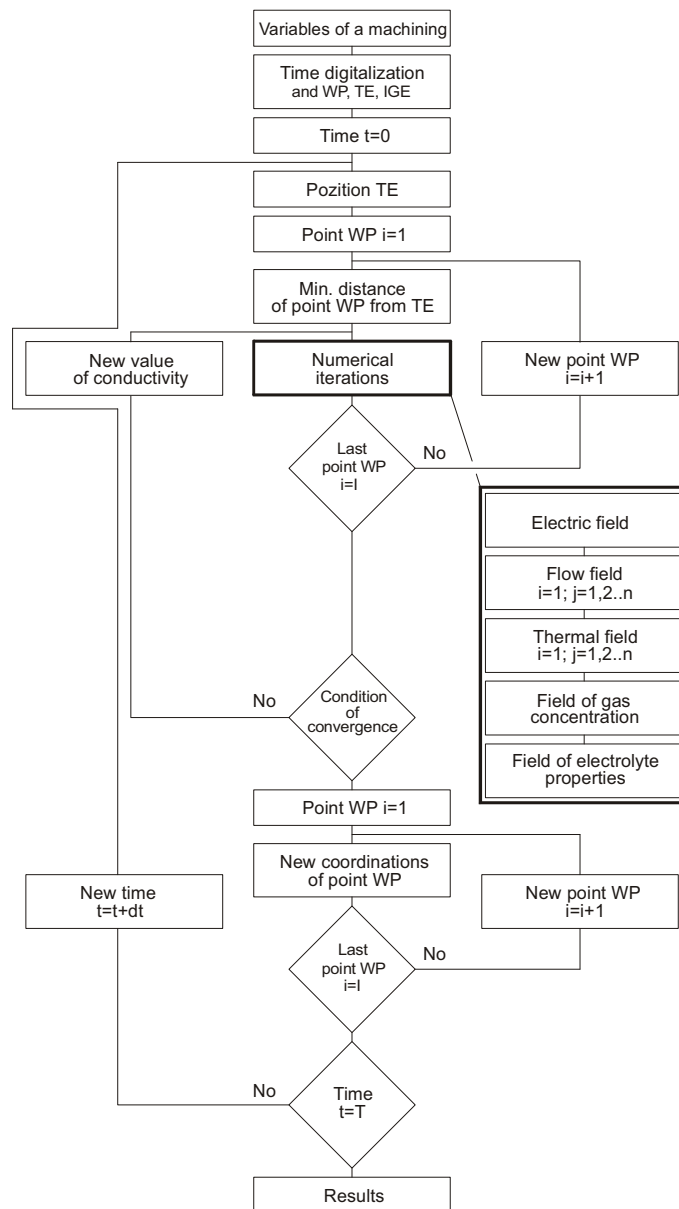


Fig.2. ECM computer simulation algorithm

For calculations the following, machining parameters were accepted:

Initial gap	h_o	0.2 mm
Speed of move forward of TE		0.01 mm/s
V_f		
Interelectrode voltage		15 V
U		
Volume rate		3 l/min
Q		
Pressure		0,1 MPa
p_z		
Rotational speed of WP		0, 1200 obr/min
n		

The obtained results have been illustrated in charts (Fig.3-8) which demonstrates distributions of: interelectrode gap height h , current density j , temperature T_m , void fraction β , velocity V_m , and pressure p along the interelectrode gap (IEG).

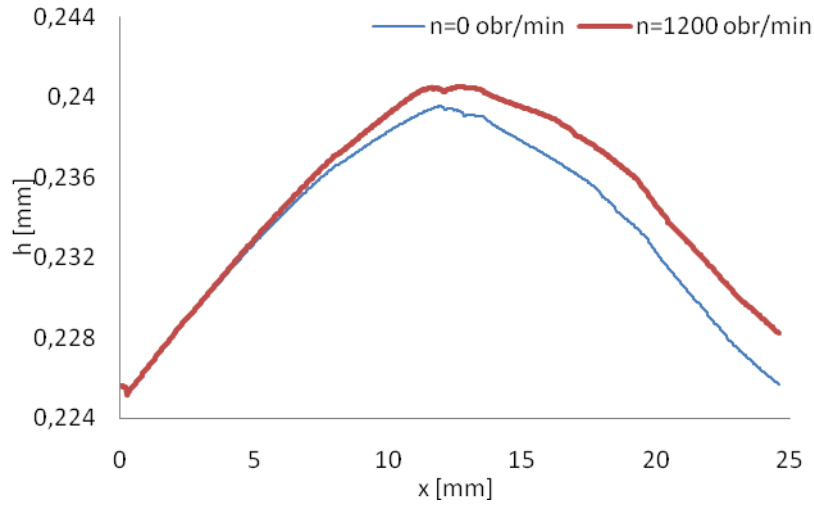


Fig. 3. Distribution of gap height h along IEG

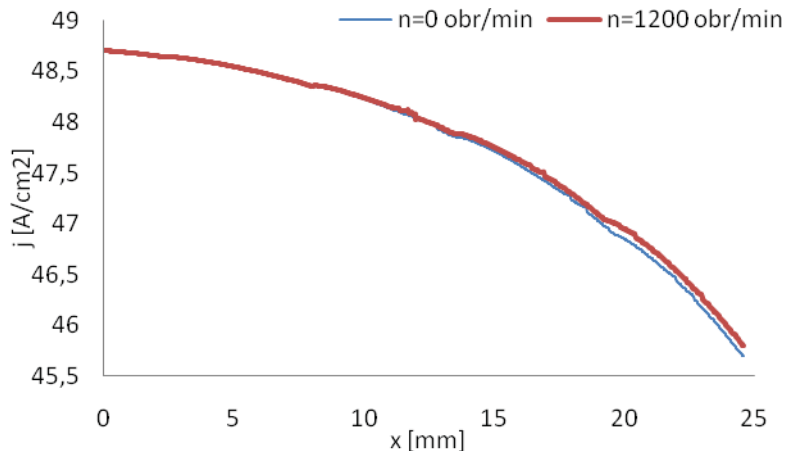


Fig. 4. Distribution of current density j along IEG

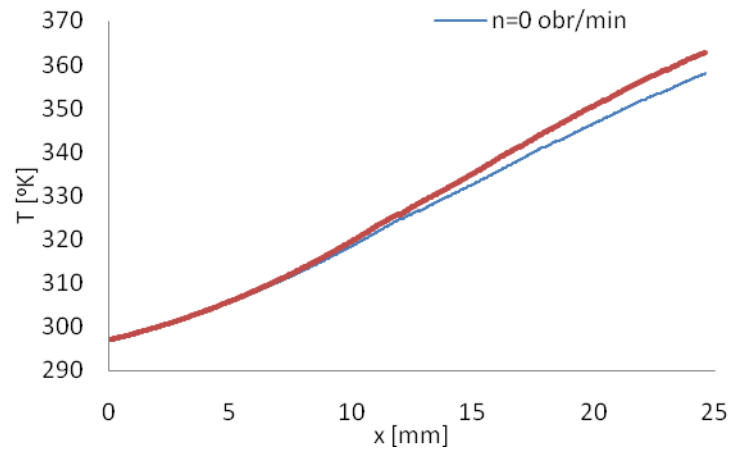


Fig. 5. Distribution of average temperature T along IEG

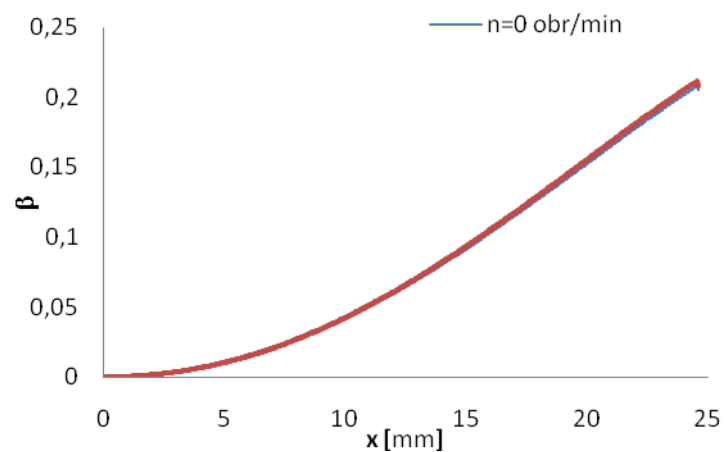


Fig. 6. Distribution of void fraction β along IEG

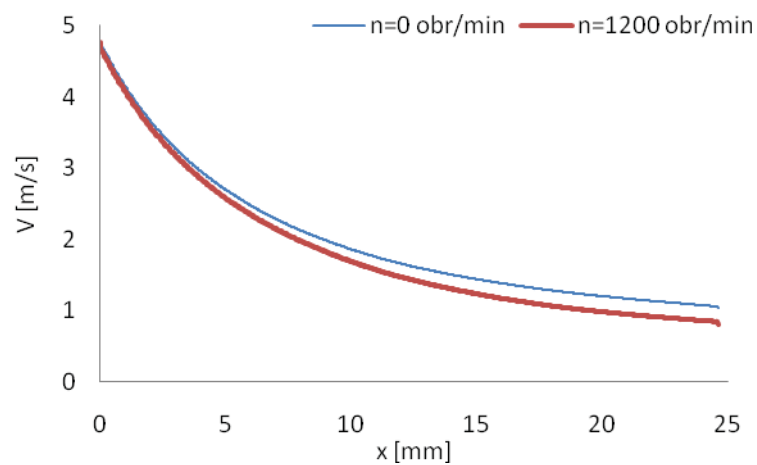


Fig. 7. Distribution of average velocity V along IEG

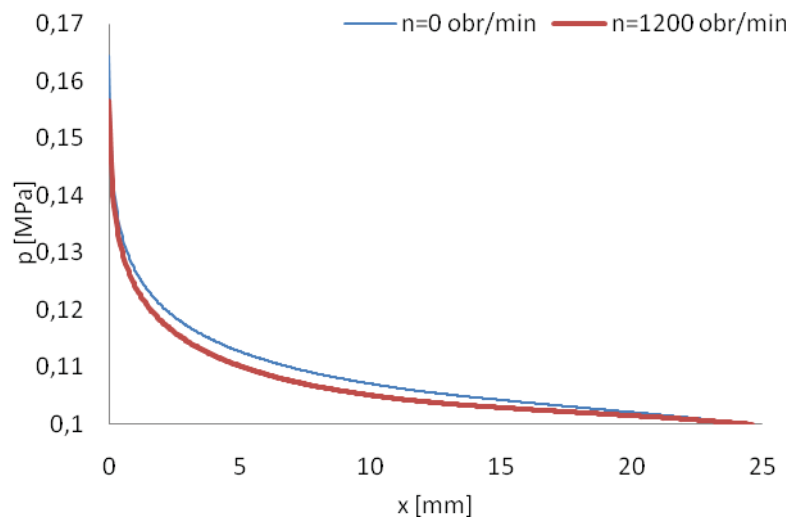


Fig. 8. Distribution of pressure p along IEG

The above presented charts allow for formulation of the following conclusions:

- Local changes of the interelectrode gap thickness are a result of different dissolution velocities as well as dynamically changing physical conditions within the interelectrode gap.
- Distribution of current density along interelectrode gap (IEG) depends on the gap section field and frequently changing physical parameters of the flow caused by electrochemical dissolution
- Temperature of the electrolyte and hydrogen mixture increases gradually along the interelectrode gap during the set machining time
- Distribution of void fracture in the interelectrode gap (IEG), determined from equation of the hydrogen flow continuity, demonstrates changes in proportions of hydrogen volume in the electrolyte along the way of the mixture flow.
- Distributions of pressure and the mean velocity along the gap is caused mainly by changes of the interelectrode gap (IEG) section field in the set machining time.
- It should be noticed that the rotational speed of the workpiece (WP) have a specially large influence on the gap height.

References

- [1] Wilson, J.F., *Practice and Theory of Electrochemical Machining*, New York, Wiley, 1971.
- [2] McGeough, J.A., *Principles of Electrochemical Machining*, London: Chapman & Hall, 1974.
- [3] Ruszaj, A.: *Niekonwencjonalne metody wytwarzania elementów maszyn i narzędzi*. IOS Kraków 1999.
- [4] Kozak, J., *Kształtowanie powierzchni obróbką elektrochemiczną bezstykową (ECM)*. Pr. Naukowe PW, Mechanika nr 41, Wydawnictwo Politechniki Warszawskiej, Warszawa. 1976.
- [5] Kozak, J., *Mathematical Models for Computer Simulation of Electrochemical Machining Process*. Journal of Materials Processing Technology, Vol. 76, 1976.
- [6] Dąbrowski, L., *Podstawy komputerowej symulacji kształtowania elektrochemicznego*. Prace Naukowe, Mechanikaz. 154, Wydaw. Politechniki Warszawskiej, Warszawa, 1992.
- [7] Łubkowski, K., *Stany krytyczne w obróbce elektrochemicznej*. Prace naukowe, Mechanika, z.163, Oficyna Wydawnicza PW, Warszawa, 1996.
- [8] Tipton, H., *Calculation of tool shape for ECM in fundament of Electrochemical Machining* (Edited by C.I. Faust), Electrochemical Society Softbound Symposium Series, Princeton. 1971.
- [9] Fitz-Gerald, J. M., McGeough, J. A., Marsh, L. McL., *Mathematical theory of electrochemical machining 2. Anodic shaping*. J. Inst. Maths Appl. 5, 1969.
- [10] Alkire, R. C., Bergh, T., Sani, R. L., *Predicting electrode shape change with use of finite element methods*, J. Electrochem. Soc. 125. 1978.
- [11] Davydov, A.D., Kozak, J., *Wysokoskorostnyje elektrochimizjeskoje formoobrazowanie*. Nauka, Moskwa, 1990.
- [12] Sautebin, R., Froidevaux, H., Landolt, D., *Theoretical and experimental modeling of surface leveling in ECM under primary current distribution conditions*. J. Electrochem. Soc. 127(5), 1980.
- [13] Jain, V. K., Pandey, P. C., *Tooling design for ECM-A finite element approach*, Trans. ASME. J. Engng Industry 103, 1981.
- [14] Prentice, G. A, Tobias, C. W. *A survey of numerical methods and solution for current distribution problems*. J. Electrochem. Soc. 119(1), 1982b.

- [15] Bialecki, R., Nahlik, R., Lapkowski, M., *Applying the boundary element method to electrochemical calculations of primary current distribution*. Electrochim. Acta 19(7). 1984.
- [16] Hume III, E. C., Deen, W. M., Brown, R. A., *Comparison of boundary and finite element methods for moving-boundary problems governed by a potential*, Int. J. Numer. Methods Engng 21, 1985.
- [17] Zhou, Y., *Finite element analysis of electrochemical machining problems validity of electroneutrality assumption. and flow in solution crystal growth system*. Ph.D. thesis. Department of Chemical Engineering and Materials Science, University of Minnesota. Minneapolis. MN. 1995.
- [18] Prentice, G. A., Tobias, C. W., *Simulation of changing electrode profiles*. J. Electrochem. Soc. 119(1), 1982.
- [19] Dukovic, J. O., *Computation of current distribution in electrodeposition*. A review. IBM J. Res. Develop. 34, 1990.
- [20] Sawicki, J., Paczkowski, J., *Obróbka elektrochemiczna krzywoliniowych powierzchni obrotowych*. Zeszyty Naukowe ATR nr 234 Mechanika 54, Bydgoszcz, 2004 r.
- [21] Paczkowski, T., Sawicki, J., *Electrochemical machining of curvilinear surfaces*, Journal of Machining Science and Technology, 2008 USA.



VERIFICATION OF SELECTED METHODS FOR RAPID DETERMINATION OF WÖHLER CURVE CONSIDERING HIGH-CYCLE FATIGUE

Janusz Sempruch¹, Przemysław Strzelecki²

*University of Technology and Life Sciences
Faculty of Mechanical Engineering,
ul. S. Kaliskiego 7, 85-789 Bydgoszcz, Poland
tel.: +48 52 3408223¹
e-mail: janusz.sempruch@utp.edu.pl¹
e-mail: przemstrzel@poczta.onet.pl²*

Abstract

The researches considered the problem for analytic determination of fatigue characteristic, treating the methods as rapid and approximate estimation of true curves. Selected two methods are presented. The selection was made on the grounds of popularity of the proposal. True characteristics were juxtapositioned with estimated ones, taken from reaches published in the references. A critical comparison of characteristics of both methods was made. Analyses for correct functioning of both methods were made on the grounds of researches on steel test samples. The result of the researches is presented in quantitative as well as qualitative form.

Keywords: fatigue strength, fatigue curves, analytic methods for Wöhler characteristics estimation.

1. Problem formulation

Determination of Wöhler curve for construction elements or materials according to recommendations of relevant standards e.g. [7] provides very precise result (which is an advantage of the approach), but unfortunately, due to time of realization for the researches, it generates considerable costs (which is a disadvantage of the method). The standard [7] recommends researches on at least 5 levels of load, minimum 3 test samples each with frequency of load change $5 \div 100$ Hz. It is also worth mentioning, that the result is very conservative as far as its connection with conditions of researches are concerned.

Such situation has lead in references to numerous proposals of analytic methods as well as analytic methods supported with simple experiment, aiming to estimated (rapid too) determination of Wöhler characteristics. The methods are mainly designed for engineering use.

2. Presentation of selected methods

The following methods were selected for the range of high-cycle strength. They enable to determine estimated fatigue curve after performing a simple experiment (tensile strength test). Another factor which influenced the selection of the methods was the ease of use for an engineer.

Recommended approach described in procedures of FITNET ([5]) assumes the use of general knowledge on fatigue reaction of some groups of materials in specified load conditions. Values on - fig. 1 – depend on the type of stress dominating during the fatigue process of destruction ($m = 5$ for normal stress and $m = 8$ for tangential stress). The value of fatigue limit is determined for point 10^6 of cycles. The above mentioned regards steel (excluding austenitic steel) and cast steel. For other construction materials and already mentioned austenitic steel, for the range of number of cycles from 10^6 to 10^8 cycles, it is estimated to use m_D , respectively 15 and 25.

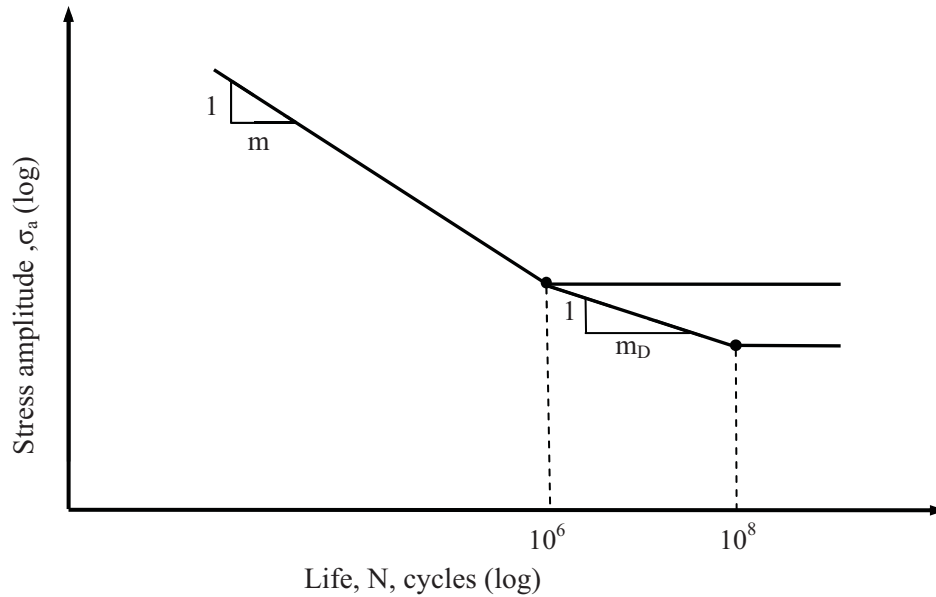


Fig. 1. Fatigue curve - estimated Wöhler curve according to [5] (designations as of the source work)

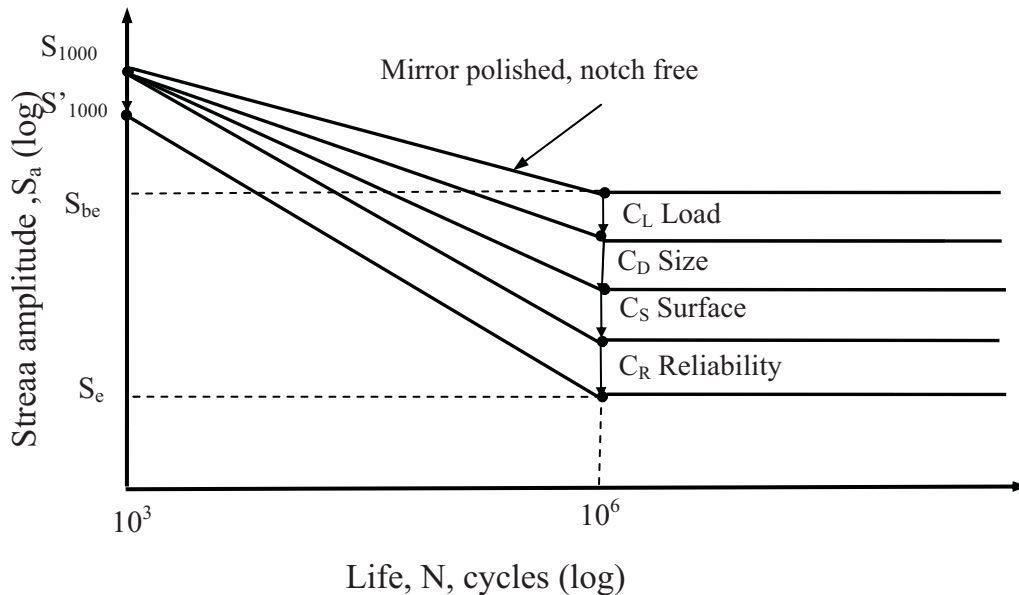


Fig. 2. Fatigue curve – modified curve S-N according to [3] (designations as of the source work)

The work [3] presents the method where determination of the line corresponding to limited fatigue strength is based on the knowledge of temporal tensile strength R_m . The value is easy to obtain via experimental methods, the data identifying the precise construction material (batch, delivery etc.). According to the data, one determines points: S_{1000} – on tensile axis and S_{be} (fatigue limit) connected with fatigue life expressed via base number of cycles.

$$S_{1000} = R_m \cdot w_1, \quad (1)$$

where:

w_1 – depends on the type of material and type of load [3],

$$S_{be} = R_m \cdot w_2, \quad (2)$$

where:

w_2 – depends on the type of material and is connected with indication on recommended base number of cycles (on fig. 2 for example 10^6) [3].

Both presented methods take calculations for smooth test samples (basic curves) into account and for test samples (quasi-construction elements) with defined state of the surface, with respect to the scale effect and the type of employed loads. It is briefly showed on figure 2.

3. The scope and verification method for analysed approaches

In order to perform verification of the above mentioned methods, required data were defined to enable determination of fatigue life according to the procedures. After required information had been obtained, determination of fatigue curves for individual materials was performed and presented on one figure. The results were used to perform quantitative analysis for methods of determination of characteristics according to the methodology from procedures of FITNET and publications [3]. The quantitative analyses employed values of unlimited fatigue life. Preliminary verification employed data of the following materials:

- S235JR to raw state [6],
- S355J0 in raw state [4],
- 15Cr2 quenched and tempered [6],
- 34CrMo4 normalised [1],
- 42CrMo4 after plastic forming [1],
- C40 normalised [1],
- C45 normalised [2],
- SAE 8630 quenched and tempered [1].

4. Verification results

Verification results presented as follows. Figures 3 to 8 illustrate lines corresponding to high-cycle fatigue characteristics for experimental data and estimated characteristics according both analysed methods.

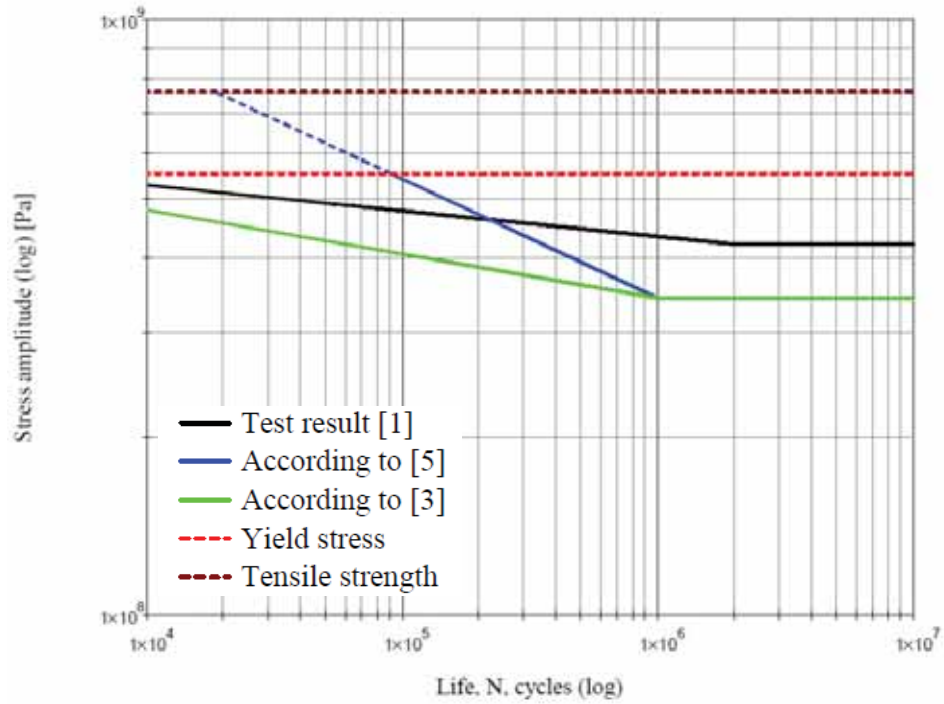


Fig. 3. Diagram presents comparison of estimation methods for high-cycle fatigue strength for 42CrMo4 steel after plastic forming

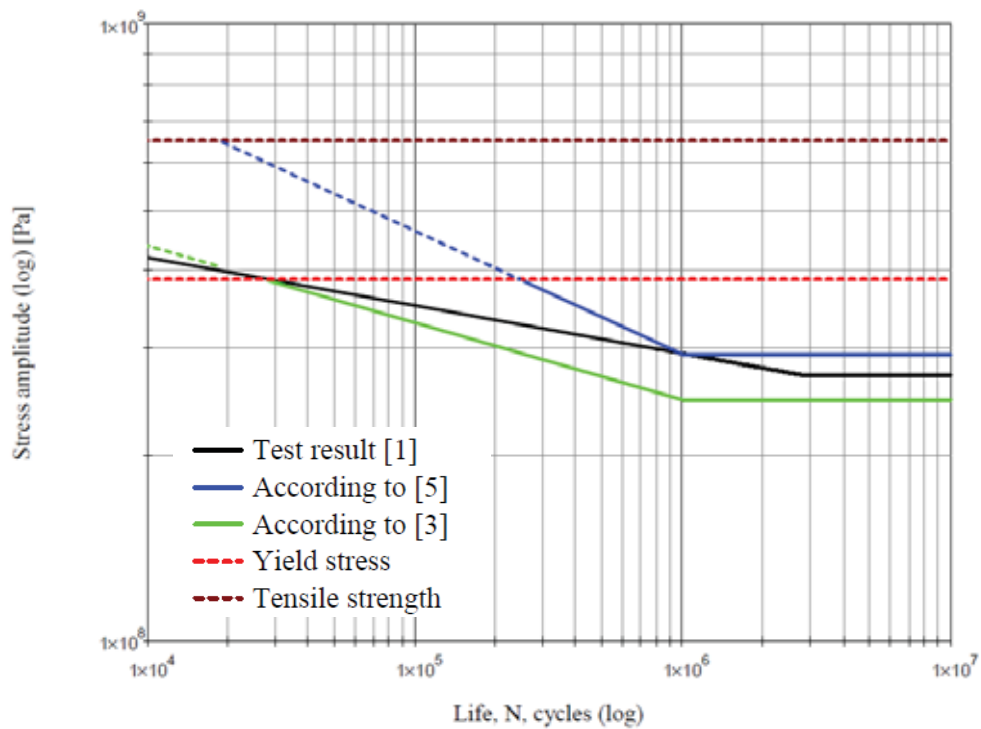


Fig. 4 Diagram presents comparison of estimation methods for high-cycle fatigue strength for C40 normalised steel

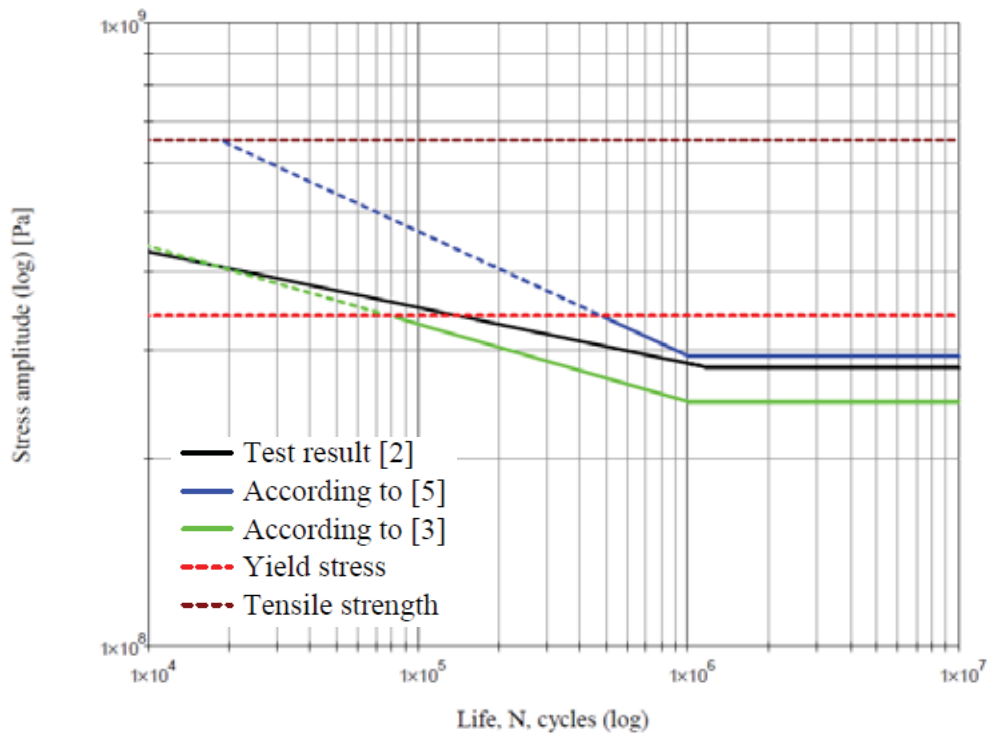


Fig. 5 Diagram presents comparison of estimation methods for high-cycle fatigue strength for C45 normalised steel

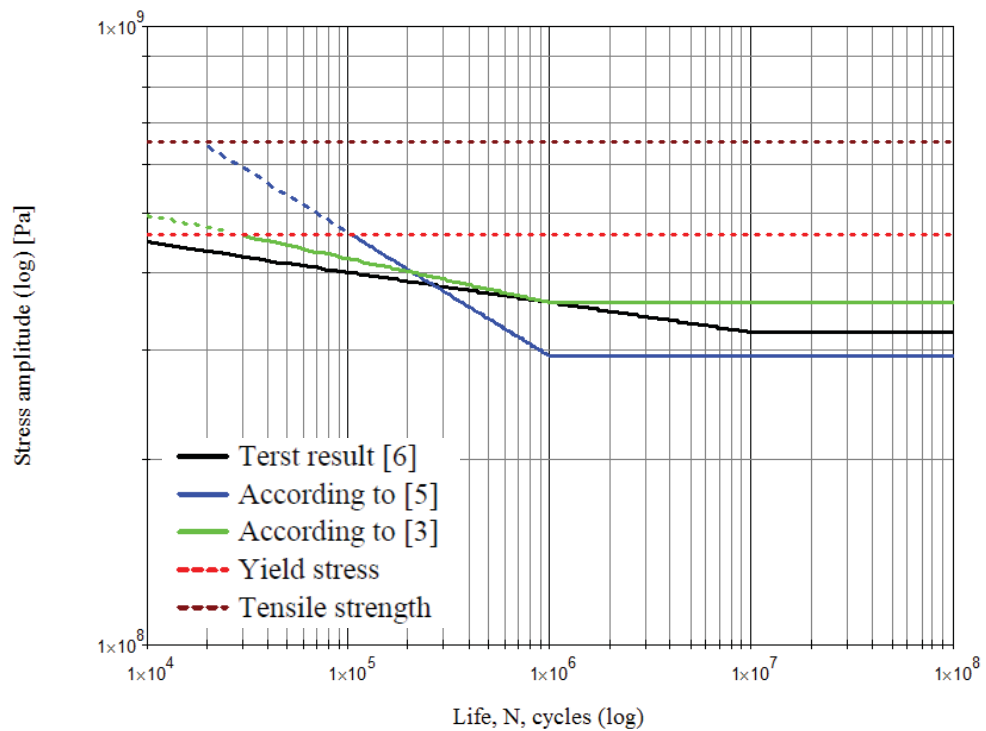


Fig. 6 Diagram presents comparison of estimation methods for high-cycle fatigue strength for 15Cr2 quenched and tempered steel

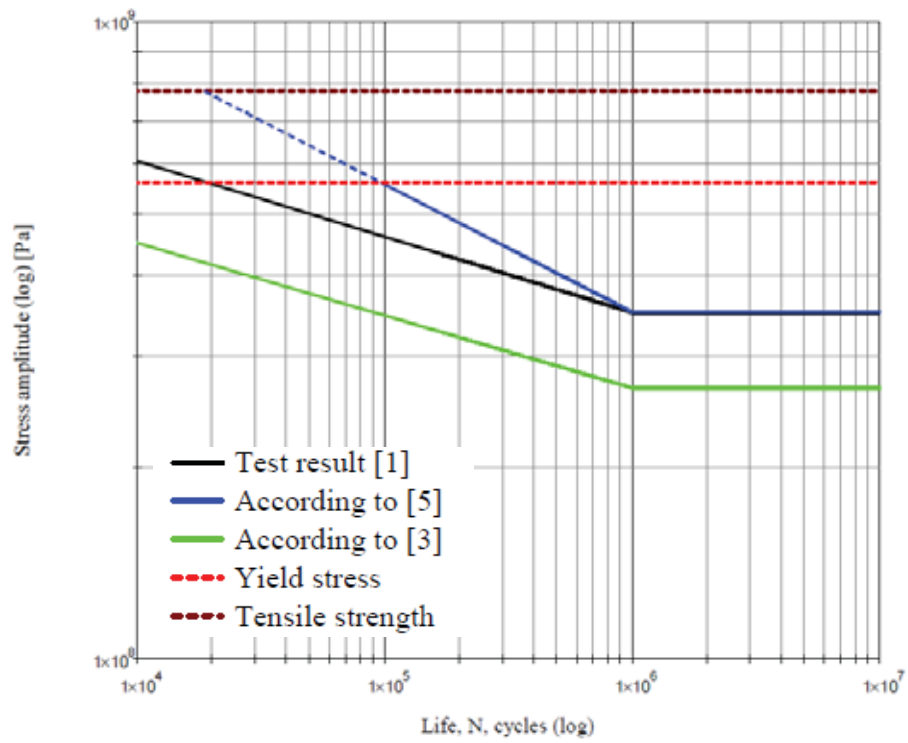


Fig. 7 Diagram presents comparison of estimation methods for high-cycle fatigue strength for 34CrMo4 normalised steel

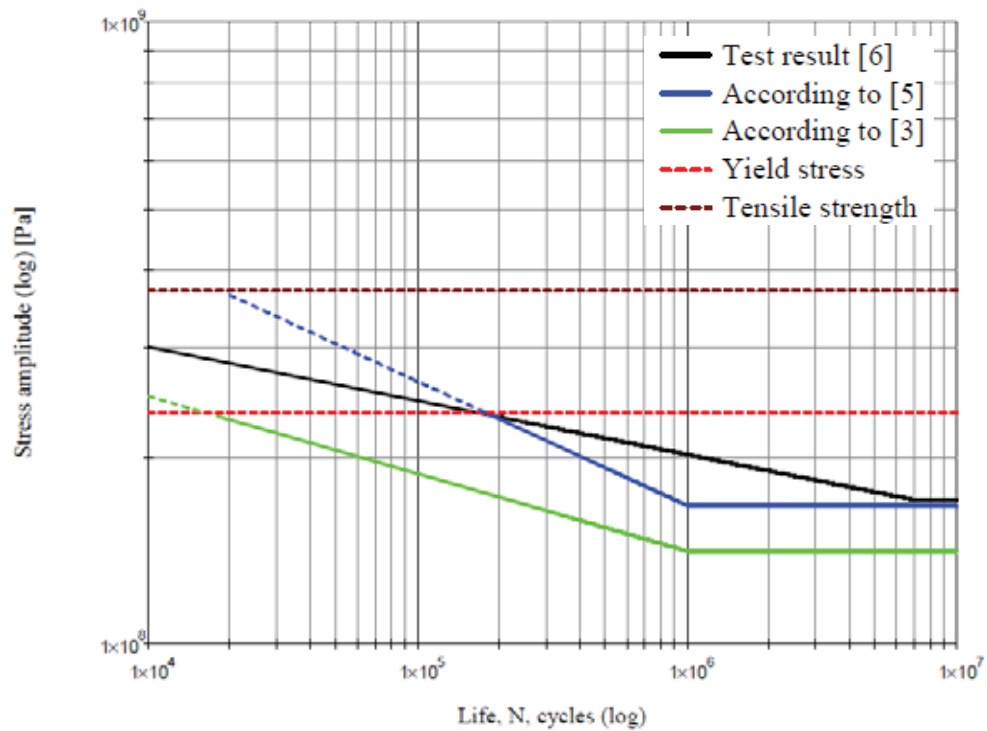


Fig. 8 Diagram presents comparison of estimation methods for high-cycle fatigue strength S235JR raw state steel

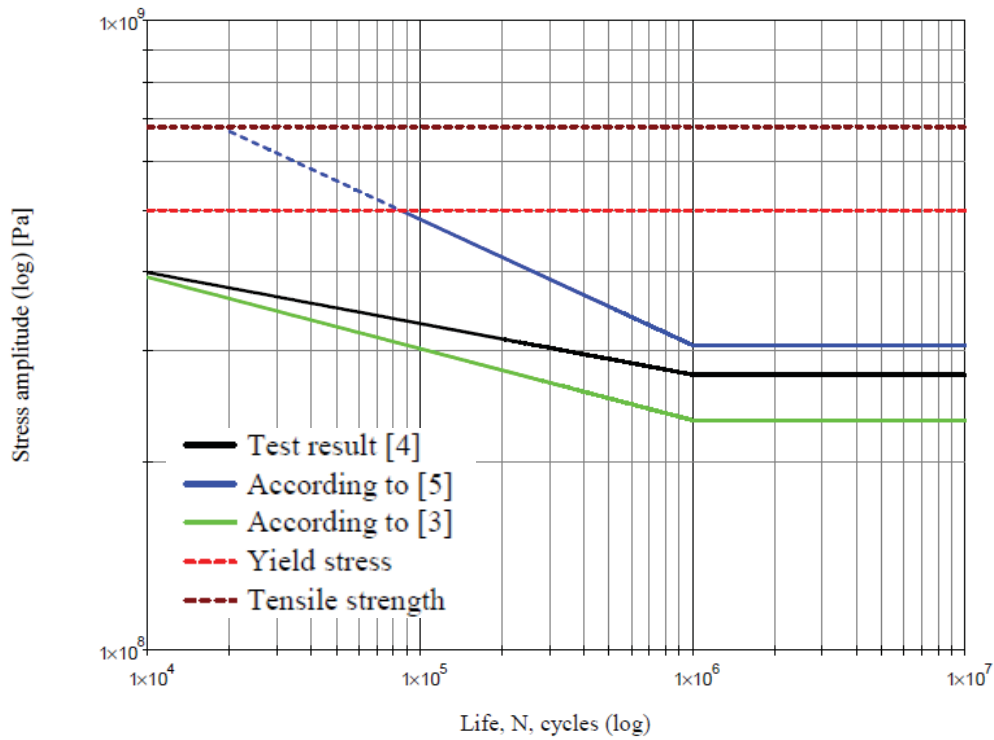


Fig. 9 Diagram presents comparison of estimation methods for high-cycle fatigue strength for S355J0 raw state steel

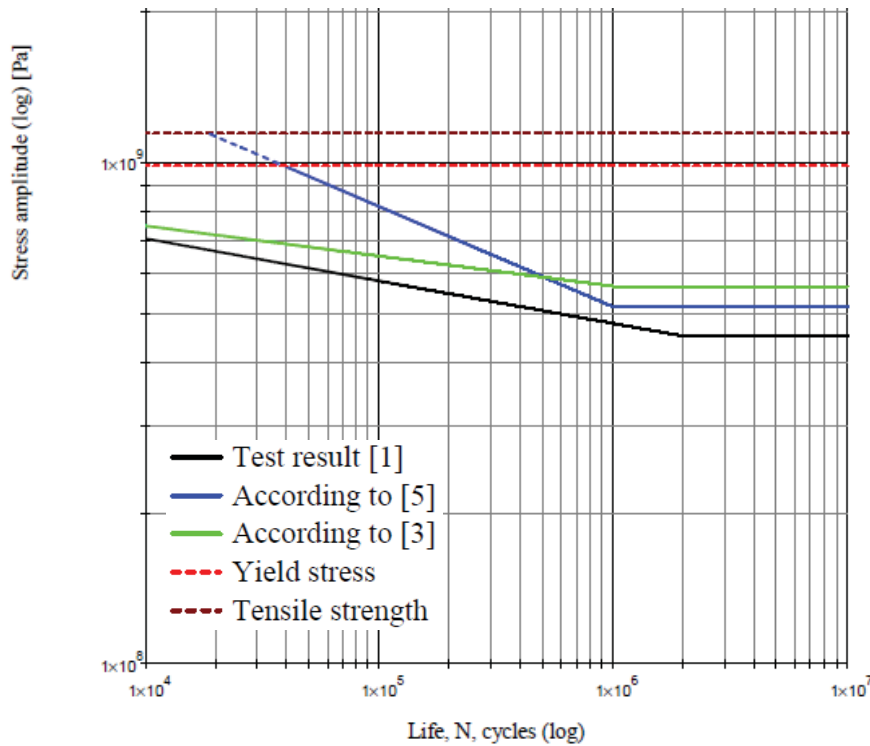


Fig. 10 Diagram presents comparison of estimation methods for high-cycle fatigue strength for SAE 8630 quenched and tempered steel

5. Quantitative and qualitative analyses

Diagram line presented on figures 3- 8 enable to perform qualitative analysis in the scope of their interlocation (on the safe side +, on the danger side -, crossing curves +/-). It is also possible to perform qualitative analysis of curve line gradient in the scope of limited fatigue life (estimated

line gradient is near to curve line according to experimental data +, worse situation from the point of view -). In the scope of unlimited fatigue life a quantitative analysis is possible (location of the estimated line below experimental data +, above -) as well as the quantitative revealing average percentage error. The results of analyses defined in such way presented in charts 1 and 2.

Tab. 1 Qualitative analysis of determination methods for high-cycle fatigue strength

Type of steel / state	A		B		C	
	[3]	[5]	[3]	[5]	[3]	[5]
S235JR/ in raw state	+	+	+	-	+	+
S355J0/ in raw state	+	-	+	-	+	-
15Cr2/quenched and tempered	-	+/-	+	-	-	+
34CrMo4/ normalised	+	-	+	-	+	+/-
42CrMo4/ after plastic forming	+	+/-	+	-	+	+
C40/ normalised	+	-	+	-	+	-
C45/ normalised	+	-	+	-	+	-
SAE 8630/ quenched and tempered	-	-	+	-	-	-
<p>Legend:</p> <p>A – Location of estimated curve line with respect to experimental line ($\sigma_a < R_e$), (+) – below experimental line, (-) – above experimental line, (+/-) – crosses experimental line.</p> <p>B – Gradient of part of the curve for limited fatigue life, (+) – gradient near to experimental line gradient, (-) – gradient noticeably different from experimental line gradient.</p> <p>C – Location of fatigue limit, (+) – below the fatigue limit of the experiment, (-) – above the fatigue limit of the experiment, (+/-) – fatigue limit is almost even.</p>						

Tab. 2 Value of fatigue limit – presented as a difference between experimental fatigue limit and fatigue limit calculated in MPa

Type of steel / state	[3]	[5]
S235JR/ in raw state	29,4	3,5
S355J0/ in raw state	42,1	-31,1
15Cr2/ quenched and tempered	-37,5	27,5
34CrMo4/ normalised	83,6	-0,6
42CrMo4/ after plastic forming	78,9	78,9
C40/ normalised	23,8	-21,6
C45/ normalised	33,0	-12,5
SAE 8630 /quenched and tempered	-116,3	-68,4

Data statement of the chart 1 shows specific tendency. Very noticeable is that of the column „B”, where the method described in [3] has gained the result of „+”. Conclusions on the analysis as follows.

6. Summary

Performed analysis enables to conclude the following:

- location of the estimated fatigue life line, regarding the group of materials for which the analysis were made, is more beneficial for the method according to the publication [3],
- performing the qualitative comparison of curve gradient in the scope of limited fatigue life, the performed analysis shows estimation from publication [3] as more beneficial,
- as far as estimation of fatigue life is concerned, both methods are comparable,
- in the scope of the qualitative analysis deviation of experimental, defined fatigue limit and limited fatigue life – average error values are more beneficial for the FITNET method.

It shall be stressed that the statement of data, analysis and its conclusions apply to limited group of materials. Verification shows defined tendency and indicates purposefulness to present a wider group of materials.

References

- [1] American Society for Metals, *Atlas of fatigue curves*, Edited by Boyer H.E. American Society for Metals, 2003.
- [2] Kocańda, S., Szala, J., *Podstawy obliczeń zmęczeniowych*, PWN, pp. 17, Warszawa 1997, Wydanie trzecie.
- [3] Lee, Yung-Li, Pan, J., Hathaway, R. B., Barkey, M. E., *Fatigue testing and analysis*, University of Alabama, Elsevier, pp. 126-171, 2005.
- [4] Materiały XXIII Sympozjum *Zmęczenie i Mechanika Pękania*, Uniwersytet Technologiczno Przyrodniczy, pp. 417, Bydgoszcz 2010,

- [5] Neimitz, A., Dzioba, I., Graba, M., Okrajni, J., *Ocena wytrzymałości, trwałości i bezpieczeństwa pracy elementów konstrukcyjnych zawierających defekty*, Politechnika Świętokrzyska, pp. 131-183, Kielce 2008.
- [6] Niezgodziński, M.E., Niezgodziński, T., *Obliczenia zmęczeniowe elementów maszyn*, PWN, pp. 18-23, Warszawa 1973.
- [7] PN-H-04325:1976, *Pojęcia podstawowe i ogólne wytyczne przygotowania próbek oraz przeprowadzania prób*.

The work has been co-funded by EFS funds and the Budget within the framework of Zintegrowany Program Operacyjny Rozwoju Regionalnego (*The Integrated Regional Operational Programme for Regional Development*), Programme grantów 2008/2009 – ZPORR”.



FATIGUE CRITERION BASED ON THE HUBER-VON MISES-HENCKY CRITERION FOR NON-PROPORTIONAL LOADINGS

Dariusz Skibicki

*University of Technology and Life Sciences
Faculty of Mechanical Engineering
ul. S. Kaliskiego 7, 85-791 Bydgoszcz, Poland
tel.: +48 52 3408247, +48 52 3408223
email: dariusz.skibicki@utp.edu.pl*

Abstract

In the present paper to determine the calculated fatigue limit, under non-proportional loads, there has been proposed a modification of the Huber-von Mises-Hencky criterion. To do so the Novoshilov interpretation of that criterion was applied. As an 'effective amplitude', there was assumed the maximum value of shear stress in the non-proportional load cycle. There was also proposed the weight function showing preference of the directions of easy slip in network A2. Verification calculations were performed for literature data. The data included experimental fatigue limits reported under biaxial loads, sinusoidally variable from phase shift. The present results were compared with the Huber-von Mises-Hencky criterion. The analysis allowed for determining that the solutions proposed demonstrate greater accuracy, especially under loadings of a high degree of load non-proportionality.

Keywords: *multiaxial fatigue, fatigue criteria, integral approach*

1. Introduction

The application of the Huber-von Mises-Hencky criterion (HMH) to calculate the fatigue life and fatigue strength for non-proportional loads is problematic [1]. The criterion can be provided with varied physical interpretations: specific distortion strain energy, octahedral shear stress, root-mean-square value of principle shear stresses or, in a form proposed by Novoshilov, root-mean-square value with shear stresses on all the planes crossing the point in question [1], namely:

$$\sigma_{equ} = \sqrt{\frac{1}{4\pi} \int_{\gamma=0}^{\pi} \int_{\varphi=0}^{2\pi} (\tau_{\gamma\varphi})^2 \sin \gamma d\gamma d\varphi}, \quad (1)$$

where:

$\tau_{\gamma\varphi}$ – vector of shear stress, defined in plane Δ ,
 φ, γ – angles describing the location of plane Δ (Fig. 1).

The last mentioned interpretation has become the springboard for a group of solutions referred to as integral approach. It is claimed that such approach makes it possible to use the HMH criterion to describe non-proportional states of loadings. The proposals in that group of criteria

differ in their definition of ‘effective amplitude’ of shear stress $\tau_{\gamma\varphi,a}$. The most common are those proposed by Simbürger [after 2], Zenner [after 2] and Papadopoulos [3].

In Simbürger’s proposal the criterion has the form of:

$$A = \sqrt{\frac{15}{8\pi} \int_{\gamma=0}^{\pi} \int_{\varphi=0}^{2\pi} A_n^2 \sin \gamma d\gamma d\varphi} \leq 1 \quad (2)$$

where effective amplitude A_n is expressed as the relationship:

$$A_n = \frac{\sigma_{v,a} - m\sigma_{v,m}}{Z_{go}} \quad (3)$$

$$\sigma_{v,a} = a\sigma_{n,a} + b\tau_{n,a}, \sigma_{v,m} = a\sigma_{n,m} + b\tau_{n,m} \quad (4)$$

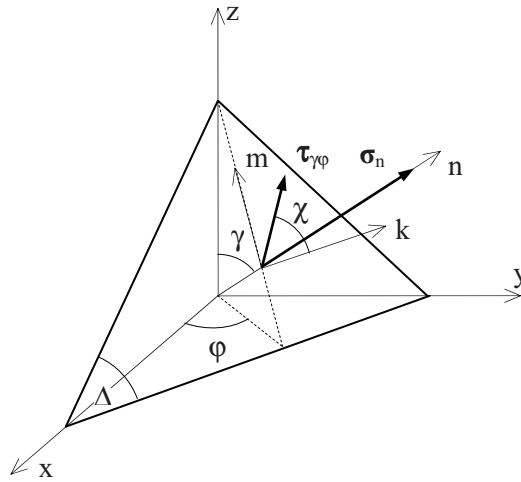


Fig. 1. Vector of shear stress $\tau_{\gamma\varphi}$ on the plane defined with angles φ and γ

Amplitudes and mean values of normal and shear stresses in (4) are determined based on the longest view method [4]. Zenner proposed a similar solution:

$$\sigma_{equ,a} = \sqrt{\frac{15}{8\pi} \int_{\gamma=0}^{\pi} \int_{\varphi=0}^{2\pi} \left[a\tau_{\gamma\varphi,a}^2 (1 + m\tau_{\gamma\varphi,m}^2) + a\sigma_{\gamma\varphi,a}^2 (1 + m\sigma_{\gamma\varphi,m}^2) \right] \sin \gamma d\gamma d\varphi} \leq Z_{go} \quad (5)$$

The Papadopoulos criterion is a sum of the greatest in all the planes Δ (Fig. 1) generalized amplitude of shear stress and maximum stress hydrostatic:

$$\tau_{eq,a} = \max_{\varphi,\gamma} (T_a) + a\sigma_{H,max} \leq Z_{so} \quad (6)$$

Generalized amplitude of shear stress for each plane Δ is determined from:

$$T_a(\varphi, \gamma) = \sqrt{\frac{1}{\pi} \int_{\chi=0}^{2\pi} \tau_a^2(\varphi, \gamma, \chi) d\chi} \quad (7)$$

where:

$$\tau_a(\varphi, \gamma, \chi) = \frac{1}{2} [\max_t \tau(\varphi, \gamma, \chi, t) - \min_t \tau(\varphi, \gamma, \chi, t)] \quad (8)$$

2. Criterion proposal

The present paper analyses the simplest solution assuming in (1), for each direction n , maximum value of shear stress $\tau_{\gamma\varphi} = \max_t(\tau_{\gamma\varphi})$ throughout the cycle. The criterion assumed the form of:

$$\sigma_{eq,a} = \sqrt{\frac{1}{4\pi} \int_{\gamma=0}^{\pi} \int_{\varphi=0}^{2\pi} (\max_t(\tau_{\gamma\varphi}))^2 \sin \gamma d\gamma d\varphi} \leq Z_{go} \quad (9)$$

For the states of stress of the components defined in line 6 table 1, the evolution of instantaneous values of stresses $\tau_{\gamma\varphi}$ for $\omega t = 0, 30, 60$ and 90° , has been presented respectively in Fig. 2.a, b, c and d. Hodograph for maximum values $\max_t(\tau_{\gamma\varphi})$ of that state of stress is visible in Fig. 2.e.

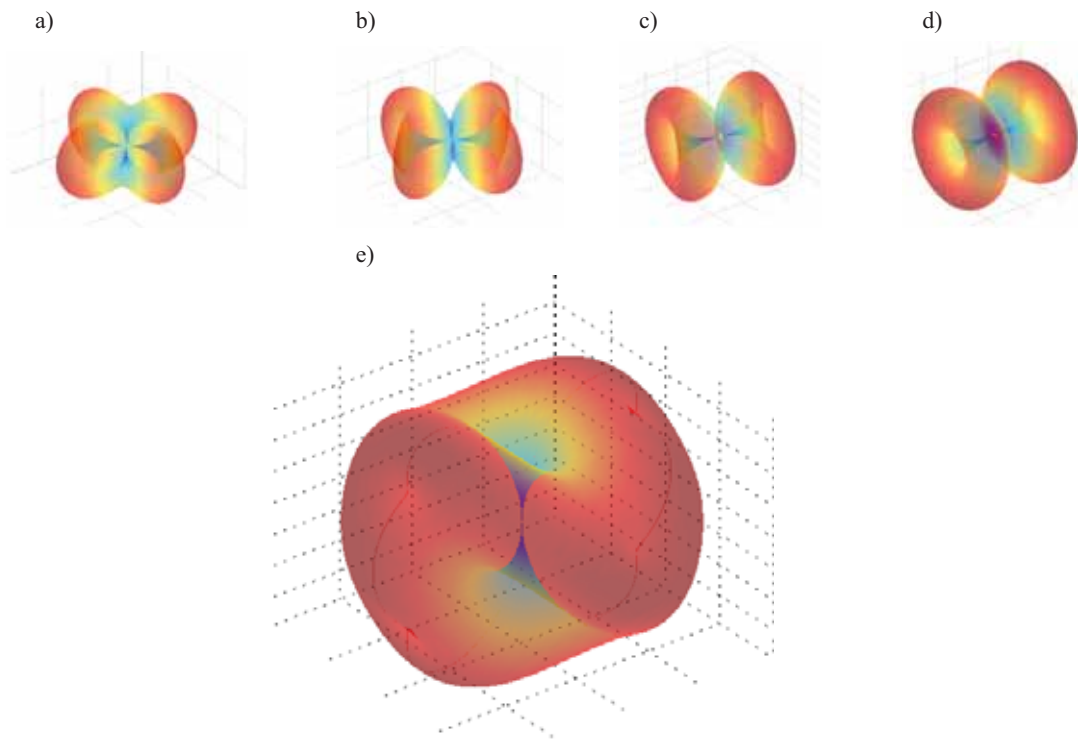


Fig. 2. Geometric form of weight function w (inside) against the respective maximum values of shear stresses throughout the loading cycle (outside)

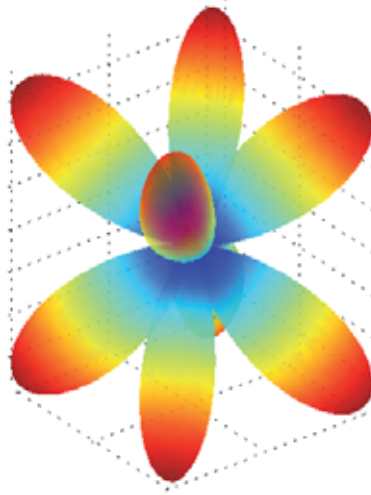
Besides, the present paper proposes the solution with weight function w demonstrating the preference of the directions of easy slip $\langle 111 \rangle$ in crystallographic network A2. The weight function has been assumed in a form of:

$$w = w_m + w_a \cdot \sin(2(\gamma - \pi/2))^2 \cdot \sin(2(\varphi - \pi/2))^2 \quad (10)$$

Its geometric form for value $w_m = 0, w_a = 1$ has been presented in Fig. 3.

The weight function must get oriented in such a way as to make its location against to the hodograph of the loading correspond to the situation of the least favourable location of the crystalline structure of the grain. The function must be rotated in a way as to make the direction of

one of its maxima coincide with the direction of the maximum value of the loading throughout the cycle. The geometric form of the rotated weight function against the maximum shear stresses is presented in Fig. 4.



Rys. 3. Geometric form of weight function w

The value of shear stress in equation (1) is determined, thus:

$$\tau_{\gamma\varphi} = \max_t(\tau_{\gamma\varphi}) \cdot w \quad (11)$$

Finally, the assumed value of the fatigue limit is obtained from:

$$\sigma_{eq,a} = \sqrt{\frac{1}{4\pi} \int_{\gamma=0}^{\pi} \int_{\varphi=0}^{2\pi} (\max_t(\tau_{\gamma\varphi}) \cdot w)^2 \sin \gamma d\gamma d\varphi} \leq Z_{go} \quad (12)$$

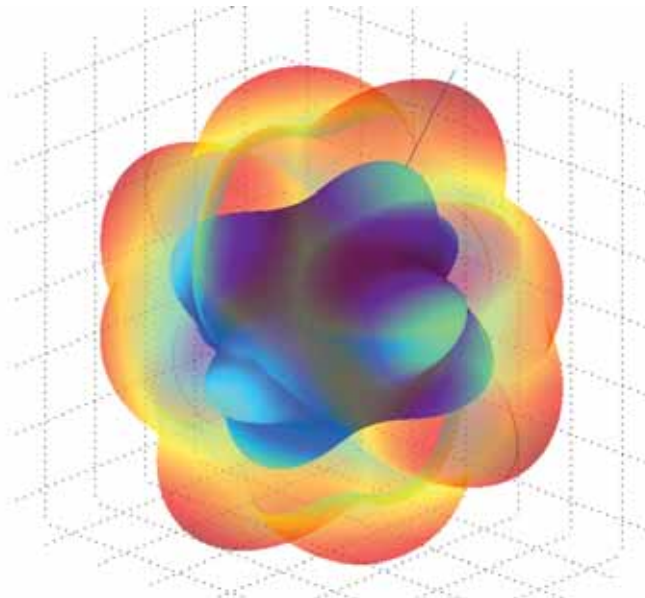


Fig. 4. Geometric form of the weight function w (inside) against the respective maximum values of shear stresses in the loading cycle (outside)

3. Results

The calculations were made for literature data [5], see breakdowns in columns 1, 2 and 3 Table 1. Those are the amplitudes of normal and shear stresses obtained from bending and torsion with phase-shift. Lines from 1 to 8 concern material ‘mild steel’ demonstrating properties $Z_{so} = 137.3$ MPa, $Z_{go} = 235.4$ MPa as well as $Z_{so}/Z_{go} = 0.58$, and lines from 9 to 18 concern material ‘hard steel’ demonstrating properties $Z_{so} = 196.2$ MPa, $Z_{go} = 313.9$ MPa as well as $Z_{so}/Z_{go} = 0.63$. For the purpose of the calculation of the values of coefficients in the equation of the weight function (10), there was assumed $w_m = 0,95$, $w_a = 0,05$.

The results of the calculations have been broken down in Table 1. In columns 4, 5 and 6 there have been noted the assumed values of fatigue limits, respectively, for the fatigue limits, respectively, for HMH criterion and both proposals. In columns 7, 8 and 9 there was noted a relative error of the calculated fatigue limit against the fatigue limit obtained experimentally.

One can note that for the proportional loadings (the angle of the phase shift equal 0) the results obtained with HMH criterion and the solution proposed (9) are identical. However, for non-proportional loadings the HMH criterion gives worse results.

The present results have been described with the mean value and standard deviation. For the HMH criterion the mean error value is 4.7% and standard deviation – 4.2%. For the criterion in integral form without weight function the results are better. There were obtained, respectively, 1.7% of the mean error value and 2.2% of the standard deviation. As for the criterion in an integral form with the weight function, the present results demonstrate the lowest mean error value – 0.3% and standard deviation of 2.2%.

Table 1. Results of calculations of the fatigue limit estimate

Item	Nisihary data [3]			Calculated fatigue limit			Relative terror of the calculated fatigue limit		
	$\sigma_{x,a}$ MPa	$\tau_{xy,a}$ MPa	ϕ °	HMH MPa	$\max(\tau_{\gamma\varphi})$ MPa	$\max(\tau_{\gamma\varphi}) \cdot w$ MPa	HMH %	$\max(\tau_{\gamma\varphi})$ %	$\max(\tau_{\gamma\varphi}) \cdot w$ %
	1	2	3	4	5	6	7	8	9
1	99.9	120.9	0	232.0	232	227	-1.4	-1.4	-3.6
2	103.6	125.4	60	240.6	231.6	226.9	2.2	-1.6	-3.6
3	108.9	131.8	90	252.9	239.7	234.9	7.4	1.8	-0.2
4	180.3	90.2	0	238.6	238.6	234	1.3	1.3	-0.6
5	191.4	95.7	60	253.2	240.4	235.9	7.6	2.1	0.2
6	201.1	100.6	90	266.1	247	242.4	13.0	4.9	3.0
7	213.2	44.8	0	226.9	226.9	222.9	-3.6	-3.6	-5.3
8	230.2	48.3	90	244.9	239	234.9	4.0	1.5	-0.2
9	138.1	167.1	0	320.7	320.7	314.3	2.2	2.2	0.1
10	140.4	169.9	30	326.1	321.9	315.5	3.9	2.5	0.5
11	145.7	176.3	60	338.3	325.6	319	7.8	3.7	1.6
12	150.2	181.7	90	348.7	330.5	323.8	11.1	5.3	3.2
13	245.3	122.7	0	324.6	324.6	318.6	3.4	3.4	1.5
14	249.7	124.9	30	330.4	324.7	318.8	5.2	3.4	1.6
15	252.4	126.2	60	333.9	317	311.2	6.4	1.0	-0.9
16	258	129	90	341.3	316.9	311	8.7	1.0	-0.9
17	299.1	62.8	0	318.3	318.3	312.8	1.4	1.4	-0.4
18	304.5	63.9	90	324.0	316.2	310.8	3.2	0.7	-1.0

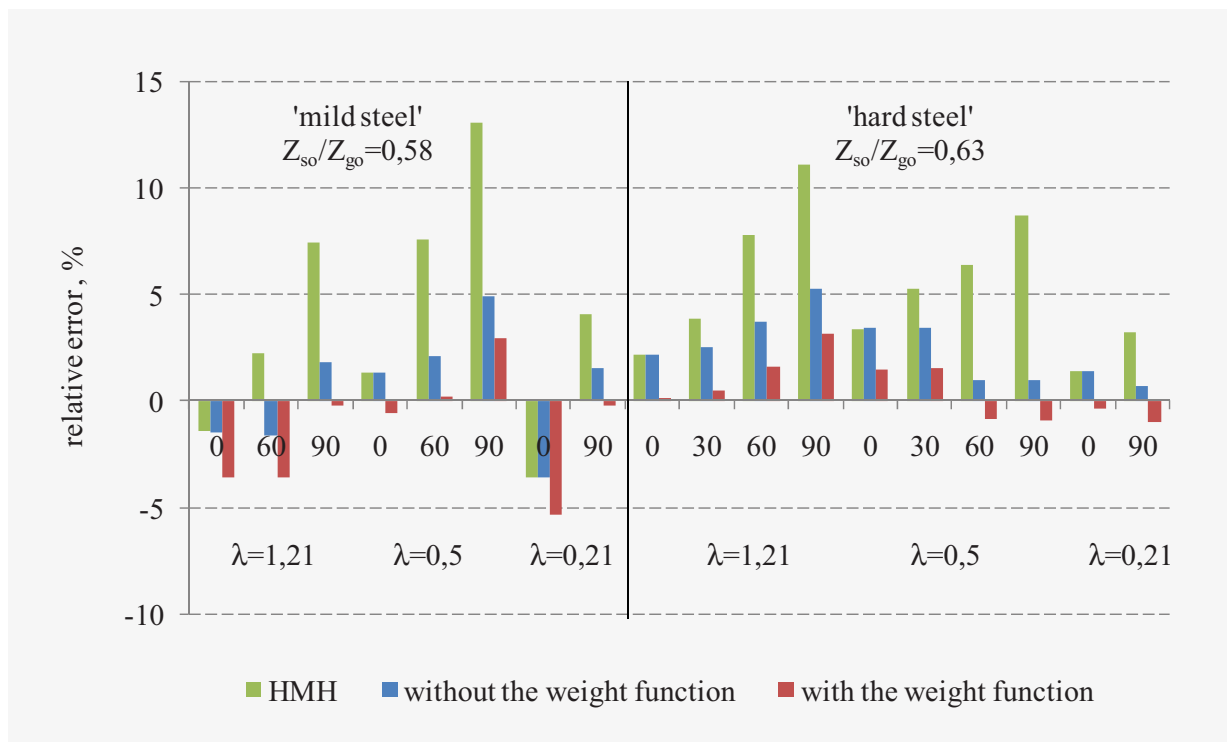


Fig. 5. Geometric form of weight function w (inside) against the respective maximum values of shear stresses throughout the loading cycle (outside)

4. Conclusions

1. The modification of the Novoshilov criterion involving the assumption the 'effective amplitude' in a form of the greatest value of shear stress in the cycle, enhanced the results of estimating the fatigue limit as compared with the Huber-von Mises-Hencky criterion, especially in the case of the loadings of a maximum degrees of non-proportionality of the loading.
2. The application of the weight function demonstrating the preference for the directions of easy slip in network A2 caused a further decrease in error of the estimated assumed value of the fatigue limit. Unfortunately, for the proportional loadings when the phase shift angle equals 0, there was recorded a slight deterioration of the results.

References

- [1] Liu, J., *Weakest link Theory and Multiaxial Criteria*, Proceedings of 5th International Conference on Biaxial/Multiaxial Fatigue and Fracture 1, pp. 45-62, 1997.
- [2] Zenner, H., Simbürger, A., Liu, J., *On the fatigue limit of ductile metals under complex multiaxial loading*, International Journal of Fatigue 22, pp. 137-145, 2000.
- [3] Papadopoulos, I., V., *A high-cycle fatigue criterion applied in biaxial and triaxial out-of-phase stress conditions*, Fatigue Fract Engng Mater Struct, pp. 18-79, 1995.
- [4] Papadopoulos, I., V., *Critical plane approaches in high-cycle fatigue: on the definition of the amplitude and mean value of the shear stress acting on the critical plane*, Fatigue Fract Engng Mater Struct 21, pp. 269-285, 1998.
- [5] Nisihara, T., Kawamoto, M., *The strength of metals under combined bending and twisting with phase difference*, Memoirs, College of Engineering, Kyoto Imperial University, pp. 85-112, 1945.



LOCAL STRAIN ANALYSIS IN FRICTION STIR WELDED 2024-T3 ALUMINIUM JOINTS UNDER CYCLIC LOADING

Robert Soltysiak

*University of Technology and Life Sciences
ul. Prof. S. Kaliskiego 7, 85-789 Bydgoszcz, Poland
tel.: +48 52 3408278, fax: +48 52 3408271
e-mail: robsol@utp.edu.pl*

Abstract

A geometrical notch effect and a structural notch effect have the main influence on the local stress and strain concentration in the welded joints. The value of this local stress and strain affects the fatigue life of the whole structural component. In order to mark this value using numerical or analytical methods, the local material properties from the individual zones need to be known.

Friction stir welding (FSW) is a relatively new joining method derived from conventional friction welding. This method of joining materials is finding a wider interest in the various industry fields, and the properties of these joints are the object of ongoing research.

In this paper, heterogeneous local strain distributions from the individual zones of a friction stir-welded sample of 2024T3 aluminum alloy are reported. Selected results of strain analysis in the form of hysteresis loops and diagrams of the plastic strain amplitude for particular joint zones for subsequent cycles are presented. The test was carried out under gradually increasing (Lo-Hi) sinusoidal cyclic loading with the stress ratio $R = -1$. Seven strain gauges with 0,6 mm gauge length were used to local strain measurement.

Keywords: FSW method, friction stir welding, local strain analysis, structural notch, strain gauge

1. Introduction

The progress in materials engineering and joining engineering results in the fact that new techniques of material joining are more and more widely used in engineering practice. The fatigue life of the welded joints made using the innovative techniques is approximate to the fatigue life of the base material. The difference in the fatigue life is primarily caused by the geometrical notch effect and the structural notch effect (e.g. caused by the temperature during joining). These notches lead to strain concentration and in consequence lead to the fatigue crack initiation.

The use of suitable rules of fatigue design in engineering practice leads to avoiding fatigue failures in welded structures. Generally we divide these rules into two basic groups: methods basing on the global approaches [9, 10] and methods basing on the local approaches [4, 8, 10, 17], including the fracture mechanics approach [6, 7, 10]. When we take into account that the initiation of the fatigue crack is located in the area of strain concentration, those local approach methods that are based on the value of the local strain deserve special attention.

Studying the strain distribution for welded joints has become a vital question, especially for those welded joints made using new techniques of material joining for which no standardized rules of assessing the fatigue strength and life have yet been established.

One of the new techniques of joining materials is the friction stir welding (FSW) method invented by The Welding Institute (TWI) in Cambridge in 1991 [21]. In the beginning the FSW method was used to join various aluminum alloy components. Today, due to rapid development, it is also used to join copper, magnesium, titanium, nickel, brass alloys, and even low-carbon and complex steel [e. g. 11, 13, 15, 16, 19, 20, 22, 23]. It is the most promising welding technique. The aviation aluminum alloys, such as 2000 and 7000 series, which are used by the aerospace industry to produce the components of airplanes such as skeleton parts, bulkheads, and longerons and so forth, were considered to be very poorly weldable. The FSW method allows for the welding of these alloys.

The FSW method makes possible the one-sided welding of 50-mm-thick aluminum alloy plate butt joints and the double-sided welding of 75-mm-thick aluminum alloy plate butt joints by welding half the thickness then turning over to complete the other side [5]. Friction stir processing is also used to modify the surfaces of casting aluminum. After this modification microstructures have relatively uniform distribution. Visible porosity and dendritic microstructures are eliminated and the ultimate tensile strengths, ductility and fatigue lives are increased [18].

The welded joints made using the FSW method are characterized by a lack of geometrical notches in the shape of porosity and slag ladle. However, modifications occur in the form of structural notches. In this type of joint researchers [e. g. 1, 2, 12] distinguished four heterogeneous zones: WN – weld nugget, TMAZ – thermo-mechanically affected zone, HAZ – heat affected zone, BM – base material. Each of them is characterized by different local material properties.

Friction stir welding is a relatively new joining method. However there are numerous scientific papers about it. Researchers [1, 2, 11, 12, 14, 15, 16, 19] presented mainly the heterogeneous macrostructure of individual zones and the local micro-hardness [1, 11, 12, 19]. Local strain analysis and the local material properties of individual zones are not marked in these papers.

This paper presents heterogeneous local strain distributions in the individual zones of a friction stir-welded sample of 2024T3 aluminum alloy. It is one of the first steps to determine the cyclic material properties in the form of stress-strain curves for individual zones. These curves are necessary to calculate local strain by using analytical methods (e. g.: the Neuber method or the Glinka-Molski method) or FEM (Finite Elements Method).

2. Research object

The welded joint was made from aluminum alloy 2024T3. The chemical composition of this aluminum was given in table 1. The material properties of samples taken parallel and perpendicular to the rolling direction (T3) are different. The properties of the parallel samples are better than the properties of the perpendicular samples. The material properties obtained in the tensile test of the perpendicular samples are presented in table 2.

Tab. 1. Chemical composition of aluminum alloy 2024T3

Chemical element	Si	Fe	Cu	Mn	Mg	Cr	Zn	Ti
%	0.06	0.16	4.70	0.63	1.50	0.01	0.16	0.03

Tab. 2. Properties obtained in tensile tests of aluminum alloy 2024T3 samples taken perpendicular to the direction of rolling

$S_{0.2}$	S_u	E	A	Z
MPa	MPa	MPa	%	%
324.20	479.00	69 676.00	20.28	24.60

The Friction Stir Welding method was used to weld two 300 x 150 x 4.1 mm aluminum alloy 2024T3 parallel to the direction of rolling. The joint was made by the Polish Welding Centre of Excellence in Gliwice using a numerically controlled friction welding machine equipped with the Triflute tool type with a shoulder diameter of 20 mm. The following parameters were used for the welding process: the tool rotational speed of 450 r/min and tool traverse speed of 160 mm/min.

The sample used for strain analysis was cut 30mm wide perpendicularly to the welding direction (Fig. 1). The face and the root of this sample were milled in order to remove the external geometrical notch, which could cause strain concentration. As a result a 2.73 mm thick sample was obtained (Fig. 2). After milling the surfaces were polished. Each of heterogeneous zones was situated in a series, transversely to the loading direction. Such a setting will enable the determination of the stress-strain curves for individual heterogeneity zones in the next results analysis [3].

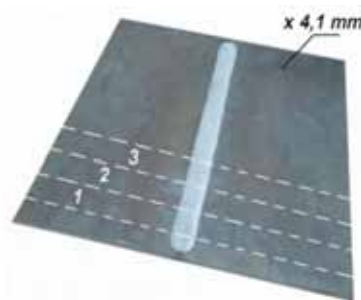


Fig. 1. The research object and the method of cutting samples.

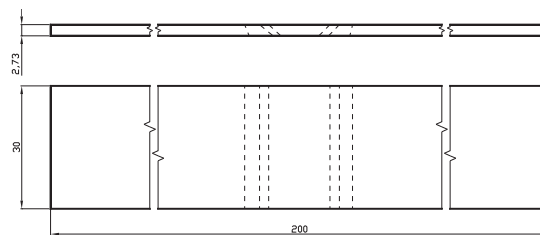


Fig. 2. The shape and the size of a sample for local strain analysis

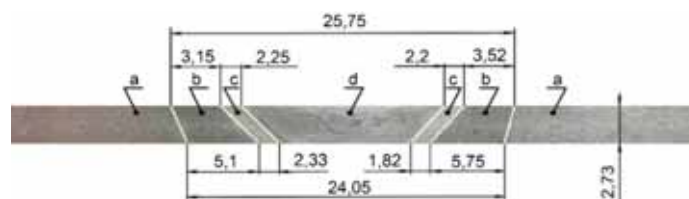


Fig. 3. Material macrostructures in a typical transversal section of an FSW joint of 2024T3 aluminum with the size and name of the heterogeneous zones: a) base material (BM), b) heat effected zone (HAZ) – without plastic deformation but thermallyaffected, c) thermo-mechanically affected zone (TMAZ) – with plastic deformation caused by the tool and significantly thermallyaffected, d) weld nugget (WN) – the recrystallized area in the TMAZ ofaluminum alloys

The macrostructure of the FSW joint was also studied. This allowed areas of the heterogeneous zones to be distinguished and their size to be defined (Fig. 3). The base material was characterized by a coarse-grained structure with visible grain deformations caused by the rolling treatment. The structure in the others zones affected by heat and also in the zones where the material has been plastically deformed by the tool were characterized by a fine-grained structure (Fig. 4).

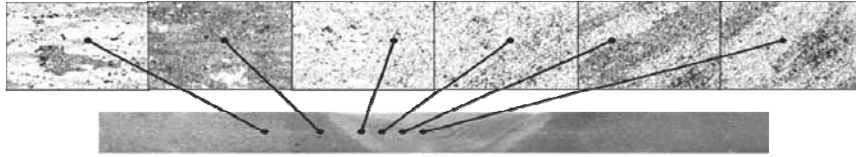


Fig. 4. Microstructure of a typical FSW joint

The hardness of the central part of the polished section was measured using the Vickers method (Fig. 5). The TMAZ was characterized by the lowest HV2 hardness, the HAZ was slightly higher, while the highest hardness, comparable to the BM, characterized the WN.

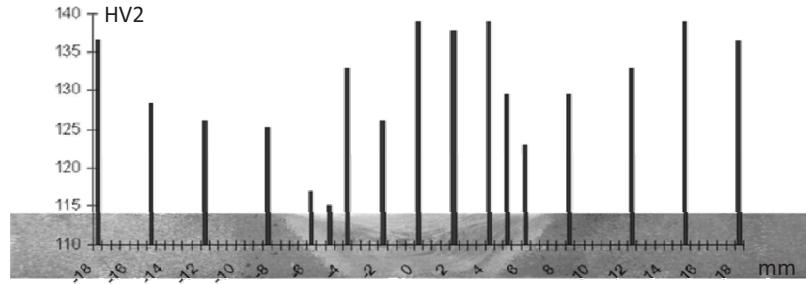


Fig. 5. HV2 hardness in an FSW joint

3. Research program

The local strain analysis was conducted at University of Technology and Life Sciences in Bydgoszcz. The loading was conducted on an INSTRON hydraulic testing machine, and the data was collected by an ESAM system and registered on a PC-class computer.

Because of the minute geometrical dimensions of heterogeneous zones strain gauges with a gauge length of 0,6mm were used. Seven such strain gauges were adhered to the tested sample according to the diagram in fig. 6. One strain gauge was attached to both sides of the TMAZ, HAZ and BM of the joint. One strain gauge was also attached to the WN. The sample was secured from buckling by 2 custom made flat bars (Fig. 7). In order to minimize friction the surface of the bars was covered with teflon tape.

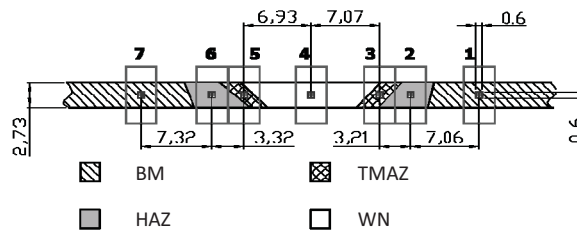


Fig. 6. The seating arrangements for seven strain gauges, no. 1- 7 represent the respective strain gauge

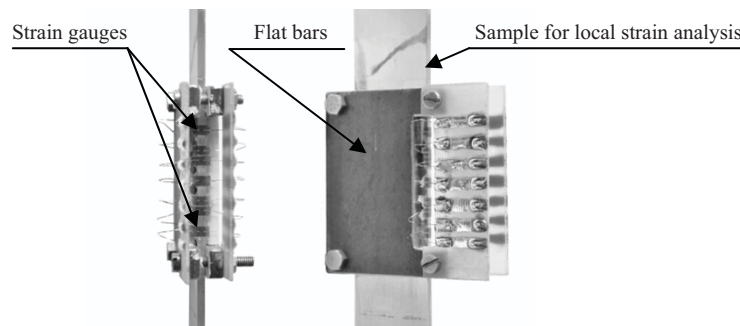


Fig. 7. Photograph of sample for local strain analysis with attached strain gauges and with two flat bars secured for buckling

Tab. 3. Research program

Loading level	1	2	3	4	5	6	7	8	9	10	11	12	13	14
Stress amplitude MPa	50	75	100	125	150	175	200	225	250	275	300	325	350	375
No. of cycles on the level N_i	100	100	100	100	100	100	100	100	100	100	100	100	100	100

Local strain analysis was conducted under a gradually increasing (Lo-Hi) sinusoidal cyclic loading with a stress ratio of $R = -1$, according to the research program presented in table 3. Loading spectrum is presented on Fig. 8.

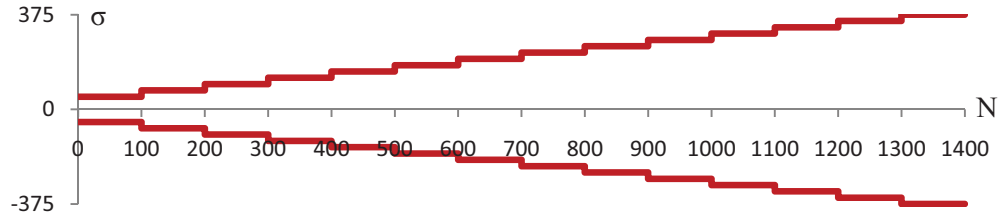


Fig. 8. Loading spectrum

4. Research results and analysis

The research was carried out on fourteen levels of stress amplitudes. One hundred hysteresis loops of each of these levels were obtained for individuals heterogeneous zones. Presented as an example are the hysteresis loops for readings obtained from strain gauges no. 1, 4, 7 (Fig. 9a) and 3, 5, 6 (Fig. 9b). Strain gauge no. 2 became partially damaged at this loading level. The hysteresis loops were taken from the middle of the 12th loading level (325 MPa), which corresponds in total to the 1150th cycle. Also presented as an example are the change in shape of the hysteresis loops for strain gauge no. 5 under increasing load (Fig. 10). The presented loops were taken from the middle of the 6th, 8th, 10th and 12th loading level.

The strain amplitude values were determined on the basis of hysteresis loops analysis. Presented as an example are the plastic strain amplitude values for particular joint zones for the subsequent cycles of the 10th loading level (Fig. 11a) and of the 13th loading level (Fig. 11b).

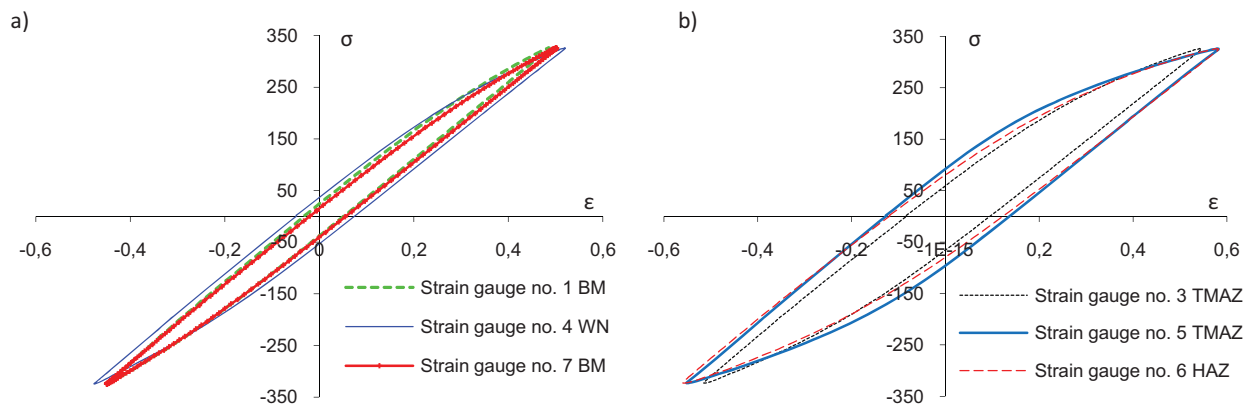


Fig. 9. The hysteresis loops obtained from the 1150th loading cycle (level 12): a) for the strain gauges no. 1, 4, 7 and b) for the strain gauges no. 3, 5 and 6

Similar plastic strain values on each loading level were obtained for the BM (strain gauge no.1 and no. 7) and for the WN (strain gauge no. 4). This lets us infer that the local material properties in these zones are nearly identical. The same conclusion is inferred from the hardness test analysis

of these zones. The highest values of the plastic strain was observed for TMAZ (strain gauge no. 5), and a somewhat lower one for HAZ (strain gauge no. 2).

The research has also shown a significant difference in the plastic strain values between same-named zones on both sides of the FSW joint. Higher plastic strain values were observed for HAZ from strain gauge no. 2 than for HAZ from strain gauge no. 6. TMAZ behaved in an opposite way, with strain gauge no. 3 giving a lower plastic stain value reading than strain gauge no. 5. TMAZ behaved in an opposite way, with strain gauge no. 3 giving a lower plastic stain value reading than strain gauge no. 5, but the behavior of the material in same-named zones was comparable. For example, the TMAZ material hardened and the HAZ material softened under increasing loading cycles. The difference in values of plastic strain amplitudes for same-named zones can most probably be attributed to the kinematics of the welding process.

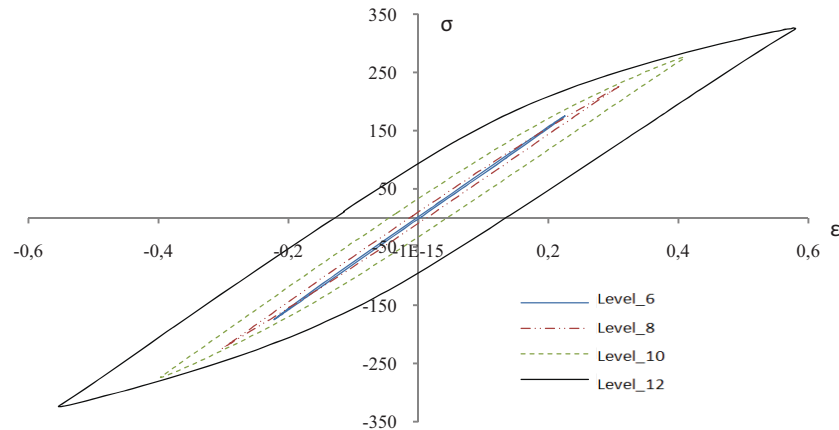


Fig. 10. The hysteresis loops of TMAZ from the middle of the 6th, 8th, 10th and 12th loading level

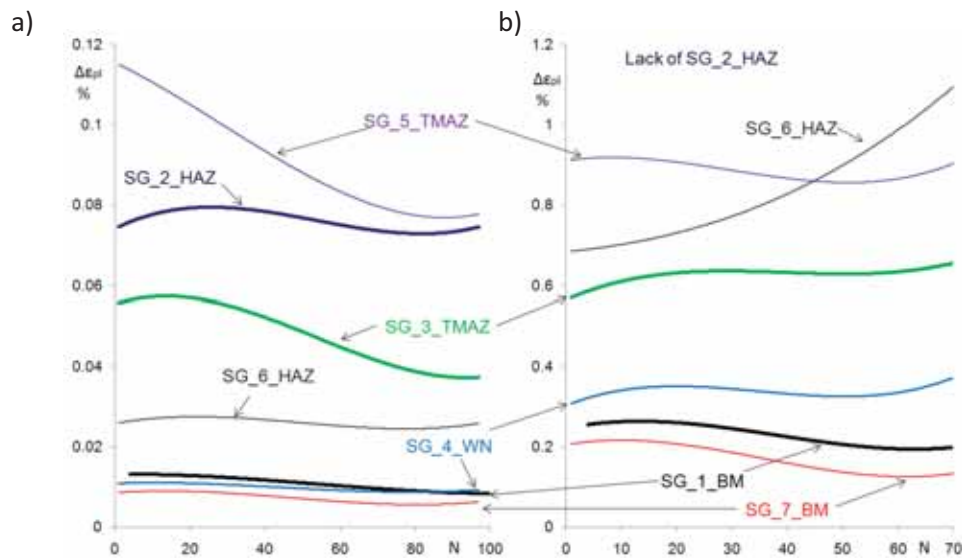


Fig. 11. The plastic strain amplitude values for particular joint zones for the subsequent cycles: a) of the 10th loading level b) of the 13th loading level

The crack initiation took place on the side of the HAZ where strain gauge no. 2 was first to become damaged. At the next level of loading the opposite HAZ was significantly softened, making it probable to become the next zone of crack initiation.

Further study of local stress analysis will enable the specification of the material properties of individual zones of an FSW joint. Use of these local material properties can improve numerical strain analysis of welded structures and at the same time contribute to the improvement of the local approach of fatigue life assessment of welded structures.

Referens

- [1] Bussu, G., Irving, P. E., *The role of residual stress and heat affected zone properties on fatigue crack propagation in friction stir welded 2024-T351 aluminum joints*, International Journal of Fatigue pp. 77–88, 25/2003.
- [2] Fratini, L., Zuccarello, B., *An analysis of through-thickness residual stresses in aluminium FSW butt joints*, International Journal of Machine Tools & Manufacture, pp. 611–619, 46/2006.
- [3] Jones, A., Hudd, R. C., *Cyclic stress-strain curves generated from random cyclic strain amplitude tests*, International Journal of Fatigue, pp. 521–530, 21/1999.
- [4] Karakas, Ö., Morgenstern, C., Sonsino, C. M., *Fatigue design of welded joints from the wrought magnesium alloy AZ31 by the local stress concept with the fictitious notch radii of $r_f = 1.0$ and 0.05 mm*, International Journal of Fatigue, pp. 2210–2219, 30/2008.
- [5] Klimpel, A., *Spawanie, zgrzewanie i cięcie metali*, WNT Warszawa 1999.
- [6] Lawrence, F. V., *Estimation of fatigue crack propagation life on butt welds*, Welding Journal, Research Supplement, pp. 212–220, Vol. 52/1973.
- [7] Lawrence, F. V., Munse, W. H., *Fatigue crack propagation in butt welds containing joint penetration defects*, Welding Journal, Research Supplement, pp. 221–225, Vol. 52/1973.
- [8] Maddox S. J., *Recommended Hot-Spot Stress Design S-N Curves for Fatigue Assessment of FPSOs*, International Journal of Offshore and Polar Engineering, TWI Limited, Granta Park, Great Abington, Cambridge CB1 6AL, UK
- [9] Maddox, S. J., *Fatigue design rules for welded structures*, Progress in Structural Engineering and Materials, pp. 102–109, vol.2, no.1, 2000.
- [10] Maddox, S. J., *Review of fatigue assessment procedures for welded aluminum structures*, International Journal of Fatigue, pp. 1359–1378, 25/2003.
- [11] Meran, C., *The joint properties of brass plates by friction stir welding*, Materials and Design pp.719–726, 27/2006.
- [12] Mishra, R. S., Ma, Z. Y., *Friction stir welding and processing*, Materials Science and Engineering, pp. 1–78, 50/2005.
- [13] Pietras, A., Zadroga, L., *Rozwój metody zgrzewania tarcowego z mieszaniem materiału zgrzeiny (FSW) i możliwości jej zastosowania*, Biuletyn Instytutu Spawalnictwa pp. 148–154, Nr 5/2003.
- [14] Pietras, A., Zadroga, L., *Zgrzewanie tarcowe aluminium z miedzią*, Problemy Eksploatacji – Zeszyty Naukowe Instytutu Technologii Eksploatacji, pp. 28–35, nr. 1/2004, Radom 2004.
- [15] Pietras, A., Adamiec, J., *Zgrzewanie aluminium z miedzią metodą FSW*, Biuletyn Instytutu Spawalnictwa, pp. 133–137, Nr 5/2005.
- [16] Pilarczyk, J., *Nowości w technologiach spawalniczych*, Inżynieria materiałowa, pp. 751–756, nr 6/2003.
- [17] Radaj, D., Sonsino, C. M., Flade, D., *Prediction of service fatigue strength of a welded tubular joint on the basis of the notch strain approach*, International Journal of Fatigue, pp. 471–480, 20 No. 6 /1998.
- [18] Santella, M. L., Engstrom, T., Storjohann, D., Pan, T.-Y., *Effects of friction stir processing on mechanical properties of the cast aluminum alloys A319 and A356*, ScriptaMaterialia, pp. 201–206, 53/2005.
- [19] Schilling, C., Sheihi, S., Dos Santos, J. F., Abspoel, M., *Zgrzewanie tarcowe FSW aluminiowych zbiorników paliwa*, Przegląd Spawalnictwa, pp. 14–16, 4/2003.
- [20] Strombeck, A., Santos, J. K., Torster, F., Laureano, P., Kocak, M., *Fracture toughness*

- behaviour of FSW joints on aluminum alloys*, 1st Symposium on Friction Stir Welding, Thousand Oaks, California, USA 1999.
- [21] Thomas, W. M., *Friction stir butt welding*, GB patent 9125978, 6.12.1991. International patent application PCT/GB92/02203.
- [22] Thomas, W. M., *Friction stir welding of ferrous materials: a feasibility study*, 1st Symposium on Friction Stir Welding, Thousand Oaks, California, USA 1999.
- [23] Thomas, W., M., Woollin, P. L., Johnson, K. I., *Friction Stir Welding of Steel, Welding: a novel technique for steel*, Steel World, vol. 4, nr 2.



PROPERTIES OF SOLID POLYURETHANE RECYCLAT OBTAINED IN THE COMPACT MULTISTAGE SYSTEM OF CUTTING MILLS

Dariusz Sykutera

*University of Technology and Life Sciences
ul. Kaliskiego 7, 85-796 Bydgoszcz, Poland
tel.: +48 52 3408224, fax: +48 52 3408222
e-mail: sykutera@utp.edu.pl*

Abstract

Due to specific elastomers properties, fine grinding of them (for example cured rubber, polyurethane elastomers) into powder of the average particles size below 1mm is realized usually in energy-consuming facilities. These lines consist of machines that are connected with transportation system and segregating system of grinded product. Because of this, powder production of elastomers is expensive and, simultaneously lack of full quality control of the received product is a usual case. Compact multistage system of cutting mills cooperation was proposed. The aim of investigations was to determine conditions for PUR grinding for further usage of received powder in composite together with other polymers, for example with new PUR. Obtained results of investigations indicate the purposefulness of multistage rotational cutting system application to polyurethane grinding. The require number of milling stages is dependent on final degree of fineness (needed size of grain). Polyurethane powder of high fineness degree and of different particles shape was received by the multistage system of cutting mills. The average grain size of polyurethane powder reached the range from 0.22 to 0.90 mm. Grain-size distribution was similar to normal distribution for all multistage grinding versions. Recycled powder obtained as a result of fine grinding can be re-used as filler to the PUR manufacturing. In this aspect geometrical features and the grain surface state were determined. The characteristics of particles geometrical features were made based on the particles project images received with the use of CCD camera and SEM.

Keywords: *elastomer, recycling, fine grinding, cutting, sieve analysis*

1. Introduction

In the area of the material recycling of cast polyurethane waste, PUR crumb plays the important role. The increase of interest in using grinded PUR for filling urethane components during their synthesis (for example cast polyurethane elastomers) is observed [1, 2]. It may be anticipated that introduction of polyurethane particles into new PUR material causes the decrease of PUR manufacturing costs [2]. Based on this, it is important to study the influence of the particle's geometry (especially a shape and a size) and a nature of this modifier (method of disintegration) as well as others factors on the composite properties (using ground cast polyurethane). For elaboration the basis of manufacturing technology of PUR composites with optimal properties at minimal cost is needed.

Due to specific elastomers properties, fine grinding of them (for example cured rubber, polyurethane elastomers) into powder of the average particles size below 1mm can be complicated and is conducted usually in energy-consuming facilities. These lines consist of machines that are

connected with transportation system and segregating system of grinded product. Therefore powder production of elastomers is expensive and, simultaneously lack of full quality control of the received product is a usual case. The received PUR powder however can be used only as a filler. In this aspect (applying the obtained ground PUR for filling others polymers) determination of geometrical features and the grain surface state plays most important role. In case of crosslinked polymers, fineness of grinded powder determinates their further usability [1-3]. In this area the reverse relation can be observed, reuse of recycled materials requires particular grain size distribution of crumbs. It was acknowledged that for cast polyurethanes the main cause of their division in a grinding chamber should be the cutting knives. Pure shear is the most profitable for elastomers [1, 3]. Cutting at the narrow slit between cutting edges of the knives assures the conditions of pure shear.

To recapitulate the above consolidations, the thesis may be formulated, that the most important condition of polyurethane fine grinding processes is making the biggest possible number of PUR cuts at a narrow slit between cutting edges of the stationary and the rotary knives of the mill. Completing this condition requires alternative solutions of single-stage construction cutting mills. In case of verification the presented thesis two original constructional solutions of further, hypothetic still grinding machine for polyurethanes are presented. First solution bases on the idea of multistage, gravity feed mill (potentially the number of material cut increases). Second constructional solution assumes for every stage (every stage is a working chamber of single-mill) a suitable geometry of cutting knives. Because of this, the aim of presented work was to determine conditions for PUR grinding for further usage of received powder in composite together with other polymers, for example with raw PUR. In case of polymer fine grinding, there is an advantageous number of grinding levels for each material of a different structure and input form of waste.

2. Concept of multistage grinding

During machine construction the correct collaboration between the individual stages must be taken into consideration. In the effect a product with specific fineness (needed fineness by reason for its further usage) should be received. Because of parallel arrangement of the knives edges, cutting of PUR is difficult and a number of cuts is limited in particular for fine grains. The latter are eliminated in the hyperboloidal-rotary cutting mill developed recently and evaluated in laboratory (Fig. 1).

After cursory analysis this solution seems to be simple in practical use, but PUR properties (particularly about low hardness) needs a qualification of suitable processing conditions and their fulfilment assures efficient working of this specific facility (cascade machine) for grinding by the hiperboloidal cutting method.

The most important requirements of proper work of mill should be obtainment "permeability effect" of whole grinding line as well as fulfillment "thermal safety" throughout of grinding. In practice it shows, that material division processes (share) on individual stages have to be held with approximate efficiency (efficiency of each following stage of cascade should be slightly higher than the previous level), however increase of temperature of grinded material on the next stage cannot be higher than temperature causing a material degradation and loss of a potency in cascade (higher than melting point of material).

Due to high number of processing factors, and also to various forms of PUR waste and their structure, investigation was conducted with the support of the model of investigations object, which was worked out for technology of grinding rubber by multistage hiperboloidal cutting (MHC). This model was described earlier [3, 4, 7]. Concept of hiperboloidal cutting is based on an analysis that the single-envelope hyperboloid comprises of two families of the generating straight lines [5]. Moreover, it is possible to generate a rotating, single-envelope hyperboloid, also comprising of two families of generatrices of the same single-envelope hyperboloid. Cutting at the

hiperboloidal interaction of straight cutting edges is evidently advantageous in comparison to parallel cutting, because width of the slit is permanently set at very low level of $0,05 \times 10^{-3}$ m. It is very important for elastomers fine grinding. To minimize influence of sizes dispersion on composite properties we disintegrated PUR in specially designed mill. Based on the aim of the investigation the test stand was provided additionally with the set of sieves and the suitable cutting knives.

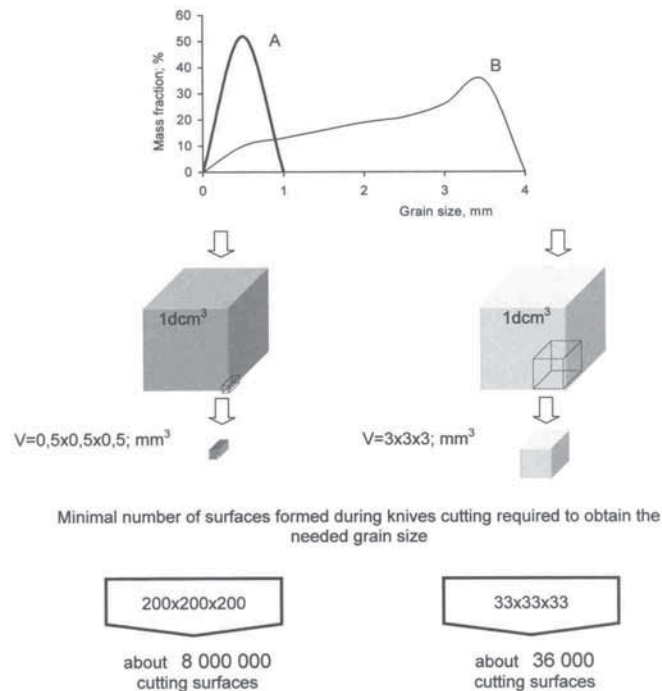


Fig. 1. Difference between fine grinding (A) and typical grinding (B) in the cutting mill

Examinations of PUR cutting and grinding were conducted at the test stand with the cutting mill as the most important element. The construction of the mill enables an application different methods of knife rotational cutting, while the knives are in different positions towards each other (for example: hiperboloidal cutting). The stand gives a possibility of simultaneous measurement of seven physical parameters (among others: shearing force, net torque).

3. Quantity and quality assessment of fine grinded product

Essential estimation criteria of grinding effectiveness is the determination of obtained product properties. The grain-size distribution of powder and geometrical features depend on material volume reduction method. This is important estimation criterion of product usability to apply it as a filler. Grain size distributions of received ground PUR were determined based on dry sieve analysis. Sieving was carried out in the vibratory and gyratory shakers. During this process particles are strongly accelerated due to the high oscillation rate and to relatively high vibration intensity of the column. For every samples of grinded material total sieving times at a level of 45 minutes was determined. Sieve analysis were conducted with the usage of 12 woven metal sieves with the mesh widths from 0.05 to 1.5mm. The results of measurement were represented as cumulative curves. Moreover obtained powders were characterized by determination of the particle's equivalent diameter, adequately to maximal value of the fraction range.

The characteristics of particles geometrical features were made based on the particles project images received with the use of CCD camera FS-5612P (Bischke, Germany) [6]. Thanks to additionally installed optical system, the pictures of 40 times magnification were obtained. With

the help of MultiScan version 4.01 software (Computer Scanning System, Warsaw, Poland), the linear dimensions l_{max} and l_{min} , projected outline P and projected surface area S of particles were described. Direct measurement of these values was performed during particles projected image observation for their stable orientation. Based on the received results, the dimensionless shape factors were determined, which were the ratios of the characteristic dimensions of the particles project image:

- elongation factor W_e , described as the ratio of maximum and minimum linear dimension of the projected particle, and
- surface development factor W_{sd} calculated from the formula:

$$W_{sd} = \frac{P^2}{S} \quad (1)$$

where:

P- projected outline of particles,

S - projected surface area of particles

In addition, the asymmetry factor W_a was employed, which describes the ratio of the particle maximum linear dimension to the hypothetical diameter of the perfect spherical particle having the same surface area as that for the particle [8]. The estimation of surface topography was made by observation of particles images received with the use of CCD camera and scanning electron microscope JSM-5600 (Jeol, Tokyo, Japan). To investigations cast polyurethanes were used about hardness's 40-70 ShD.

4. Results summary

Results of investigations show, that use of multistage cutting system to PUR grinding enables receiving the fine product. The number of used stages depends on final degree of grinded material. Several versions of PUR multistage grinding were examined. In all grinding versions homogeneous fine polyurethane powders of the average particles size below 1mm were obtained. Average size of grains, resulted from applied cascade, varied from 0.22 mm to 0.9 mm (powders about average sizes of grains 0.31mm, 0.44mm, 0.66mm were also received). The most grinded grains were received by the use of 6-stage grinding system. Grain size distributions of obtained products are similar to normal distribution, regardless the number of grinding stages (Fig. 3).

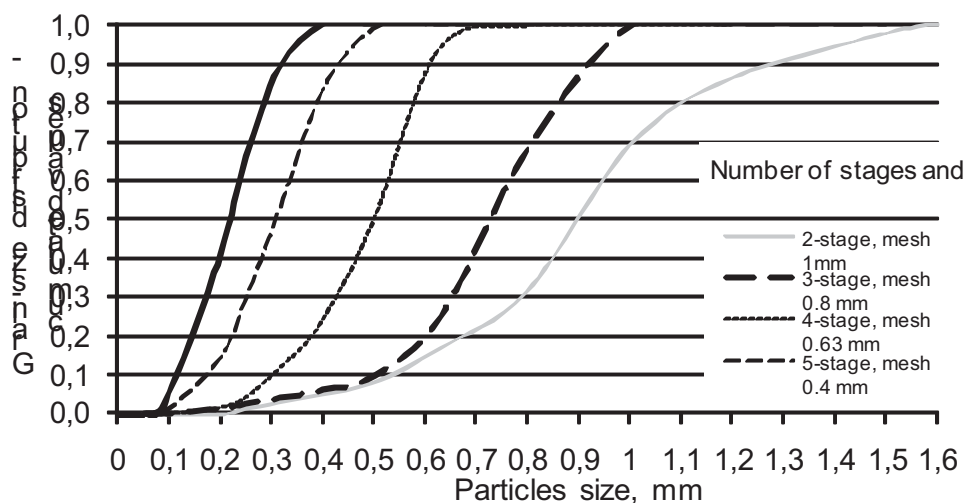


Fig. 3. Cumulated curve of ground PUR according to number of grinding stages used in the mill by hiperboloidal rotational cutting

Similar character of the grain-size distributions curves indicate the very similar manner of grains division in the milling chamber. Determined average diameters of grains are significantly lower than a sieves mesh at the finally grinding stage (the exception is smallest powder, $d_p=0.22$ mesh of sieve 0.2mm).

The largest particles received by multistage rotational cutting have the shape close to rectangular prism and a cube, regardless of their size (Fig. 4). There are scratched planes and straight cutting edges visible on the polyhedral surfaces of the particles. Small differences in minimal and maximal sizes as well as a value of asymmetry ratio show that their shapes are similar to rectangular prism, cubes and spherical bodies (Tab. 1).

Qualitative analysis shows that application of the multi-stage grinding system (using very fine mesh sieves, for example 0.2mm, 0.4 mm) caused further essential disintegration of grains and visible changes of both: their shape and the state of surface image (Fig. 4).

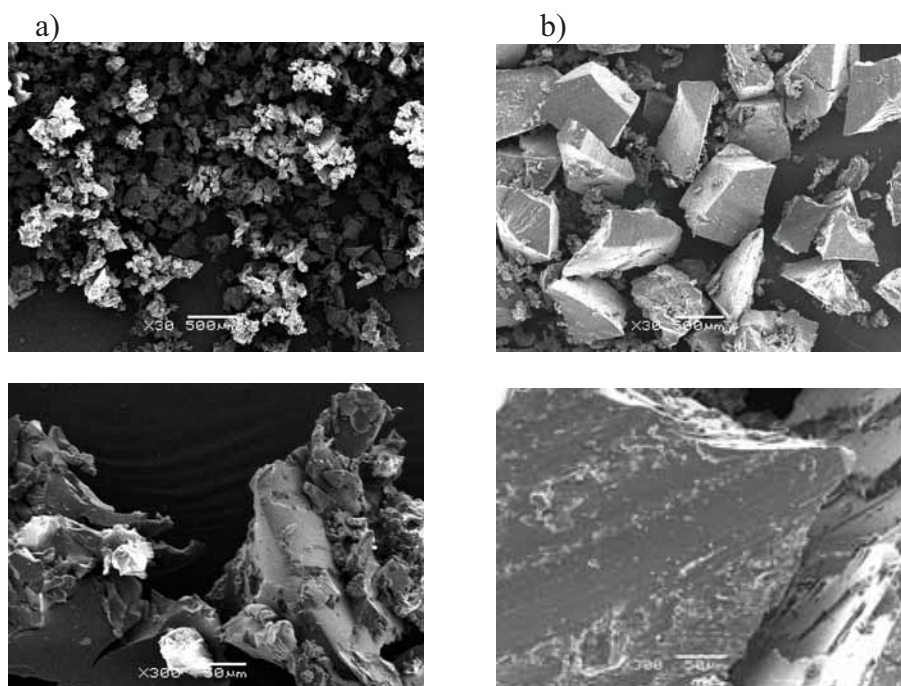


Fig. 4. Exemplary projection images of polyurethane grains obtained with use: (a) 6-stage grinding system (final sieve mesh width – 0.2mm) and (b) 3-stage grinding system (final sieve mesh width – 0.8mm). Images were made by SEM, magnification 30 and 300x

As a result, it is possible to observe simultaneous appearance of the grains with the shape similar to large particles (obtained in the single- or two-stage grinding system) and also the irregular shapes particles, which are similar to the PUR grain obtained with the usage of the other grinding method, for example by disintegration on disk mill. In this case a grinding time grows, what creates additional possibilities of further material division (not necessarily through cut). Reduction on particles size was caused mainly by variable stresses applied to the PUR at the higher (in comparison to grinding with use the sieves of the large mesh width) temperature during milling. It is evidence among others by changes in a shape of cutting surface (higher development) and large number curvilinear cutting edges. The level of these changes depends on the number of grinding stages and is most evident for the use in our investigation maximal stages number (6-stage grinding system). Such experiment was necessary for further discussion on changes in geometrical characteristics of PUR particles subjected to shear forces and to their eventual thermomechanical degradation during milling. It is necessary to mention that during continuous milling the temperature in the mill chamber did not exceed 100°C, although the grinding was conducted without cooling (for all grinding systems).

Tab. 1. Geometrical characteristics of PUR particles obtained in the multistage grinding system

Final mesh sieve width used mm	Elongation factor W_e	Surface development factor W_{sd}	Asymmetry factor W_a
1	1.394	17.03	1.308
0.8	1.429	25.44	1.331
0.63	1.463	25.6	1.333
0.40	1.458	28.1	1.286
0.20	1.526	27.13	1.315

5. Conclusions

Recapitulating the model investigations of cast polyurethane grinding as well as earlier works [3, 4, 7], it can be observed, that for characteristic types of cast polyurethane waste it is possible to affirm, that the advantageous set of a processing conditions exists (suitable knives geometry, number of grinding stages, suitable inclination angle, etc.). Study of these conditions based on experimental examination resulted in obtaining fine grinded polyurethane products of the average particles size below 1mm. It can be also stated that grain surface image is a reflection of load state, which caused the polyurethane disintegration. By indirect means, the state of this particles surface images the value of energy consumption during grinding process.

Prior to the presentation of the detail investigation results it can be affirmed, that after fulfilment of supplementary investigations, it is possible to design and to make an original, prototype technological line, for the fine grinding PUR waste, both: cast and porous structure. It should be underscored that the hiperboloidal cutting was successfully used in fine grinding polyurethanes down to 0.5 mm grain size.

It is possible to design prototyping grinding line to conduct milling by hiperboloidal cutting for cast polyurethane waste as well as for foam systems.

References

- [1] Błędzki, A. K., Pawlaczyk, K., Kardasz, D., *Recycling of polyurethane elastomers by compression molding*, Polimery, IChP, 7-8 (43), pp. 479-485, Warszawa 1998.
- [2] Ryszkowska, J., Markiewicz, B., *Material recycling of high hardness solid polyurethanes*, Polimery, IChP, 4 (47), pp. 273-278, Warszawa 2002.
- [3] Konieczka, R., Kałużny, W., Sykutera, D., *Drehschneiden im Prozess der Feinzerkleinerung von Gummi*, Kautschuk Gummi Kunststoffe, Hüthig Verlag, 9 (50), pp. 641-644, Heidelberg 1997.
- [4] Konieczka, R., Kałużny, W., Sykutera, D., *Koncepcja i metoda badań modelowych procesu precyzyjnego rozdrabniania elastomerów wielostopniowym cięciem obrotowym*, IX Seminar Plastics in Machine Design, Wyd. Uniwersytetu Jagiellońskiego, s. 181-186, Kraków 2000.
- [5] Konieczka, R., *Untersuchen des Schneidvorgangs beim Zerkleinern von Kunststoffen*, Kunststoffe, Carl Hanser Verlag, Nr. 7, pp. 598-601, Darmstadt 1989.
- [6] Sykutera, D., *Applying the Computer Method of Picture Analysis for Evaluation Ground Rubber Properties (in polish)*, IX International Conference on Machinery Recycling ICMR '99, Wyd. MTB SAWO Sp. z o.o., pp. 81-87, Bydgoszcz 1999.
- [7] Sykutera, D., *Stanowisko badawcze i wstępne wyniki badań cięcia termoplastycznych tworzyw porowatych*, Przetwórstwo Tworzyw, IMPiB, 4 (136), pp. 214-217, Gliwice 2010.



THE USE OF INJECTION MOULDING PROCESS SIMULATION SOFTWARE CADMOULD FOR INJECTION MOULD DESIGNING

Dariusz Sykutera, Marek Bieliński

*University of Technology and Life Sciences
ul. S. Kaliskiego 7, 85-796 Bydgoszcz, Poland
tel.: +48 52 3408224, fax: +48 52 3408222
e-mail: sykutera@utp.edu.pl*

Abstract

The work shows the use of simulation software for aiding the design of forming elements of injection moulds and for the analysis of the phenomena occurring while the injection mould cavities are filled with polymer material. The digital analysis was used for the design work of a research modular injection mould equipped with a hot runner system. The use of the injection moulding process simulation software significantly simplifies the analysis of the appropriateness of the assumptions concerning the plastic part shape, the location of the gating points, the gating geometry as well as facilitates the recognition of the phenomena taking place inside the mould cavity while polymer freezes. The use of the simulation software results from the necessity to adopt the right assumptions concerning the simulation model and the knowledge of the process parameters used for processing a particular plastic material. In addition to injection mould design aiding, simulation programs constitute a tool to define advantageous plastic material processing parameters.

Keywords: *polymer, simulation, injection mould, injection moulding, molded part,*

1. Introduction

New construction plastic materials, thermoplastic material structure modifications, adopting new control systems in injection machines and process automation are the most visible symptoms of the development of polymer material processing. The aim of injection moulding is to achieve plastic parts of specified geometrical characteristics and physical-chemical properties. Obtaining a part characterised by the required utilitarian properties depends on a number of factors connected both with the process settings and injection mould design (e.g. the melt feeding into the cavities, gating type or the number of cavities) [1-5, 7, 8, 10-13]. The influence of many variables, remaining in mutual interaction, causes that digital programs describing the injection process progress become a substantial tool used for injection mould design verification as well as for the injection moulding process optimisation. According to DSM Engineering Plastics, the introduction of CAE (Computer-Aided Engineering) into the plastic product development caused the reduction of the total manufacturing costs, saving of the time related to the product design and processing as well as the final product quality increase. The results of simulation are not only used for product design work concerning its geometry and the geometry of the injection mould, but also as an important tool for the processing optimisation [1, 2, 5, 11]. Consequently, applying the simulation software may significantly support even an experienced designer, especially in cases, where work

connected with the realisation of the tool design for processing reinforced plastic materials (shrinkage anisotropy) and for processing innovative construction thermoplastic materials. The result suitability depends on the mathematical model algorithm assumed by the program, which describes the basic melting and filling processes as well as the polymer material properties, and are, in addition, the derivative of the quality of the plastic part model. The value of the results depends also on the correct assumption concerning the part model, the processing settings and gate geometry [1-4, 6-8, 9-13]. The next approximation of the real injection moulding conditions is introduction into the calculations the correct rheological plastic material model, which will take into account the viscosity changes depending on other inputs. [6, 7, 10, 11, 13]. If one aims at the absolute imaging of the real process conditions, the simulation project should also take into account the position and sizes of the mould cooling or heating channels, but as well the materials used for manufacturing the particular mould elements [1, 2, 5, 6, 11, 13]. The implementation of the new product is accompanied by the necessity of injection mould trial shooting, whose aim is to eliminate the injection mould design errors and defining the optimum processing parameter setting.

One of the most popular simulation programs aiding the polymer injection moulding process is Cadmould by the company Simcon (Germany). The program also allows to read momentary injection process parameter values at a required moment of the process at a required section and point of the moulded part. The analysed course of the melt filling the cavity can be presented in the animated form. The course is obviously, realised until the moulding is removed from the cavity, and, consequently, it takes into account the material volume change during the holding and cooling phases. In addition to the results of the filling and holding pressure distribution, the moulded part temperature distribution during filling and cooling, the shear stress values, the shrinkage and shear velocity distribution, the melt filling and freezing times, it is also possible to define the location of the gating points, the sizes and types of gating, as well as the weld line positions, air traps and fibre orientation. The shrinkage distribution and melt flow analysis allow to describe the maximum values of shape deformations. The simulation model, which is used by Cadmould, is a surface model, which allows to conduct the analysis on 25 independent layers of the moulded part, where only the neighbouring nodes influence the final results in particular model points.

2. Exemplary self-conducted digital research conducted in Cadmould

2.1. Defining of the polypropylene freezing time in a pinpoint gate

Pinpoint gate is a significant element of an injection mould flow system. In case, where semi-crystalline polypropylene is injected, due to its high value of the volume shrinkage, the holding time should on average amount to about 8 seconds for 1 mm of the part thickness (for a moulded part of the wall thickness between 3 and 4 mm). Filling up the mould cavity with the melt resulting from volume counteraction while the moulded part freezes will be effectively realised in the assumed time only if the viscoplastic polymer will not freeze earlier in the gate. As a result, the gating point should have the appropriate diameter. For the research work, a geometrical model of the gate was prepared and its sections assigned to test the freezing time (Fig. 1).

It was established that the size of the pinpoint gate diameter significantly influences the polypropylene freezing time. What is worth mentioning, is that the melt material freezes the fastest in section 3 (Fig. 1) for the channel diameter over 1.5 mm (Fig. 2). It is the consequence of the fact that a considerable amount of heat is generated during the melt flow through the small-diameter narrowing, which causes an additional polypropylene temperature rise in this area.

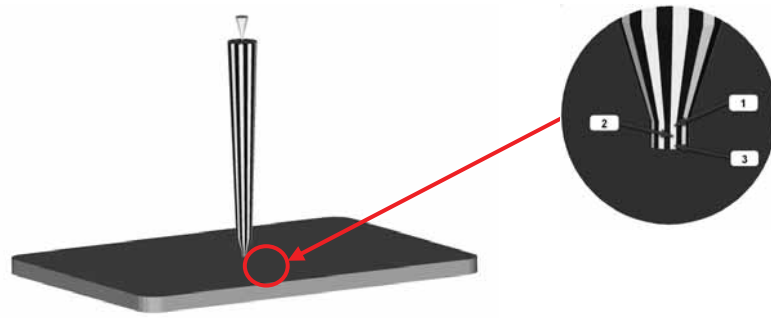


Fig. 1. Pinpoint gate model with characteristic freezing time measurement diameters

The influence of the analysed gate lengths on the freezing time of PP is less significant, and the differences amount maximally 0.2 s. For channels of the diameter above 1.5 mm the length increase causes the delay in polypropylene freezing.

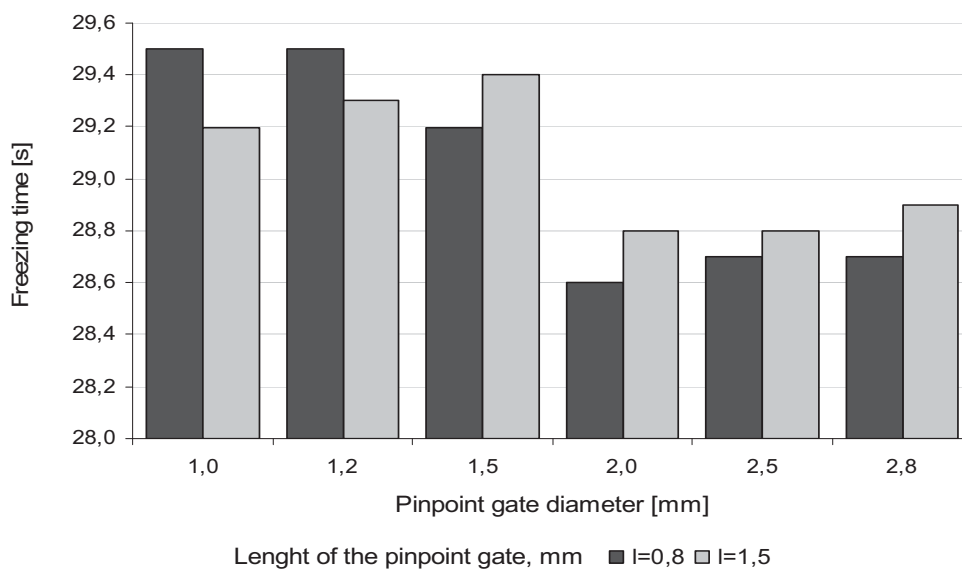


Fig. 2. The influence of the pinpoint gate cross-section and its length on the PP freezing time in a narrowed feeding channel

2.2. Defining the conditions of ABS/PMMA blend injection moulding for a large-size thin-walled part. Selected results.

A large-size plastic part characterised by a complex geometry and thin walls with construction latch elements usually generates many problems during injection moulding process realisation (Fig. 3). During the filling and holding phases, the melt of a specific viscosity must fill the thin-walled volume located the furthest from the gating point, which is usually connected with the necessity of applying very high injection and holding pressures. The conducted analysis of the real part surface quality proved that a minor wall thickness (from 1.6 up to 2.3 mm) and a number of construction latch elements generates problems with filling the cavity with the melt plastic. The part was produced of a ABS/PMMA polymer blend of the company Evonik of the trade name of Plexalloy NTA-4. The use of polymer blends is one of the observed manners of polymer property modification. The use of PC/ABS and ABS/PA blends for manufacturing the white and brown household product housings might be the evidence. Due to the high melt flow rate of PC/ABS, it is used for mobile phone housing production. Digital research was preceded by generating a 3D model, which was the exact image of the shape and dimensions of the real plastic part. In the

digital program the rheological model of the ABS/PMMA melt worked out by the company Simcon was applied.

The realised simulation research indicates the possibility of the proper mould cavity filling with the ABS/PMMA polymer blend through combining the high injection velocity with the appropriate polymer melt temperature and the temperature of the injection mould cavity (Fig. 4a).

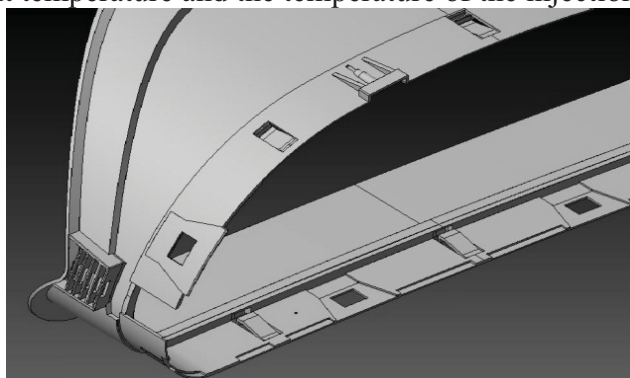


Fig. 3. A fragment of a digital model of a thin-walled part of the wall thicknesses between 1.6 mm and 2.3 mm

In case of large-size thin-walled parts, ABS/PPMA blend processing should be realized at high temperatures of the cavity and processed melt (close to the upper limit suggested by the producer). The high temperature settings should be accompanied by high cavity filling velocity, which, however, should not exceed the value of 200 mm/s. In case of the analysed thin-walled part, injecting the blend into the cold injection mould (temperature of 30 and 50 °C) causes that the polymer melt freezes too fast, which, in turn, causes that the fragments of the part that are the furthest from the gating point as well as the fragments of complex geometry and very thin walls are not filled or filled with difficulty (Fig. 4b). The complete stop or slow-down of the melt front movement means its temperature decrease resulting from the prolonged contact with cold walls of the mould. A high dynamics of the melt polymer movement causes faster cavity filling with the plastic material of a lower viscosity and higher temperature (Fig. 4c). However, one should remember that this may cause a sudden melt pressure decrease in the cavity, which requires the use of an injection machine of a very high nominal injection pressure. Due to this reason, the estimated maximal injection velocity was of the value of 200 mm/s.

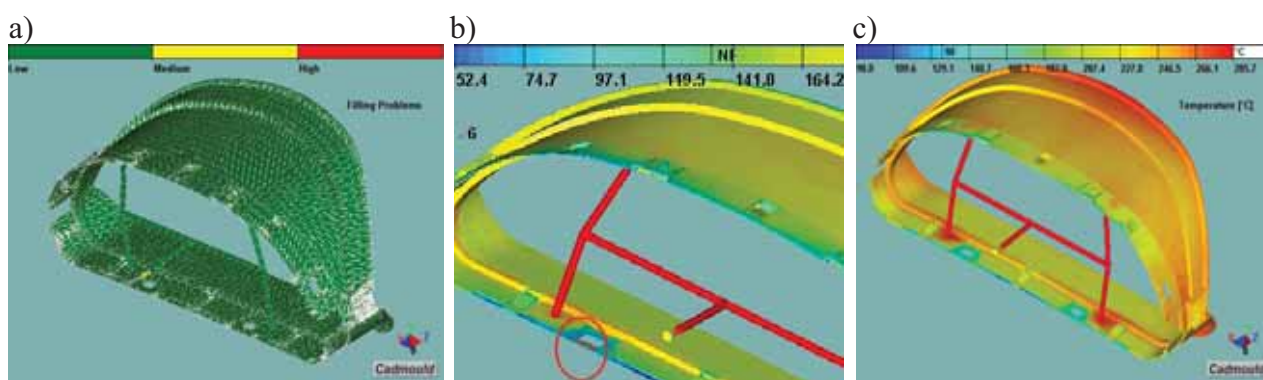


Fig. 4. Examples of the test results: a) the melt flow direction in the cavity, b) unfilled fragment resulting from the too fast melt freezing (simulation realised at a low cavity temperature of 30 °C and low injection velocity of 30 mm/s), c) temperature distribution in the mould cavity after the filling phase for the appropriately produced plastic part (injection velocity of 145 mm/s and cavity temperature of 70 °C)

The injection process realisation with a long cavity filling time at simultaneously low temperatures of the plastic material and tool cavity, caused the greatest shape distortions,

especially on the surfaces with the greatest curvature, significantly remote to the gating points (Fig. 5a). Increasing the temperature and reduction the cavity filling time considerably decreased the warpage differences in the particular part fragments, with the greatest deformation not bigger than 1 mm (Fig 5b). Consequently, applying the appropriate injection settings may significantly influence the plastic part quality.

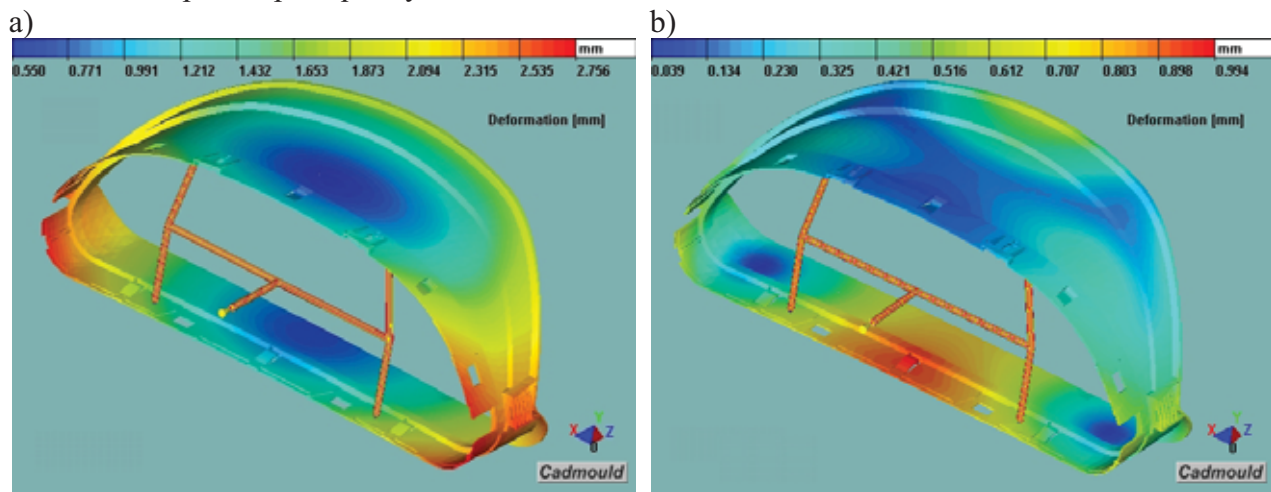


Fig. 5. Examples of deformation distribution: a) for a sample realised at the injection velocity of 30 mm/s and low values of temperatures of the melt and mould cavity, b) for a moulding produced in a hot injection mould (70 °C) at the injection velocity of 145 mm/s and the melt temperature of 250 °C

2.3. Research injection mould design with the use of the simulation program

The experience gained in the area of simulation research, caused that the research on designing and manufacturing a research injection mould for standard research mouldings (dumbbells) was started. Considering the numerous conditions concerning the research samples described in standards, it was decided that the injection mould would be modular with the possibility of fast exchange of forming elements. The design and tool shop work was preceded with the simulation research analysis, which was conducted on different research sample models and with a group of plastic materials. The example of mould cavity pressure distribution for a strength research dumbbell is presented in Fig. 6a. As a result, a modular two-cavity mould with interchangeable inserts equipped with a modern hot runner nozzle by the company HASCO (Germany) was designed and manufactured (Fig. 6b).

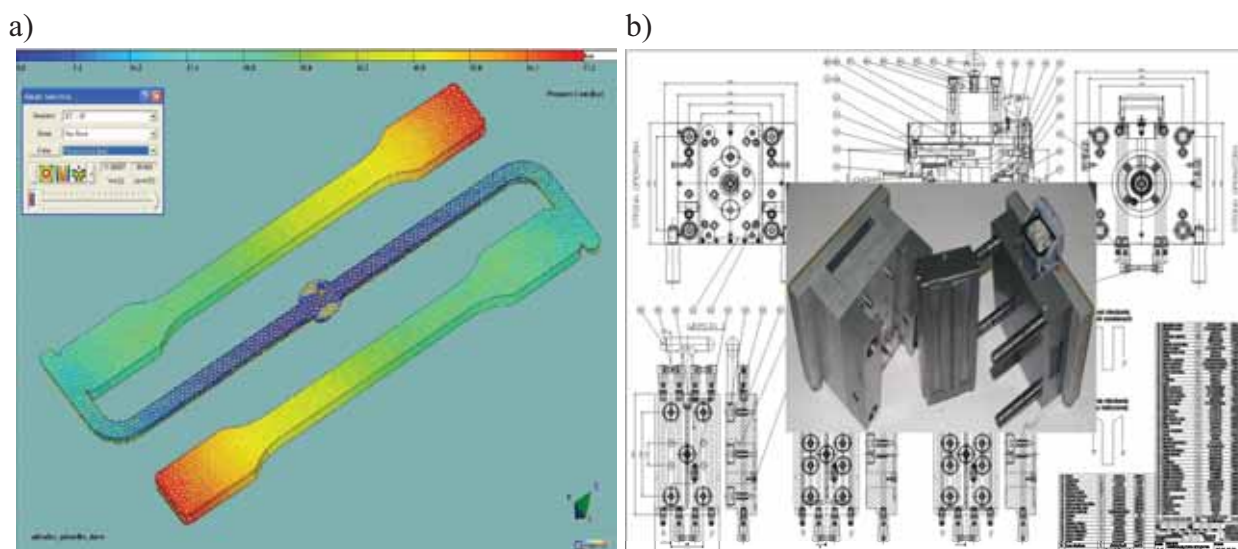


Fig. 6. a) Selected results of PP injection process simulation – gradient of pressure changes in the mould cavity after the filling phase, b) the design and manufacturing of the two-cavity research injection mould

3. Conclusions

Digital software significantly aids the work connected with the injection mould design, especially in the area of final cavity shape forming, as well as the cooling elements and gating points, considerably decreasing the time needed for the project implementation. With the proper initial assumptions and a well-prepared digital model it is possible to achieve the simulation results close to the results obtained in real conditions.

Injection mould design basing only on the designer's experience and intuition or on the practical testing becomes insufficient in today's plastic processing.

The use of a digital software for the filling and holding phase realisation allows to correct the possible mould designer's errors at the stage of the design. The analysis of the melt flow and the kinetics of the part constitution in the mould cavity allows to better understand the phenomena taking place in the melt during the freezing phase in the injection mould.

References

- [1] Bociąga, E., *Procesy determinujące przepływ w formie wtryskowej i jego efektywność*, Monografie nr 82, Wyd. Politechniki Częstochowskiej, Częstochowa 2001.
- [2] Bociąga, E., *Modelowanie procesu wypełniania gniazda formy wtryskowej*, Polimery, IChP, 2 (47), pp. 122-129, Warszawa 2002.
- [3] Bociąga, E., *Wpływ konstrukcji przewężki formy wtryskowej na wybrane właściwości wyprasek z polietylenu*, Polimery, IChP, 2 (45), pp. 89-97, Warszawa 2000.
- [4] Bociąga, E., *Wpływ temperatury formy wtryskowej i prędkości wtryskiwania na wybrane właściwości wyprasek polietylenowych*, Polimery, IChP, 11-12 (45), pp. 830-836, Warszawa 2000.
- [5] Byung, H. L., *Injection molding simulation in dealing with part quality variance and correlation study*, Annual Technical Conference and Exhibition ANTEC Technical Papers, Society of Plastics Engineers, pp. 1309-1313, Charlotte 2006.
- [6] Ilinca, F., Hetu, J.-F., Derdouri A., *3D Modeling of Nonisothermal Filling*, Polymer Engineering and Science, Society of Plastics Engineers, 4 (42), pp. 760-769, Newtown 2002.

- [7] Nabiałek, J., Koszul, J., *Modelowanie wybranych zjawisk zachodzących podczas wypełniania formy wtryskowej*, Zeszyty Naukowe Politechniki Poznańskiej nr 4, Wyd. Politechniki Poznańskiej, s. 167-172, Poznań 2007.
- [8] Osswald, A. T., Hernandez-Ortiz, J., P., *Polymer Processing. Modeling and Simulation*, Carl Hanser Verlag, Munich 2006.
- [9] Sykutera, D., *Próba weryfikacji wyników symulacji procesu wtryskiwania w warunkach rzeczywistych*, Mechanika M/2009, Nr 3, Wyd. Politechniki Krakowskiej, s. 317-321, Kraków 2009.
- [10] Sykutera, D., *Wybrane przykłady zastosowania symulacji numerycznej do oceny cech konstrukcyjnych wyprasek i geometrii przewęzek*, Konferencja Forma wtryskowa- wyzwanie dla inżyniera, Proceedings of the Wadim Plast, Bydgoszcz 2009.
- [11] Sykutera, D., Hejnowski, M., *Warunki wtryskiwania tworzyw konstrukcyjnych o dużym stopniu napężenia*, Zeszyty Naukowe Politechniki Poznańskiej, Wyd. Politechnika Poznańska, Nr 4, s. 255-260, Poznań 2007.
- [12] WenHsien, Y, Dan, Ch., Venny, Y, PeiChi, Ch., ShengJye, H., *True 3d numerical simulation for micro injection molding*, Annual Technical Conference and Exhibition ANTEC Technical Papers, Society of Plastics Engineers, pp. 1270-1274, Charlotte 2006.
- [13] Wilczyński, K., *The cadmould-3D computer system for modeling injection molding process simulation of the filling phase*, Polimery, IChP, 6 (44), pp. 407-4141, Warszawa 1999.



EMPIRICAL EXAMINATION OF THE IMPACT OF THE CYCLE ASYMMETRY COEFFICIENT OF THE LOAD ON THE FATIGUE LIFE OF S355J0 STEEL

Grzegorz Szala

*University of Technology and Life Sciences in Bydgoszcz
ul. Prof. Kaliskiego 7 85-789 Bydgoszcz, Poland
tel.: +48 52 340 82 95, fax: +48 52 340 82 71
e-mail: gszala@utp.edu.pl*

Abstract

In the calculations of the fatigue life of structural components subjected in service load conditions to stochastic loads the load spectra being a set of sinusoidal cycles of different asymmetry occur. The cycle asymmetry is characterized by the asymmetry coefficient $R=S_{\min}/S_{\max}$. In the case of load mentioned above, R coefficient changes in wide limits from $-\infty$ to $+\infty$. In the work the empirical examinations of the impact of the cycle asymmetry coefficient of the load on the fatigue limit of S355J0 steel are presented.

Keywords: *fatigue life, two-parametric characteristics, S355J0 steel*

1. Introduction

The elaboration on the random service load of the structural components in form of spectra and programmes of load applied in calculations and programmed examinations of fatigue life leads to determination by methods of counting the cycles, sets of cycles of various values of the cycle asymmetry coefficient $R = S_{\min}/S_{\max}$.

Spectra of variable cycle parameters (S_a , S_m) or (S_{\min} , S_{\max}) are depicted in form of so called correlation tables [1].

Experimental data concerning the cyclic values of materials in range of the high-cycle fatigue known in the literature concern in most cases the determination of the S-N curves in conditions of fatigue limit under oscillating load ($R = -1$), more seldom pulsating load ($R = 0$). In the work the examination with the variable value of the R coefficient are described, as well as two-parametric fatigue characteristics elaborated on their basis. The problem has been illustrated with results received for S355J0 steel (former 18G2A).

The basis of the determination of the fatigue diagrams in system amplitude S_a – mean value S_m of stresses are, S-N curves described also in the literature as Wöhler curves. These diagrams are presented in various forms, e.g.: $S_a(N)$, $S_{\max}(N)$, and so on. In the figure 1 the set of diagrams $S_a(N)$, drawn with assumption of the constant value of the cycle asymmetry coefficient $R = \text{const}$, has been depicted. The privileged diagrams from the given set are the S-N curves for $R = -1$ (oscillating load of $S_m = 0$) and for $R = 0$ (pulsating load $S_{\min} = 0$). For the durability $N > N_0$, the fatigue limits have been marked on the diagram with points: 1- R_{-1} ; 2- $0,75 \cdot R_{0,5}$; 3- $0,5 \cdot R_0$ and 4- $0,25 \cdot R_{0,5}$ respectively.

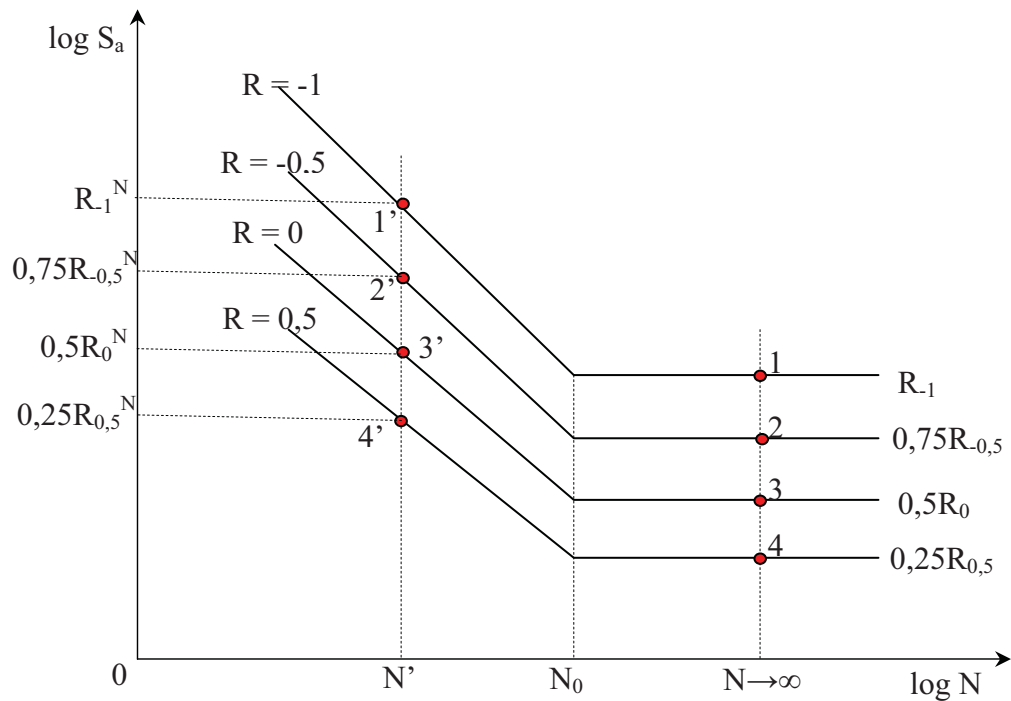


Fig. 1. Set of diagrams S_a drawn by assumption of the stable value of the cycle asymmetry coefficient $R = \text{const.}$

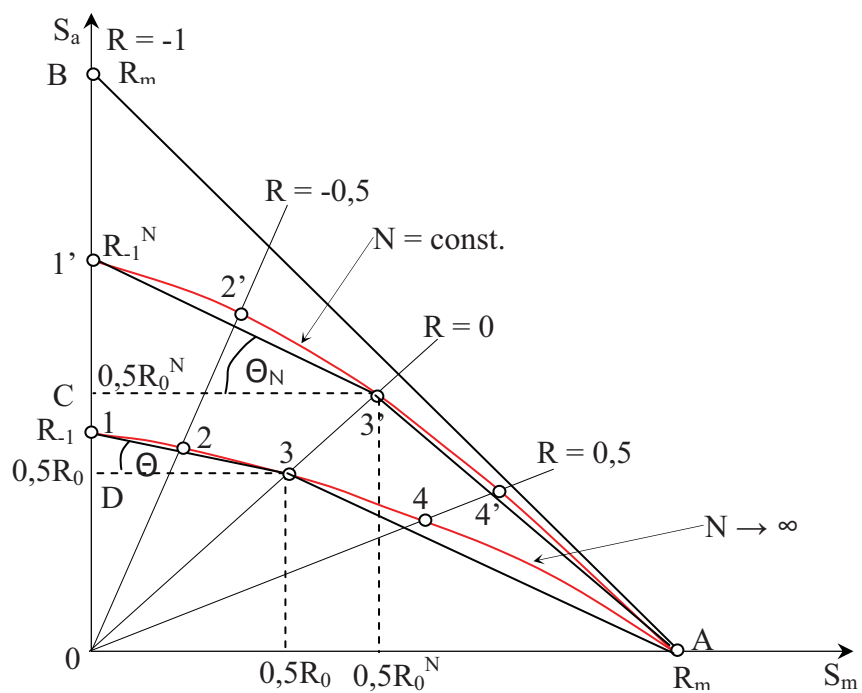


Fig. 2. Diagrammatic depiction of the diagram of two-parametric fatigue characteristics $N(S_a, S_m)$.

On the base of these points a diagram of fatigue limit 1-2-3-4 shown in the figure 2 has been drawn. Similarly, any line of constant value $N = \text{const.}$ can be drawn. For N' from the diagrams in

the fig. 1 one receives respectively points 1', 2', 3', 4', transferred to the fig. 2 they give a line 1'-2'-3'-4'.

2. Fatigue examination of the samples of S355J0 steel

Fatigue examination of the samples of S355J0 steel have been conducted for the following values of the cycle asymmetry coefficient R : 0; -0,5; -1,0; -1,25; -2,0. In the literature the research results for $R < -1$ do not occur, which corresponds to the negative average values of the cycle. Data concerning the fatigue properties, static and cyclic, have been shown in table 1.

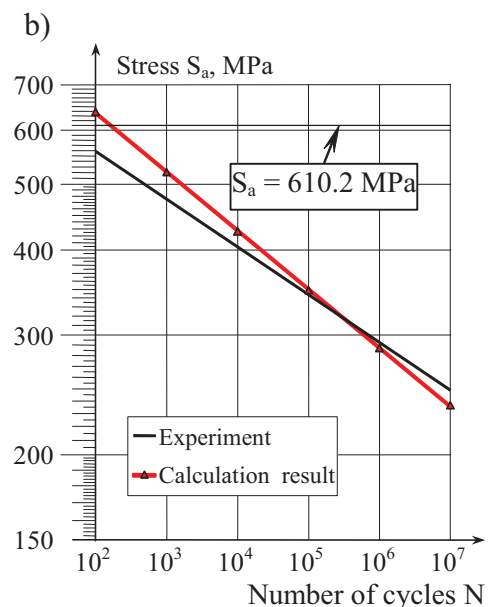
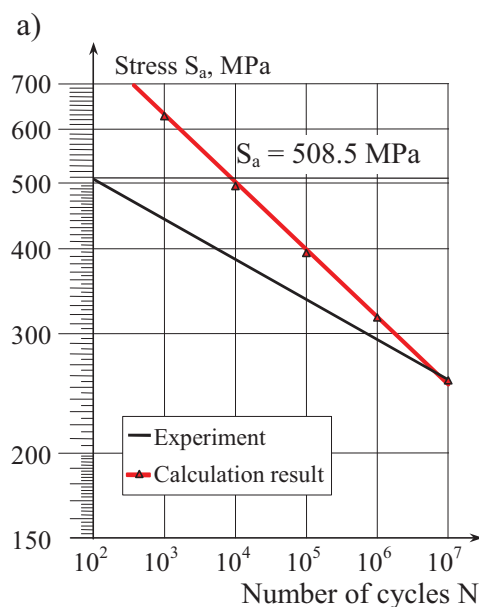
Table 1. Properties of S355J0 steel

R_m	R_m	E	A_5	Z	R_{-1}	N_0	m_0	C_0
MPa	MPa	MPa	%	%	MPa			
678	500	$2,08 \cdot 10^5$	17,2	59,8	274	10^6	12,33	$1,156 \cdot 10^{36}$
commentary: R_m – material tensile strength, R_e – material yield point, E – Young's modulus, A_5 – elongation, Z – contraction, R_{-1} – fatigue limit for $R = -1$, N_0 ; m_0 ; C_0 – constants from the S-N curve								

On the base of the research results the S-N curves for specified values of the coefficient R have been determined, as well as a diagram of two-parametric fatigue characteristics $N(S_a, S_m)$ has been elaborated on their basis. In the fig.3 fatigue diagrams for S355J0 steel for the cycle asymmetry coefficient R have been depicted: a) $R = -2$, b) $R = -1.25$, c) $R = -1.0$, d) $R = -0.5$, e) $R = 0$. General description of the fatigue diagrams has been described by formula (1):

$$\log S_a = -a \log N + b \quad (1)$$

where constants a and b for the cycle asymmetry coefficients of the cycle R , assumed above, have been compiled in table 2



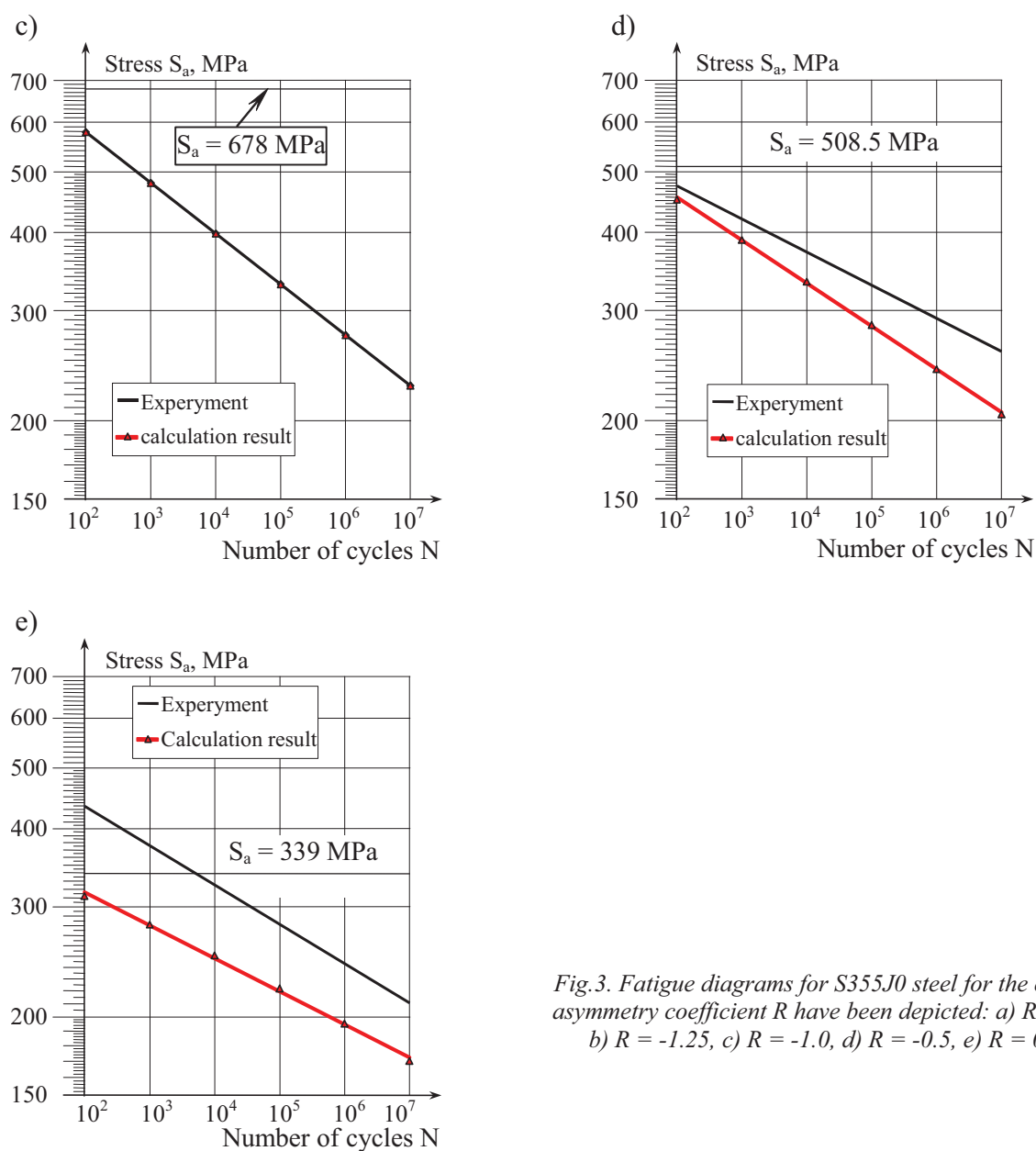


Fig.3. Fatigue diagrams for S355J0 steel for the cycle asymmetry coefficient R have been depicted: a) $R = -2$, b) $R = -1.25$, c) $R = -1.0$, d) $R = -0.5$, e) $R = 0$.

Table 2.: Constant values a and b

	Cycle asymmetry coefficient R				
	0	-0,5	-1,0	-1,25	-2,0
a	-0.0628	-0.0528	-0.0811	-0.0703	-0.0592
b	2.7630	2.7810	2.9247	2.8873	2.8233

3. The analysis of the research results and conclusions

S-N curves for the mentioned values of the coefficient R and the diagram of two-parametric fatigue characteristics $N(S_a, S_m)$, elaborated on their basis, have been shown in the figures 4 and 5. The data included there can be a basis for calculation of structural components, especially subjected to the impact of random load of wide spectrum.

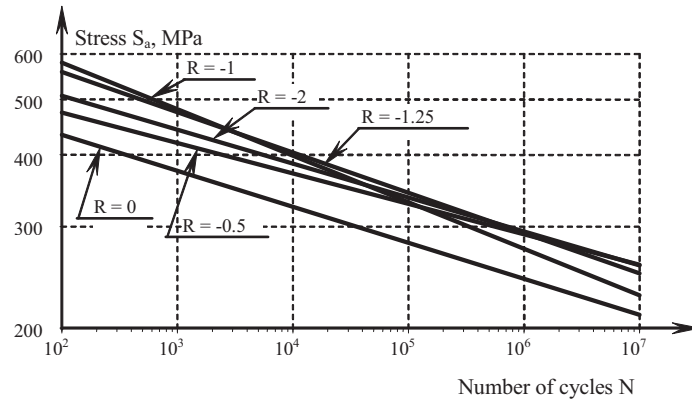


Fig. 4. Fatigue diagrams for S355J0 steel for the cycle asymmetry coefficient R : 0; -0,5; -1,0; -1,25; -2,0.

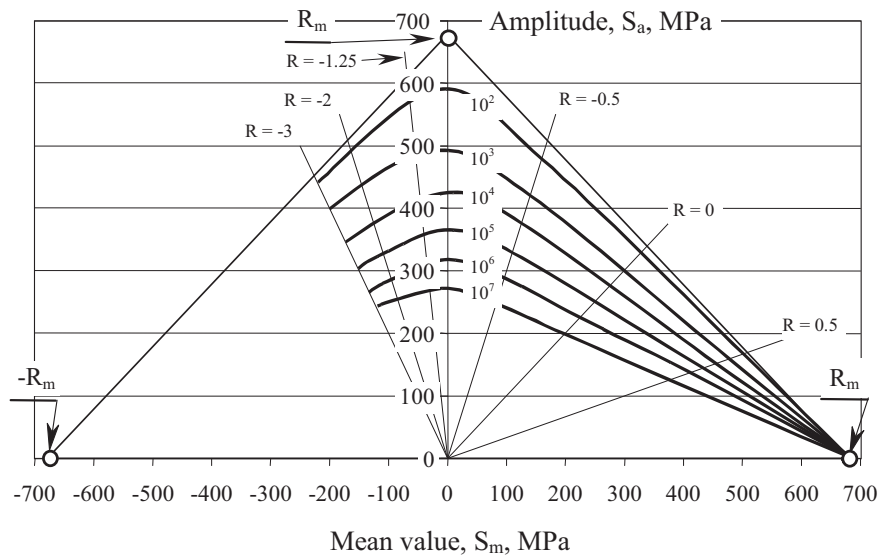


Fig. 5. Experimental two-parametric fatigue diagram for S355J0 steel.

On the base of these results also the verification of the two-parametric models of fatigue characteristics can be done.

Reference

- [1] Ligaj, B., *Wpływ wybranych programów obciążeń wygenerowanych na podstawie tablicy korelacyjnej na trwałość zmęczeniową stali 18G2A*, Problemy Eksploatacji – Zeszyty Naukowe 3/2007 (66), ss. 129-146.
- [2] Ligaj, B., Szala, G., *Uogólnienie wykresu zmęczeniowego Goodmana na zakres wysokocyklowego zmęczenia*, Materiały XXIII Sympozjum Zmęczenia i Mechaniki Pękania, Bydgoszcz – Pieczyska, 2010.

Note : This work has been elaborated in the frame of the project No. 0715/B/T02/2008/35 financed by Polish Ministry of Sciences and Higher Education



EXPERIMENTS WITH SYNTHETIC JET FOR DETECTING POTENTIAL TERRORISTS

V. Tesař*, K. Peszyński**

**Academy of Sciences of the Czech Republic v.v.i., Institute of Thermomechanics
Dolejškova 5, 182 00 Praha 8; Czech Republic
tel.: +420 2 6605 2270,
e-mail: tesar@it.cas.cz*

***University of Technology and Life Sciences, Division of Control Engineering
ul. Prof. S. Kaliskiego 7, 85-789 Bydgoszcz, Poland
tel.: +48 52 340 8248, fax: +48 52 340 82 45
e-mail: kazimierz.peszynski@mail.utp.edu.pl*

Abstract

Authors performed hot-wire anemometer investigations of the aerodynamics of an actuator designed to generate annular synthetic jets reaching to very large distances. The actuator is to be used for detecting illegal substances – and thus identifying terrorists and criminals who recently came into contact with explosives or drugs. It is designed to generate the synthetic jet with an annular cross section, thus creating between the nozzle exit and the cloth surface a space that is separated from the surrounding atmosphere in which in the present air-jet designs in detector the substance traces become diluted. The main problem encountered, because of the variability of the examined persons, is the need to reach to very large distances.

Keywords: *synthetic jets, annular jets, terrorism, hot-wire anemometry*

1. Introduction

In their previous paper [3], the authors describe the reasons why it may be useful to use an annular, low-frequency synthetic jet in the detectors used as an effective preventive measure for detecting traces of explosives and other dangerous substances left on clothes of those people who recently handled them. This detection is currently mostly done by trained dogs, which is rather expensive and cannot be made at the necessary very large scale in railway stations, airports, and public buildings. Also described in that paper is the layout of the proposed actuator combined with the collectors leading the examined substance traces into an analyser – and the laboratory model of the actuator used in the investigations. The main problem encountered, because of the variability of the examined persons, is the need to reach to very large distances.

As described by Tesař, Peszynski [3], the alternating flow in the annular nozzle was generated by standard woofer loudspeaker ARN-165-01/4 – Fig.1. In Fig. 2 photograph of the experimental setup is presented. The model actuator is at left, at right is the hot-wire anemometer probe moved in the meridian plane by the two mutually orthogonal traversing gears, the vertical one controlled directly by the data acquisition computer. The laboratory measurements, performed in the setup shown in Fig. 2, concentrated on measurement of air flow velocity in the generated synthetic jet.

The used instrumentation was the hot-wire anemometer system CTA 54T30 (DANTEC Dynamics) with standard single-wire probe type 55P16.

Actual program of experiments was rather extensive. In the present contribution, the discussion will be limited to the results of two experimental series, in both of which the evaluated quantity was the time-mean velocity magnitude, computed as the mean value of the velocity magnitudes acquired (and stored in the oscilloscope) at a particular location of the probe in the flowfield.

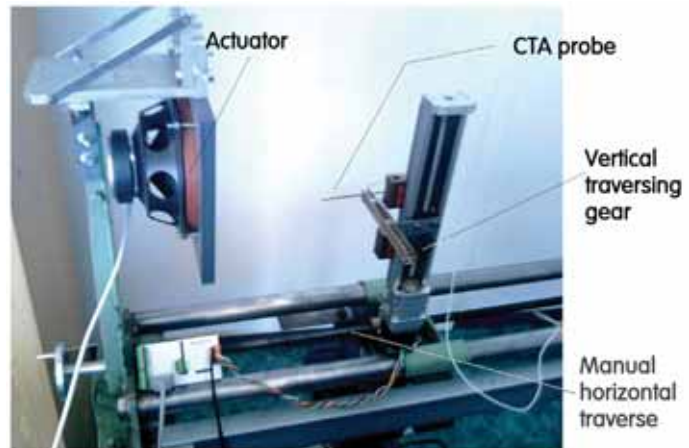
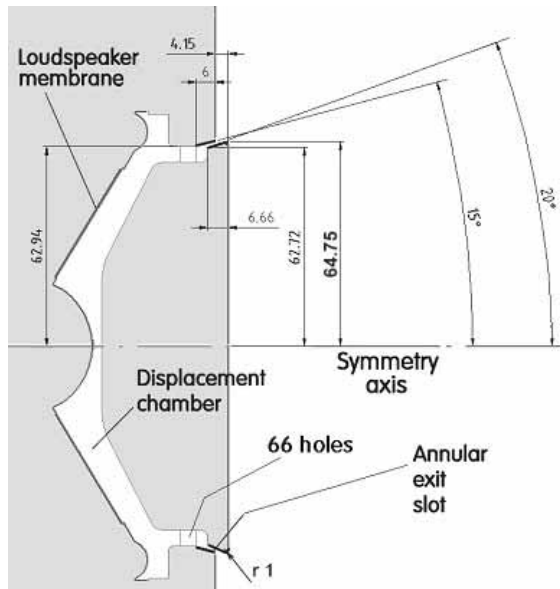


Fig. 1. (Left) Geometry and dimensions of the cavities of the actuator model

Fig. 2. (Right) The actuator model with the hot-wire probe traversing gear during the laboratory tests

2. Size of the recirculation region

In this first test series, the measurements were made in each location of the matrix of 20×14 measuring points separated by 5 mm steps: the upper 20×5 points of this matrix are visible in Fig. 4, which also shows typical character of the oscilloscope traces as they were observed in two locations near to the nozzle exit. The matrix points in this experiment nearest to the nozzle exit were at the 8.4 mm streamwise axial distance. This separation from the actuator components was chosen for avoiding any possibility of probe collision with them.

Over most of the matrix points, the measured time-mean velocity magnitudes were very small, indeed negligible. Thus of interest were only those locations near to the path of the annular jet issuing from the nozzle slit, as they are seen in Fig. 4. In this diagram, it was possible to identify, by interpolating between the matrix points at the same axial distance from the nozzle, the position of the velocity maxima. These are marked by the black data points in Fig. 4, where these points are connected by the continuous dark line. These points define the extent of the recirculation bubble.

Of course, as the jet width increases in the downstream direction due to the entrainment of the outer air, the precision of determining the maxima decreases. The velocity profiles became very flat and wide. Nevertheless, the maxima could be determined and in Fig. 5, only these maximum points defining the outer boundary of the recirculation bubble are shown. Even though it was not possible to perform the measurements at larger distances from the nozzle, it is obvious that the measured recirculation bubble is quite large – it extends to as far as ~ 120 mm downstream from the nozzle exit.

This value agrees comfortably with the requirement of the active distance for the proposed anti-terrorist application in the detection portals. Thus these measurements document the applicability

ty of the actuator for this particular use. It should be noted that the experiment was performed with driving frequency $f = 10$ Hz, well below the audible range, which is a signify.

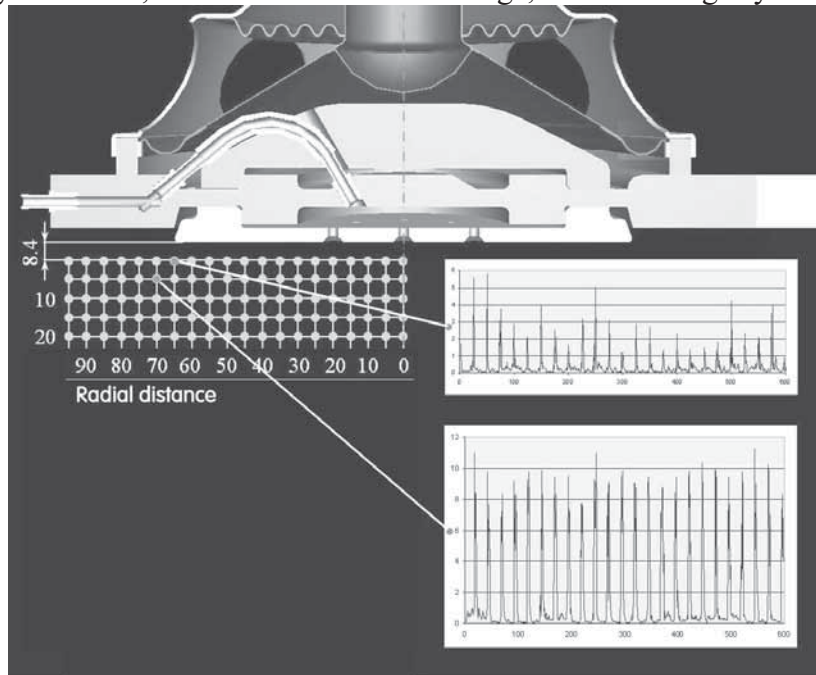


Fig. 3. Typical character of the oscilloscope traces obtained by the measurements near the nozzle exit.

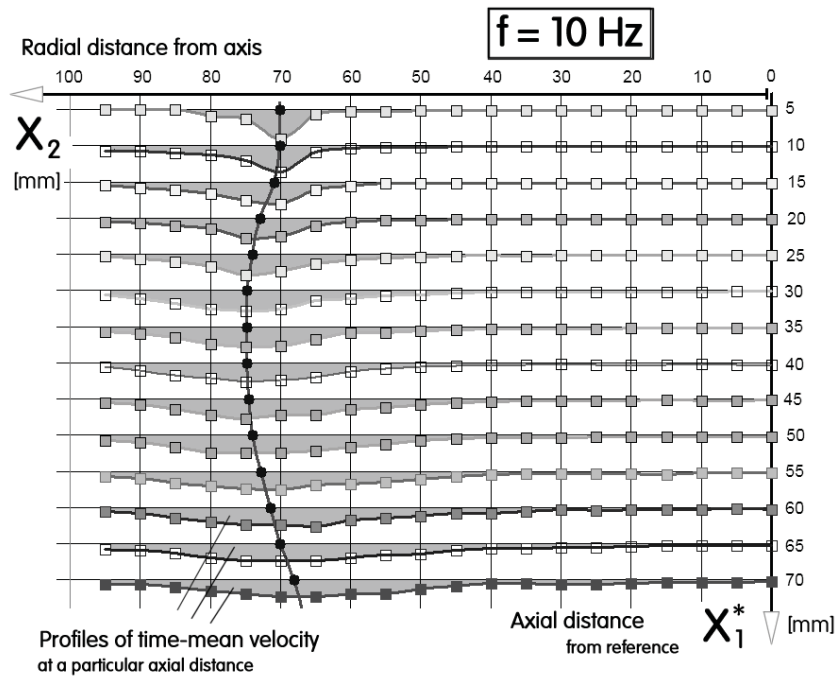


Fig. 4. Velocity measurements in the 5 mm x 5 mm step matrix of location points downstream from the actuator nozzle identified the positions of velocity maxima in individual streamwise profiles

cant factor for the applicability – and audible noisy device is not likely to be accepted by the general public

3. Details of velocity profiles and the effect of frequency

This second series of experiments concentrated on the conditions very near to the nozzle. The region in which the velocity magnitude measurements were made is presented in Fig. 3. Safe course of the experiments with the hot wire probe traversed near to the actuator component overcame the initial fears and the hot wire was now positioned as near as 2.4 mm streamwise from inner the core lip (extended from the outer frame). The transverse steps at which the probe was moved were decreased to 1 mm. The profiles were measured at driving frequencies gradually increased in 5 Hz steps from 5 Hz minimum to 65 Hz maximum value.

Typical examples of the velocity profiles obtained in this measurement series are presented in Fig. 8. They all exhibit a steep maximum roughly in the middle of the traversing range. Immediately apparent is the continuous increase of the velocity with the increasing driving frequency. Also apparent fact is the asymmetry: the velocities away from the maximum are visibly higher on the outer side (i.e. at radii larger than the radius of the nozzle slit measured from the jet axis). At first sight this asymmetry is somewhat strange. The diameter of the nozzle slit is so much larger than the nominal 1 mm slit width that an effect of radial divergence might be expected to be negligible. The explanation of this asymmetry effect we have at this moment is the omnidirectional sensitivity of the hot-wire probe (in the meridian plane) in association with the entrainment flow from outside. The higher velocities the probe found on the outer side are due to the inflow of the outer air from the atmosphere. No doubt another factor that may be responsible is also the already mentioned 4.15 mm stagger of the exit lips: the velocities on the inner side (at smaller radii) are measured at a smaller distance from the wall.

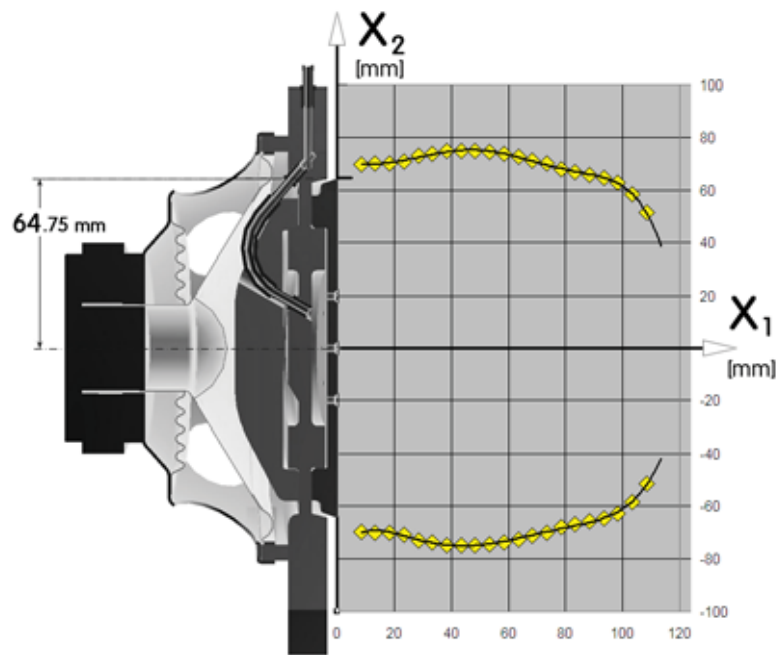


Fig. 5. The extent of the separation bubble identified from the velocity measurements as shown in Fig. 4. The annular synthetic jet was demonstrated to reach to a streamwise distance roughly comparable to the diameter of the nozzle slit.

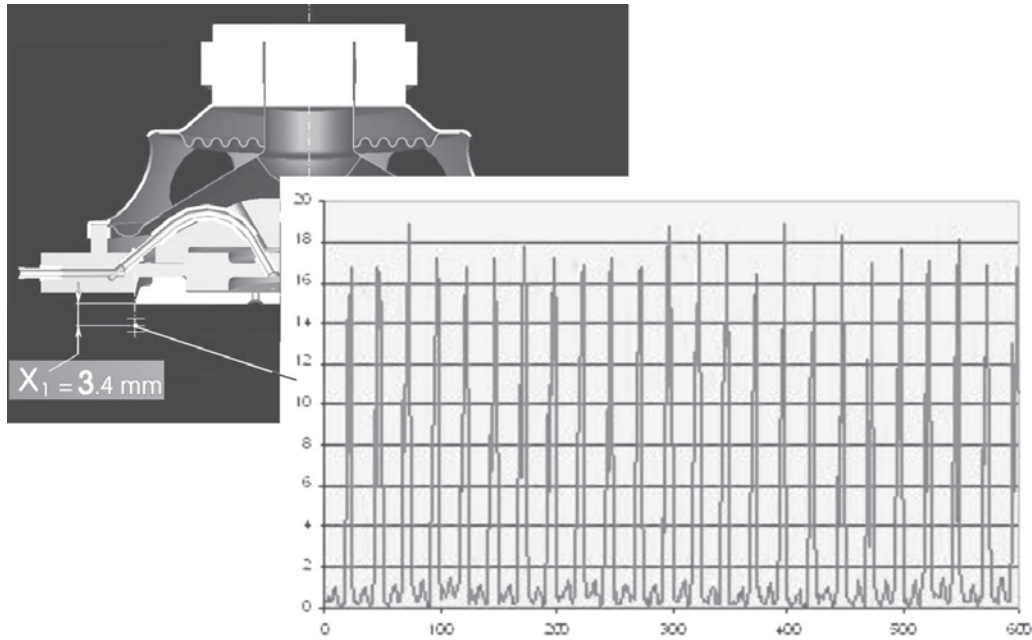


Fig. 6. Characteristic oscilloscope signal trace with the small secondary peak between the large velocity pulses, found in the locations immediately downstream from the nozzle generating the annular synthetic jet

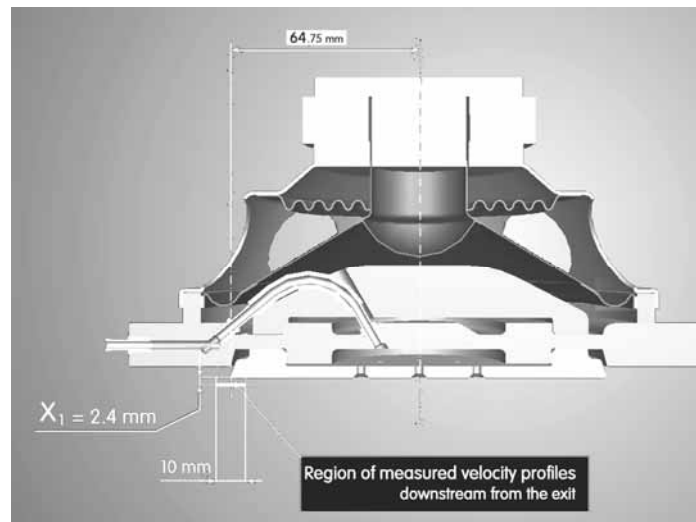


Fig. 7. Location of the region immediately downstream from the nozzle. The velocity profiles with the small, 1mm transverse step across the 10 mm wide range were investigated to reveal the influence of the excitation frequency

Another presentation of essentially the same data is in Fig. 18. In this diagram, the velocity magnitudes at selected radial positions are plotted as a function of the driving frequency. All data points presented there indicate a continuous growth of the velocity with increasing frequency. Initial slope of the growth is significantly larger. It slows at the frequency about ~ 25 Hz, but remains positive. Obviously, the 10 Hz driving applied in the experiments the result of which is shown in Fig. 4 is way below of what could be generated with the same actuator. Of course, the associated increase of the audible noise may make this simple way towards a higher effectiveness not acceptable from the practical point of view.

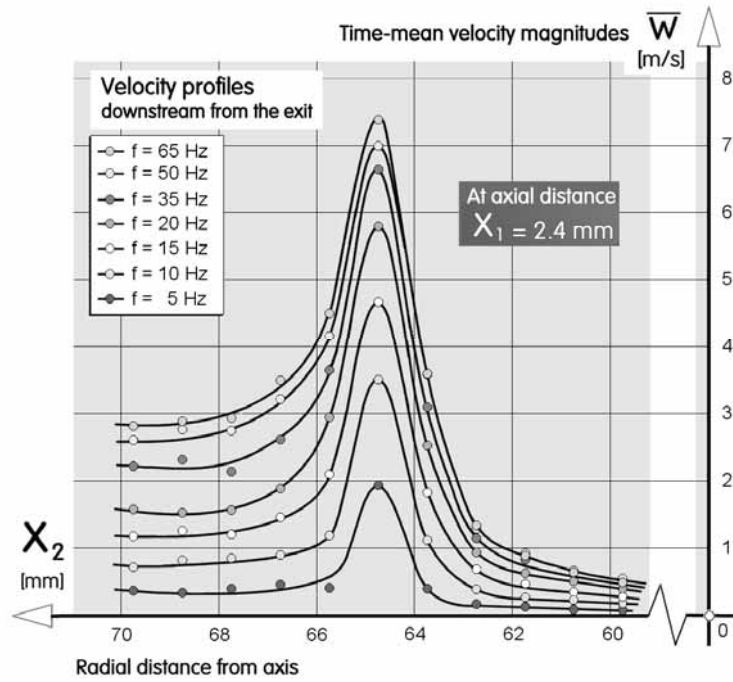


Fig. 8. The velocity magnitude profiles obtained by the measurements near the nozzle exit according to Fig. 7

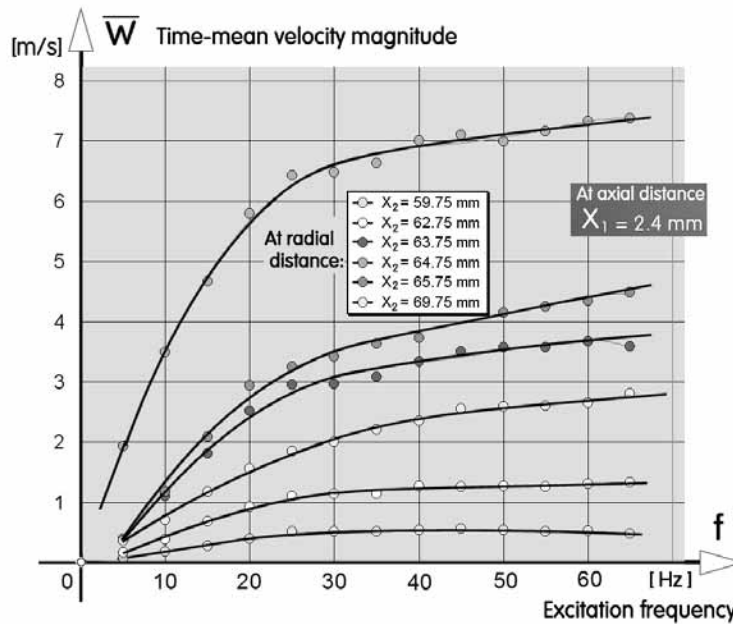


Fig. 9. The monotonous growths of the time-mean velocity with increasing excitation frequency in the profiles from Fig. 7

The response to the varied frequency of the investigated actuator was already investigated early – in particular it was the subject of the paper by Krejčí et al. [1]. These results were also presented in [24]. Rather surprisingly, the two sets investigation results disagree. In these previous experiments, the frequency dependence exhibited a clear maximum near to $f = 40$ Hz – evaluated not only in a series of experiments but also predicted theoretically by Dr. Trávníček. The explanation of this enigmatic fact is to be our next task in foreseeable future. One of the key factors to be considered is the circumstance of the frequency dependence measured by by Krejčí et al., [1], by means of a Pitot probe (of 0.8 mm i.d., positioned at a location 2 mm downstream from the annular

nozzle exit). Another circumstance to be considered is the fact that in the Krejčí et al. measurements the electric driving power was closely watched and adjusted – in the present case, this was not done and the actual driving power could be influenced by the frequency characteristic of the driving source.

5. Conclusions

The experimental data support the basic idea of the infrasonic long-range annular synthetic jet detector and actuator. The data were also used in the concurrent numerical flowfield computations performed by doc. J. Vogel, see [6], with a complete success. Apart from the time-mean velocity distributions, reported in the present paper, we have also accumulated data on the spatial distributions of energy of fluctuation, evaluated by the same approach as described in Tesař and Kordík [7, 8]. The data demonstrate applicability of the concept.

6. Acknowledgement

The authors acknowledge gratefully the support by the grant IAA200760705 from the Grant Agency of the Academy of Sciences of the Czech Republic, and by the grant 101/07/1499 from the Grant Agency of the Czech Republic. The hot wire probe traversing as well as an elegant method of data acquisition were devised by Mr. M. Pavelka.

References

- [1] Krejčí, P., Trávníček, Z., Tesař, V., Kordík, J., Pavelka, M., *Frequency Characteristics of an Annular Synthetic Jet Actuator of Large Inner Diameter*, Proceedings of Conf. ‘Experimental Fluid Mechanics 2007’, Liberec 2007.
- [2] Tesař, V., (2007) *Pressure-Driven Microfluidics*. Artech House Publishers, Boston - London, pp. 389 – 393
- [3] Tesař, V., Peszynski, K., *Synthetic jet applied to detect potential terrorists*, Journal of Polish CIMAC, 2010
- [4] Tesař, V., Peszynski, K., *Annular Synthetic-Jet Actuator for Large Active Distances*, Proc. of Conference “ENGINEERING MECHANICS 2009”, ISBN: 978-80-86246-35-2, pp. 1309-1320, Svratka, Czech republic, May 2009
- [5] Tesař, V., Peszynski, K., *Experimental Investigations of Very Long Range Infrasonic Annular Synthetic Jet*, Proc of Conf. “ENGINEERING MECHANICS 2010”, ISBN: 978-80-87012-26-0, Svratka, May 2010
- [6] Tesař, V., Vogel, J., Trávníček, Z., (2008) *Annular Synthetic jets for Anti-Terrorist Warfare*, Proc. of 12th Intern. Conf. on Developments in Machinery Designs and Control, Publ. by Univ. of Technology and Life Sciences in Bydgoszcz, Poland
- [7] Tesař, V., Kordík, J., *Quasi-Similarity Model of Synthetic Jets*, Sensors and Actuators A. Physical, ISSN: 0924-4247, Vol. A 149, pp. 255 – 265, 2009
- [8] Tesař, V., Kordík, J., *Time-Mean Structure of Axisymmetric Synthetic Jets*, Sensors and Actuators: A. Physical, Vol. 161, pp. 217-224, 2010



SYNTHETIC JET APPLIED TO DETECT POTENTIAL TERRORISTS

V. Tesař*, K. Peszyński**

**Academy of Sciences of the Czech Republic v.v.i., Institute of Thermomechanics
Dolejškova 5, 182 00 Praha 8; Czech Republic
tel.: +420 2 6605 2270, fax: +420
e-mail: tesar@it.cas.cz*

***University of Technology and Life Sciences, Division of Control Engineering
ul. Prof. S. Kaliskiego 7, 85-789 Bydgoszcz, Poland
tel.: +48 52 340 8248, fax: +48 52 340 82 45
e-mail: kazimierz.peszynski@mail.utp.edu.pl*

Abstract

As an alternative to impinging steady flow jets used in detectors of illegal substance traces on clothings of people who recently came into contact with explosives or drugs, authors investigated synthetic jets with zero time-mean nozzle flow rate. The actuator designed to generate the synthetic jet has an unusual annular nozzle, creating between the nozzle exit and the cloth surface a space separated from the surrounding atmosphere. The detected traces are carried through this space to the detector inlet. The problem encountered, because of the variability of the examined persons, is the need to reach to very large distances.

Keywords: *synthetic jets, annular jets, terrorism, detection of illegal material*

1. Introduction

Terrorism became one of the fundamental problems at the beginning of 21st century. The critical factor behind the relative success of terrorists is economy favouring the terrorist's activity [1]. It is much cheaper to perform the attack than to prevent it. The crude explosive devices terrorists use are inexpensive while securing safety requires deploying, maintaining, and manning costly systems and organisations. Essential is early warning which, to be an efficient deterrent, calls for large numbers of detectors deployed at many locations. The most effective preventive measure is detecting traces of explosives and other dangerous substances left on clothes of those people who recently handled them. This detection is currently mostly done by trained dogs. These are almost always in short supply, and their long-term training and the need for dedicated supervisor persons are very expensive.

Technology replacing the detection by dogs has been gradually developing, in its most effective form consisting of the detectors arranged in into portal units (Fig. 1) through which persons have to pass one by one [3]. Their operation actually, to a certain degree, mimics the detection as performed by dogs, which is done in two phases. To release the detected substances from the surface on which they are immobilised, in the first phase dog generates jets of air exhaled from lungs. In the subsequent second phase this alternates with inhaling by which the air with released substances is moved towards the olfactory sensing organs. The problem is the required extreme sensi-

tivity of the analyser. In the current portal units this problem is aggravated by the acting air jets (Fig. 2) that inevitable disperse the released, already very small traces, into the surrounding atmosphere. The collectors taking the sample into the analyzer are usually positioned in the top part of the portal (using the thermal air convection currents produced by the person). Obviously, the traces reaching the collectors are very much diluted.

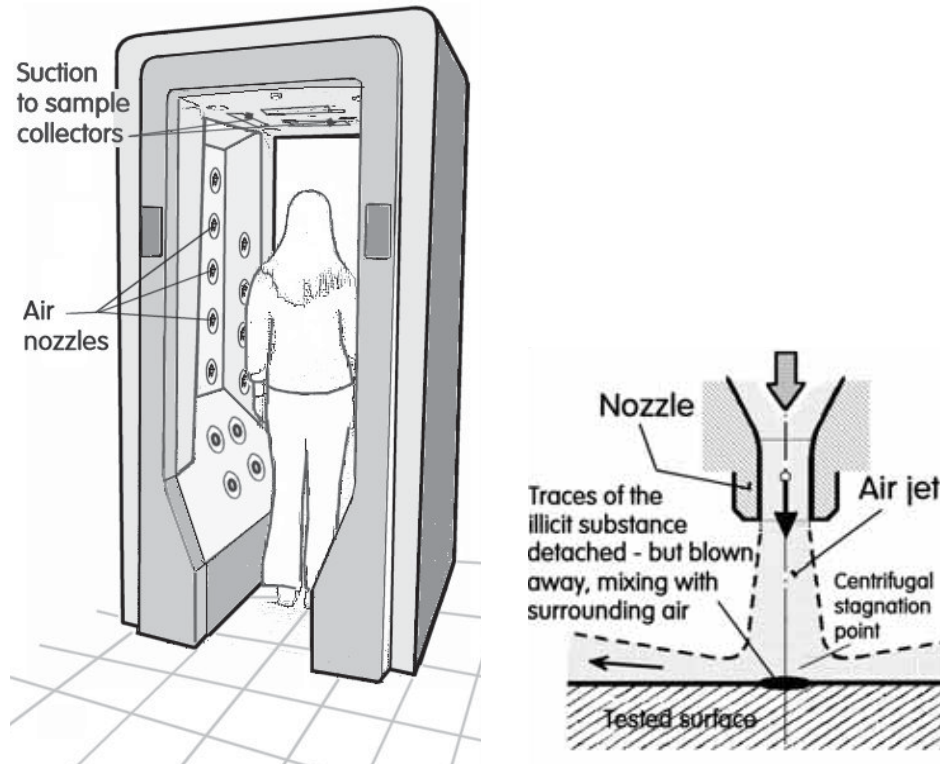


Fig. 1. (Left) A typical present-day portal detector with air-jet actuators unit for releasing traces of dangerous and illegal substances from clothes of persons passing through them

Fig. 2. (Right) The air jets used in present detectors mix the critically small amounts of detectable traces uncontrollably with surrounding atmospheric air

This dilution will be decreased, according to Fig. 3, if the nozzles that generate the air jet are provided with an annular exit - and are combined with the collector, leading to the analyser. The jet surrounds the space in which the detected substances move away from the investigated surface. The generated annular jet provides a protection of this space, preventing an uncontrollable mixing of the sample with the atmospheric air. Nevertheless, the annular jet is also formed by bringing into the detection space a relatively large amount of additional air (supplied from a compressor) and the sample is inevitable mixed with some of this air. A solution is proposed [20] in using the annular synthetic jet, according to Fig. 4. This is formed by means of the aerodynamic rectification phenomenon [9, 15], which was investigated by the present principal author for uses in fluidic systems [5, 6, 7, 8, 9, 10, 12,13] before it received its present name by prof. Glezer [4].

2. Investigated laboratory model 85

For verification of the idea, present authors investigated a laboratory model of the detector combined with the synthetic-jet actuator, based on the idea presented in Fig. 5. To reach the necessary large distances, the annular nozzle is of a very large 130 mm diameter. For generation of the alternating flow the actuator uses a standard loudspeaker, as shown in section view in Fig. 6. To minimise the problems associated with the acoustic noise, the actuator was operated at an infra-

sonic frequency 0 – 20 Hz. The loudspeaker was therefore a low-frequency woofer ARN-165-01/4 of rated short-term maximum power 100 W; actually operated throughout the tests by harmonic driving signal at much lower electric input power 4 W.

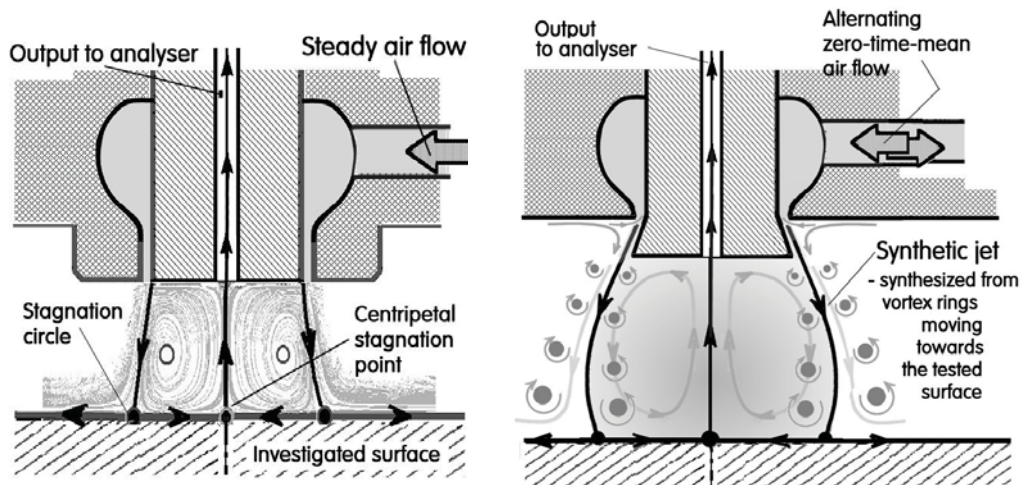


Fig. 3. (Left) An annular jet can surround the space between the collector leading to the analyser and the source of the detected substances - so that the latter are prevented from moving away into the atmosphere. However, the large amounts of supplied air still mix with the small amounts of the substances and this places extreme requirements on analyser sensitivity

Fig. 4 (Right) The proposed alternative: synthetic annular jet with zero time-mean supplied air flow. The pulsatile character also helps in releasing the detected traces from the surface

The basic question to be answered by the performed laboratory tests was how large action distance between the annular nozzle exit and the investigated surface (the textile on the clothing surface of the person) may be achieved. The problem with the recirculation regions formed by annular nozzles, both for steady (Fig. 2) and synthetic (Fig. 3) jets, is they tend to be decreased by the radial pressure forces generated by the entrainment of the surrounding air into the jet. The generated annular jet removes the air from the internal protected space and carries it away. This generates low pressure in this space and this effect leads to convergence of the outer boundaries.

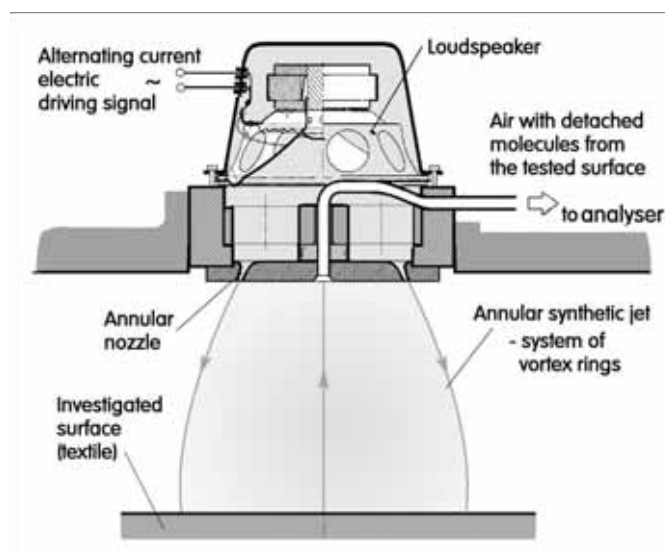


Fig. 5. The basic idea of the detector sensor combined with an actuator generating an annular synthetic jet [20]

To counter the convergence of the time-mean pathlines of the issuing flow, the nozzle was designed with significant radial outward diverging orientation of the exit velocity vector. This makes the recirculating region wider: the apex half-angles of the inner and outer cones are 20° and 15° , respectively. Moreover, also to direct the issuing jet more into the outward direction, the nozzle orifice was designed with the 4.15 mm stagger of the exit lips (the internal core is longer than the outer frame). The (nominal) width of the nozzle slot is $b = 1$ mm. The inner diameter of the exit is defined by the exchangeable centrebody plate, which also contains the 9 collector orifices through which the suction is to be applied to remove the sample and send it into the analyser. In the present investigations these orifices were closed off and the centrebody plate was not changed. Earlier experience with pulsating flow through orifices [17] have shown that the efficiency of generating the alternating output flow may be significantly decreased by the capacitance [14] of the cavities upstream from the exit. Instead of forming the jet, the pulsating supply tends just to compress and expand the air inside the cavities. To suppress this effect, the volume inside the conical membrane of the loudspeaker was decreased by the inserted solid centrebody.

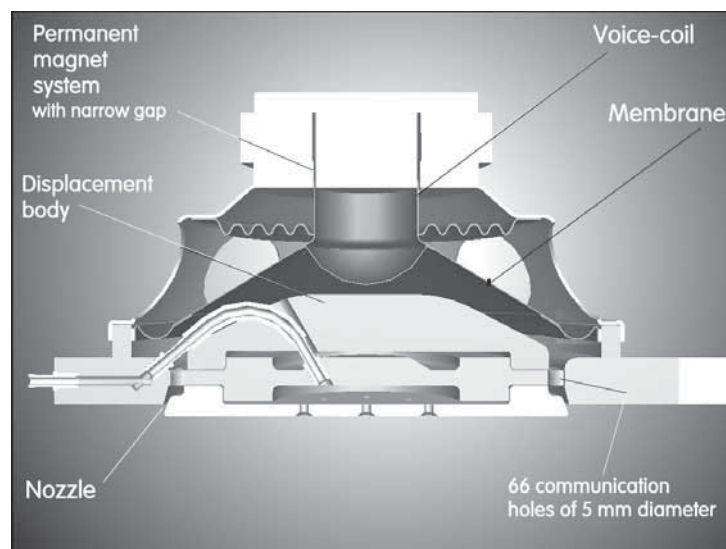


Fig. 6. The actuator model – shown in meridian section - used by the authors in their experiment. The key component is a standard loudspeaker ARN-165-01/4 .

3. Experiments

As described above, the alternating flow in the annular nozzle was generated by standard woofer loudspeaker ARN-165-01/4. The nominal diameter of the annular nozzle exit was 130 mm. The measurements performed by the authors concentrated on measuring air flow velocity in the generated synthetic jet. The used instrumentation was the hot-wire anemometer system CTA 54T30 (DANTEC Dynamics) with standard single-wire probe type 55P16. The probe was traversed in the radial direction by an automatic traversing gear, driven by a stepping motor. At each location the probe remained stationary for the duration of the data acquisition. The computer control of the traversing, as well as an elegant method of data acquisition using the data storage properties of the digital oscilloscope RIGOL DC 1042CD. Before the actual experiment, the anemometric system was calibrated by comparison with Pitot probe positioned into the same location in the potential core of an auxiliary air jet. The parameters of the adjustment – in particular the probe currents – were used as supplied by the probe and anemometer manufacturer. Since the measured velocities in the actual experiment were in most of the jet flow-field very low, the calibration procedure was set up so as to concentrate on the low-velocity end of the range. The calibration diagram and the quadratic law by which it was fitted are presented in Fig. 7.

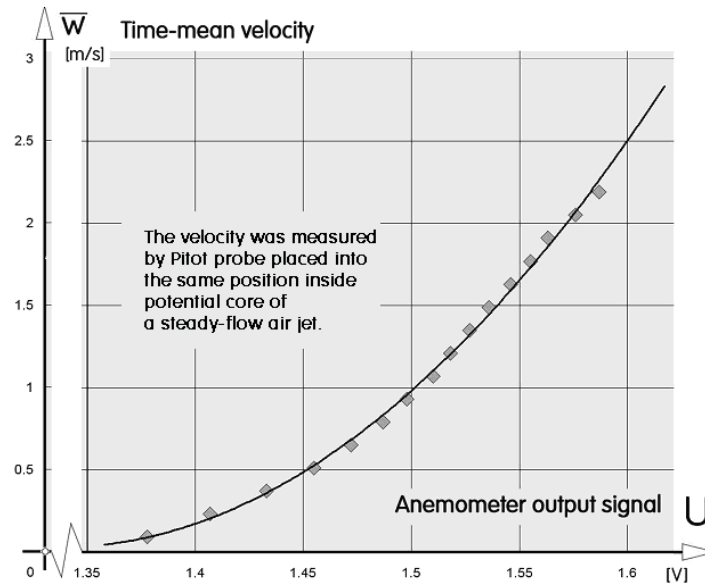


Fig. 7. Calibration curve of the hot-wire probe as used in the tests. The calibration procedure was specially set up so as to reach the range of very low velocities

It should be noted that because of the probe being of the single-wire type, it was sensitive not only to the axial component of the air flow velocity, but also to the radial component – since the heated wire was held oriented with its axis in the tangential direction relative to the nozzle axis. This is why – given the negligible tangential velocity component – the measured value is here described as velocity magnitude. Also, as usual with hot-wire probes, it was impossible to discriminate between positive and negative direction of the velocity.

3. Conclusions

The paper describes the purpose and the layout of the investigated laboratory model of an annular synthetic jet designed to reach to very large axial distances. The main reason for the measurements was accumulating data to be used in the concurrent numerical flowfield computations performed by doc. J. Vogel, see [21]. This was done with a complete success. Apart from the time-mean velocity distributions, to be reported in a forthcoming paper, we have also accumulated data on the spatial distributions of energy of fluctuation, evaluated by the same approach as described in [17, 18].

4. Acknowledgement

The authors acknowledge gratefully the support by the grant IAA200760705 from the Grant Agency of the Academy of Sciences of the Czech Republic, and by the grant 101/07/1499 from the Grant Agency of the Czech Republic. The hot wire probe traversing as well as an elegant method of data acquisition were devised by Mr. M. Pavelka.

References

- [1] Jain, S., Mukand, W., *The economics of high-visibility terrorism*, European Journal of Political Economy, Vol. 20, p. 479, 2004.
- [2] Krejčí, P., Trávníček, Z., Tesař, V., Kordík, J., Pavelka, M., *Frequency Characteristics of an Annular Synthetic Jet Actuator of Large Inner Diameter*, Proceedings of Conf. 'Experimental Fluid Mechanics 2007', Liberec 2007.

- [3] Settles, G. S., *Fluid Mechanics and Homeland Security*, Annual Review of Fluid Mechanics, Vol. 38, p. 87, 2006.
- [4] Smith, B. L., Glezer, A., *The formation and evolution of synthetic jets*. Physics of Fluids, p. 2281, Vol. 10, No. 9, 1998.
- [5] Tesař, V., *Čerpadlo nebo dmychadlo, zejména pro dopravu obtížně čerpatelných tekutin (Pump or blower, in particular for transporting fluids difficult to pump - in Czech)*, Czechoslovak Certificate of Authorship No. 192 082, 1976.
- [6] Tesař, V., *Aktivní fluidický uzavírací ventil, (Active Fluidic Turn-Down Valve - in Czech)*, Czechoslovak Certificate of Authorship Nr. 212 802, 1980.
- [7] Tesař, V., *Fluidic pump driven by alternating air flow*, Proc. Colloquium on Pneumatics and Hydraulics PNEU-HIDRO '81, Győr, Hungary, p.57, 1981.
- [8] Tesař, V., *Zařízení k odstraňování prachu z nosiče záznamu, zejména při reprodukci z gramofonové desky (Facility for removal of dust from recoding medium, in particular during a reproduction from gramophone record – in Czech)*, Czechoslovak Certificate of Authorship Nr. 238 658, 1981.
- [9] Tesař, V., *Fluidic jet-type rectifier: experimental study of generated output pressure*, Fluidics Quarterly, Ann Arbor U.S.A, Vol. 14, Nr. 4, 1982.
- [10] Tesař, V., *Zákonitost pro strhávání okolní tekutiny při střídavém vtoku a výtoku tryskou (Law governing entrainment of surrounding fluid during alternating inflow into and outflow from an orifice - in Czech)*, PO 86-84, Czechoslovak Patent Office, Prague, Czech Republic 1984
- [11] Tesař, V., *Ztráty při pulsujícím výtoku z trysky (Hydraulic Loss of a Nozzle Supplied with Pulsating Flow – in Czech)*, Proc. of Conf. 'Aplikácia experimentálnych metód', p. 23, Tatranske Matliare, Slovakia, 1989.
- [12] Tesař, V., *Strhávací účinek střídavého vtoku a výtoku tryskou (Etrainment action of an alternating inflow into and outflow from a nozzle - in Czech)*, Acta Polytechnica, 1, (II,1), p. 43, 1991.
- [13] Tesař, V., *Fázové trajektorie pulsujícího výtoku vzduchu tryskou (Phase Trajectories of a Pulsating Flow through a Nozzle – in Czech)*, Proc. of Colloq. "Dynamika tekutin '96", publ. by Institute of Thermomechanics AS ČR, ISBN:80-85918-23-4, p. 61, 1996
- [14] Tesař, V., *Pressure-Driven Microfluidics*. Artech House Publishers, Boston - London, pp. 389 – 393, 2007.
- [15] Tesař, V., *Valve-Less Rectification Pumps*, Chapter in “Encyclopedia of Microfluidics and Nanofluidics“, Ed.: Dongqing Li, publ. by Springer Science+Business Media, LLC., ISBN: 978-0-387-48998-8, pp. 2132-2139, 2008.
- [16] Tesař, V., Jílek, M., Randa, Z., *Topology Changes in an Annular Impinging Jet Flow*, Proc. of Conf. "Topical Problems of Fluid Mechanics 2001", p.12, ISBN 80-85918-62-5, Publ. by Inst. of Thermomechanics AS CR, Prague, Czech Republic, 2001.
- [17] Tesař, V., Kordík, J., *Quasi-Similarity Model of Synthetic Jets*, Sensors and Actuators A. Physical, ISSN: 0924-4247, Vol. A 149, pp. 255 – 265, 2009.
- [18] Tesař, V., Kordík, J., *Time-Mean Structure of Axisymmetric Synthetic Jets, Sensors and Actuators: A. Physical*, Vol. 161 , pp. 217-224, 2010.
- [19] Tesař, V., Trávníček, Z., *Pulsating and Synthetic Impinging Jets*, Journal of Visualization, ISSN 1343-8875, The Visualisation Society of Japan, Vol. 8, No. 3, p. 201, 2005.
- [20] Tesař, V., Trávníček, Z., *Apparatus for Collection of Samples from the Surface of Examined Objects*, in Czech, Patent Application No. PV 2006-214, Patent Office of the Czech Republic, 2006.
- [21] Tesař, V., Vogel, J., Trávníček, Z., *Annular Synthetic jets for Anti-Terrorist Warfare*, Proc. of 12th Intern. Conf. on Developments in Machinery Designs and Control, Publ. by Univ. of Technology and Life Sciences in Bydgoszcz, Poland, 2008.
- [22] Trávníček, Z., Tesař, V., *Annular Synthetic Jet Used for Impinging Flow Mass Transfer*, International Journal of Heat and Mass Transfer, Vol. 46, Issue 17, p. 3291, 2003.



COMPETITIVE GROWTH AND COUPLET GROWTH ZONE IN EUTECTIC ALLOYS IN DIRECTIONAL SOLIDIFICATION

Małgorzata Trepczyńska-Lent

*University of Technology and Life Sciences,
ul. S. Kaliskiego 7, 85-796 Bydgoszcz, Poland
tel.: +48 52 3408719, fax: +48 52 3408245
e-mail: trema@utp.edu.pl*

Abstract

Although significant studies on eutectic systems have been carried out in the past, some critical fundamental questions still remain unanswered. The following several critical aspects of coupled growth are being examined in this study: (a) the influence of interface energy and its anisotropy on the lamellar to rod transition; (b) the ability to form coupled (or cooperative) growth of the two phases in eutectic systems; (c) the stability of eutectic structure under rapid solidification conditions.

Keywords: eutectic, kinetics, solidification, competitive growth, couplet zone

1. Introduction

Basic concepts of the theory of eutectic alloys are a small but theoretically and practically important part of the science of metals. In accordance with the old and universally accepted ideas the components of eutectic systems, which are almost insoluble (in many systems) in solid state, are infinitely miscible in the liquid state, i.e., at a temperature above the liquidus line on the phase diagram alloys are treated as liquid solutions of components. When cooled to the eutectic temperature T_e , a solution becomes supersaturated with both components; its crystallization occurs by diffusion decomposition into a mixture of crystals of almost pure components (solid solutions on their base, i.e., α and β). Eutectic equilibrium is described as $L = \alpha + \beta$.

In a melt of eutectic components, which is represented by double-phase dispersion, the dispersed particles and the dispersion medium form a solvate complex with eutectic composition, which is preserved in crystallization. This composition corresponds to a specific (for the given dispersion) proportion of components at which the entire dispersion medium is in a bound state (as a result of salvation) of interatomic interaction with the force field of the dispersed particles. The eutectic solvate complex crystallizes and melts completely at a constant temperature the lowest for the given dispersion [1].

2. The kinetics of eutectic solidification

The concepts of the mechanism of eutectic crystallization, of the structure and formation of main units of the macroscopic structure of a casting (ingot), i.e., eutectic grains (macrograins), have changed substantially from the beginning of the study of the topic. At first, a eutectic structure was often treated as a mechanical mixture of fine crystals not connected with each other.

Such a eutectic grows due to alternate nucleation and growth of crystals of both eutectic phases. This approach makes the search for any structural component (eutectic grain) other than fine crystals of eutectic phases in a casting senseless [2].

The linear rate of growth of the eutectic is specified by the expression $V_E = K_{VE} (\Delta T)^2$, where K_{VE} is a constant for the given alloy. This expression is a result of the solution of the two-dimensional problem on the distribution of the dissolved component in the melt in front of the double-phase crystallization front of the eutectic. It should be noted that strictly speaking, its use is not justified for growth stages accompanied by variation of the temperature. Such variation of the temperature is observed in the initial stage of formation of eutectic grains and during hardening of the last portions of the melt. However, the duration of these processes is very short relative to the duration of the EC as a whole, which allows us to use this expression [2,3].

Kinetics of eutectic transformation leads to additional deviation from equilibrium, because melting of extremely non-uniform eutectic system requires mass transfer of eutectic components through liquid phase. Atoms of eutectic alloy are transferred for distances comparable to structural parameters of solid eutectic. That is many times as much as for melting transition in pure metal where only minimal displacements of atoms from crystal lattice nodes are required [4].

The mentioned difference in the crystallization of alloys with nearly eutectic concentration and primary crystals belonging and not belonging to the base phase is representable by the diagram given in Fig. 1a. When the second phase of the eutectic nucleates on a primary crystal of the base phase, it rapidly covers the entire surface of the primary crystal; the independent growth of the primary crystal stops, and the EC begins. Geometrically this situation is describable by a ring model (Fig. 1a). When the first crystal does not belong to the base phase, its growth does not stop

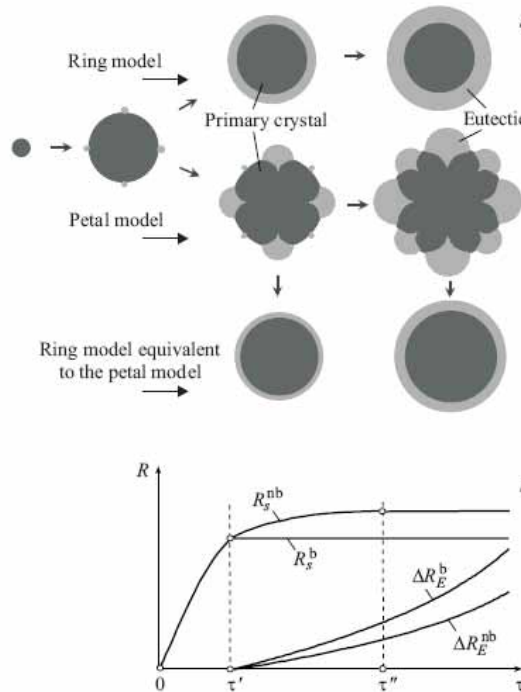


Fig. 1. Ring and petal models of eutectic crystallization (a) and difference in the kinetics of their growth (b): τ' and τ'' are moments of nucleation of second phase on the surface of the first phase and of enclosure of the surface of the primary crystal by eutectic, respectively; R_s^b and R_s^{nb} are radii of primary crystals of the base and nonbase phases; ΔR_E^b and ΔR_E^{nb} are thicknesses of eutectic shells on primary crystals of the base and nonbase phases [2]

upon the nucleation (inoculation) of crystals of the second phase. The primary crystal continues to grow until the eutectic grains, the linear rate of growth of which exceeds that of the primary

crystal, close around it. This kind of structure is known as a petal one. Since the mapping of a petal model is difficult to obtain, we use an equivalent model for geometric representation. The difference in the growth kinetics of the ring and petal models is shown in Fig. 1b [2].

3. Competitive growth of different phases in eutectic alloys

A competitive growth mechanism of eutectic has been suggested by Tammann and Botschwar [5] from a study of formation ability of eutectic structures. That is to say, the microstructure of alloys near the eutectic point is determined by competition between the eutectic structure and the primary phase. Only when the growth of phases takes precedence over that the primary phase, the eutectic-like microstructure can be produced. Otherwise, the primary phase is dominant.

In directional solidification, the interface growth temperature of the primary phase at different growth rates can be described by [6]:

$$T_j^i = T_L^i - \frac{G_L D_L}{V} - A_j V^{1/2}, j = \alpha, \beta \quad (1)$$

where:

T_L^i - the liquidus temperature at the alloy composition C_o ,

V - the growth rate,

G_L and D_L - the temperature gradient and diffusion coefficient in liquid, respectively.

The parameter A_j in eq. (1) is given as:

$$A_j = \left[-\frac{8\Gamma_j m_j C_o (1 - k_j)}{D_L} \right]^{1/2}, j = \alpha, \beta \quad (2)$$

where:

Γ_j , m_j and k_j - Gibbs-Thomson coefficient, slope of j -phase liquidus and solute distribution coefficient, respectively.

For eutectic solidification, the interface growth temperature of coupled eutectic in directional solidification can be calculated using the model described by Magnin and Trivedi [7] as:

$$T_e^i = T_E - (\phi + 1/\phi)(K_1 K_2)^{1/2} V^{1/2} = T_E - B V^{1/2}, \quad (3)$$

where $B = (\phi + 1/\phi)(K_1 K_2)^{1/2}$,

$$K_1 = \frac{\bar{m} C_e^o P}{D_L f_\alpha f_\beta}, \quad (4)$$

$$K_2 = 2\bar{m} \delta \left(\frac{\Gamma_\alpha \sin \theta_\alpha}{|m_\alpha| + m_\beta} + \frac{\Gamma_\beta \sin \theta_\beta}{m_\beta f_\beta} \right), \quad (5)$$

$$\bar{m} = \frac{|m_\alpha| m_\beta}{|m_\alpha| + m_\beta}, \quad (6)$$

$$C_e^o = C_\beta^o - C_\alpha^o. \quad (7)$$

For lamellar eutectic growth, the parameters P and δ can be written in simplified forms as:

$$P \cong 0,3383(f_\alpha f_\beta)^{1,661}, \quad (8)$$

$$\delta = 1. \quad (9)$$

For rod eutectic growth, the parameters P and δ can also be simplified as:

$$P \cong 0,167(f_\alpha f_\beta)^{1,25}, \quad (10)$$

$$\delta = 2\sqrt{f_\alpha}, \quad (11)$$

where:

T_E - the equilibrium solidification temperature of eutectic,

\overline{m} - the average slope of eutectic defined in eq. (4),

f_α, f_β - the volume fractions of α phase and β phase respectively,

C_e^o - the composition difference between the solubility limits of β phase (C_β^o) and α phase (C_α^o) defined in eq. (7) at the eutectic solidification temperature [7].

A methodology of competitive growth outlined above provides an adequate framework to understand the major features of the transition from eutectic to dendritic growth. However more subtle variations in eutectic microstructure occur under conditions close to the transition that require a more complete analysis of interface stability [9].

4. Prediction of eutectic coupled zone

The argument in this respect is whether the thermal undercooling ΔT_t and kinetic undercooling ΔT_k can be omitted when dealing with the lamellar eutectic growth within an undercooled alloy melt. The bulk undercooling ΔT of a liquid alloy is usually divided into four parts [10,11]:

$$\Delta T = \Delta T_c + \Delta T_r + \Delta T_t + \Delta T_k, \quad (12)$$

where:

ΔT_c and ΔT_r - the solute undercooling and curvature undercooling.

So far, there has been no analytical model to specify the thermal undercooling for eutectic growth. If the bulk undercooling is not very large, ΔT_c and ΔT_r play the dominant roles, whereas ΔT_t and ΔT_k only make minor contributions.

This has been confirmed by the experimental work of many investigators. In fact, there exist two undercooling thresholds for the “lamellar eutectic–anomalous eutectic” structural transition

[10]. Below the lower undercooling threshold ΔT_1^* of about 30–60 K, lamellar eutectic is the unique growth morphology. Above the upper undercooling threshold ΔT_2^* of about 150–200 K, only anomalous eutectic can grow. In the intermediate undercooling regime of $\Delta T_1^* - \Delta T_2^*$, both lamellar eutectic and anomalous eutectic coexist. Metallographic analyses demonstrate that anomalous eutectic is the product of rapid solidification during recalescence, while lamellar eutectic forms in the slow period of solidification after recalescence. Because the remnant undercooling at the end of recalescence becomes quite small, lamellar eutectic growth corresponds to the small undercooling condition even within the intermediate undercooling regime.

As a first order approximation, it is reasonable to neglect the influences of thermal undercooling ΔT_t and kinetic undercooling ΔT_k on lamellar eutectic growth. Consequently, eq. (1) leads to the following approximate relation [10,11]:

$$\Delta T \approx \Delta T_c + \Delta T_r \quad (13)$$

5. Coupled growth zone

The couplet growth zone marks the range of the chemical composition, the growth rate and the temperature gradient, which assure the obtainment of the exclusively eutectic structure (without hypoeutectic phase). Way of marking couplet zone on the basis of the theory of the competitive growth was showed on the Fig. 2 [11, 12].

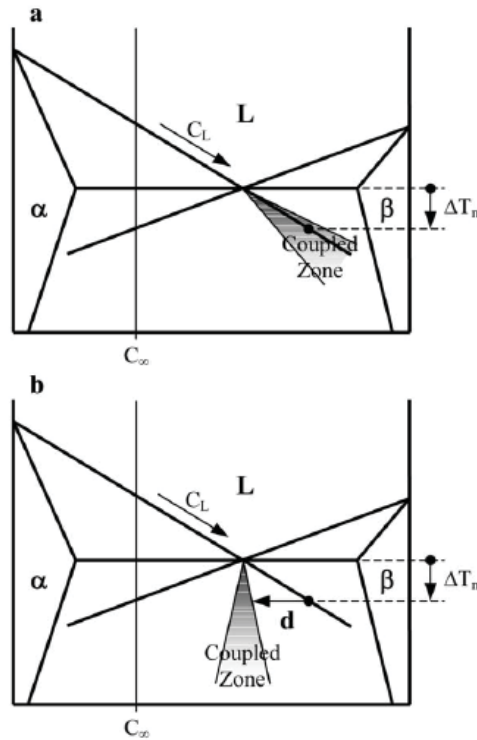


Fig. 2. (a) The coupled zone encompasses the α liquidus extension: coupled eutectic growth occurs directly from the primary α dendrites. (b) The coupled zone does not encompass the α liquidus extension: haloes of β form around the primary α dendrites for any significant β nucleation undercooling ΔT_n [11,13]

Figure 3 is a kind of phase diagram in eutectic systems that the coupled zone encompasses the α liquidus extension. Interface growth temperatures of the single α phase, single β phase and coupled eutectic ($\alpha + \beta$) calculated by eq. (1) and eq. (3) are illustrated schematically as a function of growth rates at a given composition C_o in hypereutectic alloy on the right side of Fig.3.

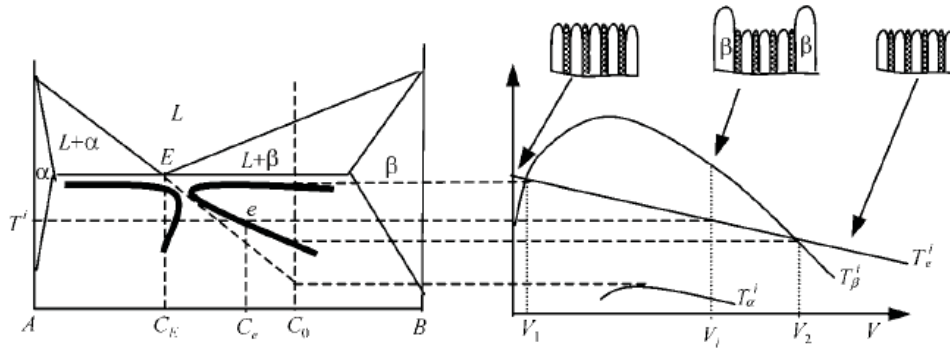


Fig. 3. Coupled zone encompasses the α liquidus extension in eutectic systems and interface growth temperatures of the single α phase, single β phase and coupled eutectic ($\alpha+\beta$) are calculated by eq. (1) and eq. (3) as a function of growth rates at a given composition C_0 in a hypereutectic alloy [8]

Coupled growth zone can be outlined with the same interface growth temperature and composition for the single phase and coupled eutectic. From Fig. 3, at lower growth rate V_1 and higher growth rate V_2 , the interface temperature of the single β phase T_β^i and coupled eutectic T_e^i , are equal at the given composition C_0 . When the imposed growth rate V_i is below V_1 , coupled eutectic ($\alpha+\beta$) becomes stable due to the sharp drop in the single-phase temperature, which contributes to the presence of the positive gradient through the term, $G_L D_L / V$ in eq. (1). Thus for finite G_L , the single-phase interface temperature is given by eq. (1) in which the contribution from the third term on the right hand side is negligible. Eq. (1) and eq. (3) can be simplified at low growth rate V_1 as:

$$T_\beta^i \approx T_L^\beta - \frac{G_L D_L}{V} - A_\beta V^{1/2} \approx T_E + m_\beta (C_0 - C_E) - \frac{G_L D_L}{V}, \quad (14)$$

$$T_e^i = T_E - B V^{1/2} \approx T_E, \quad (15)$$

where:

C_E - the eutectic composition, by equating eqs. (14) and (15), the value of the growth rate V_1 , at which the primary β phase-coupled eutectic ($\alpha+\beta$) transition occurs at low undercoolings can be derived as:

$$V_1 = \frac{G_L D_L}{m_\beta (C_0 - C_E)}. \quad (16)$$

At high growth rate, the term $G_L D_L / V$ in eq. (1) is small and can be neglected. Under this assumption, eq. (14) can be approximated as:

$$T_\beta^i \approx T_L^\beta - \frac{G_L D_L}{V} - A_\beta V^{1/2} \approx T_E + m_\beta (C_0 - C_E) - A_\beta V^{1/2}. \quad (17)$$

Equating eq. (3) and eq. (17), the value of the high growth rate V_2 at which the primary β phase coupled eutectic ($\alpha+\beta$) transition occurs at high undercoolings shown in Fig. 2 can be written as:

$$V_2^{1/2} = \frac{m_\beta(C_o - C_E)}{A_\beta - B} \quad (18)$$

The right hand side of eq. (18) should be positive and values of A_β and B can be calculated using eq. (2) and eq. (3), respectively. From eq. (16) and eq. (18), with the composition C_o approaching the eutectic composition C_E , the value of the low growth rate V_1 increases and the value of the high growth rate V_2 decreases. If V_1 is equal to V_2 , the alloy composition C_o corresponding to coupled eutectic ($\alpha+\beta$) growth at any growth rates can be obtained in directional solidification. Moreover, with the increasing growth rate, coupled eutectic ($\alpha+\beta$) will be refined as shown in Fig. 3. In addition, if the imposed growth rate is very large, it should be noted that the directional heat flux would be destroyed and the solidified microstructure would not be the directionally coupled eutectic and it may be the equiaxed eutectic [8].

6. Discussion and conclusion

The study of eutectic growth characteristic has shown that the shape and size of the eutectic couplet zone is determined by growth features and solidification conditions. For example, to obtain a proper eutectic growth in the eutectic system containing a pair of faceted/non-faceted phases, the growth of non-faceted phase should be suppressed (or promoted), due to the strong growth anisotropy of the faceted phase.

The undercooling range for the coupled eutectic growth enlarges due to the kinetic effect. The kinetic effect is dependent not only on the growth velocity, but also on the type of phase diagram. As the crystallization temperature range of eutectic phases at the eutectic composition decreases, the kinetic effect is enhanced.

The significant difference in linear kinetic coefficient of non-faceted and a faceted phase results in a remarkable difference in kinetic undercooling that plays an important role in influencing the shape of the couplet zone in rapid solidification. To maintain the couplet growth of eutectic phase, the solute undercooling of the faceted phase is weakened in comparison with that of the non-faceted phase by shifting the eutectic composition to the faceted phase side and thus leading to the formation of a skewed locus of eutectic composition in rapid processing. The symmetrical couplet zone with a non-faceted/non-faceted reaction can also be well clarified when their comparable contribution in kinetic undercooling are taken into account.

References

- [1] Zalkin, V. M., *On the theory of eutectic alloys and presentation of the theory in textbooks on physical metallurgy*, Metal Science and Heat Treatment Vol. 51, No. 3-4, pp.153-159, 2009.
- [2] Vol'nov, I. N., *Computer simulation of the kinetics of eutectic crystallization*, Metal Science and Heat Treatment Vol. 46, No. 1-2, pp. 61-66, 2004.
- [3] Dioszegi, A., Svensson, I.L., *Inverse kinetic analysis method to study eutectic growth*, International Journal of Cast Metals Research, vol. 18, no. 1, pp. 41-46, 2005.
- [4] Li, J.F., Zhou, Y.H., *Eutectic growth in bulk undercooled melts*, Acta Materialia 53, pp. 2351-2359, 2005.
- [5] Tammann, G., Botschwar, A.A., *Über die Kristallisationsgeschwindigkeit in binären und ternären Mischungen, aus denen die reinen Komponenten kristallisieren*. Zeitschrift für anorganische und allgemeine Chemie vol. 157, pp. 26-40, 1926
- [6] Burden, M. H., Hunt, J. D., *Cellular and dendritic growth*, Journal Crystallization Growth, Vol. 22 (2), pp. 109-116, 1974.

- [7] Magnin, P., Trivedi, R., *Eutectic growth: A modification of the Jackson and Hunt theory*, Acta Metall. Materiala, 39(4), pp. 453–467, 1991.
- [8] Shuangming, L., Bole, M., Xiaoli, L., Lin, L., Hengzhi, F., *Competitive growth of different phases in eutectic alloys under directional solidification*, Science in China Ser. E Engineering & Materials Science Vol.48 No.3, pp. 270-281, 2005.
- [9] Cahn, R.W., Haasen, P., *Physical metallurgy*, vol. 3, 1996.
- [10] Yao, W.J., Cao, C.D., Wei, B., *Reply to comments on free eutectic and dendritic solidification from undercooled metallic melts*, Scripta Materialia 54 , pp. 1433–1437, 2006.
- [11] Li, K., Yoda, S., Kuribayashi, K., *Asymmetrical of eutectic growth kinetics on the doublet growth in rapid eutectic solidification*, Philosophical Magazine, Vol. 85, No. 23, pp.2581-2591, 2005.
- [12] Fraś, E., *Krystalizacja metali*, WNT, Warszawa, 2003.
- [13] Nave, M.D., Dahle A.K., StJohn D.H., *Halo formation in directional solidification*, Acta Materialia 50, pp. 2837–2849, 2002.



RULES IN THE GENESIS OF MACHINES STATE

Henryk Tylicki

*University of Technology and Life Sciences
ul. S. Kaliskiego 7, 85-789 Bydgoszcz, Poland
tel.: +48 52 340828, fax.: +48 52 308283
e-mail: tylicki@utp.edu.p*

Abstract

The study concerns the problem of indication of the procedures employed in the machines state genesis which are the foundation for the compilation of the rules of inference for determination of the reasons behind the state of machine incapacity.

Keywords: *genesis the condition of machine, the algorithmization of procedures, the rules of inference.*

1. Problem characteristics

Implementation of the genesis of the vehicles state methods in the exploitation process, what is the base of automation of state identification process, requires, among others, optimization of the diagnostic parameters and genesis methods.

The solution to those problems depends on many factors connected with their degree of dependence on the complexity of the machines, the use of multi-symptom observations, the quality of the exploitation process and utilization process.

Genesis of vehicles state is the process which should enable the forecast of the machine state in the past tense based on the incomplete history of the diagnostic tests results. It allows for machine state estimation or machine breakdown reason finding in examination moment.

The question of the choice, which seems to be especially important in the genesis of the state process, are:

- a) the set of diagnostic parameters dependent on the machine working time, examination frequency and the average quantity of the optimal set of diagnostic parameters
- b) the genesis method dependent on the machine horizon, the minimal number of the time chain elements necessary for the genesis start-up and the machine working time.

The study of the problems introduced above, the dynamics of their construction, high users expectations as well as the current legal regulations concerning the users safety and environmental protection are the sufficient urge to search new diagnosis methods as well as to determine new measurements and tools to describe the current diagnostic states in their exploitation process. All of above is presented below, as suitable procedures, algorithms and rules flow of them.

2. Procedure concerning optimization of the set of diagnostic parameters

The set of diagnostic parameters stands out of the set of initial parameters. On the base of the

already conducted tests, the aim of which was to confirm some suggestions included in the literature concerning diagnostic information reduction in forecasting process, it is assumed that the following problems need to be taken into account while determination of the set of diagnostic parameters in the prognosis and genesis of the machine state [1,2,3,4,11]:

- a) the ability of machine state modeling during its exploitation,
- b) the amount of information concerning machine state,
- c) the proper variability of the diagnostic parameters values during machine exploitation.

Thus the proper algorithms, with taking to account above, are introduced below as the following methods:

1. Correlation method of the diagnostic parameters and machine state which is testing the correlation of diagnostic parameters and machine state $r_j = r(W, y_j)$ (alternatively with exploitation time ($r_j = r((\Theta, y_j)$). In case of lack of data from the W collection these are replaced with machine exploitation time, on the assumption that indication of machine state diagnostic procedures is realized in the period of normal utilization time. Then $r_j = r(\Theta, y_j)$; $j=1, \dots, m$; $k=1, \dots, K$ (r_j – correlation factor between $\Theta_k \in (\Theta_1, \Theta_b)$ (Θ_k – machine exploitation time) and y_j).

2. Maximum information capacity of the diagnostic parameter method.

The aim of this method is to choose the parameter which provides the largest number of information concerning machine state. The importance of the diagnostic parameter rises according to its correlation with the machine state and correlation decreasing with other diagnostic parameters. This correlation is shown in the shape of indicator of diagnostic parameter capacity h_j , which is modification of the indicator concerning the set of variables explaining econometric model.

The advantage of the methods introduced above is the fact that they let choose from the set of initial parameters both one-element as well as multi-element set of diagnostic parameters. One-element set concerns the case when machine is decomposed into the units and it is necessary to choose only one diagnostic parameter. Multi-element set is received when more lenient limits have been employed in the introduced procedures. By more lenient one should understand the situation when parameters of bigger or smaller indicating value have been classified in the set of diagnostic parameters, for which indicators value are higher (lower) in comparison to accepted for high (low) numbers method.

The algorithm for indicating the optimal set of diagnostic parameters values is the following:

1. Data acquisition:

- a) the set of diagnostic parameters values in the function of the machine time exploitation $\{y_j(\Theta_k)\}$, gathered during the realization of passive-active experiment, where $\Theta_k \in (\Theta_1, \Theta_b)$;
- b) the set of diagnostic parameters: $\{y_j(\Theta_1)\}$ - nominal values, $\{y_{jg}\}$ - boundary values, $j=1, \dots, m$
- c) the set of machine states $\{\Theta_k: \{s_i\}, k=1, \dots, K; i=1, \dots, I\}$, achieved during the realization of passive-active experiment, where $\Theta_k \in (\Theta_1, \Theta_b)$;
- d) the cost of diagnostic parameters $c(y_j) = \text{const}$.

2. Optimization of the set of diagnostic parameters values (only in the case of a large quantifiy of Y set, e.g. $m > 10$). The set of diagnostic parameters is determined by means of:

- a) correlation method of diagnostic parameters values and machine state (with exploitation period, $r_j = r(W, y_j)$, ($r_j = r((\Theta, y_j)$):

$$r_j = \frac{\sum_{k=1}^K (\Theta_k - \bar{\Theta})(y_{j,k} - \bar{y}_j)}{\sqrt{\sum_{k=1}^K (\Theta_k - \bar{\Theta})^2 \sum_{k=1}^K (y_{j,k} - \bar{y}_j)^2}} \quad (1)$$

$$\overline{\Theta} = \frac{1}{K} \sum_{k=1}^K \Theta_k, \quad \overline{y_j} = \frac{1}{K} \sum_{k=1}^K y_{j,k} \quad (2)$$

- b) the method concerning the amount of information of diagnostic parameters about the machine state:

$$h_j = \frac{r_j^2}{1 + \sum_{j,n=1, j \neq n}^m |r_{j,n}|} \quad (3)$$

$$r_{j,n} = \frac{\sum_{k=1}^K (y_{j,k} - \overline{y_j})(y_{n,k} - \overline{y_n})}{\sqrt{\sum_{k=1}^K (y_{j,k} - \overline{y_j})^2 \sum_{k=1}^K (y_{n,k} - \overline{y_n})^2}} \quad (4)$$

$$\overline{y_j} = \frac{1}{K} \sum_{k=1}^K y_{j,k} ; \quad \overline{y_n} = \frac{1}{K} \sum_{k=1}^K y_{n,k} \quad (5)$$

where: $r_j = r(W, y_j)$; $j=1, \dots, m$ - the factor of correlation between W (machine state) and y_j variables.

In case of lack of data from the W collection these are replaced with machine exploitation time, on the assumption that the indication of the machine state procedures is realized in the period of normal utilization time. Then $r_j = r(\Theta, y_j)$; $j=1, \dots, m$; $k=1, \dots, K$ (r_j - correlation factor between $\Theta_k \in (\Theta_1, \Theta_b)$ (Θ_k - machine exploitation time) and y_j variables).

In order to choose the set of diagnostic parameters the weight values are used

- a) computable weight :

$$w_{1j} = \frac{1}{d_j}, \quad d_j = \sqrt{(1 - r_j^*)^2 + (1 - h_j^*)^2} \quad (6)$$

$$r_j^* = \frac{r_j}{\max r_j}, \quad h_j^* = \frac{h_j}{\max h_j} \quad (7)$$

- b) the criterion of diagnostic parameter(s) choice here is maximum of the weight values w_{1j} and the choice of diagnostic parameters according to the described criterion.
c) in order to match the users preferences it is possible to introduce weights w_2 (standard values) from the (0,1) section and to choose diagnostic parameters according to the described criterion.

3. Genesis of the machine state procedure

While discussing the problem of the machine state genesis, some genesis methods should not be considered better than others. It all depends on the subject of the study and the aim of the machine state genesis. While employing some criteria concerning [5,6,7,8,12]:

- a) the character of the genesis (the value of the symptom genesis, the estimated machine state in the past, the value of the past work or a different character of the machine state genesis),
b) the influence of the change of the machine exploitation conditions and the operational activities on the machine exploitation attributes, which need to be considered while choosing the genesis method,

- c) genesis methods likely to be used (e.g. quality methods, modified trend extrapolation methods and modified adaptation methods),

Algorithm of the machine state genesis method according to the estimation of the diagnostic parameters value scheme includes the following elements:

1. The set of diagnostic parameters genesis $\{y_j^*\}$:
 - a) with help of diagnostics parameter y_j^* value approximation methods in time range (Θ_1, Θ_b) with approximation tolerance radius r_a for “tolerance channel”;
 - b) by means of diagnostic parameter y_j^* interpolation in the time range (Θ_1, Θ_b) with approximation tolerance radius r_a for “tolerance channel” using glued functions method 1, 2, 3 equation;
 - c) the choice of method according to nominal or maximal value of tolerance radius for approximation or interpolation (machine tolerance e_G).
2. Analysis of the cause of $s_i(T_{LU})$ state:
 - a) the set $\{s_i(\Theta_k), i=1, \dots, 1; k=1, \dots, K\}$ presentation.
 - b) determination of the common point of the „tolerance channel” indicated by the tolerance radius $r_j^* = \max(r_{ja}, r_{ji})$ and the diagnostic parameter y_j^* boundary value at the moment $\Theta_s \in (\Theta_1, \Theta_b)$ moment, which means that the reason for the localized state s_i was the temporary appearance of that state in the time (Θ_1, Θ_b) ;
 - c) defining more number of the common points of the “tolerance channel” indicated by the tolerance radius $r = \max(r_a, r_i)$ and the diagnostic parameter y_j^* boundary values in the moments $\Theta_s \in (\Theta_1, \Theta_b)$ means that the cause of the localized state s_i was the rising development of that state in the time (Θ_1, Θ_b) ;
 - d) in case of lack of common points defining the minimal length of the “tolerance channel” from the boundary value in the moment $\Theta_s \in (\Theta_1, \Theta_b)$, which means that the cause of the localized state s_i was probably temporary incomplete appearance of that state in the (Θ_1, Θ_b) time;
 - e) analysis of identity of the set of states $\{s_i(\Theta_k), k=1, \dots, K\}$ and the localized by T_{LU} of s_i state for the determination of its appearance in the context of alternative common points or minimal length of approaches.

4. The rules of making conclusion in the defining of the causes of machine incapacity

The analysis of the task demands in relation to state forecasting and next maintenance time defining, occurred, that in the data base, beside sets of boundary, values, nominal values and diagnostic parameters values registered during exploitation, rules for diagnostic conclusions are necessary.

Analysis of the results of the research into methodology of machine state forecasting [11,12,13] allows for formulation of the rules for conclusion of type “IF-THEN” or “IF-THEN-ELSE” in the field of

- a) optimization of diagnostic parameters;
- b) machine state genesis.

For example for 6203 car bearing and for the internal combustion engines in Star 11422 cars generated rules are as below:

1. Conclusion rules for 6203 bearing:
 - a) for diagnostics parameters Y^0 set optimization:
 - if $w_{1j} \geq 0,02$ to $y_j \in Y^0$,
 - or if $w_{1j} = w_{1j\max}$ to $y_j \in Y^0$;
 - b) for the state genesis:
 - if the set of probable bearing damage occurs, defining of the state of incapacity according

to the level of occurrence probability follows the $p(s_i) \geq 0,5$ to $s_i \in S$ rule,

- if there is no probable damage to bearing, defining the states of incapacity according to the measure of exploitation: if $\Theta_i \geq \Theta_1$ to s_i ($\Theta_1 \in S$),
- if the mistake of the second degree approximation for the set $Y^0 \leq$ mistakes genesis interpolation method of the first degree for the set Y^0 then the genesis method for the set of values in the Y^0 set is the first degree interpolation method, or else the second degree interpolation method,
- if the genesied diagnostic parameter distance $y_j \in Y^0$ with genesis mistake from boundary parameter $y_{jG} \in Y^0$ values is: $d(y_{jG} - \text{value}(y_{jG} + r_G))$ for $y_{jG} > y_{jG}$, $d(\text{value}(y_{jG} - (y_{jG} - r_G)))$ for $y_{jG} < y_{jG}$ than minimum value $d(\bullet)$ is the minimum distance d_{\min} ,
- if $d_{\min} = 0$, than there is one common point with boundary value (number of $[d_{\min}] = 1$), if $d_{\min} < 0$, than there is more than one common point for boundary value (number $[d_{\min}] > 1$), if $d_{\min} > 0$, than there is no common points with boundary values,
- if $d_{\min} = d_{\min}(\Theta(s_i))$, than minimum value of $d_{\min}^{\bullet} = d_{\min}$ occurred in state in $\Theta_S \in (\Theta_1, \Theta_b)$ time, what means, that the reason of located state during s_i T_{LU} test was the temporary appearance of s_i state during (Θ_1, Θ_b) , in other case, $d_{\min} \neq d_{\min}(\Theta(s_i))$, what means, that the reason of s_i state ocured during T_{LU} test, is impossible to explain,
- if the number $[d_{\min}^{\bullet}] > 1$, it means that reason of located state s_i was caused by increasing development in $\Theta_S \in (\Theta_1, \Theta_b)$ time of s_i occurrence conditions (defined during T_{LU} test),
- if $d_{\min} > 0$ and there is no common point with boundary value, it means that most feasible reason of located s_i state (defined during T_{LU} test) was temporary, un full occurance of that state in (Θ_1, Θ_b) time;

2. The rules of meaking conclusions for Star 11422 car combustion engine:

a) for diagnostic parameters Y^0 set optimization:

- if $w_{1j} \geq 0,07$ then $y_j \in Y^0$,
- or if $w_{1j} = w_{1j\max}$ to $y_j \in Y^0$;

b) for state genesis:

- if there is set of most feasible combustion engine break down for Star 11422, defining, the set of its out of work states according to initial breakdown probability level rule: if $p(s_i) \geq 0,5$ than $s_i \in S$,
- if there is no set of most feasible Star 11422 combustion engine breakdown, defining the set of its out of work states according to exploitation measure value: if $\Theta_i \geq \Theta_1$ than s_i ($\Theta_1 \in S$),
- if the genesis approximation ,2 equate, method mistake for set $Y^0 \leq$ genesis mistake 1 equate for Y^0 set, then interpolation 1 equate is the genesis method for Y^0 set, in other case, 2 equate approximation i the genesis method,
- if the approximation 2 equate genesis mistake for Y^0 set \leq genesis method with 1 equate interpolation for Y^0 set, than the 1 equate interpolation is the genesis method for Y^0 set values, in other case 2 equate approximation is the method,
- if genesis diagnostic parameter $y_j \in Y^0$ value distance with genesis mistake from parameter y_{jG} boundary value: $(y_{jG} - \text{value}(y_{jG} + r_G))$ for $y_{jG} > y_{jG}$, $d(\text{value}(y_{jG} - (y_{jG} - r_G)))$ for $y_{jG} < y_{jG}$ then the minimal distance d_{\min} is the minimum value $d(\bullet)$,
- if $d_{\min} = 0$, than tere is only one common point with boundary value (number of $[d_{\min}] = 1$), if $d_{\min} < 0$, then there is more then one common point with boundary value (number $[d_{\min}] > 1$), if $d_{\min} > 0$, than there is no common points with boundary value,
- if $d_{\min} = d_{\min}(\Theta(s_i))$ than minimum value $d_{\min}^{\bullet} = d_{\min}$ occurred with state during $\Theta_S \in (\Theta_1, \Theta_b)$, what means that temporary s_i state appearance in $\Theta_S \in (\Theta_1, \Theta_b)$ time was the reason of occurred located s_i state T_{LU} test, in other case $d_{\min} \neq d_{\min}(\Theta(s_i))$ what means that it is impossible to define reason of s_i state during T_{LU} test,

- quantity $[d_{\min}^f] > 1$ mean, that the increasing of s_i occurring conditions development during $\Theta_S \in (\Theta_1, \Theta_b)$ time was the reason of located s_i (defined during T_{LU} test),
- if $d_{\min} > 0$ and there is no common point with boundary value means, that temporary, unfull s_i located state occurring during (Θ_1, Θ_b) time was the most feasible s_i located state occurring (s_i defined during T_{LU} test).

Presented making conclusion rules in range of machine state genesis, after suitable verifications can be the base for dedicated machine state estimation application in on-line mode for specific system or off-line mode for stationary system.

5. Conclusion

The above presentation of the vehicle state genesis procedure allows for the following conclusions:

1. Presented procedures allow for defining optimal, according to the assumed, criterion:
 - a) the set of diagnostic parameters;
 - b) diagnostic parameter values genesis and estimation of the causes of the machine state;
2. Taking the above into consideration, in order to define the set of diagnostic parameters and genesis the presented procedures may constitute the foundation for defining the rules of inference in the fields:
 - a) defining the optimal set of diagnostic parameters;
 - b) estimation of diagnostic parameters values in the past and estimation of the cause of the state of the object in the moment of testing.

References

- [1] Ameljańczyk, A., *Multiple optimization* (in Polish), WAT, Warszawa 1986.
- [2] Batko, W., *Synthesis methods of prediction diagnoses in technical diagnostics* (in Polish), Mechanika, z. 4. Zeszyty Naukowe AGH, Kraków 1984.
- [3] Bowerman, B., L., O'Connel, R., T., *Forecasting and Time Series*, Doxbury Press (USA), 1979.
- [4] Box, G., Jenkins, G., *Time series analysis, forecasting and control*, London 1970.
- [5] Brown, R., G., *Statistical Forecasting for Inventory Control*, Mc Graw-Hill, New York 1959.
- [6] Cempel, C., *Evolutionary symptom models in machine diagnostics* (in Polish), Materiały I Kongresu Diagnostyki Technicznej, Gdańsk 1996.
- [7] Cholewa W., Kaźmierczak J.: Data processing and reasoning in technical diagnostics. WNT, Warszawa 1995.
- [8] Inman, D., J., Farrar, C., J., Lopes, V., Valder, S., *Damage prognosis for aerospace, civil and mechanical systems*, John Wiley & Sons, Ltd. New York 2005.
- [9] Staszewski W., J., Boller C., Tomlinson G., R.: Health Monitoring of Aerospace Structures. John Wiley & Sons, Ltd. Munich, Germany 2004.
- [10] Theil, H., *Applied economic forecasting*, North-Holland, Amsterdam 1971.
- [11] Tylicki, H., *Optimization of the prognosis method of mechanical vehicles technical state* (in Polish), Wydawnictwa uczelniane ATR, Bydgoszcz
- [12] Tylicki, H.: Inference rule in machine state forecasting. Commission of Motorization and Power Industry in Agriculture. Polska Akademia Nauk, Oddział w Lublinie, vol. VIIA, Lublin 2007, pp. 114-120.
- [13] Żółtowski, B., *Diagnostic system for the metro train*, ICME, Science Press, pp. 337-344, Chengdu, China 2006.



MODERNIZATION OF THE SYSTEM MAINTENANCE THE MACHINES LINE HOR 6000

Rafał Bochen, Henryk Tylicki

*University of Technology and Life Science
ul. S. Kaliskiego 7, 85-789 Bydgoszcz, Poland
tel.: +48 52 340828, fax.: +48 52 308283
e-mail: tylicki@utp.edu.p
e-mail: r_bochen@wp.pl*

Abstract

Article concerns maintenance strategy for HOR 6000 production line machines, which is realized during their exploitation. The main goal of the article is to point at weak points of HOR 6000 production line and justification of the proposal of going from plan-preventive strategy to technical condition valuation strategy for HOR 6000 production line machines.

Key words: *production line HOR6000, weak point, opinion of state, maintenance strategy*

1. Introduction

Implementation of the optimum methods in the exploitation process requires setting diagnostic parameters and tests as well as genesis and prognosis methods. The solution of those tasks depends on many factors connected with the degree of complexity of the machines and the quality of the exploitation process.

Thus, there is the need for performing the research concerning compilation of the genesis monitoring procedures depending on those factors. In order to move from the traditional operating system based on the plan-preventive maintenance strategy to the machines state maintenance strategy the study of new procedures to be used for the monitoring of the state of the machine process are required. Also the algorithmization is required which will enable the compilation of the new computer program design and its implementations.

2. Characteristics of the HOR 6000 line machine operating system

HOR 6000 production lines, which are placed in the Philips Lighting Poland in Pila, which are the subject of this study are able to produce fluorescent lamps TLD 8/8" diameter at the speed from 6900 to 7100 items per hour [1].

At the beginning of the line there are the two cassette coating machines. They are used to deposit the suspension which changes the invisible into the visible light. The glass tube is

provided automatically by automatic Laser Guided Vehicles in the special, dedicated containers, which are put in the unloading subsystem (Fig.1.).

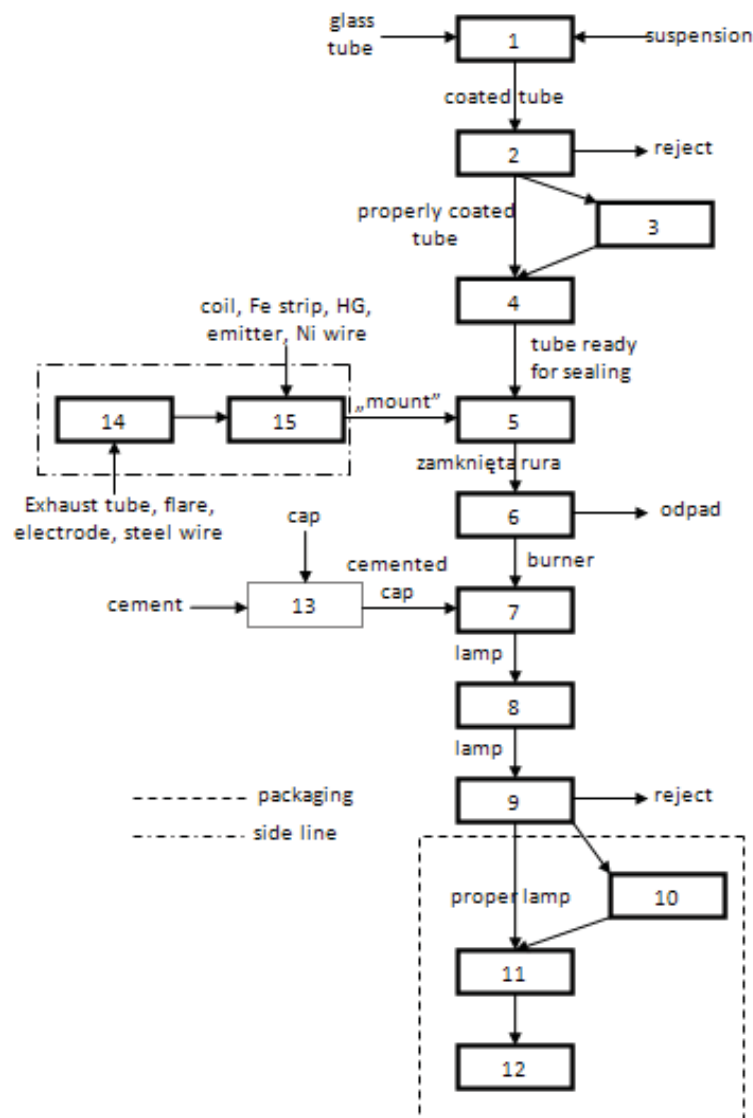


Fig.1. Functional schema of HOR6000 production line:

Main line: 1– coating machines, 2 – visual controls system, 3 – coated tubes robotized buffer, 4 – sintering oven with wiping machine, 5 – sealing machine, 6 – pumping machine, 7 – capping machine, 8 – hardening machine, 9 – flashing machine. Packaging group: 10 – robotized lamps buffer, 11 – single packaging machine, 12 – group packaging machine, 13 – cementing machine. Side line: 14 – steam making machine, 15 – mounting machine.

Following the coating machines there is the visional control system which checks if the quality of coating is according to technical specification. Then there is the buffer robot which buffers coated tubes e.g. for the time of the change of the produced lamp colour, which happens mainly in coating machines.

The next machines are wiping machines and the sintering oven in which flu-powder is dried so that it sticks to the sides of the tubes. In wiping machine the ends of the tubes are cleaned, what is very important for the sealing process. Sealing operation, which is done on sealing machine, is the process of closing both sides of the tube through connecting them with the mounts. After the connection process the tube is filled with the right gases mix in the pumping machine. The next machine - capping machine - is where the cap is putted thru. After the cement hardening on hardening machine the lamp is complete and theoretically ready for use, but it still needs to be tested in the flashing machine. Ready and tested lamps are packed and sent to customers.

During the production of the final product, which is TLD fluorescent lamp, the only activity required, providing that line is working well, is providing the components. Apart from that, in some machines there are short-lived machine parts which need to be renovated in highly specialized workshop.

Despite HOR6000 production line is automated (Siemens S7 system) the whole process needs to be monitored by highly-qualified machine operators. There are seven people required for the whole process to work properly.

The line functions thanks to the following electricity, ice water ($<5^{\circ}\text{C}$), demineralized water, earth gas, oxygen, compressed air – *high and low pressure*. The production process is stable and does not demand constant regulating. Some minor corrections on the machines are nevertheless necessary because of the difference in the used components.

The change in the range of the produced lamps concerns the change of the color or the power of the lamp.

The colour change takes place mainly in the coating machines area where liquid flu-powders are changed (suspension) currently produced lamp into the suspension which composition is adequate to colour desired after changeover. Actions connected with the colour changeover also take place on the side line - the change in the amount of mercury and in the product quality control systems through introduction of the parameters proper for the certain colour.

The change of the power in a lamp concerns the changes in the geometric setting in the main line, because different power lamps are of different length. Additionally, on the side line coil must be changed and the lamp control systems must be set for the proper power of the lamp.

Maintenance of the HOR 6000 production line is realized through the plan-preventive maintenance strategy. Once a week the line is stopped in order to maintenance during which, according to schedule, the parts and sub-systems of the machines are checked and replaced if needed. Similar checks are realized once a month and throughout a year.

The boosting of the exploitation effectiveness of HOR 6000 production line is possible through implementation of the exploitation strategy based on the state and monitoring of the machine state is indispensable for that. It is stated based on study of similar exploitation systems.

3. Analysis of the HOR 6000 production line systems

HOR 6000 production line has three systems which could be included in the monitoring of the machine state but the information gathered from the system is not complete and post factum [4,5,6]. Two of those systems are focused on the process data, and the third one concerns mainly the parameters of the machine work.

Also two of the accessible systems are fully automated and the third one is operated by the employees on the HOR 6000. Fully automated systems are CIRCLE (Control, Information, Recording, Communication, Labeling, Evaluation) based on the properly programmed PC computers and PLC Siemens S7 controllers with the suitable software, and particular breakdowns diagnosis system based on Siemens S7 controllers with suitable software.

CIRCLE system collects and archives process data which concern a small number of HOR 6000 (Fig.2.) machines units which have a direct impact on the production process.

Based on the CIRCLE system data a Process Engineer is able to estimate the state of some units of the machines which are directly involved in the production, e.g. looking at reject generated by particular machines, or the ready product parameters but he cannot estimate other sub-systems or their influence on the process parameters.

The first reaction for the increase of the reject is the regulation during the working of the machines. However, when there is no positive reaction to the corrections, or it is negative and the waste is rising to the interface value, determined by economic conditions, the machine is stopped, and it usually involves the whole production line to be stopped.

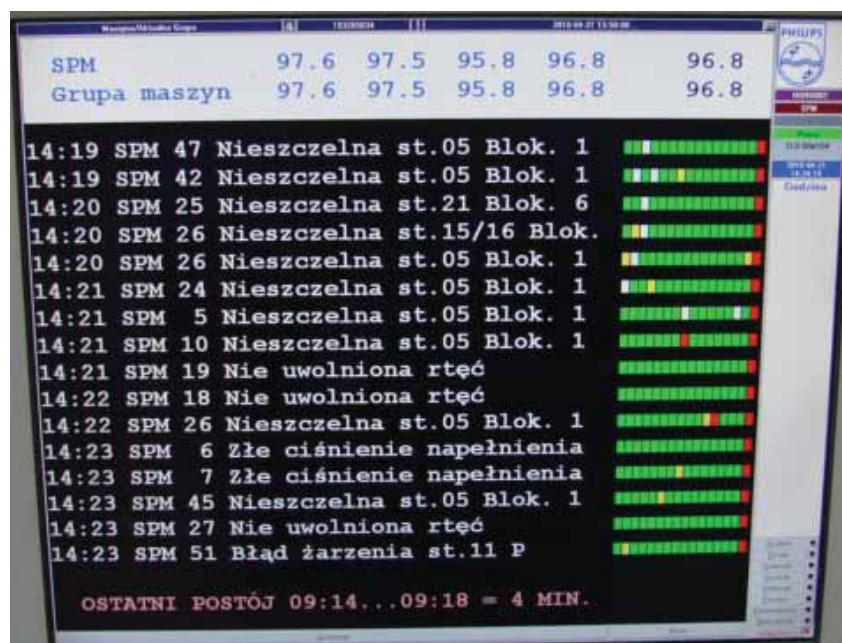


Fig. 2. CIRCLE screen



Fig. 3. Siemens S7 control panel

In the next step certain units of the machine are surveyed to localize the waste generating cause. It often happens that the replacement of the faulty element does not affect the decrease of the generated reject, which may bring the next stop of the machine and the line and the replacement of another unit of the machine. The type of the waste send the information to the expert about the potentially faulty units but only their check will assure the 100 percent certain diagnosis.

Siemens S7 (Fig.3.) computer system which controls work of the production line is programmed to detect the group of faults which can be identified based on the digital signals from the 1-binar detectors. Additionally, the machine working time is monitored and at the right

moment (predicted by the constructor), by means of the programmed announcements, informs about the necessity of the specified elements check.

Because the signal from the detectors is one-binar it provides the information whether the given unit is usable or not, but only at the moment when the production line is stopped due to a faulty unit. It shortens the time of enabling the machine and the line to work, but does not let estimate the state of the unit (e.g. useful, operatable but not necessary, requires operation, useless).

In the recent time (e.i. since mid-January 2010) HOR 60006 struggles with the waste reaching 18 percent of the production. All regulations and unit replacements based on CIRCLE system and expertise seem not to be effective (the waste at the moment is about 10 per cent). The situation gives a good reason for extending of the machine diagnosing in the state estimation, or even connecting the state estimating system with the process control system (CIRCLE).

State estimation procedure, which would be a part of the line monitoring system, would allow for the quick localization of the problem, and constant estimation of the machine state. That would allow for the fuzzy logic implementation and, together with process parameters monitoring, and for determining whether the worsening machine parameters are mechanic or process source (component, settings)

4. Damage analysis on the HOR 6000 production line

The first step of changing into the maintenance strategy based on the machine state, which seems to be much more suitable for production line with such high tech level, is indication of the weak points and determination of their incapacity states [1, 2, 3, 8].

For that aim all the damage in all the machines has been analyzed and it was shown that two thirds of all damage have the source in the following machines: *mounting machine*, *pumping machine*, *sealing machine*. The problem has been described by means of the following indicators [1,7,9,10,11]:

- the main - probability of the machine damage (Fig.4.)
- subsidiary - the time of breakdown in minutes over the period of one year (Fig.5.).

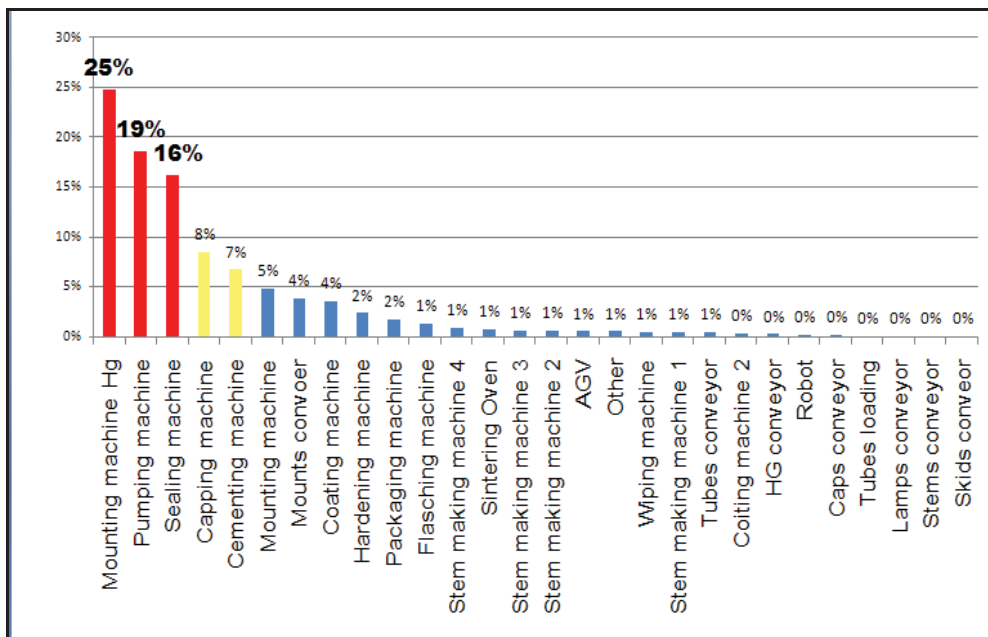


Fig.4. Probability of machines breakdowns

The subsidiary indicator has been chosen for the economic reasons. The cost of producing one lamp assumes the certain machine efficiency and each stop of the production causes the efficiency decrease. The results of analysis of the stop times throughout the year has confirmed that damage of the most breakdown prone machines are also the most troublesome.

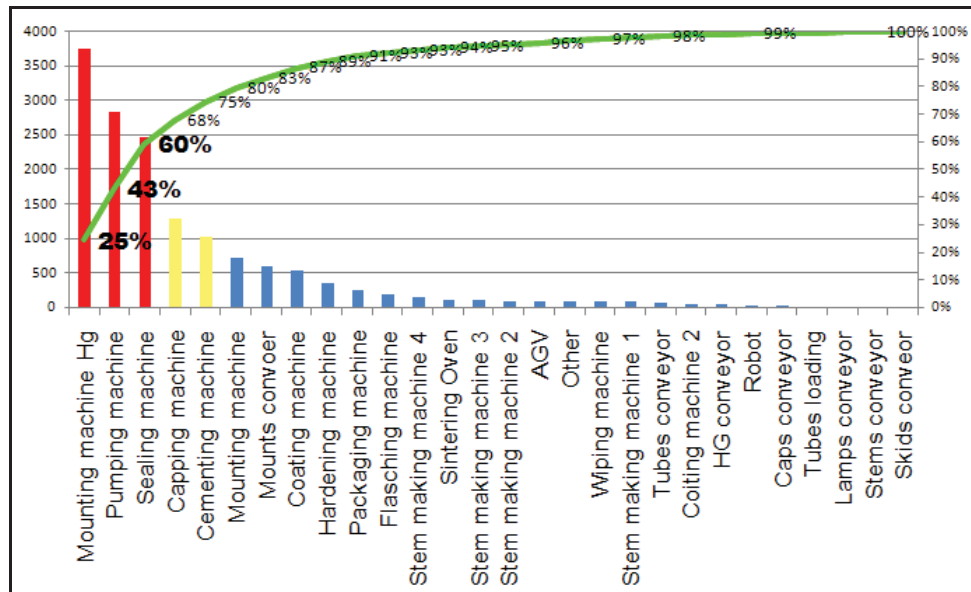


Fig.5. Time of breakdowns in min

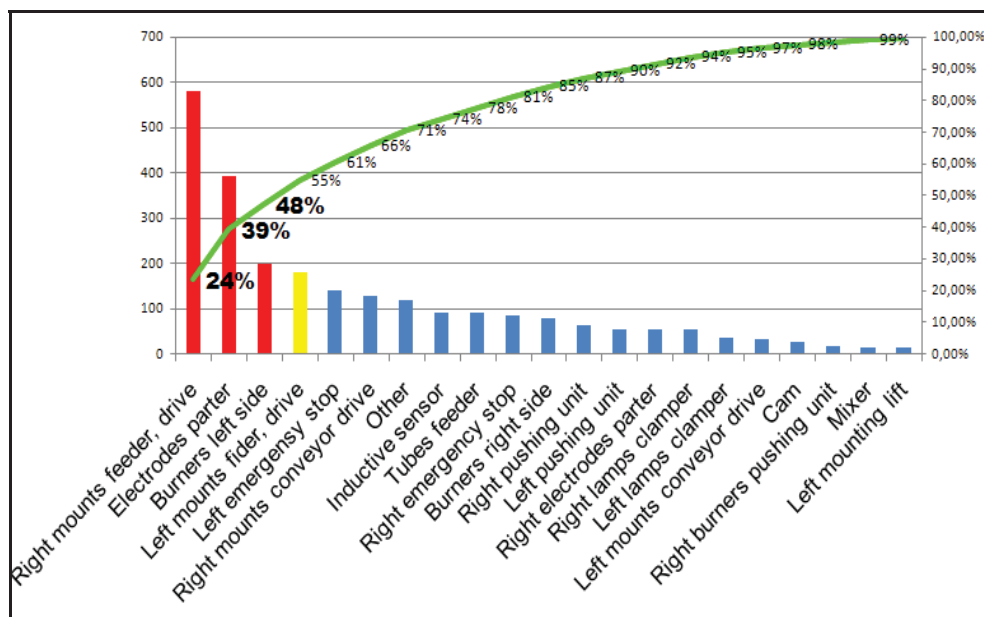


Fig.6. Breakdown time for sealing machine units

The very indication of the weak points in the set of several machines is not good enough information for building the monitoring system and that is why analysis of the weak points on a lower level has been done (e.g. the analysis of the faulty mechanisms of the sealing machine has been made). The result of the analysis is indication of the group of the machine unit which cause the biggest trouble (Fig.6) in the context of breakdown burner on the left side of the machine, electrodes partter on the left side as well as mounts feeder with drive.

The probability of the unit breakdown has been defined and also the auxiliary indicator has been introduced in the shape of *breakdown time particular unit of machine*. The values of the auxiliary indicator (Fig.7) for the certain mechanisms confirms the choice of those mechanisms: burners left side, electrodes left side parter and mounts feeder with drive.

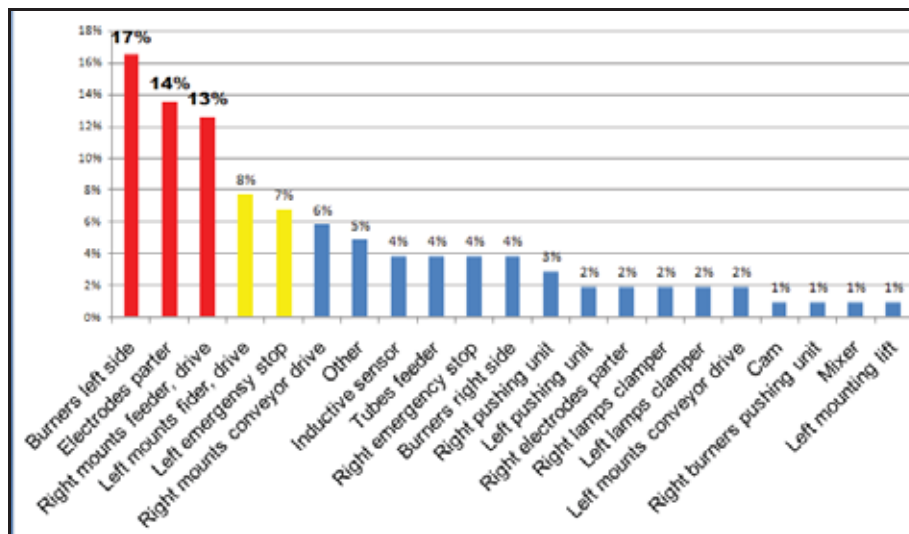


Fig.7. Breakdowns probability of sealing machines units

5. Conclusions

To sum up, the above study as well as the analysis of the breakdowns, the current operating system is not efficient enough, because the breakdowns done during the current maintenance strategy does not allow for the determination of some damages. This inability leads to the decrease in the trust level necessary for the production planning, which influences the company image. Changing into the new strategy may not only facilitate the controlling processes but will probably allow planning of the stops according to the needs, which may bring benefits such as decreasing the amount of stored items, lowering the time-consuming of the operation system and will lead directly to saving the financial means.

References

- [1] Będkowski, L., *Elementy diagnostyki technicznej*, WAT, Warszawa 1991.
- [2] Box, G., Jenkins, G.: *Time series analysis, forecasting and control*, London 1970.
- [3] Cempel, C., *Ewolucyjne modele symptomowe w diagnostyce maszyn*, Materiały I Kongresu Diagnostyki Technicznej, Gdańsk 1996.
- [4] Cholewa, W., *Diagnostyka techniczna maszyn*, Wyd. Politechniki Śląskiej, Gliwice 1992
- [5] Korbicz, J., Kościelny, J.M., Kowalczyk, Z., Cholewa, W. (red.): *Diagnostyka procesów*. WNT, Warszawa 2002
- [6] *Linia produkcyjna HOR 6002*, Materiały Philips Lighting Poland S.A., Piła 2006.
- [7] Niziński, S., Michalski, R., *Diagnostyka obiektów technicznych*, ITE Radom 2002.
- [8] Tylicki, H., *Optimization of the prognosis method of mechanical vehicles technical state*, Wydawnictwa uczelniane ATR, Bydgoszcz 1998.
- [9] Uhl, T., Batko, W., *Wybrane problemy diagnostyki maszyn*, CCATIE 4, Kraków 1996
- [10] Żółtowski, B., *Podstawy diagnostyki maszyn*. Wydawnictwa Uczelniane ATR, Bydgoszcz 1997.
- [11] Żółtowski, B., Niziński, S., *Modelowanie procesów eksploatacji maszyn*, WITPiS, Sulejówek 2007.



ANALYSIS OF THE KNIFE-BAR DYNAMICS MOVEMENT IN CUTTING UNIT

Marcin Zastempowski, Andrzej Bochat

*University of Technology and Life Sciences in Bydgoszcz
Faculty of Mechanical Engineering
ul. Kaliskiego 7, 85-796 Bydgoszcz, Poland
e-mail:zastemp@utp.edu.pl*

Abstract

Presented in this article are the results of the analysis of the movement dynamics of a scissor-fingers cutting unit, propelled by an asymmetric crank unit. The analysis was undertaken in order to create a database for the purpose of building a model of mathematical cutting process and carrying out simulative calculations needed for efficiency optimization of crop harvesting. The analysis of the movement dynamics of a scissor-fingers cutting unit presented in this paper enables to calculate the coefficient of friction in actual machine-working condition.

Keywords: *scissor-fingers cutting unit, dynamics of a knife-bar, friction in the scissor-fingers cutting unit*

1. Introduction

A scissor-fingers cutting unit is the basic working unit in numerous agricultural machinery. It is often used in combine harvesters, forage harvesters and mowers.

The idea behind the design of the scissor-fingers cutting unit is that the unit is comprised of a moving knife-bar and a stationary fingers-bar. Knives riveted to the knife-bar form a trapeze. Blades of the knife are smooth or nicked.

Fingers attached to the fingers-bar are used for separating sheared material into portions.

The fingers are incisioned, what enables the knives' reciprocating movement and they are anteriorly narrowed – allowing easier material separation. In some designs stalks are clinched to fingers forming counter-cutting edges. However in other designs the side edges of fingers serve this function. Appropriate adhesion between knives and a stalk is provided by stresses bolted to the fingers-bar. Moreover, knife-bar rests upon a slide. The design of a scissor-fingers cutting unit is presented in Fig 1.

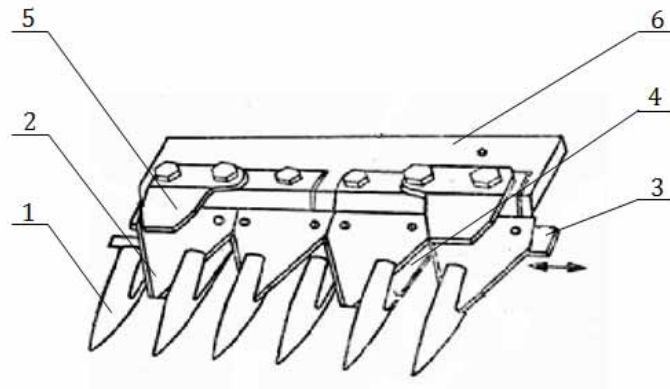


*Fig. 1. An example design of a scissor-fingers cutting unit [3]:
1-finger, 2-knife, 3-knife bar, 4-counter-cutting edge, 5-knife-bar stress, 6-fingers-bar*

Presented in Fig. 2, on the other hand, is a cross-sectional example of a scissor-fingers cutting unit.

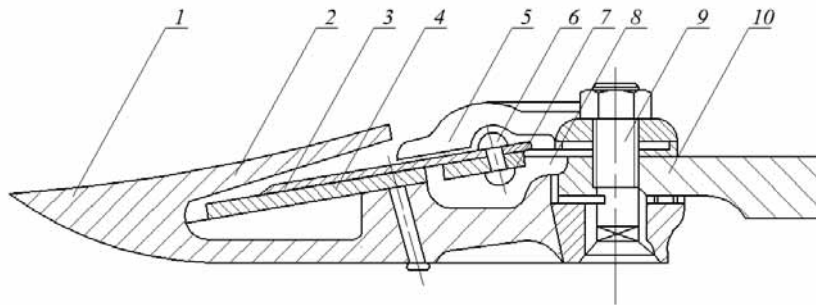


*Fig. 2. A cross-sectional example of a scissor-fingers cutting unit [3]:
1 – finger, 2 – fingers blade, 3 – knife, 4 – stalk, 5 – stress, 6 – rivet, 7 – moving knife-bar, 8 – slide, 9 – screw, 10 – stationary fingers-bar*

The operating principle of a scissor-fingers cutting unit is that fingers separate sheared plants and divide them into portions. Subsequently every knife squeeze stalks of plants into the side edges of fingers so-called stalks (counter-cutting edges) and perform the shearing.

The most often used form of propulsion for a knife-bar's reciprocating movement are asymmetric crank mechanisms, which provide the lowest abrasion.

Shearing of plant material by the use of a scissor-fingers cutting unit is the basic technological process under crop harvesting.

The existing design solutions for cutting units are characterized by significant energy consumption of the cutting process, what consequently leads to equipping their propulsion units with high output engines. This points out the fact that known design solutions were created based mostly on constructor's intuition. It is related to the lack of mathematical models describing the cutting process by the use of a scissor-fingers cutting unit, upon which simulative calculations could be carried out that are the basis for optimization of the design of cutting units and a possible increase in the effectiveness of the cutting process ex. crop shearing.

Construction of such models is not possible without a detailed analysis of the movement of a scissor-fingers cutting unit.

2. Analysis of the movement of a knife-bar of a scissor-finger cutting unit

The work analysis of a scissor-fingers cutting unit in a dynamic aspect is somewhat troublesome because of the complexity of the whole system and the imperfection of the dynamic dependences describing it. In a scissor-fingers cutting unit we can distinguish the following parts:

- spinning wheel with a crank,
- rod,
- knife-bar,
- fingers-bar with a slide.

Experimental research of a scissor-fingers cutting unit in a dynamic aspect carried out by the authors does not provide a sufficient answer due to the fact, that it is referring to the sum of pressures inflicted on each element and does not isolate the causes of their occurrence. Additionally, the research indicates significant drag of the knife-bar's idle movement.

Therefore, the authors of this paper carried out the analysis of the dynamics of a scissor-fingers cutting unit. The model of the dynamics was compiled based on the following assumptions:

- the eccentric disc is spinning with a constant angular velocity ω ,
- coulomb friction is present between the knife-bar and the slide,
- frictional resistance between a knife-bar and a rod, and between a rod and a crank are omitted.

Presented in Fig. 3 is the schematic of an asymmetric crank mechanism.

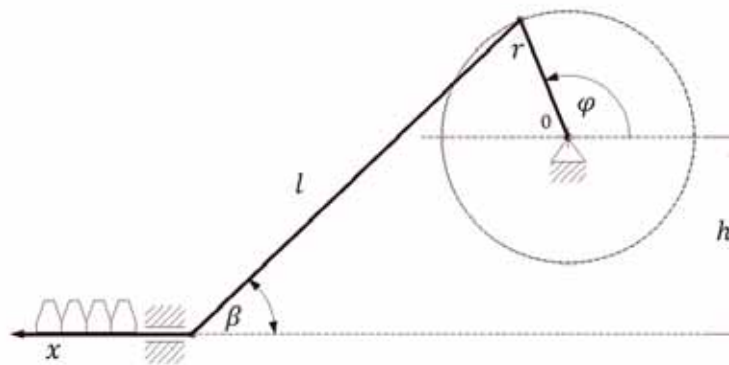


Fig 3. Schematic of an asymmetric crank mechanism:

r – crank's radius, l – rod's length, φ – crank's rotation angle, x – Knife-bar's displacement (the knife-bar in the figure has been rotated by 90° in relation to the real plain of movement), β – rod's angle against knife-bar's plain of movement, h – distance between crank's rotation axis and knife-bar's plane of movement

In order to determine knife-bar's inertia forces B_n and rod's inertia forces B_k their masses have been designated. For the design of a scissor-finger-cutting unit propelled by asymmetric crank unit the rod's mass has been designated to equate $m_k = 2,60$ kg and the knife-bar's mass to equate $m_n = 4,12$ kg.

Knife-bar's inertia force B_n is described by the equation:

$$B_n = m_n |\alpha_n|, \quad (1)$$

where:

m_n – knife-bar’s mass,
 a_n – knife-bar’s acceleration.

Whereas rod’s inertia force B_k is described by the equation:

$$B_k = m_k \sqrt{a_x^2 + a_y^2} \quad (2)$$

where:

m_k – rod’s mass,
 a_x – ingredient along the x axis of rod’s acceleration,
 a_y – ingredient along the y axis of rod’s acceleration.

The diagram of inertia forces described by equations (1) and (2) is presented in Fig. 4.

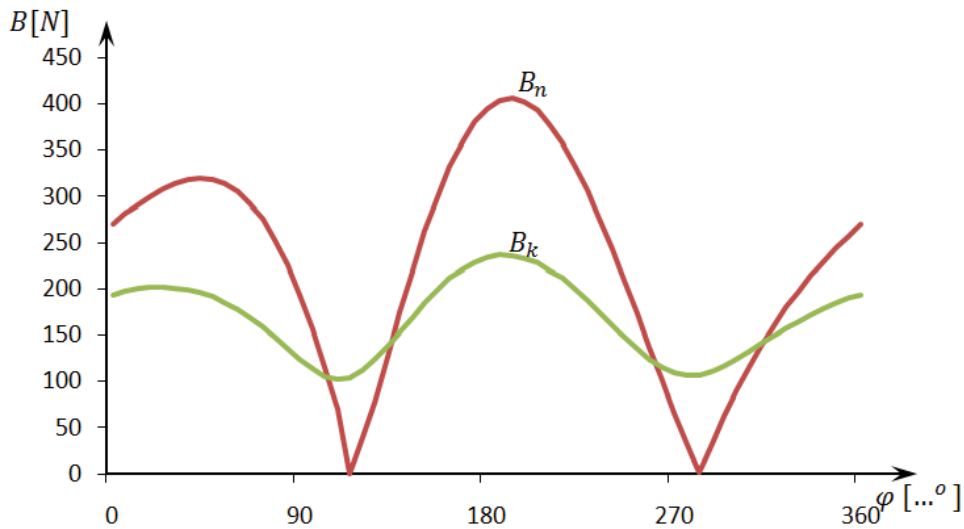


Fig. 4. The diagram of rod’s inertia force B_k and the diagram of knife-bar’s inertia force B_n

It is derived from Fig. 4 that rod’s inertia force B_k reaches values approximately similar to knife-bar’s inertia force B_n . This is the reason why during the analysis of a cutting unit’s dynamics the rod’s inertia forces B_k are omitted, what is a common practice in recognized publications [2, 3] and being unfounded can lead to faulty results.

That is why the disposition of forces working on a rod in a scissor-fingers cutting unit has been evaluated, what is presented in Fig. 5. Forces working on the rod R and P , can be described by ingredients $R = (R_x, R_y)$ and $P = (P_x, P_y)$.

Force R originates from the crank working on the rod in the point of their kinematic linkage. Force P is connected with the crank working on the rod also in the point of their kinematic linkage.

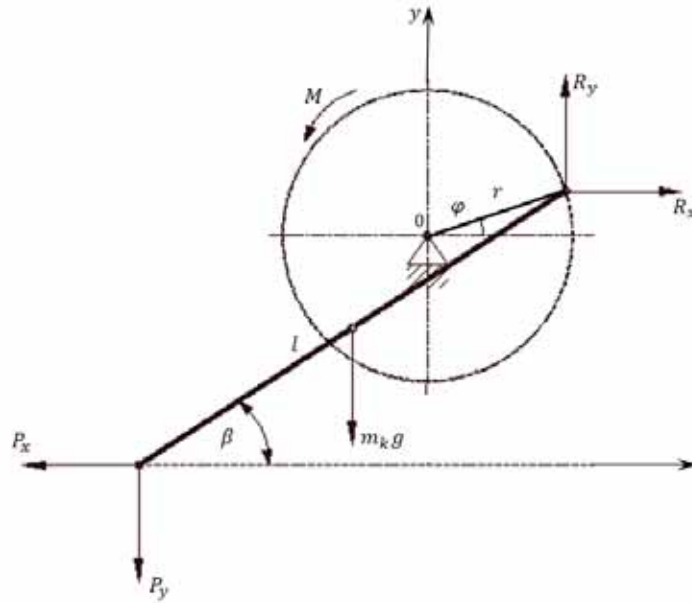


Fig. 5. The division of forces working on the rod in idle movement in a scissor-fingers cutting unit

Crank's action against the rod is described by the dependence:

$$-R_x r \sin(\pi - \varphi) + R_y r \sin\left(\frac{\pi}{2} + \varphi\right) = M, \quad (3)$$

where:

M – instantaneous torque.

Fig. 6 presents the division of forces working on a knife-bar.

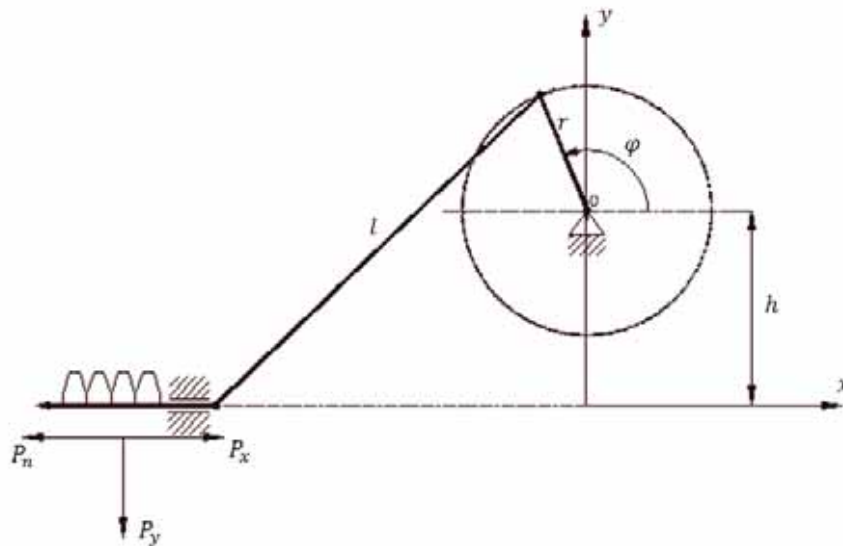


Fig. 6. Forces working on the knife-bar in idle movement

Equation of knife-bar's dynamics during its idle movement is described by the dependency (4):

$$P_n - T = m_n \frac{dv_n}{dt}, \quad (4)$$

where:

P_n – horizontal force $P_n = -P_x$,

T – abrasive force of a knife-bar in a slide,

m_n – knife-bar's mass,

v_n – knife-bar's velocity described by the equation.

Assuming that the rod's movement is a flat movement and designating the point of rod's center of gravity as a point used for describing the motion, an analysis has been carried out which provided three equations:

- sum of ingredient forces on x axis equals center of gravity's force of inertia,
- sum of ingredient forces on y axis equals center of gravity's force of inertia,
- sum of torques toward the center of gravity equals a derivative of rod's winding.

The three equations described above in combination with the equation (3) produce a closed system of four equations, from which forces can be designated.

The sum of torques toward center of gravity c can be described by the following dynamic equation:

$$R_y \frac{l}{2} \sin\left(\frac{\pi}{2} + \beta\right) + P_y \frac{l}{2} \sin\left(\frac{\pi}{2} + \beta\right) - R_x \frac{l}{2} \sin(\pi - \beta) - P_x \frac{l}{2} \sin(\pi - \beta) = J_k \frac{d\omega_k}{dt}, \quad (5)$$

where:

l – rod's length,

J_k – mass moment of inertia,

ω_k – rod's angular velocity toward rod's center of gravity.

After transforming the equation (5) a formula for calculating the abrasive factor μ is received:

$$\mu = \frac{\frac{\bar{M}}{r} + lm_k \omega^2 f_1 - m_n \omega^2 r f_2}{m_n g f_3 - lm_k \omega^2 f_4}. \quad (6)$$

Equation (6) is an entangled dependence due to the abrasive factor μ that is why its designation requires an application of numeric procedures used for solving nonlinear equations.

The whole dynamic analysis of the scissor-fingers cutting unit, including the designation of the abrasive factor μ was carried out based on original computer program written using Turbo Pascal.

Dependency (6) enables to designate the abrasive factor for each component of a scissor-fingers cutting unit and crank's given angular velocity. In order to designate the abrasive factor μ it is necessary to know the average torque \bar{M} working on the crank. Exemplary results of abrasive factor μ calculations are compared in Tab. 1. Torque's value \bar{M} of the idle movement at crank's given angular velocities have been determined experimentally.

Tab. 1. Exemplary abrasive factor values calculated from dependence (6)

<i>Crank's angular velocity ω [rad/s]</i>	<i>Torque of the idle movement M [Nm]</i>	<i>Abrasive factor μ</i>
30,92	22,80	1,416
47,57	23,36	1,234
103,70	28,44	0,710

3. Summary

The dynamic analysis of a scissor-fingers cutting unit presented in this paper allows to determine an abrasive factor μ in the machine's real working conditions.

During the analysis of the bibliography a similar approach in order to determine the abrasive factor in working conditions of a cutting unit has not been found..

Values of the abrasive factor presented in publications on the subject are most probably based on experiments on a moving bar without an installed crank [1]. The values of the abrasive factor determined in such manner are several times lower than the results presented in this article.

Based on dependence (6) it is conclusive from the determined values of the abrasive factor μ that with the increase of the crank's angular velocity ω the value of the abrasive factor decreases.

References

- [1] Dmitrewski, J., *Teoria i konstrukcja maszyn rolniczych*, TOME III. PWRiL, Warszawa, 1978.
- [2] Gach, S., Kuczewski J., Waszkiewicz Cz., *Maszyny rolnicze. Elementy teorii i obliczeń*, SGGW Publishing House, Warszawa, 1991
- [3] Kanafojski, Cz., Karwowski, T., *Teoria i konstrukcja maszyn rolniczych*, TOME II. PWRiL, Warszawa, 1980.
- [4] Zastempowski, M., *Badania energochłonności cięcia nożycowo-palcowym zespołem tnącym*, Phd. Thesis, UTP, Bydgoszcz 2008.



IMPORTANCE OF COMMINATION IN PLASTICS PROCESSING

Joachim Zimniak

*University of Technology and Life Sciences
Faculty of Mechanical Engineering
ul. Prof. S. Kaliskiego 7, 85 – 789 Bydgoszcz, Poland
tel.: +48 52 340 87 21, fax.: +48 52 340 82 45
e-mail: zimniak@utp.edu.pl*

Abstract

The state-of-the-art concerning size reduction of polymer materials has been presented in this paper. The main objectives of this operation as well as the ways of their realization have been discussed. The variants of matching action of cutting edges when comminuting polymers have been gathered in tables. The universal stand for carrying tests of energetic verification for the new rotational size reduction techniques as well as preliminary results have been shown. It has been stated that geometry of matching cutting edges has considerable influence on energy consumption. The directions of further investigation have been pointed out.

Keywords: polymeric materials, disintegration of polymer, cutting forces, test stand

1. Introduction

In 2005, global production of plastics exceeded the magical limit of 200 million tonnes [1] which means that the total resource mass of secondary materials (commonly referred to as waste) has also proportionately increased. Many research centres in the world undertake research and development as well as implementation work which is aimed at proper use and management of secondary resources (including cross-linked polymers and elastomers), through material, raw material recycling [2]. High requirements of development and improvement of composite components preparation techniques for further processing by extrusion, injection or molding method are often demanded for material recycling and composite materials technology.

Comminution occurs very often, apart from separation, washing, or decomposition, as one of the preparatory processes (components) in the formation of composite materials which means that it is a very important and still valid problem to be solved from the technological, structural, economic and environmental protection point of view. Comminution – scientifically attributed by R. Sikora [3] to the discipline of machining of plastics.

Preparation of composite material components by comminution is usually conditioned by: the expected degree of comminution, appropriate granular distribution, desired morphology of elementary particle and others [2-6]. The mechanical comminution performed by the rotating knife cutting [6], to be discussed in detail in point 2.2 of the study may meet the mentioned requirements for polymeric materials and cross-linked elastomers.

2. Comminution implementation

2.1 Phenomenological models

The basic comminution methods use three main types of loads: compression, tension and shearing. Depending on the physical, strength-related properties and type of comminuted material, a proper shape and particle size-reduction should be applied in the construction design to achieve high efficiency of the process, which can be achieved through:

- crushing obtained by squeezing a particle using two surfaces rotating with equal speed (Fig.1-1),
- breaking by impacts, induced by high-speed machinery elements acting on the particles (Fig. 1-2),
- rotary cutting performed by knives' cutting edges (Fig.1-3),
- quasi-shearing as an eco-friendly method of material comminution (Fig. 1-4),
- mulling by rubbing two surfaces, one of which is stationary (Fig. 1, 5, 6).

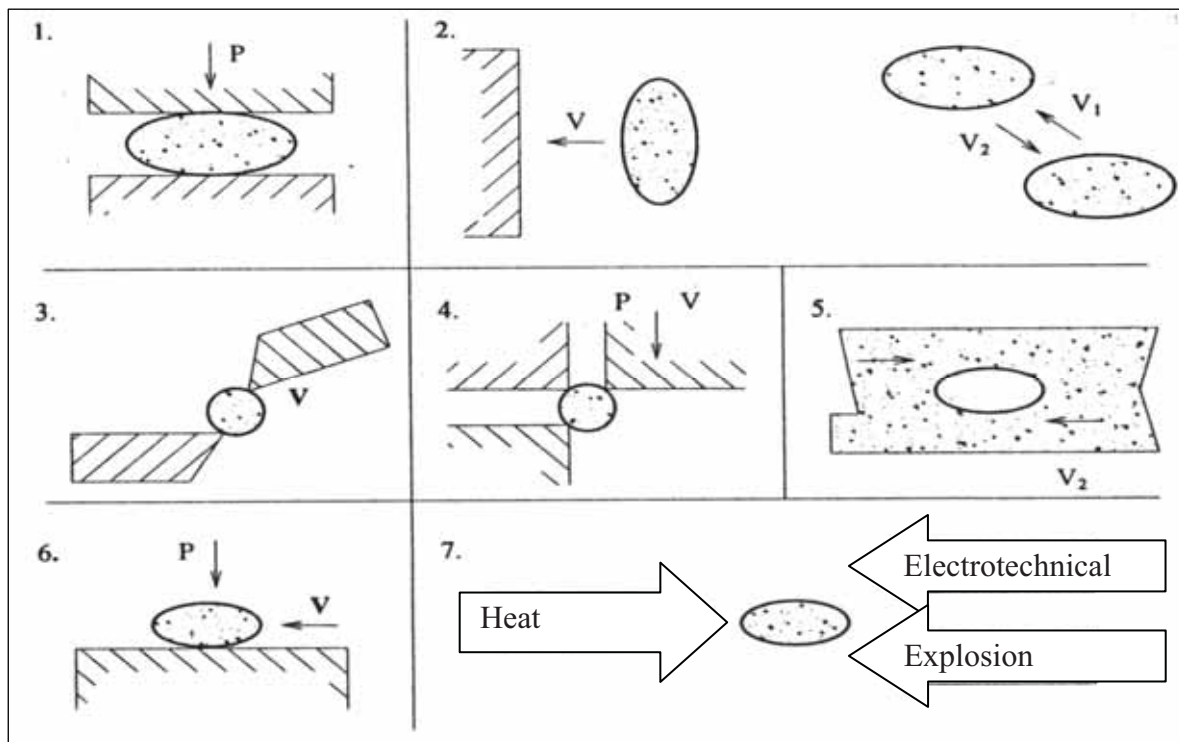


Fig. 1. Phenomenological models of size-reduction [4,5,7]

For thermoplastics (also for elastomers), the dominant role does comminution by knife cutting (Fig. 1-3), also known as rotary. Noteworthy is also polymer comminution through the so-called quasi-shearing (phenomenological model marked as fig. 1-4) which is characterized, among others, by low energy consumption, low noise and excellent repeatability of granular classes. This method of comminution is described in greater detail in the work of J. Flizikowski in [4].

2.2 Rotary knife cutting

The comminution method of rotary cutting is carried out in knife mills. A schematic diagram of a typical device for comminution of polymeric materials is shown in Figure 2. Rotary cutting of plastics and secondary elastomers (commonly known as waste) is a result of the collaborative work of a rotating knife executing a rotary movement (centrifugal) and a stationary knife

embedded in the comminution device housing. An effective division of the comminuted material (secondary rubber) occurs only if, moved around in the pulveriser chamber, it finds its way into the clearance between the cutting edges of the knives : stationary and rotary.

Rotary knife cutting, which is shown in general in fig. 3, is a result of the collaborative work of a movable knife, rotating knife and stationary knife embedded in the comminuting machine housing. During rotary cutting, the polymer lies on the stationary knife rake face surface from which a piece of element (particle, grain) is cut off (separated).

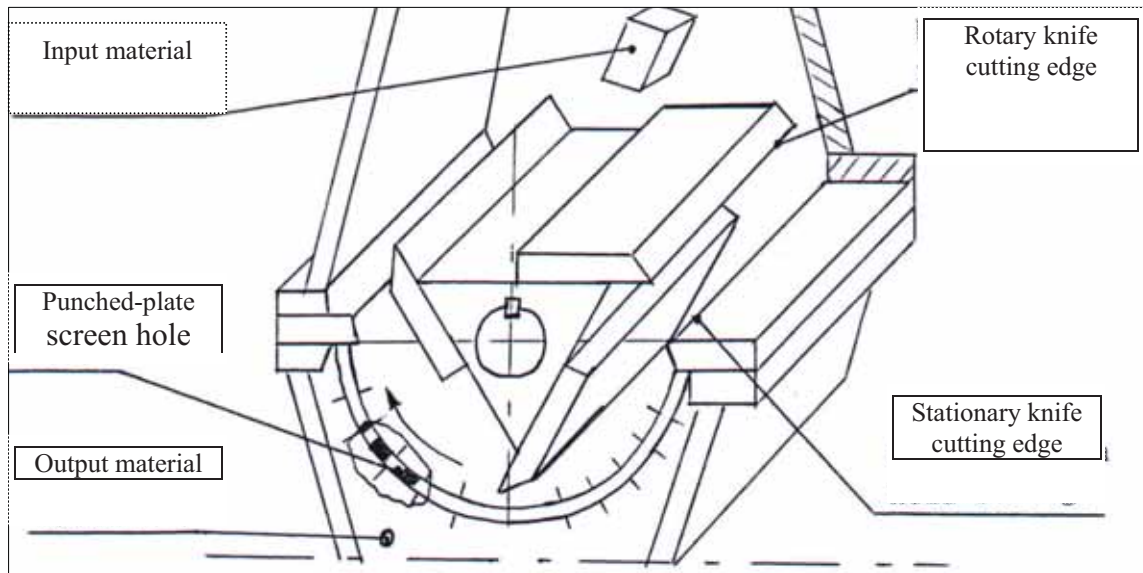


Fig.2. The view of typical device for size reduction of plastics and elastomers [5,6].

The force components of, which are the result of the cutting force F_c , affect the part separated. These are as follows:

- the F_p material particle acceleration force (depending on cutting speed),
- the F_d material particle deformation force (depending mainly on the rotary knife value),
- the F_r force of friction of rubber against the rake face surface of the rotary knife (depending mainly on the stiffness of the material cut and the values of the friction coefficients) the F_v force of rubber separation (depending mainly on the resistance value).

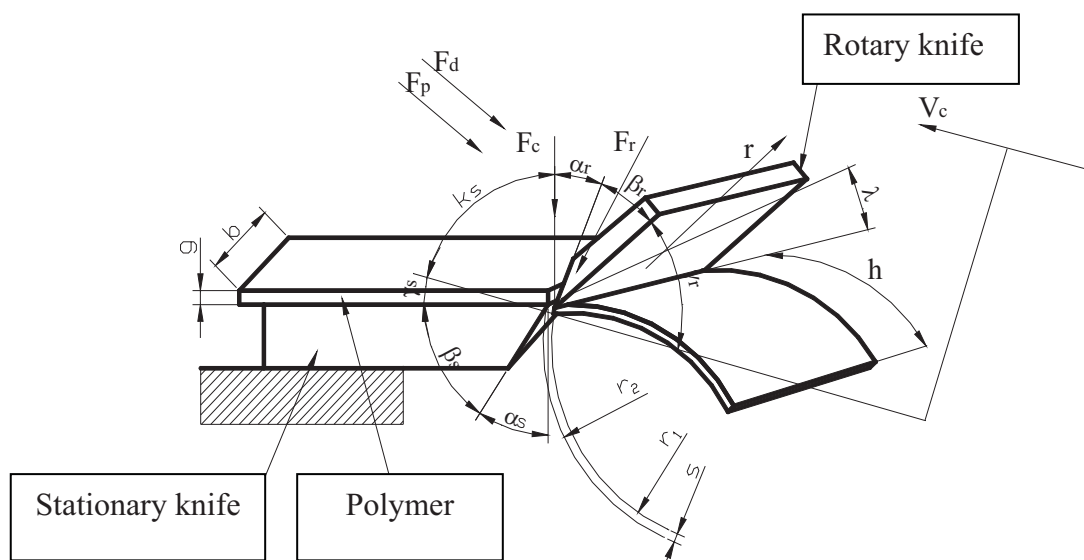


Fig.3. Scheme of the geometry of the rotating knife size-reduction method [6].

Given the above preliminary analysis, it can be assumed that the resultant cutting force will depend on: the cutting speed, the dimensions of the elements comminuted (feed size) and material stiffness, the coefficient of friction between material and steel, the cutting resistance, geometry of stationary and rotary knife blades (especially the blade angles) and the inclination angle of the main cutting edge of the stationary and rotary knives in relation to the pulveriser rotor axis. It can therefore be assumed that the overall semantic model of the resultant cutting force value - unknown as to the precise direction – during rotary cutting is presented by the following formula [4-6]:

$$F_c = f(b, g, h, \alpha_r, \beta_r, \gamma_r, \alpha_s, \beta_s, \gamma_s, \lambda, v_c, \dots)$$

where:

b, g - the width and thickness of materials,

h - the length of the material element being cut,

α_r and α_s – application angles of the knife: rotating and stationary (stationary and rotating knife geometry)

β_r and β_s - knife blade angles: rotary and stationary,

γ_r and γ_s - knife rake angles: rotary and stationary,

λ - the inclination angle of the stationary and rotating knife main cutting edge in relation to the rotor axis,

v_c – cutting tangential velocity

s – clearance between the knife cutting edges: stationary and rotary,

σ_c - cutting resistance and others.

Most of the basic parameters of the knife geometry during comminution (for example α_r and α_s , β_r and β_s , γ_r and γ_s , λ) are relatively well known and have been described in the literature [4-9]. Investigation of other parameters requires research and development work

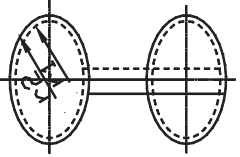
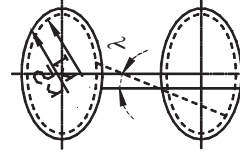
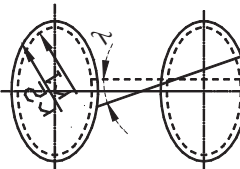
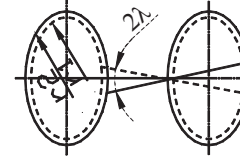
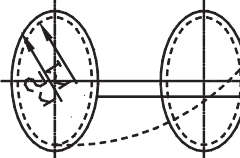
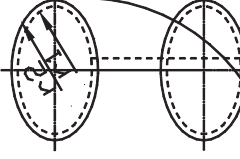
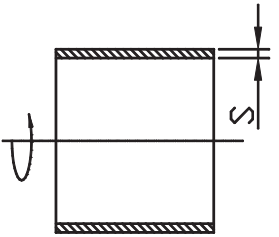
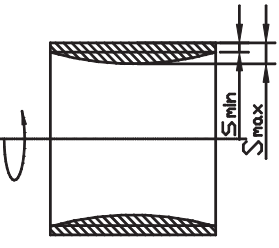
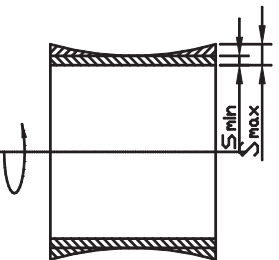
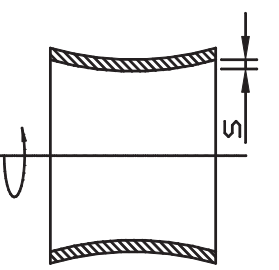
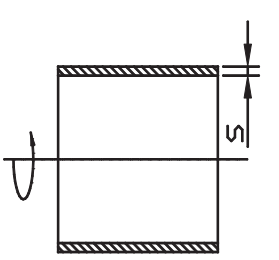
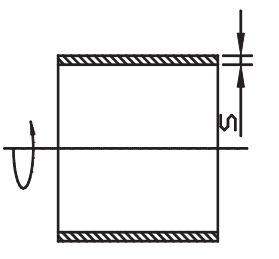
2.3 Cooperation variants of knife cutting edges

Rotary and stationary cutting edges of the knife can work together in a varied mutual arrangement. Table 1 summarizes variants of the knife cutting edge co-operation known from literature and own studies, providing the respective cutting edge co-operation scheme, the levelling of the surfaces developing through the cutting edges spinning around their axis, the shape of the clearance between the blades [6,9,11,12]. As is clear from the analysis of literature, comminution equipment design solutions often use a cutting edge cooperation case as indicated in Table 1 as B or C, with regard to the issue of reducing comminution energy consumption and noise level compared to cooperation, marked A. In recent years, the type of cooperation recommended (indicated in Table 1 as D) is referred to as "hyperboloidal"- as described by R. Konieczko [6,10] and is also referred to by H. Bauer [9] as "double-diagonal" for which energy consumption and noise levels are much lower compared to B and C cooperation.

As follows from preliminary tests conducted and results obtained, by applying an appropriate cutting edge cooperation design solution conventionally referred to as "quasi-tangent" [11,12], it is possible to reduce comminution energy consumption compared to D cooperation. These observations, preliminary results and own deliberations qualify the author to formulate the following hypothesis:

It can be assumed that there are rotary and stationary cutting edge cooperation conditions under which the energy consumption of the comminution process (or cutting force) will be smaller than for variants known and used in practice so far.

Table 1. Variants of matching edges of cutting knives [6,11,12]

	Rotary and stationary cutting edges of the knife in parallel to rotation axis. $\lambda = 0^\circ$	Rotary cutting edge of the knife at the angle of λ , stationary cutting edge of the knife in parallel to rotation axis	Rotary cutting edge of the knife in parallel, stationary cutting edge of the knife at the angle of λ to rotation axis	Rotary and stationary cutting edges of the knife inclined in the opposite direction at the angle of 2λ	Helical shaped cutting edge of rotary knife, stationary cutting edges in parallel to rotation axis*	Helical shaped cutting edge of stationary knife, rotary cutting edge in parallel to rotation axis
	A	B	C	D	E	F
Scheme of cutting edges mate						
Surface equations created by rotation of knives' cutting edges	Rotary cutting edge $x^2 + y^2 = r_1^2$ Stationary cutting edge $x^2 + y^2 = r_2^2$	Rotary cutting edge $\frac{x^2 - y^2}{a^2} - \frac{z^2}{c^2} = 1$ Stationary cutting edge $x^2 + y^2 = r_2^2$	Rotary cutting edge $x^2 + y^2 = r_1^2$ Stationary cutting edge $\frac{x^2 - y^2}{(a+s)^2} - \frac{z^2}{c^2} = 1$	Rotary cutting edge $\frac{x^2 - y^2}{a^2} - \frac{z^2}{c^2} = 1$ Stationary cutting edge $\frac{x^2 - y^2}{(a+s)^2} - \frac{z^2}{c^2} = 1$	Rotary cutting edge $y = x \cdot \operatorname{tg} \frac{z}{k}$ Stationary cutting edge $x^2 + y^2 = r_2^2$	Rotary cutting edge $x^2 + y^2 = r_1^2$ Stationary cutting edge $y = (x+s) \cdot \operatorname{tg} \frac{z}{k}$
Clearance shape between cutting edges						

3. Research purpose and methodology

This study aims to compare the energy consumption of the rotary knife cutting process (by defining the resultant cutting force) for selected types of cutting edge cooperation identified in Table 1 as C, D and E. Two types of materials were used for the studies: polystyrene (PS) and soft polyvinyl chloride (PVC) in the form of plates with a thickness of $g_1 = 1.2$; $g_2 = 2.4$ and $g_3 = 3.6$ mm. The clearances between the cutting edges were as follows. $S_1 = 0.1$ and $S_2 = 0.2$ mm. In order to compare the energy consumption for the types of cutting edge cooperation referred to, research was conducted in two stages. During exploratory research, not recounted in this paper, optimum values of angles λ and 2λ were first determined (for C and D according to Table 1), for which the cutting force value was the lowest. The optimal values of λ and 2λ determined were then used for the main research –comparative.

4. Research station

To achieve the assumed research goal and verify the hypothesis formulated, a universal comminution research station was developed whose versatility means that it can implement all types of knife cutting edge co-operation given in Table 1. In addition, a relatively wide range of clearances between the cutting edges can be used, the values of which are recommended in production facilities. A schematic diagram and major operating elements of the comminution device are shown in Figure 4.

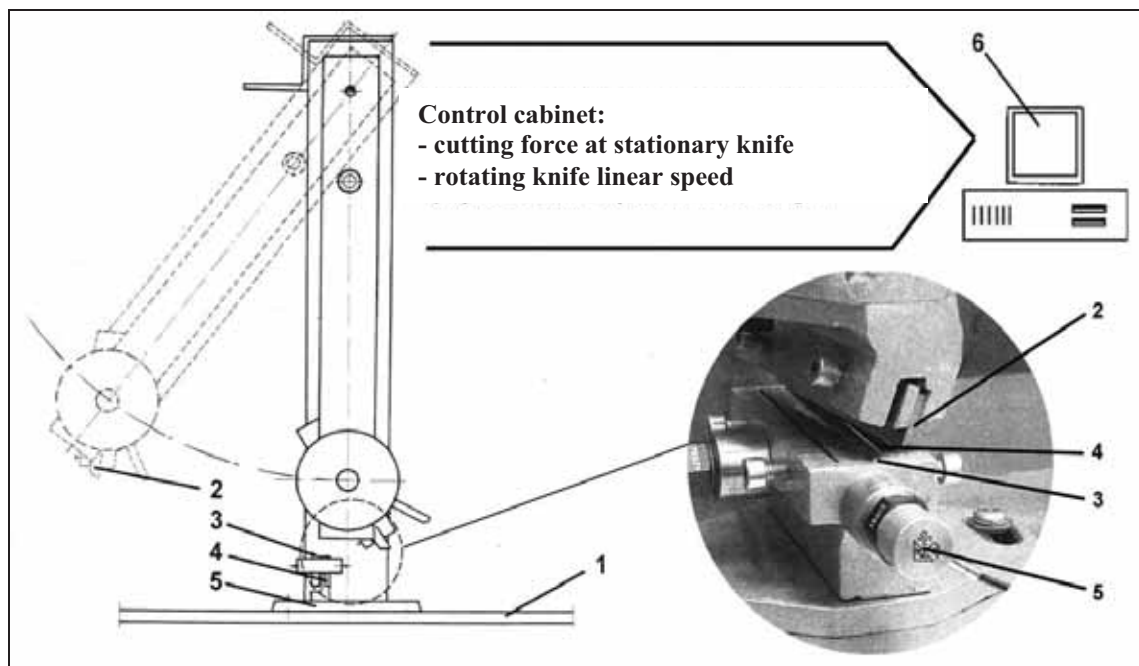


Fig. 4. Scheme of test stand for size reduction of polymers: 1-base, 2-rotating knives, 3-stationary knife, 4-material to be size reduced, 5-piezoceramic sensors, 6-control cabinet

An important feature of the research station is that for all comminution variants, it makes it possible to record the cutting force components in the direction of the x and y axis and, if required, also in the direction of the z axis [11,12]. The research station shown in Figure 4.,uses piezoceramic transducers that work with a type SVAN vibration analyzer with a four-channel SV06A preamp (Brühl and Kjaer) [12].

5. Test results

The test results of the impact of the type, thickness of the polymer material and the clearance between the knives for the cutting edge co-operation types adopted, i.e. A, C and E on the cutting force are shown in Figure 5 and 6. When analyzing the results obtained, note that in the area surveyed, the cutting force for PS and PVC is the lowest for variant E. This results from the fact that the cutting

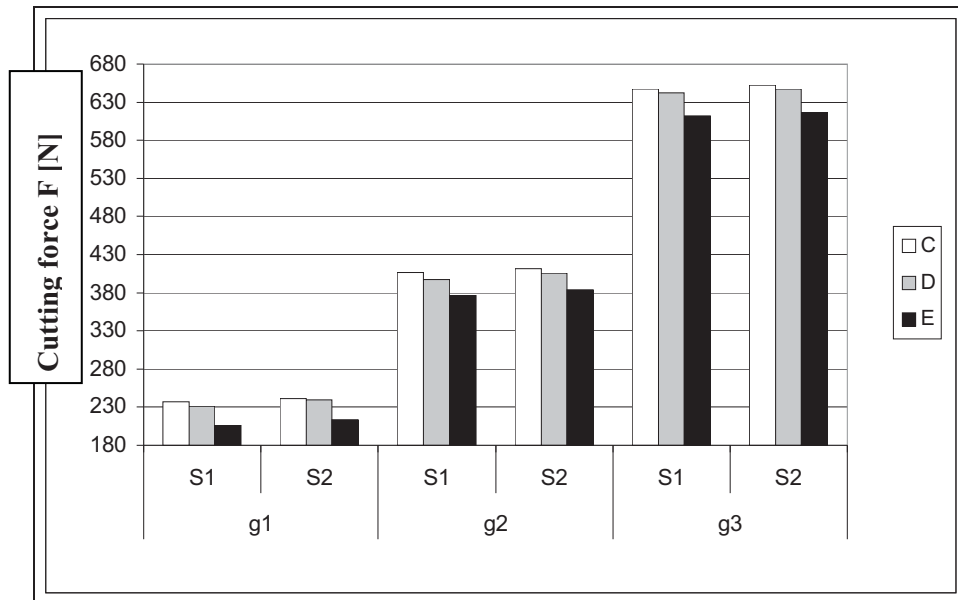


Fig. 5. Relationship between cutting force F and knife cutting edge cooperation type, value of clearance between knives S , thickness of material g (for PS)

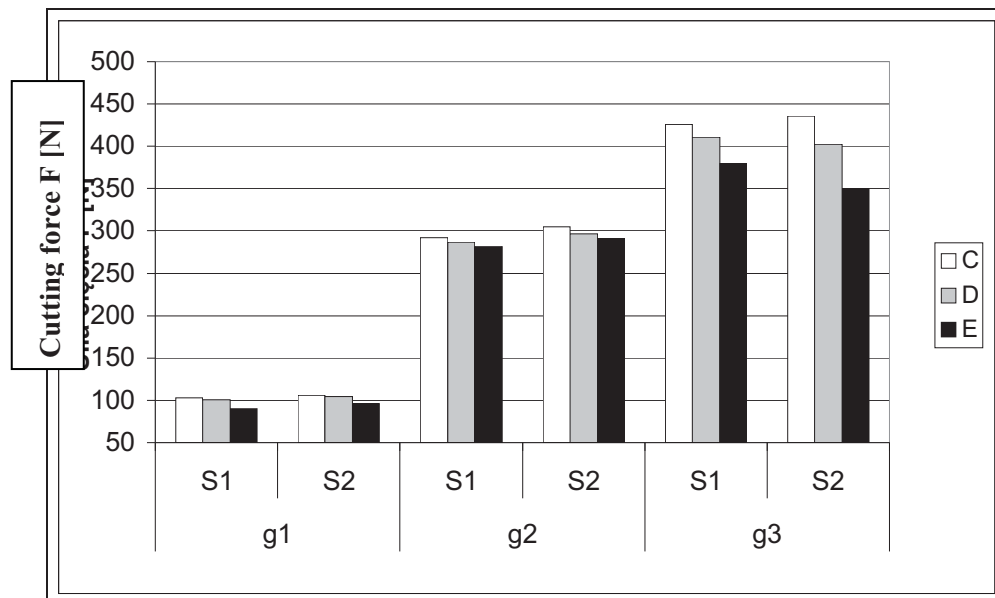


Fig. 6. Relationship between cutting force F and knife cutting edge cooperation type, value of clearance between knives S , thickness of material g (for PVC)

force is perpendicular to the material comminuted which is, among others, the essence of the patent obtained by the author [11]. Unlike in the case of C and D, no pushing of material along the cutting edge occurs here, which, as mentioned by R. Konieczka [6.11], is a result of a tangential

component, whose share in the total (resultant) cutting force, as established by W. Bauer, is quite significant, and highly depends on angle 2λ [9].

6. Conclusion

As follows from the preliminary research results obtained, a cutting force reduction was achieved for the polymer materials investigated, i.e. PS and PVC by about 20%. The results of own laboratory tests and literature reports indicate that there are reserves for a reduction in the cutting force required to separate the polymer material, which is directly related to the reduction in energy consumption of the comminution process while maintaining high quality of the comminution product. The knife-based comminution design solutions used to date do not use all the knife cutting edge cooperations possible to be implemented. The results obtained at the model research stations should be a basis for the implementation of science and technology development using a knife pulveriser with a suitable design. Further work in this area is recommended, given the high energy consumption of comminution.

References

- [1] <http://de.wikipedia.org/wiki/Kunststoff>. *Kunststoff aus Wikipedia, der freien Enzyklopädie*, 2006.
- [2] Brandrup, J., Bittner, M., Michaeli, W., Menges, G., *Die Wiederverwertung von Kunststoffen*. Carl Hanser Verlag München - Wien 1995.
- [3] Sikora, R., *Obróbka tworzyw wielkocząsteczkowych*. Wydawnictwo Edukacyjne, Warszawa 1995.
- [4] Flizikowski, J., *Rozdrabnianie tworzyw sztucznych*. Wydawnictwa Uczelniane ATR w Bydgoszczy, Bydgoszcz 1998.
- [5] Pahl, M.H., *Zerkleinerungstechnik*. Verlag TÜV, Rheinland 1994.
- [6] Konieczka, R., *Untersuchen des Schneidvorgangs beim Zerkleinern von Kunststoffen*. Kunststoffe Nr 7/1989..
- [7] Herbold, K., *Feinmahlen von Kunststoffabfällen löst Qualitätsprobleme*. Kunststoffe Nr 11/1997.
- [8] Mientkewitz, O., Bauer, W., *Zerkleinerung von Hochleistungskunststoffen*. Kunststoffe Nr. 12/2000.
- [9] Bauer, W., *Untersuchung des Einzelzerkleinerungsvorganges in Schneidmühlen am Beispiel von Polypropylen*. VDI Verlag, Reihe 3: Verfahrenstechnik, Düsseldorf 2001.
- [10] Plochocki, A., Konieczka, R., *Hyperboloidal rotary cutter – modeling and application in recycling of polyethylene film in pelletizing – line aggregation*. Plastics Bridging the Millennia “ANTEC’99”, 2-6 May New York 1999.
- [11] Polish patent No 335245 „*Urządzenie rozdrabniające*”. Author: J. Zimniak, 2008r.
- [12] Zimniak, J., *Energetyczna weryfikacja nowej techniki rozdrabniania próbek polimerowych PS i PVC*. Inżynieria i Aparatura Chemiczna (44), nr 1-2/2005.